**FACULTY
OF MATHEMATICS
AND PHYSICS**
Charles University

DOCTORAL THESIS

Jakub Kandra

The Belle II vertex detector alignment studies and prompt $\sin 2\phi_1$ analysis

Institute of Particle and Nuclear Physics

Prague 2021

I declare that I carried out this doctoral thesis independently, and only with the cited sources, literature and other professional sources. It has not been used to obtain another or the same degree.

I understand that my work relates to the rights and obligations under the Act No. 121/2000 Sb., the Copyright Act, as amended, in particular the fact that the Charles University has the right to conclude a license agreement on the use of this work as a school work pursuant to Section 60 subsection 1 of the Copyright Act.

In . . . . date . . . .
<div align="right">Author's signature</div>

Acknowledgements

Title: The Belle II vertex detector alignment studies and prompt $\mathbf{\sin 2\phi_1}$ analysis

Author: Jakub Kandra

Institute: Institute of Particle and Nuclear Physics

Supervisor: prof. RNDr. Zdeněk Doležal, Dr., Institute of Particle and Nuclear Physics

Abstract: This thesis is focused on the alignment studies of the vertex detector during first years of the Belle II detector operation and the first prompt $\sin 2\phi_1$ analysis using the first relevant data collected by the detector. Firstly, the Belle II detector and the SuperKEKB accelerator is introduced. Secondly, the software framework and tools operation is explained, then the alignment procedure and developed validation procedures are described in detail. Fourth section reports about the first years of the detector operation. Next three sections are related to different alignment studies during thee different periods of the vertex detector operation: the Phase 2, VXD Commissioning and beginning of the Phase 3 early. The last section covers the time-dependent CP Violation and mixing measurements performed using the data collected prior to the 11^{en} of May 2020.

Keywords: Belle II, vertex detector, alignment, mixing measurement, time dependent CP Violation measurement

Contents

Introduction

The Standard Model is a particle physics theory that tries to categorize all known elementary particles and explain their interaction. It is essential in our understanding of the evolution of the early Universe. Violation of the combined charge conjugation and parity (CP) symmetries is required to describe the observed dominance of matter over antimatter in the observable Universe. Unlike the electromagnetic and strong interactions, the weak interaction in the quark (hadron) sector does not conserve the CP symmetry. In 1964, the violation of CP symmetry was discovered in the decays of neutral kaons. To this day, another CP symmetry violations have been observed in charmed mesons or bottom quarks. All observed cases of CP violation can be completely explained in terms of the Cabibbo-Kobayashi-Maskawa (CKM) model of the flavour-changing weak interaction among quarks [1, 2].

In 1987, the discovery of $B^0 - \overline{B}^0$ mixing introduced a possibility of testing the CKM model in neutral B mesons. The idea of studying CP asymmetry in neutral B-meson decays motivated the creation of an entirely new type of particle physics experiment, designed to produce massive amounts of $B^0\overline{B}^0$ pairs - the *B factory*. In the 1990s, two B factories were built and operated: PEP-II/BaBar and KEKB/Belle. The PEP-II and KEKB accelerators were built as asymmetric-energy circular $e^+ e^-$ colliders with two main storage rings: PEP-II in the SLAC National Accelerator Laboratory (Stanford, USA), and KEKB in the High Energy Accelerator Research Organization (KEK) in Tsukuba, Japan. The Belle detector used a crab-crossing scheme to improve peak luminosity on $2.1 \times 10^{34} \mathrm{cm}^{-2}\mathrm{s}^{-1}$, more than twice the original design goal. The KEKB and PEP-II produced 772×10^6, resp. 465×10^6 $\mathrm{B^0\overline{B}^0}$ pairs [3, 4].

In the early 2000s, Pantaleo Raimondi proposed a new final focusing system for e^+e^- colliders called the *crab waist*, opening a possibility to increase the amount of data produced by a Belle or BaBar type B-factory by two orders of magnitude. This motivated the design and construction of a new generation of B-factories. The one that was actually put in operation in the late 2010s was the SuperKEKB/Belle II at KEK in Tsukuba, Japan, and the facility inherited the general infrastructure of KEKB/Belle. This *Super-B* factory is expected to provide huge amounts of data that will advance the precision of particle physics measurements and thus allow more rigorous tests of the Standard Model [5, 6].

The *time-dependent CP violation* measurement in neutral $B^0 - \overline{B}^0$ is based on two principles: decays with interfering amplitudes and the CP asymmetry. The interference between mesons is described by the term $V_{\mathrm{cd}}^*V_{\mathrm{cd}}V_{\mathrm{td}}V_{\mathrm{tb}}^*$, where $V_{\mathrm{cd}}, V_{\mathrm{td}}$ are elements of the CKM matrix and $V_{\mathrm{cd}}^*, V_{\mathrm{td}}^*$ are complex conjugated elements. The phase of this quartet in the CKM model can be parameterized as ϕ_1 (Belle notation) $= \beta$ (BaBar notation). The CP asymmetry can be determined between $B^0 \to J/\psi K_{\mathrm{S}}^0$ and $\overline{B}^0 \to J/\psi K_{\mathrm{S}}^0$. The amplitude of the direct process $B^0 \to J/\psi K_{\mathrm{S}}^0$ corresponds to the V_{cb} element of the CKM matrix. This process can also decay as $B^0 \to \overline{B}^0 \to J/\psi K_{\mathrm{S}}^0$. The measured deviation between these

amplitudes is related to phase $2\phi_1$. Due to the mixing of neutral B mesons with a frequency Δm_{d}, the deviation can be estimated as a function of the time difference between two B mesons, where one decays into the CP eigenstate $J/\psi K_{\mathrm{S}}^0$ and other decays into a flavour-specific (*flavour tagged*) final state. The advantage of the flavour tagged process is that the B-meson flavour can be estimated using final-state particles [4, 7].

The extraction of $\sin 2\phi_1$ from time difference distributions can be done using time-dependent probability to identify CP eigenstate in tagged B^0 or $\overline{B}^0$ mesons [4, 7]:

$$P_{B^0 \to J/\psi K_{\mathrm{S}}^0}(\Delta t) \equiv g^+(\Delta t) = \frac{e^{-\frac{\Delta t}{\tau_{B^0}}}}{4\tau_{B^0}} \left[1 + S_{\mathrm{f}} \sin(\Delta m_{\mathrm{d}} \Delta t) - C_{\mathrm{f}} \cos(\Delta m_{\mathrm{d}} \Delta t)\right],$$

$$P_{\overline{B}^0 \to J/\psi K_{\mathrm{S}}^0}(\Delta t) \equiv g^-(\Delta t) = \frac{e^{-\frac{\Delta t}{\tau_{B^0}}}}{4\tau_{B^0}} \left[1 - S_{\mathrm{f}} \sin(\Delta m_{\mathrm{d}} \Delta t) + C_{\mathrm{f}} \cos(\Delta m_{\mathrm{d}} \Delta t)\right]. \quad (1)$$

where τ_{B^0} is the lifetime of a neutral B meson, Δm_d is the mixing frequency, S_f is the time-dependent CP violation parameter ($S_f = \sin 2\phi_1$), and A_f is the direct CP violation parameter. The flavour of the tagged B meson is estimated by an algorithm with finite precision, so its inaccurancy also enters the equation 1:

$$g^\pm(\Delta t) = \frac{e^{-\frac{\Delta t}{\tau_{B^0}}}}{4\tau_{B^0}} (1 \mp \Delta w \pm (1 - 2w) \left[S_{\mathrm{f}} \sin(\Delta m_{\mathrm{d}} \Delta t) \mp C_{\mathrm{f}} \cos(\Delta m_{\mathrm{d}} \Delta t)\right], \quad (2)$$

where w is the wrong-tag fraction and Δw is the difference in the wrong-tag fraction between a B^0 and a $\overline{B}^0$. Both quantities can be estimated using a *control sample*, which is a decay of a neutral B meson into a flavour-specific final state. In parallel, the mixing frequency Δm_d can be extracted from a control sample:

$$P_{B^0 \overline{B}^0 \to B^0 \overline{B}^0}(\Delta t) \equiv g^{\mathrm{OF}}(\Delta t) = \frac{e^{-\frac{\Delta t}{\tau_{B^0}}}}{4\tau_{B^0}} \left[1 - \Delta w + (1 - 2w) \cos(\Delta m_{\mathrm{d}} \Delta t)\right],$$

$$P_{B^0 \overline{B}^0 \to B^0 B^0 / \overline{B}^0 \overline{B}^0}(\Delta t) \equiv g^{\mathrm{SF}}(\Delta t) = \frac{e^{-\frac{\Delta t}{\tau_{B^0}}}}{4\tau_{B^0}} \left[1 + \Delta w - (1 - 2w) \cos(\Delta m_{\mathrm{d}} \Delta t)\right], \quad (3)$$

where "OF" and "SF" mean the opposite and the same flavour of B mesons in the final state.

The key ingredients for the CP violation and mixing measurements are $\Delta t, w$ and Δw variables. The w and Δw require a precise flavour knowledge of the tagged B meson. The Δt is calculated from precise vertex position measurement of reconstructed and tagged B mesons. The vertices are reconstructed by combining charged particle trajectories. To know the real particle trajectory, particle hits in detectors should be found and correctly attributed to a trajectory. At B factories, vertex detectors are designed to precisely detect hits close to the interaction point. Precise measurements of track points close to the interaction point, we can study the differences between the expected and measured information. Such differences indicate our insufficient knowledge of the positions and shapes of the sensing elements of silicon detectors, imprecise calibration or other

inconsistencies, which can then be fixed. This is a continuous procedure, since sensor positions and calibrations can change in time and repeated re-alignment and re-calibration is required [4, 7].

This focus of this thesis is the alignment of the Belle II vertex detector and physical analyses that require precise vertex resolution. Regarding the detector alignment, the author provides several alignment studies that culminate in an estimation procedure of sensor surface deformation in the Belle II vertex detector implemented in the Belle II software and reconstruction framework. The author also developed a tool for monitoring χ^2 invariant modes of the Belle II vertex detector - that is, of sensor misplacements that are "invisible" or poorly visible to the detector alignment procedure. The author personally participated in the analysis, and he contributed to skimming, reconstruction, systematic studies of vertex detector misalignment, and data vs. Monte Carlo comparison studies. The author studied several decay channels and detector performance in the respective time-dependent CP violation measurements. Nine decay channels were studied:

- $B^0 \to J/\Psi(\to \mu^+ + \mu^-) + K_S^0(\to \pi^+ + \pi^-)$

- $B^0 \to J/\Psi(\to e^+ + e^-) + K_S^0(\to \pi^+ + \pi^-)$

- $B^0 \to \pi^+ + D^-(\to K^+ + \pi^- + \pi^-)$

- $B^0 \to \pi^- + D^{*+}(\to \pi_{\text{slow}}^+ + D^0[\to K^+ + \pi^- + \pi^+ + \pi^-])$

- $B^0 \to \pi^- + D^{*+}(\to \pi_{\text{slow}}^+ + D^0[\to K^+ + \pi^-])$

- $B^\pm \to K^\pm + J/\Psi(\to \mu^+ + \mu^-)$

- $B^\pm \to K^\pm + J/\Psi(\to e^+ + e^-)$

- $B^\pm \to \pi^\pm + D^0(\to K^+ + \pi^- + \pi^+ + \pi^-)$

- $B^\pm \to \pi^\pm + D^0(\to K^+ + \pi^-)$

The next author's duty was implement additional continuum background suppression technique based on boosted decision trees. The technique was applied, tested using all studied physical channels, the results were discussed at working group meetings several times, but it was not applied for this thesis. The fitting procedure was developed and processed by colleges from Max Planck Institute in Munich.

In the first chapter, the SuperKEKB accelerator and the Belle II detector are introduced and described with focus on the Belle II vertex detector and on track reconstruction using hits in a combination of pixel and strip solid-state silicon semiconductor detectors.
The second chapter describes Belle II analysis and software environment with detailed descriptions of the tracking package.
The alignment procedure including author's extensions related to validation of vertex detector alignment is described in the third chapter.
The fourth chapter describes the first years of SuperKEKB/Belle II operation.

The following three chapters discuss the author's alignment studies of the vertex detector with some additional software extensions.

The last chapter is focused on prompt $\sin 2\phi_1$ measurement based on the first data collected using the Belle II detector.

1. The Belle II detector

The Belle II detector represents the new generation of B factories and is the upgrade of the famous Belle detector. It is located on an upgraded accelerator infrastructure called SuperKEKB. Both, the accelerator and the detector would like to continue in the success of their predecessors using many upgrades and new components. The accelerator was designed to dramatically increase peak and integrated luminosity. Also, the detector was designed to record all interesting data with higher precision. In order to perform particle physics measurements, the Belle II detector construction followed a well-known structure. The vertex detector, combining pixel (PXD) and strip (SVD) detectors, was built close to the interaction point. The central drift chamber (CDC), as the main tracking detector, surrounds it. The particle identification is the next level of detector composed of the time of propagation (TOP) and the aerogel ring imagination Cherenkov (ARICH) detector. The electromagnetic calorimeter (ECL) provides the energy measurement of produced particles. The outermost level of detection farthest from the collision point is the K_L-muon (KLM) system. The cross-section of the Belle II detector can be found in Figure 1.1 [6].
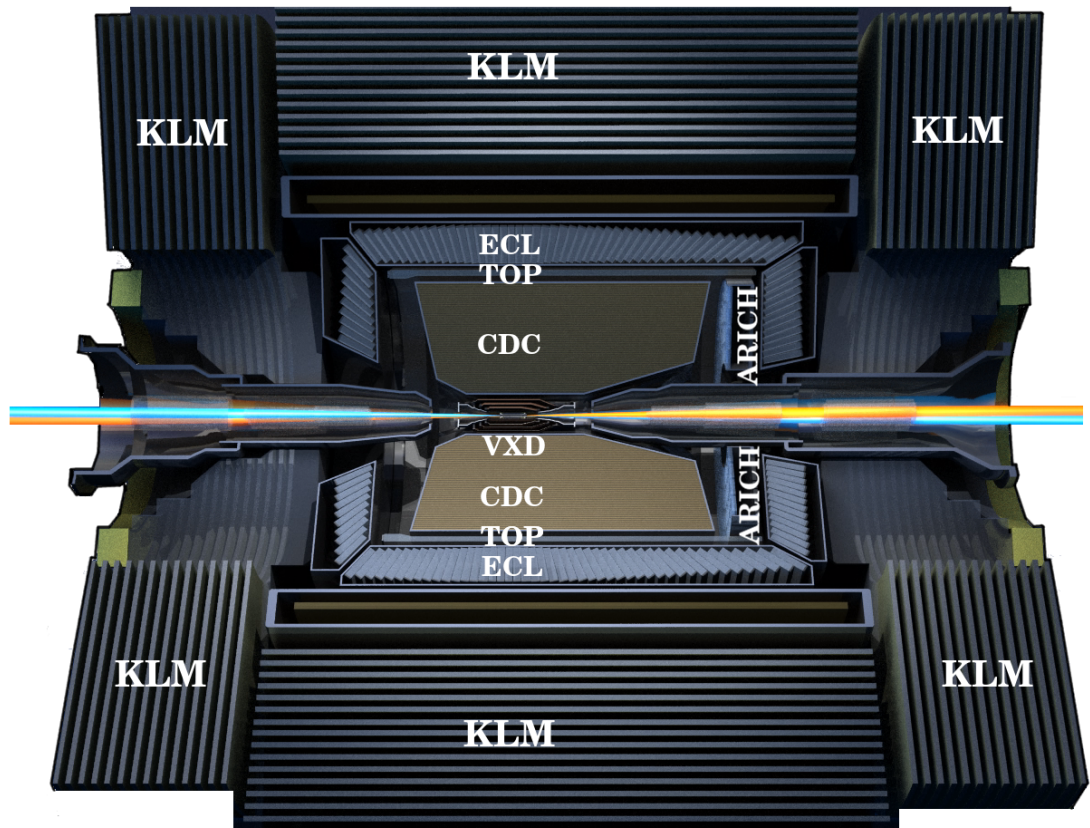
Figure 1.1: Cross-section of the Belle II detector: the vertex detector (VXD) composed by pixel and strip detector, the central drift chamber (CDC), time of propagation (TOP) detector, aerogel ring imagination Cherenkov (ARICH) detector, electromagnetic calorimeter, K_L-muon (KLM) system [8]

1.1 SuperKEKB

The SuperKEKB is an e^+e^- asymmetric energy double-ring collider. The collider is composed of an injector, a positron damping, a high (HER) and a low (LER) energetic rings (Figure 1.2). Electrons and positrons are accelerated to final energies and injected into the rings by the injector. In order to have low emittance positron beam, the accelerator is extended by a positron damping ring. Accelerated electrons with beam energy 7 GeV circulate in high energetic ring and positrons with beam energy 4 GeV are running in low energetic ring. At the interaction point, around which the Belle II detector is built, electrons and positrons collide to produce the $\Upsilon(4S)$ resonance. The produced resonance is boosted ($\beta\gamma = 0.28$) in the electron beam direction, because of asymmetric energies of collide particles [9, 10].
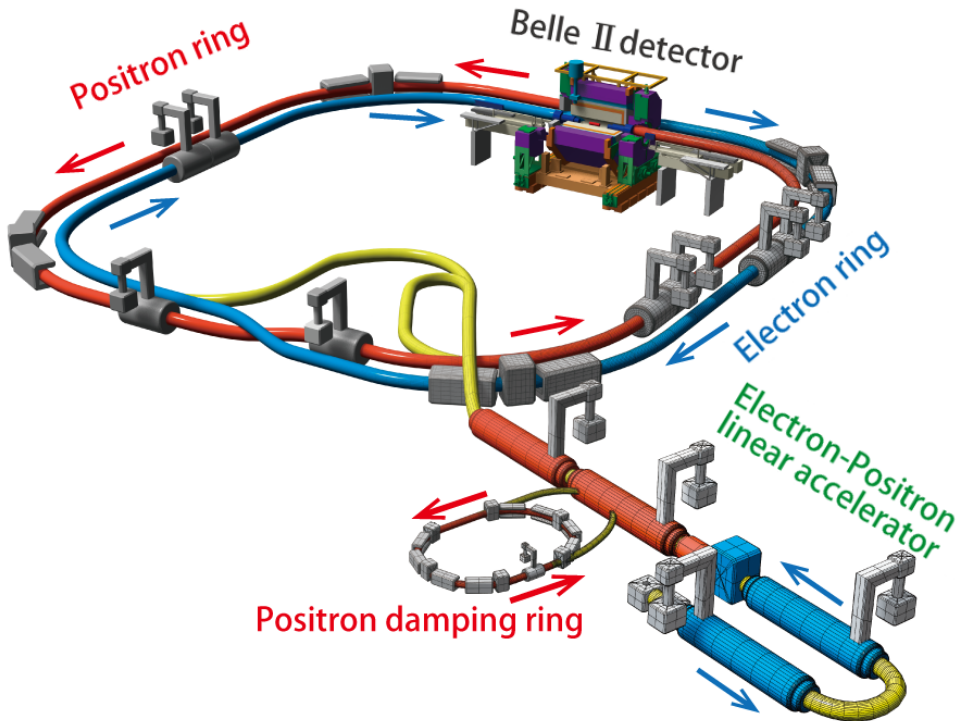
Figure 1.2: Schematic view of SuperKEKB: Injector composed of electron-positron linear accelerator and positron damping ring; electron and positron storage rings; the Belle II detector at the interaction point

1.1.1 Producing, acceleration and storing of beams

A photocathode radio frequency (RF) gun generates high-current electrons with low emittance. The RF gun is composed of Nd: YAG laser, which excites electrons in Ir_5Ce cathode. Quasi-travelling-wave side-couple cavity accelerates and focuses excited electrons into an electron bunch with a charge up to 4 nC and emittance of 10 mm·mrad. For production of high current positrons, electron flux with charge of 10 nC is generated by a thermionic gun. Primary electrons are focused

onto a tungsten target. Positrons are captured using a flux concentrator and large aperture accelerating structures. To reduce positron emittance, the bunch is damped at 1.1 GeV damping ring, and its charge is 4 nC. The positron and electron bunches are accelerated in two independent virtual accelerators of a linear accelerator. The length of the linear accelerator is 600 m, and it consists of 60 high-power radio-frequency units. Each unit operates at 50 Hz. By using pulse-to-pulse acceleration, the positron bunches are injected into positron ring at 4 GeV and the electrons into electron ring at 8 GeV. The injector injects electron and positron bunches into main rings continuously to keep electron current at 3.6 A and positron current at 2.6 A. Because positron bunches loss 1.76 MeV and electrons 2.43 MeV per turn in the main rings the beams are accelerated to compensate it.

1.1.2 Crab-waist scheme and interaction point

To collide electron and positron bunches, the crab-waist scheme is used. The bunches with sufficiently small horizontal beam size σ_x^* collide at a large horizontal crossing angle (Figure 1.3).
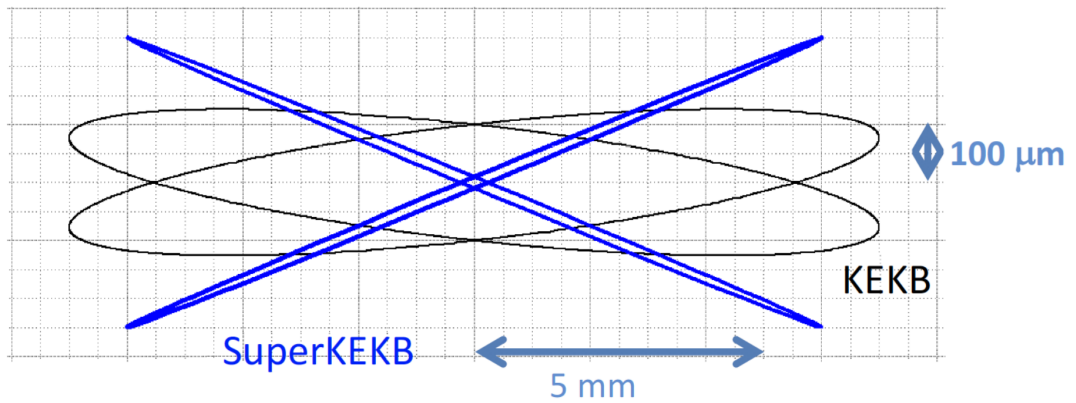
Figure 1.3: The crab-waist scheme in the horizontal plane: Comparison between KEKB's crab-crossing and SuperKEKB's crab-waist colliding scheme [10]

The collision scheme creates challenging conditions for the detector: very high luminosity, synchrotron radiation and detector background. To ensure tiny vertical beta function of the collisions at IP β_y^* large focusing magnet system is needed. The SuperKEKB focusing system, called final-focus superconducting magnet system (QCS), consists of (Figure 1.4):

- eight focusing quadrupole magnets:

  - permanent quadrupole magnets: QCS2LE, QCS2LP, QCS2RE,

  - superconducting quadrupole magnets: QCS1LE, QCS1LP, QCS1RP, QCS1RE and QCS2RP

- 43 correction magnets: each quadrupole magnet has four or five correction magnets to align beams, adjust beam orbit and optimize dynamics aperture

- four compensation solenoid coils: ESL, ESR1, ESR2 and ESR3 for cancelling Belle II solenoid field integrally along the beam lines
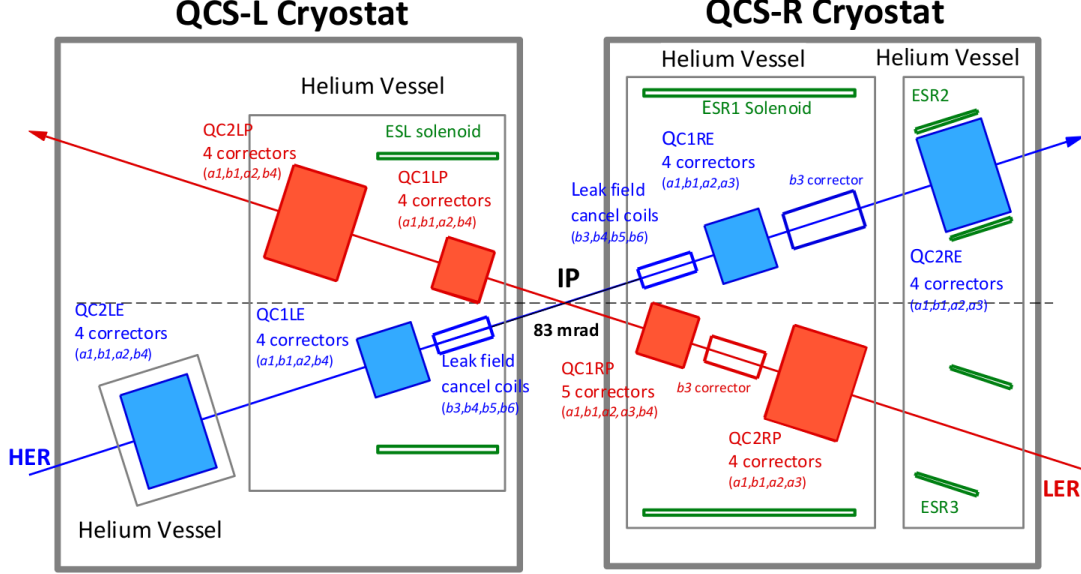
Figure 1.4: The final focusing superconducting magnet system [10]

The magnets lead the bunches to collission point at an interaction point chamber (Figure 1.5). The chamber is 10 mm thin. To shield it from the particle shower background, the central part of the chamber is made of double-wall beryllium and the crotch parts are made of tantalum. The chamber is cooled with water and paraffin because of synchrotron radiation and wall current heating. To achieve fast and precise beam feedback, the beam position monitors are mounted on the chamber. The temperature monitor sensors are distributed throughout the volume of the chamber. To prevent fatal accidents, the interlock system is used and works well during the accelerator operation [11].

1.1.3 Luminosity and accelerator parameters

The luminosity $\mathcal{L}$ at SuperKEKB accelerator can be defined as [9]:

$$\mathcal{L} = \frac{\gamma_\pm}{2er_e}\left(1 + \frac{\sigma_y^*}{\sigma_x^*}\right)\left(\frac{I_\pm \xi_{y\pm}}{\beta_{y\pm}^*}\right)\left(\frac{R_L}{R_{\xi_y}}\right) \tag{1.1}$$

where $\gamma_\pm$ are the Lorentz factors for electrons (-) and positrons (+), e is the charge of electron, r_e is the classical electron radius, $\sigma_{x,y}^*$ are the beam sizes at the interaction point (IP), $I_\pm$ are the beam currents, $\xi_{y\pm}$ are the vertical beam-beam tune shift parameters, $\beta_{y\pm}^*$ are vertical beta functions at the IP and parameters R_L and R_{ξ_y} are the corrections factors introduced due to the hourglass effect and the crossing angle at the IP. We assumed $\sigma_{x,y}^*$ and $\beta_{y\pm}^*$ to be the same in both rings. More details about the accelerator parameters of SuperKEKB can be found in Table 1.1. Two times higher current and twenty times reduced beta function create forty times higher luminosity than that of KEKB. The expected integrated luminosity delivered by the SuperKEKB is about 50 ab^{-1} for the full running time of accelerator.
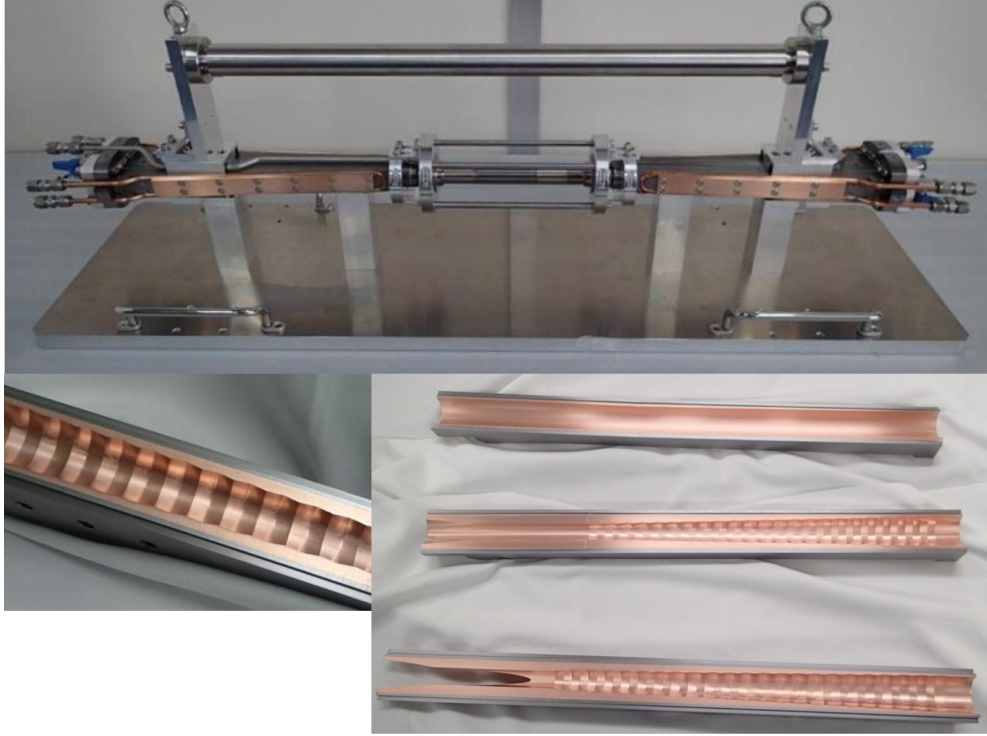
Figure 1.5: The interaction point chamber: the chamber with handling tools (top), inner ridge (bottom left) and inner pieces of chamber (bottom right) [11]

		LER (e^+)	HER (e^-)	Units
Beam energy	E	4.0	7.0	GeV
Crossing angle	θ_x	83		mrad
Beam current	I	3.6	2.6	A
Number of bunches	n_b	2500		
Particles per bunch	N	9.04	6.53	10^6
Energy loss per turn	U_0	1.76	2.43	MeV
Horizontal beam size	σ_x^*	10.1	10.7	μm
Vertical beam size	σ_y^*	48	62	nm
Bunch length	σ_z	6.0	5.0	mm
Horizontal beta function at IP	β_x^*	32	25	mm
Vertical beta function at IP	β_y^*	0.27	0.30	mm
Horizontal beam-beam parameter	ξ_x	2.8	1.2	10^{-3}
Vertical beam-beam parameter	ξ_y	88	81	10^{-3}
Circumference	C	3016.315		m
Beam power	P_b	8.3	7.5	MW
Luminosity	$\mathcal{L}$	8.0×10^{35}		cm^{-2}s^{-1}
Integrated luminosity	$\mathcal{L}_{int}$	50		ab^{-1}

Table 1.1: Accelerator parameters of SuperKEKB [9]

1.2   Vertex detector

In the collisions, new particles are produced. They fly out into the surrounding space. To study the conditions of the areas very close to the collisions, produced

particles should be detected, and their properties should be measured. First detection system is located on the outer wall of the interaction point chamber. Due to high luminosity, the system has to face conditions as high synchrotron radiation and other additional detector background. Otherwise, the requirements for the next generation of B factories are high precision; low energy losses in the material of detector and fast readout system. To satisfy all the requirements and conditions, new vertex detector was built. It is a silicon-based detector divided into six layers each of which consists of semiconductor sensors. Inner two layers use pixel sensors, and outer four layers use double side strip sensors [6].

1.2.1 Pixel detector

The pixel detector uses the DEPFET (DEPleted Field Transistor) technology, which combines detection and in-pixel amplification. It was invented by Josef Kemmer and Gerhard Lutz. The Max Plank Institute Semiconductor laboratory manufactured DEPFET sensors for several applications. The sensors can be implemented in transmission electron microscopy, astrophysics, dark matter searches and particle physics [12, 13, 14].
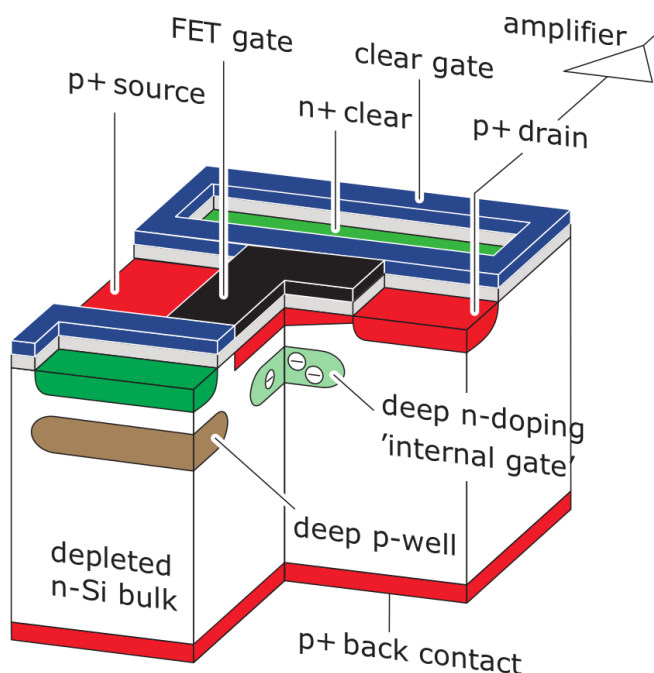
Figure 1.6: The DEPFET pixel [12]

The DEPFET (Figure 1.6) is field-effect transistor depleted on n-type silicon bulk. The DEPFET has FET gate and additional "internal" gate implemented a few micrometres under FET channel by a n^+ implantation. The internal gate creates a local potential minimum for electrons. All electrons created by a particle passing through the DEPFET bulk are collected by the internal gate. When the transistor is activated by setting the external gate voltage above a threshold,

the collected charge modulates the transistor current. Each DEPFET forms a pixel in a matrix (Figure 1.7). The transistor is activated by row-wise readout, and the signal currents are read out column-wise. After the readout cycle, the charge in the internal gate is removed by applying a positive reset to CLEAR contact.
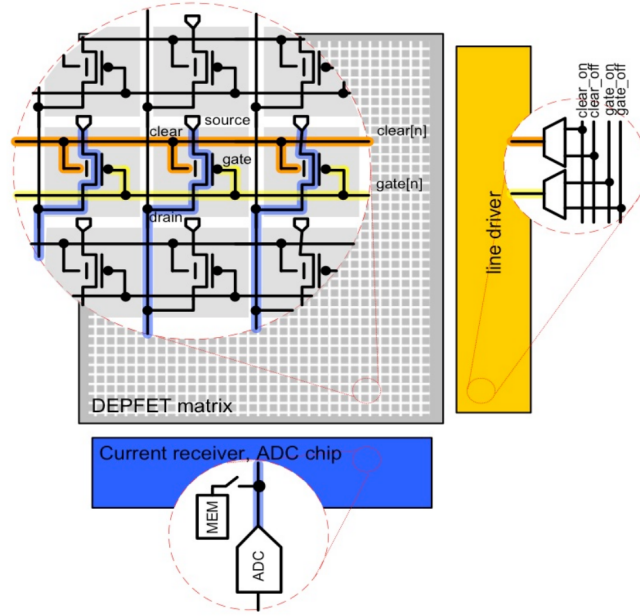
Figure 1.7: The arrangement and control of DEPFET matrix: the DEPFET matrix (gray), driver line (yellow/orange) and current receiver (blue) [15]

A module (Figure 1.8) is formed by a matrix. The module matrix has 250 columns and 768 rows. The DEPFET signals are read out row-wise by drain current digitizer (DCD) chip. The readout algorithm needs 192 steps to finish a read-out of a complete module matrix, which takes 20 μs with digitization. Each DCD chip is followed by data handling process (DHP) chip for pedestal subtraction, common-mode correction and 0-suppression. The data from one frame are, after receiving the external trigger, transmitted to the data acquisition system. The gate and clear signals for DEPFET are generated by Switcher chip. The power consumption of the sensor is minimal because of the rolling shutter mode matrix readout and non-active transistor during charge collecting. The active area of the module is cooled by moderate flow of cold nitrogen. However, DCD and DHP chips need cooling by evaporating liquid CO_2 in cooling channels of a sintered steel block.

According to the design, the pixel detector is composed of two layers; the first of them is constructed of eight ladders and second layer of twelve ladders. Every pixel ladder (Figure 1.9) consists of two modules. The sensitive area of first layer module is 12.5×44.8 mm^2, where pixel size of 256 rows closest to the centre of the ladder is 50×55 μm^2 and 50×60 μm^2 for other rows. The sensitive area of second layer module is 12.5×61.44 mm^2, where pixel size of 256 rows closest to the centre of the ladder is 50×70 μm^2 and 50×85 μm^2 for other rows. The
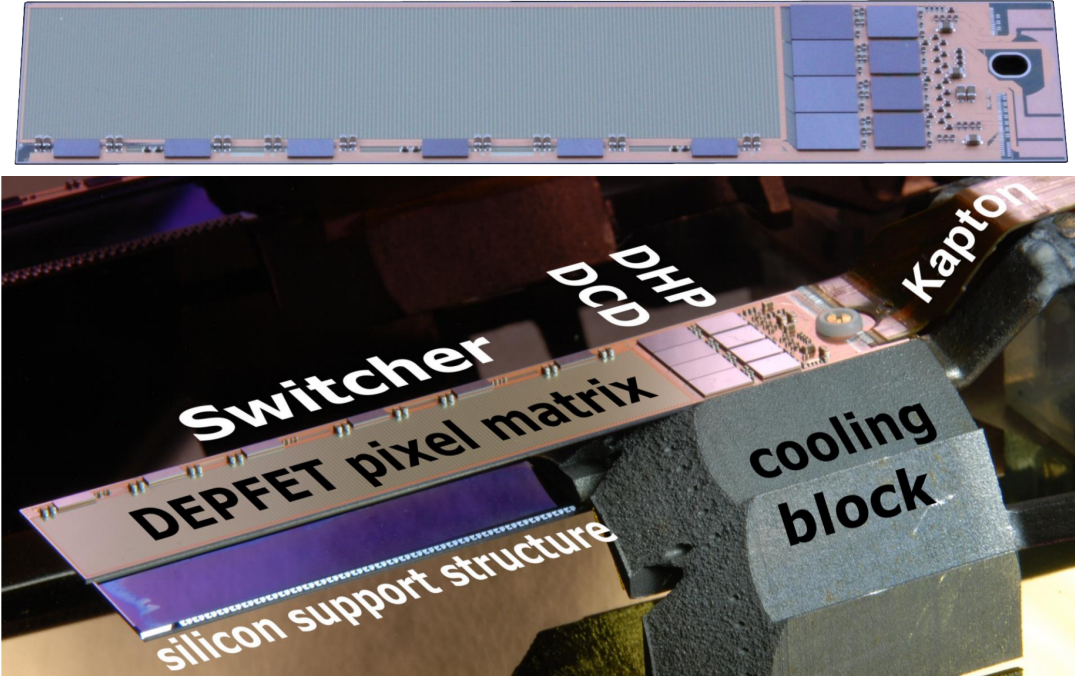
Figure 1.8: The detail of DEPFET sensor (top) and its support (bottom) [12, 16]

Figure 1.9: The ladder of pixel detector [17]

thickness of the sensitive area of all modules is 75 μm. The inner layer module size is 67.975 × 15.4 mm^2 and 84.975 × 15.4 mm^2 for outer layer. The ladders in the first layer have ladder size of 136 × 15.4 mm^2 ladder size, but the second layer ladder size is 170 × 15.4 mm^2. Pixel layers radii are 14 mm for first, respectively 22 mm for the second layer. The partial pixel detector was successfully mounted on beam pipe in KEK in September 2018 (Figure 1.10).

1.2.2 Strip detector

The second part of silicon vertex detector is based on strip detection technology. The common requirements for silicon detector are [6, 19]:

- Cover full Belle II angular acceptance of 17° < θ < 150°

- Fill area between PXD (38 mm radius) and CDC (140 mm radius)

16
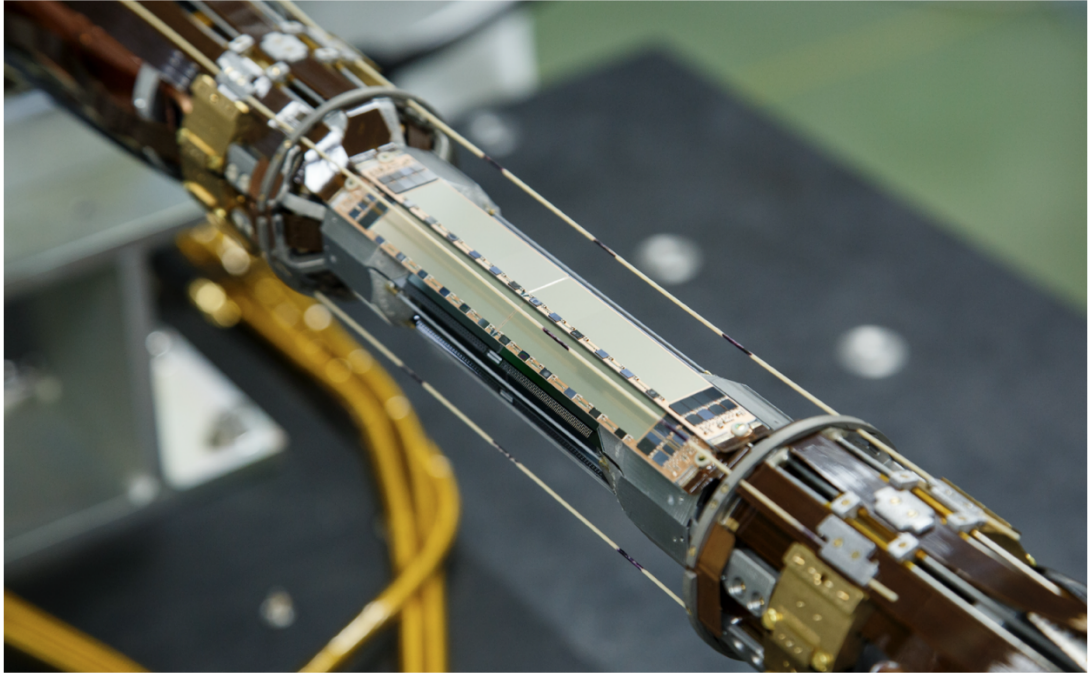
Figure 1.10: The pixel detector installed in 2018 into the Belle II detector [18]

- High efficient track extrapolation from CDC to PXD detector

- Reduce background tracks using association of PXD and CDC hits

- Tracking of low p_T tracks and reconstruction vertices outside of PXD volume

- Efficient operation with low dead-time and 30 kHz trigger rate in the high background

The strip detector is based on the double-sided strip detector (DSSD). The detectors were manufactured by Hamamatsu Photonics (perpendicular sensors) and Micron Semiconductor (slanted modules). The DSSD is a well-known technology and is often used in various scientific or commercial fields. The DSSD sensitive volume (Figure 1.11) is composed of the N^- bulk, N^+ strips, perpendicular P^+ strips on the opposite side, and it is covered by a layer of silicon dioxide. In principle charged particle crossing DSSD bulk generates electrons and holes along its path. Both types of strips collect carriers depending on their charge. The aluminium readout strip transports collected signal to APV25 chip. The APV25 chips are connected to junction boxes. The data are sent to flash analogue-to-digital converters (FADC). After first level data processing and formatting, digital data are distributed to a unified Belle II data acquisition system and PXD readout system.

The strip detector is made of two basic sensor shapes (Figure 1.12): trapezoidal (forward) and rectangular (central). The rectangular sensors are installed in two sizes.
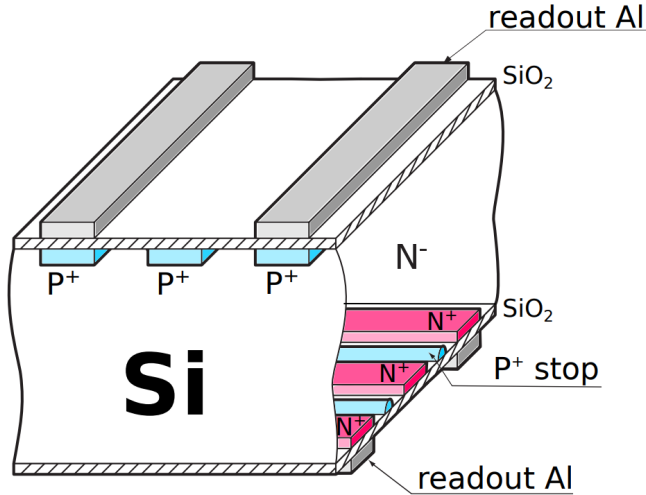
Figure 1.11: The DSSD strip detector [20]

Geometrical properties of trapezoidal sensor are 41.02 mm for short base, 60.63 mm for long base and 125.58 mm width. The active area is from 38.42 to 57.59 × 122.76 mm². A variable pitch from 50 to 75 μm is applied for 768 positive-side strips. The 512 negative-side strips are perpendicular to a central strip of p-side with pitch size 240 μm. The thickness of trapezoidal sensors is 300 μm.

The rectangular sensors of the inner layer of the strip detector are smaller than other, and its sensor area is 124.88 × 40.43 mm². Their active area is 122.90 × 38.55 mm² and thickness of sensors is 320 μm. Half of 1537 P^+ strips are read by 768 readout strips. The P^+ pitch size is 25 μm for strips, respectively 50 μm for readout strips. On the negative sensor side, there are 1537 strips and 768 readout strips with 80 μm and 160 μm pitch size, respectively.

The overall area of the larger sensors is 124.88 × 59.60 mm² with active area of 122.90 × 57.72 mm². Their thickness is equivalent to smaller sensors. Similarly, the 768 readout strips read 1535 strips with the pitch 75 μm, resp. 37.5 μm on the positive side. The opposite side is composed of 1023 N^+ strips and 512 readout strips with 120 μm, resp. 240 μm pitch size.

The strip sensors are combined into ladders (Figure 1.13). The inner layer of the strip detector is composed of seven ladders, which consist of two small perpendicular sensors. Ten ladders form the second layer with one forward trapezoidal and two large rectangular perpendicular sensors. Twelve ladders create the third strip layer, where there is one slanted trapezoidal and three large rectangular sensors. The last layer is formed by sixteen ladders, including one forward trapezoidal and four large rectangular perpendicular sensors. The radii of layers are 39, 80, 104 and 135 mm. The strip detector halves (Figure 1.14) were completed in summer 2018 in KEK.
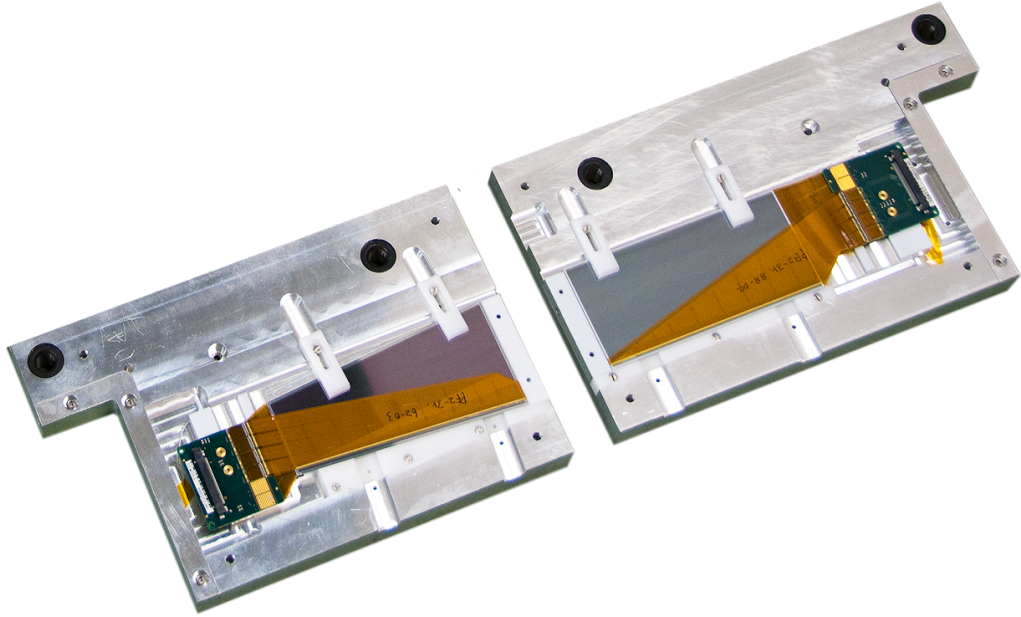
Figure 1.12: The shapes of strip sensors: trapezoidal (left) and rectangular (right) in transport docks [19]

1.2.3 Vertex detector labelling

The completed vertex detector composed of silicon sensors organized to ladders, layer and halves. The vertex detector sensitive area is illustrated in Figure 1.15 [6, 22].

First and second layers make up the pixel detector. The strip detector layers are labelled from three to six. To know sensor place in vertex detector structure, every sensor is labelled by a unique number. The number is defined as #layer.#ladder.#sensor. For ladder labelling, it can be used too, but the sensor number is removed. Ladder and sensor labelling are illustrated in Figures 1.16 and 1.17. Total, sensor and ladder population depends layer are shown in Table 1.2.

	Radius [mm]	Ladders	Sensors per ladder	Sensors
PXD Layer 1	14	8	2	16
PXD Layer 2	22	12	2	24
SVD Layer 3	39	7	2	14
SVD Layer 4	80	10	3	30
SVD Layer 5	104	12	4	48
SVD Layer 6	135	16	5	80
Total		65		212

Table 1.2: Number of vertex sensors by layer and ladder
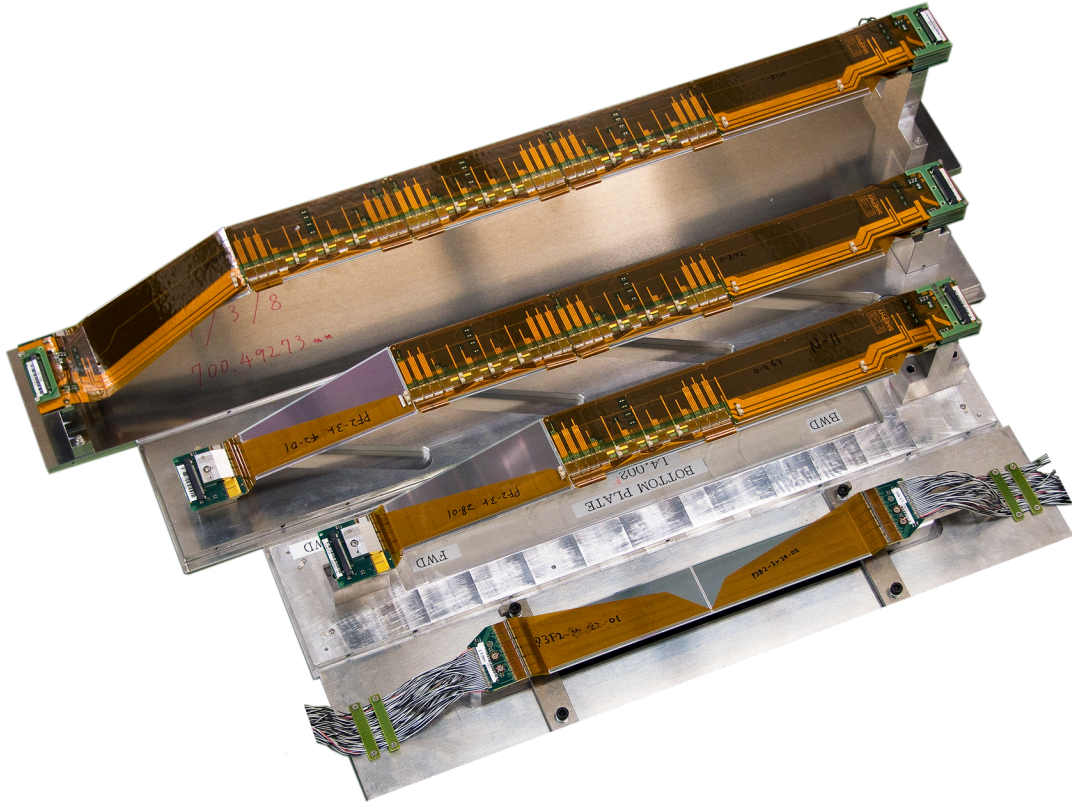
Figure 1.13: The ladders of strip detector: fourth (top), third (center top), second (center bottom) and first (bottom) layer [19]

Based on the way it is constructed, the vertex detector can be divided in to four pieces called halves. The pixel detector halves are called Ying ("Y+") and Yang ("Y-") (Figure 1.18). The strip detector is composed of so-called Pat ("X+") and Mat ("X-") halves (Figure 1.19).

1.3   Central drift chamber

The central drift chamber (CDC) is the main tracking detector of the Belle II. The CDC measures charge particles trajectories. Thanks to the 1.5 T magnet located in the CDC, the charged particles momentum is measured. Particle identification measurement is based on energy loss in a gas volume of the CDC. The drift chamber detector (Figure 1.20) is a hollow cylinder with 16 cm inner radius and 113 cm outer radius, and it has asymmetric shape because of asymmetric energy collisions [6, 23].

The CDC consists of 14 336 sense and 42 240 field wires. Each cell is composed by one gold-plated tungsten sense wire surrounded by eight aluminium wires without plating field (Figure 1.21). Diameters are 30 μm for sense and 126 μm for field wires. In inner layers, the smallest cell size is about 0.6 cm, and the largest cell size in the outer layer is 1.8 cm.
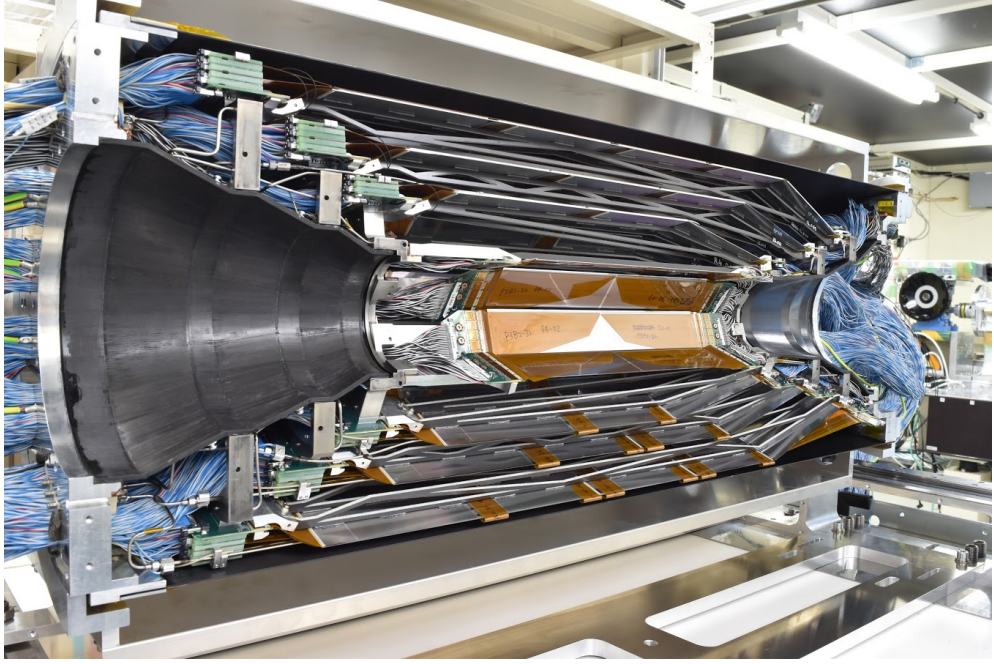
Figure 1.14: The strip detector halfshell after completion [21]
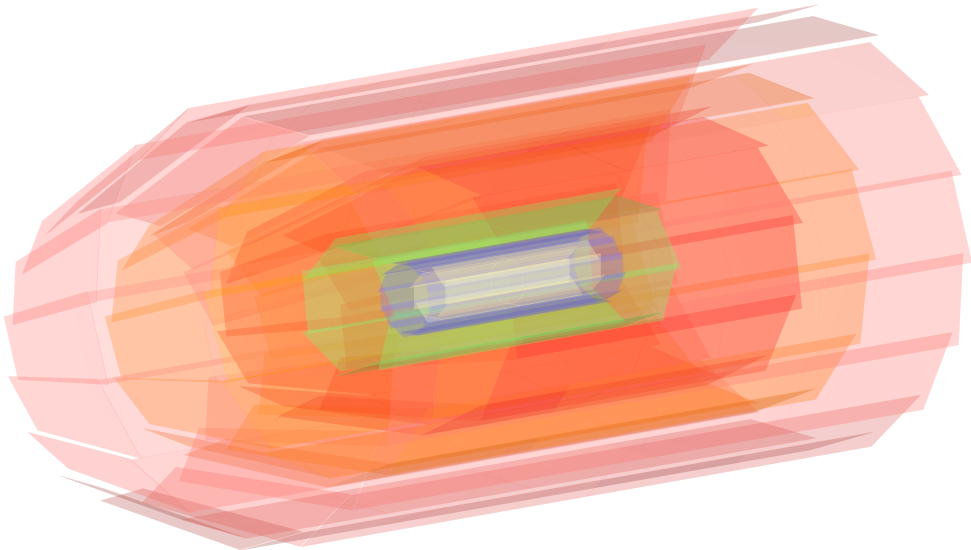
Figure 1.15: Coloured composition sensitive area of vertex detector: first (gray), second (blue), third (green), fourth (red), fifth (orange) and sixth (pink) layer; for layers above the third one, the trapezoidal (slanted) sensors are on forward (left) side

All wires are installed in 56 layers creating nine super-layers. Based on the wire orientation as a function of the z-coordinate we distinguish between three different orientations: parallel axial (A), positive stereo (U) and negative stereo (V) super-layers. The super-layers are organized according AUAVAUAVA pattern (Figure 1.22). The CDC volume is filled with helium-ethane gas with a one-to-one ratio. The CDC volume is enclosed by two carbon-fibre reinforced plastic
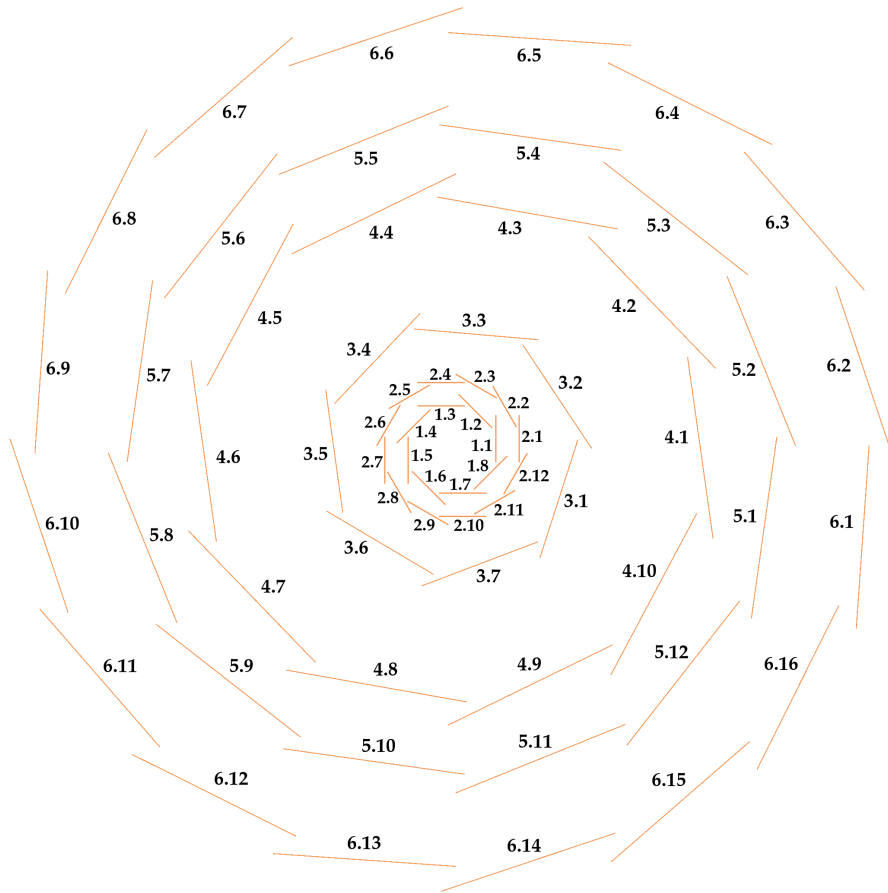
Figure 1.16: Ladder labelling of vertex detector
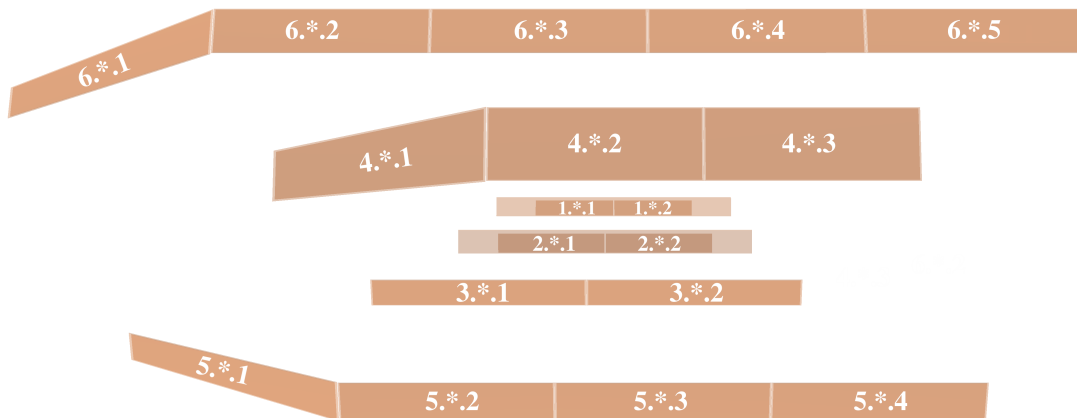
Figure 1.17: Sensor labelling as function of layers

(CFRP) cylinders and two aluminium endplates.
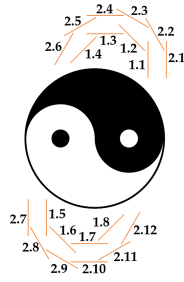
Figure 1.18: The pixel detector halves: Ying (top) and Yang (bottom) with corresponding group of ladders.
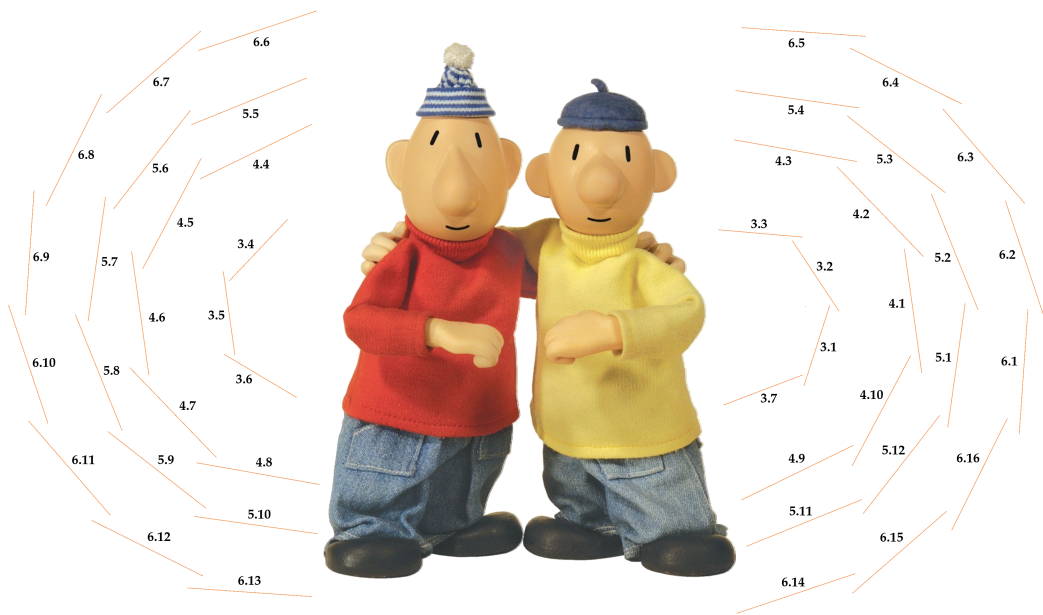
Figure 1.19: The strip detector halves: Mat (left) and Pat (right) with corresponding group of ladders.

Front-end readout electronic boards read the signal collected by wires collected. Each signal is processed by amplifier-shaper-discriminator chip producing two output signals: analogue for pulse-height measurement and digital for timing measurement. The analogue signal is digitized by the analogue-to-digital converter (ADC) chip. The timing signal is fed into a multiple-hit time-to-digital converter (TDC). Both signals are stored in the data buffer for a trigger signal, and they are sequentially transferred to the data acquisition system.

1.4 Particle identification detectors

The tracking system is followed by the particle identification system the main task of which is to efficiently distinguish between kaons and pions with high
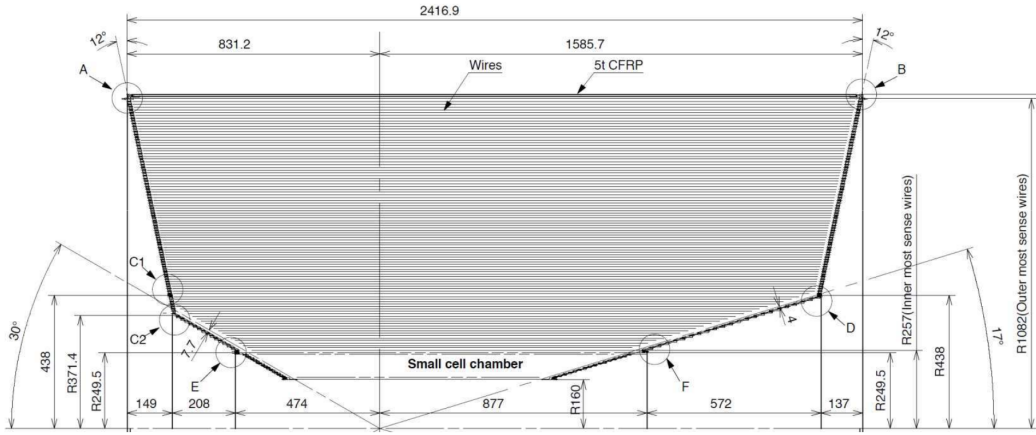
Figure 1.20: Cross section of central drift chamber [23]
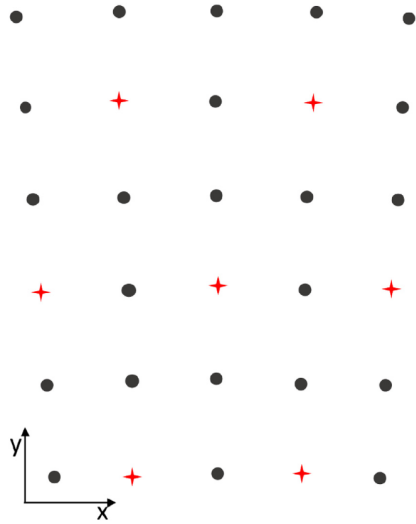
Figure 1.21: Wire configuration of the CDC: sense wires (red) and field wires (**black**) [23]
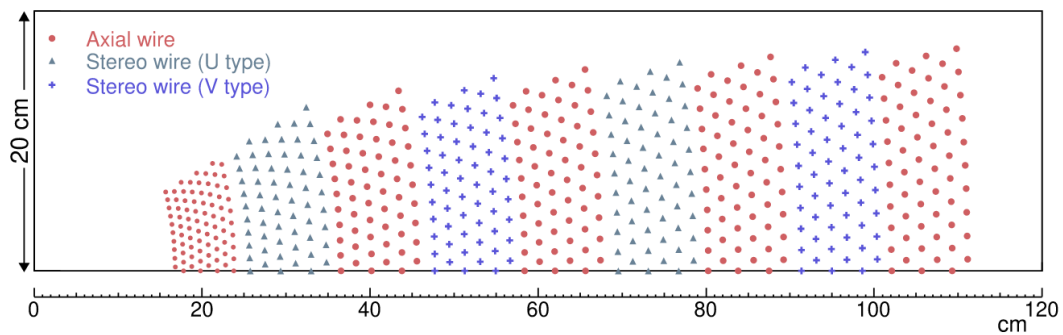
Figure 1.22: Super-layers configuration of the CDC [23]

momentum. In Belle II detector case, the particle identification is based on Cherenkov photons' detection using the time of propagation (TOP) counter in the central region and aerogel ring imaging Cherenkov (ARICH) counter in the forward region [6].
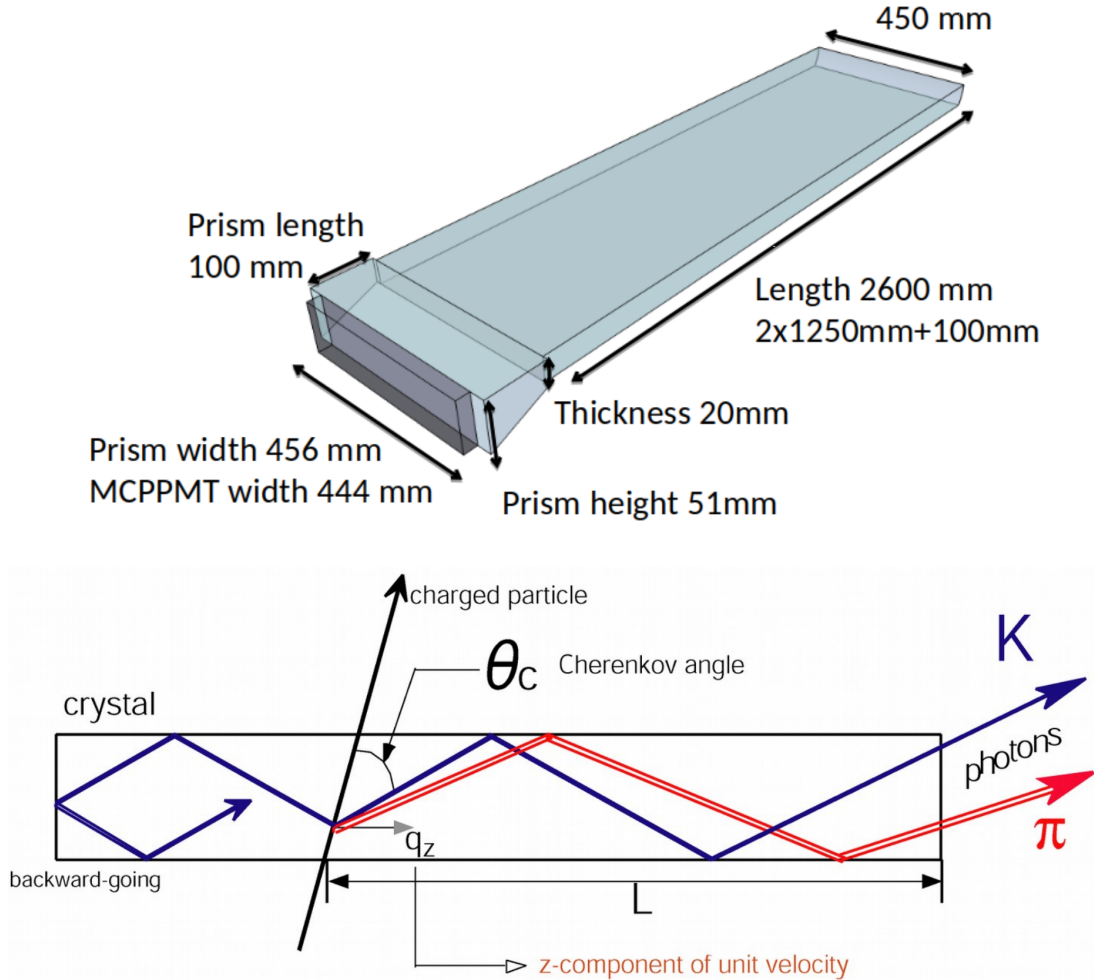
Figure 1.23: Time of propagation counter: a TOP module arrangement (top) and schematic illustration of the photon propagation in a quartz bar (bottom) [24]

1.4.1 Time of propagation counter

The TOP counter is composed of sixteen identical modules arranged in barrel-like geometry. Each module (Figure 1.23) consists of four parts glued together: two fused silica (quartz) bars of dimensions $125 \times 45 \times 2$ cm acting as Cherenkov radiator, a mirror located at the forward end of bars and a 10 cm long prism that couples the bar with an array of micro-channel-plate photo-multiplier tubes (MCP-PMT). A readout module corresponds to 8 MCP-PMTs per quartz bar. Incoming charged particle generates the Cherenkov radiation propagated in the bar. Cherenkov photons are totally internally reflected thanks to a high critical angle of the quartz-air interface. Photons with preserved angular information are detected by MCP-PMT array on the backward end. The propagation time

of Cherenkov photons from generation to detection is a function of their angle (Figure 1.23). The Cherenkov photon signal from MCP-PMTs is read out, and the time of photo pulses is extracted. Then extracted data are distributed to off-detector electronics and data acquisition system [6, 24].

1.4.2 Aerogel ring imagination Cherenkov counter

The ARICH counter consists of silica aerogel radiators and hybrid avalanche photodetectors (HAPDs). Silica aerogel is composed of two layers of different refractive indices ($n = 1.045, 1.055$). Cherenkov lights radiated when a charged particle passing through a silica aerogel is observed as a ring image on HAPDs. The particle is identified using the difference of rings images as kaon-pion ring difference in Figure 1.24. A distance of 200 mm separates the aerogel radiator plane and photodetection plane. The radiator plane consists of 124 pairs of aerogel tiles while photodetection plane contains 420 HAPDs. To reflex outside going photons to the detection plane, planar mirrors are located at the outermost side. The signal from photodetectors is amplified, shaped, discriminated and digitized. The processed signal is transferred to the data acquisition system [6, 25].
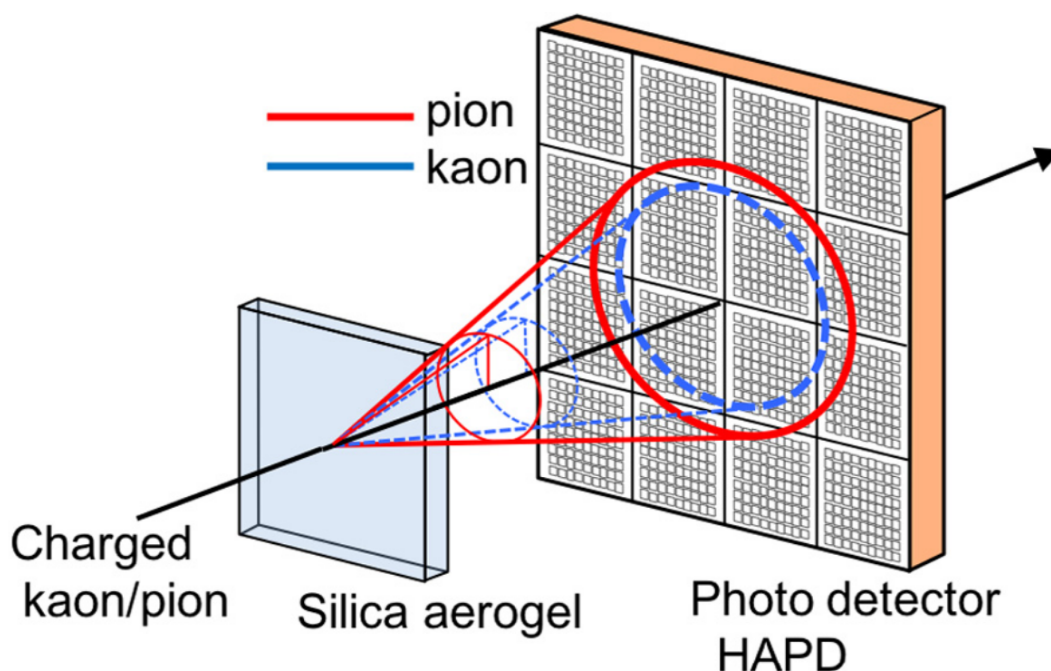
Figure 1.24: Kaon-pion difference rings at ARICH counter: charged pion or kaon (**black arrow**), kaon's Cherenkov photons (blue circle) and pion's Cherenkov photons (red circle) [26]

1.5   Electromagnetic calorimeter

For photon registration, separation of electrons and hadrons, luminosity measurement and generation of the signal trigger, the electromagnetic calorimeter (ECL) was constructed. Due to the fact that many of the produced particles decay into photons, the calorimeter should have a high energy resolution with a wide energy range. It is formed by 8736 scintillation counters based on CsI(Tl) crystals. The calorimeter consists of three sectors (Figure 1.25): the front end part, the back end part and the cylindrical section. Parts contain 1152, 960 and 6624 scintillation counters, respectively. The crystal axis is oriented towards the beam interaction region. To increase light collection, the crystals are wrapped in a layer of teflon as a diffuse reflector, and then they are covered by aluminised LAVSAN for electrical shielding. The photodiodes, which are attached to a crystal outer edge, transform scintillated light from the crystal into an electrical signal. The photodiodes pulse is transformed into a voltage pulse with two charge sensitive preamplifiers. The preamplifiers are equipped with pulse generator for calibration. The counter signal is divided into two channels: detector and trigger channel. For the detector channel, the preamplified signal is summed, shaped and digitised in readout electronics. Digitised data are compressed and transmitted to a data acquisition system. The summation of signals from all counters and its subsequent formation is carried out in the trigger channel. The trigger signal is shaped, digitised and analysed. Passing through threshold, the trigger signal is transmitted to global decision logic (GDL) of detector trigger [6, 27].
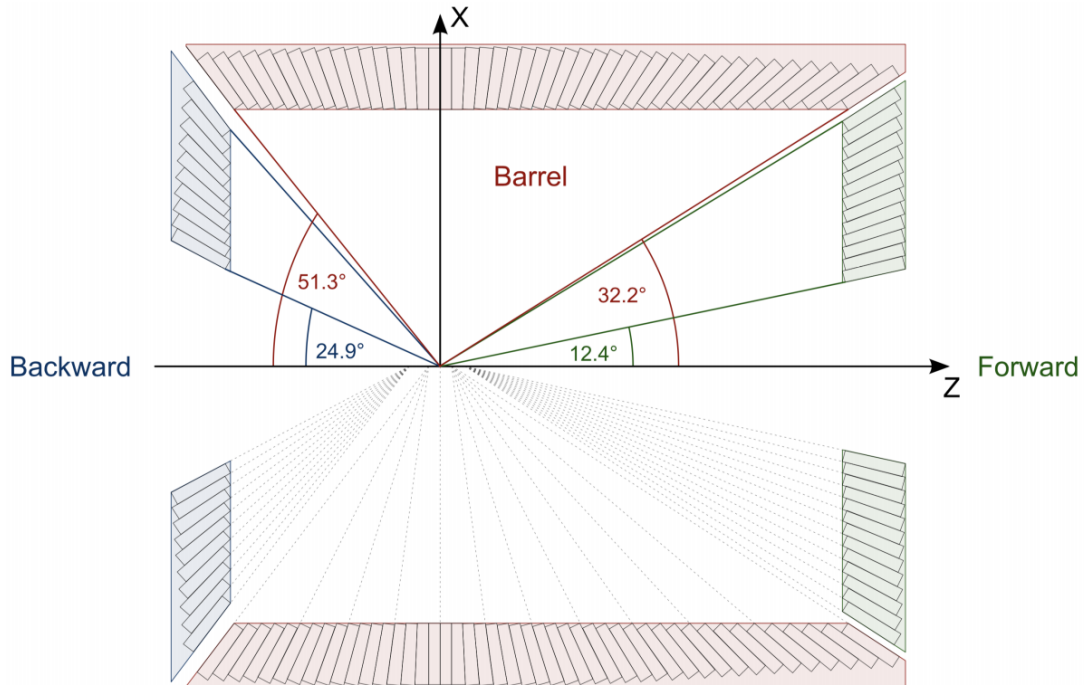
Figure 1.25: The electromagnetic calorimeter of the Belle II detector: the backward endcap (blue), the forward endcap (green) and the barrel (red) calorimeters [28]

1.6 K_L^0 and muon system

The K_L^0 and muon system (KLM) is designed to detect long-living neutral kaon and muons. It is located outside of 1.5 T magnetic field. The KLM detector can be divided into two endcap parts and central barrel part (Figure 1.26). Each endcap part consists of four sectors, and the barrel part has 16 sectors. The structure of KLM is sandwich-type with 15 layers for the barrel, 14 layers for forward and 12 layers for backward endcap. The KLM layers are composed of passive iron plates and active detector elements. The working principle of the active area of thirteen outer layers of the barrel detector is based on resistive plate chambers (RPC). The RPCs are high voltage electrodes filled with gas between them. For the first two inner layers of barrel detector and all layer of the endcap detector, the active detector area is built of scintillator strips. The produced light is coupled with wavelength-shifting fibre and read by silicon photomultipliers. The signal from photomultipliers and RCPs is read and processed for data acquisition and trigger system [6, 29].
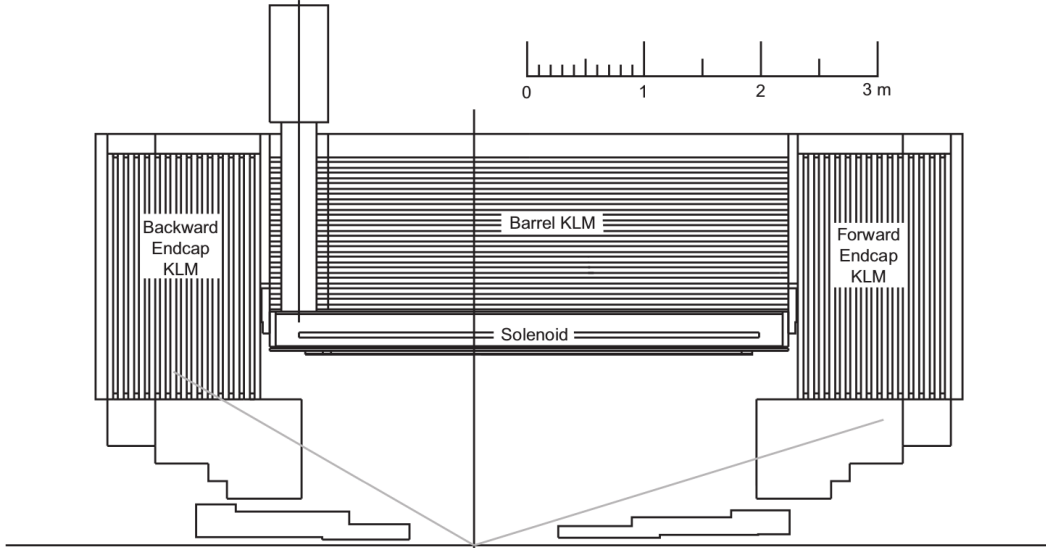
Figure 1.26: Cross section of the K_L^0 and muon system KLM [6]

1.7 Trigger system

In order to reconstruct 99.9 % of hadronic events from $\Upsilon(4S) \to B\overline{B}$ and continuum the trigger system was developed. Due to the SuperKEKB upgrade and target luminosity of Belle II detector, the designed maximum trigger rate of data acquisition system is 30 kHz with 5 μm latency of trigger. The Belle II detector has the capacity to reconstruct other processes with trigger rates listed in Table 1.3. The trigger system is designedto work quickly and precisely under challenging conditions such as high detector background. [6, 30].

Physics process	Cross section [nb]	Rate [Hz]
$\Upsilon(4S) \to B\overline{B}$	1.2	960
Hadron production from continuum	2.8	2200
$\mu^+\mu^-$	0.8	640
$\tau^+\tau^-$	0.8	640
e^+e^- ($\theta_{\mathrm{lab}} \geq 17°$)	44	350*
$\gamma\gamma$ ($\theta_{\mathrm{lab}} \geq 17°$)	2.4	19*

Table 1.3: Trigger rate and total cross sections at target luminosity of Belle II: trigger rate of Bhabha scattering and $\gamma\gamma$ process are pre-scaled by factor 0.01(*)

The Belle II detector's trigger system contains the hardware trigger called Level 1 (L1) and the software trigger called high-level (HLT). The L1 trigger level consists of global reconstruction logic (GRL) and global decision logic (GDL). Detector and trigger information is addressed to GRL where reconstruction procedure using this information is performed. Reconstructed data are forwarded to GDL to initialize trigger. For L1 trigger decision, reconstruction of the central drift chamber (CDC) and the electromagnetic calorimeter (ECL) detector information is used. The CDC helps to detect charged tracks. The ECL generates fast trigger signals for neutral and charged particle oriented physics events. The events with high electromagnetic energy deposition are labelled as total energy triggers. Physics events containing hadrons with low energetic clusters and/or minimum ionizing particles are detected and isolated as cluster triggers. Bhabha scattering or $\gamma\gamma$ events are processed to provide online luminosity measurement and data taking monitoring.

1.8 Data acquisition system

The data acquisition (DAQ) system transfer data from the frontend electronic to the hardware trigger. The DAQ system is composed by Belle2Link, COPPER, the events builder and the HLT system, where the Belle2Link is unified data link, the COOPER is readout platform. The digitized information is transferred into COOPER systems through optical fibres using the Belle2Link. On the COOPER level, the data are formatted and events built. The HLT farms processed data for software event selection. The HLT process the L1 trigger output to process a Level 3 (L3) trigger. The events passing L3 trigger are reconstructed using the offline algorithms, all sub-detectors information except PXD are used, because of huge PXD event size. Based on reconstruction information, the events are separated to categories, e.g. $\mu\mu$, ee, in physics trigger. The PXD data are reduced by finding a region of interest (RoI) in pixel sensors. Founded pixel hits are addressed to the next level event builder for combining with other data [6, 30].

2. Software

The Belle II detector requires software environment for processing, analysing and monitoring the collected amount of data and simulation of samples. The Linux-based software is organised into the Belle II Analysis Software Framework (basf2) for Belle II-specific code, the externals for third-party code on which basf2 depends and the tools for installation and configuration. The software is based on `GCC` compiler, `Python 3` language and `git` versioning software. Several HEP specific software tools, such as `ROOT`, `Geant4` and `EvtGen`, are implemented. The installation and configuration are both based on shell and python scripts [6, 31].

2.1   The Belle II Analysis Software Framework

The Belle II-specific code is compressed into about 40 packages, e.g. base-level framework, components corresponding to each sub-detector, track reconstruction, simulation, post-reconstruction and physics analysis. The code is written in `C++`. The basf2 users typically work with centrally installed versions of basf2. The basf2 framework is available from the CERN virtual machine file system (CVMFS). Otherwise, the pre-compiled version is available, or the tools compile the above-mentioned version of the source. The code is maintained in a `git` repository.

The data recorded by the Belle II detector and simulations are organized into a set of variable-duration runs, each containing a sequence of independent events. These runs support separation of events depending on the purpose, e.g. physics and cosmic runs. A set of runs with similar hardware state and operation characteristics is classified as an experiment. The framework executes a series of dynamically loaded modules to process a collection of events. A module is written in `C++` or `Python`. Modules exchange data via the `Data Store` that provides a globally accessible interface to mutable object or arrays of objects. Objects of the `Data Store` can have either permanent or event-level durability. For longevity and easy accessibility, the `ROOT` files are used. Content of the `Data Store` is written down into a `ROOT` file, which consists of first `TTree` with branches for each of the `Data Store` entries and second `TTree` with permanent-durability information as the number of events, experiment or run range. The full event data model is defined dynamically by creating the object in the `Data Store`. It identifies an event by combination of its event, run and experiment numbers.

For applying data processing tasks, arranging appropriate modules into a path and starting event processing, the basf2 provides use with `Python` interface. Users perform tasks using scripts called "steering files", but interactive use is also supported. The possibility to write modules in `Python` helps users to write their own module code because it can be embedded in the steering file. Using `Python` users can access the `Data Store`. Typical HEP user-level analysis for processing large data samples are mostly based on the execution of small scripts in Python or ROOT macros. The `jupyter notebooks` allow a user to develop `Python`-based applications. They provide an enriched browser-based working environment that

is a front-end to an interactive `Python` session that might be hosted centrally on a remote high performance computing cluster.

To reduce memory usage, parallel processing is implemented to basf2. The processes start by forking, and each of the furcated processes then analyse the data of a separate complete event. Each module gives the framework an indication whether it can run in parallel-processing mode or not. Because reading and writing of ROOT files can not be parallelized, the framework can divide the path of modules into three sections. The first and the last section are each executed in a single process. Only the middle section is executed in multiple processes.

In addition to event data and constant values, several settings or calibrations can evolve over time but not on a per-event rate. These numbers are called "conditions", and their values are stored in central Condition Database. Conditions are divided into payloads, and each of them has one or more "intervals of validity" (IoV) as a run interval during which the payload is valid. A global tag identifies one complete set of payloads and their IoVs. Multiple global tags can provide different calibration versions of same run ranges.

The basf2 uses the same detailed geometry description for simulation and reconstruction. It is implemented using Geant4 geometry primitives. Each sub-detector package defines and configures a geometry creator. The framework builds and sets up full geometry of the Belle II detector. Payloads provide all parameters for geometry description in the condition database. The magnetic field description is loaded from the condition database too. The magnetic field creator can handle a list of field definitions. In basf2 several magnetic fields are implemented: constant, 2D radial symmetric, full 3D field map and some special implementation due to special magnetic field close to the beams. One of the special cases is the no-magnetic field option with zeros in full detector volume. For standard simulation and analysis jobs, the segmented 3D field map with a fine grid in the inner detector region and a total of three coarse outer grids for the two endcaps and outer barrel region is implemented.

The basf2 can visualise the geometry, the simulated and the reconstructed data. The visualisation module can be added to the path in the steering file or started using a stand-alone executable. The module is based on the `Eve` toolkit and an event visualisation framework which is part of `ROOT`. Its result is `OpenGL`-based three-dimensional rendering of generic shapes and high-level interfaces for particle physics concepts. It can convert `Geant4` geometry using Virtual Geometry Model (VGM) [32].

2.2 Simulation and Monte Carlo generators

Monte Carlo simulation is provided in the basf2 in the three steps: events generation, detector simulation and digitization. The physics signal and background events are generated using `Pythia` and `EvtGen`. Additional generators are implemented for specific purposes: tau physics, beyond standard model physics, dark physics and cosmic rays. In the second step, the interaction between generated

particles and the Belle II detection system is imitated using all of its different detector geometries, materials and records of the particle's energy deposits in sensitive volumes. The `Geant4` internally provides the detector simulation. Physical interaction in a sensitive area of a detector produces a hit. In the last step, the information is digitized using simulation of in-detector physics process and by applying electronic effects due to external conditions such as detector geometry and magnetic field. Final simulated data can be stored and processed in further reconstruction. During analysis, the simulated information is used as a reference [6, 33].

2.2.1 Cosmic ray generators

For cosmic ray generation CRY algorithm is implemented. The external package CRY is based on Monte Carlo simulations of proton-induced cosmic-ray cascades in the atmosphere. It is used in muon tomography, neutrino experiments and developments of detector shielding materials. The galactic protons with energy in a range of 1 GeV - 100 TeV are injected into the modelled atmosphere. The secondary particles are produced. To decrease computation power requirement, the CRY authors developed the system of tables for secondary particles. The CRY algorithm takes into account the solar cycle, location on the Earth and time passed singe the shower generation. After secondary particles are read from the table they are reconstructed at "global box", particles are then extrapolated to targeting "accept box", and an event with at least one particle in "accept box" is kept. The particles outside of "keep box" are removed. The algorithm allows to define the global, keep and accept boxes as three-dimensional blocks and also the choice of secondary particles, which can be generated [34, 35, 36, 37].

2.3 Track reconstruction

Specific basf2 package is implemented for reconstruction of charged particle trajectories. The tracking system is based on vertex silicon detector and central drift chamber. In pixel detector, the neighbouring pixels above charge threshold are combined into PXD clusters, position and charge of these clusters is passed down to the tracking system. The pixel detector does not participate in HLT decision. The HLT defines the Region of Interest (RoI) of PXD planes using the tracking information, hits from which can be processed and stored. The strip clusters are formed by strips which cross the signal-over-noise threshold. By combining all of the clusters on one side of the strip with the clusters on the other we can obtain space points. During clustering, the clusters are filtered depending on cluster time. The cluster time, position and charge of space points are transferred to the tracking system. The central drift chamber measures time between the event's trigger time and the arrival of the drift electrons at sense wire. Using calibration constants actual wire distance between the sense wire and a passing particle can be computed and used for tracking purposes. The task of the tracking software can be divided into two independent stages: creating a collection of the tracking detector hits and fitting the collection as a charged track using a helix parametrisation (Figure 2.3) [6, 38]:

- d_0: stands for the signed distance of the point of closest approach (POCA) to the z axis,

- ϕ_0: the angle defined by the x axis and the track transverse momentum at the POCA,

- ω: the track's curvature signed with the particle charge (inverse to track radius R),

- z_0: z coordinate of the POCA,

- $\tan \lambda$: tangent of the dip angle
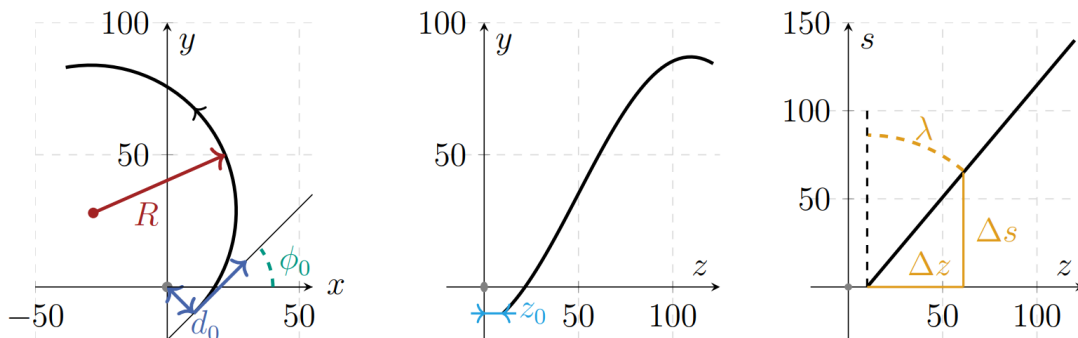
Figure 2.1: Helix parametrisation for tracks [38]

Firstly, hits and their properties are collected and stored in a container called `RecoTrack`. Due to three tracking detectors with different properties, the collection stage is based on several track finding algorithms. In the CDC, the `RecoTrack` is filled using two algorithms: a global track finding based on the Legendre algorithm and local algorithm employing cellular automaton. Both results are merged and fitted using a deterministic annealing filter (DAF). Combinatorial Kalman filter is implemented for extrapolation from the CDC to the strip detector and extends the CDC hits with SVD clusters. The tracks with low p_{T}, which are not able to reach the volume of the CDC, or with inadequate CDC hits are found using standalone SVD track finder based on advanced filter concept called Sector Map and cellular automaton. The combined track is again fitted with the DAF. The track is extrapolated to the pixel detector with second CKF and PXD hits are implemented into the final `RecoTrack` container.

Secondly, the `GENFIT2` external package provides a fit of track candidate using the DAF assuming energy losses and material effects. The track candidates are fitted with three specific particle hypotheses: π, K, p. The track reconstruction results are stored in a `Store Data` object called "Track".

2.3.1 Standalone SVD track finder

The tracks with the majority of SVD hits are reconstructed using the standalone SVD algorithm consisting of three steps. Firstly, the three-dimensional space

points are read and assorted into graphs using geometrical information. Subsequently, the relations between hits are created based on Sector Maps. It is a technique based on information about how space points in different regions of the strip detector can be related to tracks. Each sensor is divided into nine sectors. The geometry allows defining directed relations between sectors, which are associated with the same track. Additionally, the Sector Map includes the selection criteria which need to be fulfilled by a combination of space points on the related sectors. The criteria provide a probability of a pair or a triplet of space points belonging to the same track.

In an event, all space points are combined into pairs, which are filtered by the Sector Map technique. Selected pairs are combined again to form triplets of space points and evaluated again by Sector Map algorithm. The triplets are delivered to cellular automaton for final track finding, and Sector Map filtering is not applied any more. Due to less background occupation, the algorithm starts combining triples from outer layers.

To reduce fake and clone candidates, number of possible track candidates is reduced. In case some track candidates are sharing the same SVD cluster, the best candidate is chosen.

2.3.2   Combinatorial Kalman filter

The next track finding algorithm is the combinatorial Kalman filter (CKF). After seeding, the algorithm searches for a new hit candidate according to a track candidate's actual position and uncertainties. Next hit candidate that passes selection criteria is added to the track candidate. Expanded track candidate tries to find the next hit to be added. Sometimes more hit candidates pass the selection criteria and the track is duplicated and subsequently treated. In the end, only one candidate is chosen.

In the first step, a track candidate found by the CDC track finding algorithm is extrapolated to SVD sensors and SVD space points are attached. Due to large inefficiencies, poor resolution in $|z_0|$ and the necessity to find low momentum tracks the unmerged CDC tracks are combined with additional SVD track candidates by CKF in the second step.

All reconstructed CDC-SVD tracks are used to define the region of interest in PXD sensors and PXD clusters from these regions are then used as new hit candidates. This algorithm is similar to the one applied during CDC-SVD tracks creation.

2.4   Data processing

The collected raw data are processed at KEK and copied to the PNNL (Pacific Northwest National Laboratory). The output of the raw data processing are mDST files, a format containing all relevant information for physics analysis [6, 31]:

- `Track`: the object representing a reconstructed trajectory of charged particle containing track fit result and quality indicator

- `TrackFitResult`: the result of track fit for given particle hypothesis: five helix parameters, their covariance matrix, a fit p-value and the pattern of layers with hits in tracking system

- `V0` candidate a K_S^0 or Λ decay of converted photon with reference to the pair of positively and negatively charged tracks and their fit results

- `PIDLikelihood`: the object that stores the likelihoods of a charged track being an electron, muon, pion, kaon, proton or deuteron from each sub-detector providing particle identification information

- `ECLCluster`: reconstructed cluster in the electromagnetic calorimeter containing energy, position measurement and their correlations along with shower shaped variables (extrapolated track is required)

- `KLMCluster`: reconstructed cluster in K_L^0 and muon detector providing position measurement and momentum estimation with uncertainties (extrapolated track is required)

- `KlId`: K_L^0 meson candidate providing particle identification information with weights of its relation to KLM and ECL clusters

- `TRGSummary`: information about Level 1 decision before and after pre-scaling stored in bit patterns

- `SoftwareTriggerResult`: the decision of high-level trigger implemented as a map of trigger names to trigger results

- `MCParticle`: the information about simulated particle containing momentum, production and decay vertex, relation to mother and daughter particle and information about traversed detector components

The mDST files are stored on both sites and copied to grid sites around the world. The grid sites are used for one more task, production of Monte Carlo simulations, the output of which are also mDST files. Users process the simulated or data files on-grid site. Final analysis would be done on local resources, shared resources in KEK, DESY or the user's institute.

3. Alignment of vertex detectors

The vertex detector system is built for accurate measurement of decay vertices. Silicon-based sensors detect a position of charged particles very precisely. To reconstruct tracks and vertices in space, accurate knowledge of the silicon sensor in space is required. The requested precision can not be achieved during detector installation, and additional software solution should be applied. The correct position of the sensors in space must therefore be estimated from tracks using a linear combination of tracking residuals. This procedure is implemented in major experiments to improve tracking accuracy and it is defined as alignment by tracks. On the other hand, various conditions (e.g. vibrations, temperature, humidity, mechanical degrees of freedom) which change over time can smear out the clear sensor position information [4, 6, 7].

3.1   Track based alignment

The alignment's task is to calculate position, rotation and surface shape corrections to the nominal sensor position. Each silicon sensor requires at least six alignment parameters, but a hundred sensors require implementation of a thousand of corrections. Estimating values of these correction parameters requires a large collection of the tracks with enough degrees of freedom remaining after track fitting. Based on previous experience, the size of the track collection does not allow to achieve perfect alignment. Topographically rich sets of tracks play a more important role in alignment algorithms due to the elimination of the linear combinations of alignment parameters. These combinations are labelled as "χ^2 invariant modes". We can provide precise alignment by applying constraints to alignment parameters or by using a richer set of tracks [39].

3.2   Alignment algorithm

The normalized tracking residuals are [39, 40]:

$$z_{ij} = \frac{u_{ij}^{m} - u_{ij}^{p}(\boldsymbol{\tau}_j, \boldsymbol{a})}{\sigma_{ij}} = \frac{r_{ij}(\boldsymbol{\tau}_j, \boldsymbol{a})}{\sigma_{ij}}, \tag{3.1}$$

where u_{ij}^{m} is a recorded measurement of hit i on the track j, u_{ij}^{p} is predicted measurement from track model dependent on track parameters $\boldsymbol{\tau}_j$ and alignment parameters $\boldsymbol{a}$, σ_{ij} is the uncertainty of the measurement and r_{ij} is a single residual. Then, the sum over all hits and tracks defines the total χ^2-function:

$$\chi^2(\boldsymbol{\tau}, \boldsymbol{a}) = \sum_{j}^{\text{tracks}} \sum_{i}^{\text{hits}} z_{ij}^2(\boldsymbol{\tau}_j, \boldsymbol{a}). \tag{3.2}$$

Minimizing χ^2-function, the alignment algorithm finds the final result. The algorithm can use single tracks or tracks from decays with constraints imposed on mass or vertex position. In the Belle II detector, the alignment procedure is based on the Millepede II algorithm. Global linear χ^2 minimization with constraints is

provided. The method linearizes the normalized residuals z_{ij} in the χ^2 function [41]:

$$\chi^2(\boldsymbol{\tau}, \boldsymbol{a}) = \sum_{j}^{\text{tracks}} \sum_{i}^{\text{hits}} z_{ij}^2(\boldsymbol{a}, \boldsymbol{\tau}_j) \simeq \sum_{j}^{\text{tracks}} \sum_{i}^{\text{hits}} \frac{1}{\sigma_{ij}^2} \left[r_{ij}(\boldsymbol{\tau}_j^0, \boldsymbol{a}^0) + \frac{\partial r_{ij}}{\partial \boldsymbol{a}} \delta \boldsymbol{a} + \frac{\partial r_{ij}}{\partial \boldsymbol{\tau}_j} \delta \boldsymbol{\tau}_j \right]^2,$$

(3.3)

where $\boldsymbol{\tau}_j^0, \boldsymbol{a}^0$ are initial alignment and track parameters, $\delta \boldsymbol{\tau}_j$ and $\delta \boldsymbol{a}$ are corrections to these alignment and track parameters, respectively. Due to their association with a particular track, the track parameters are called local parameters. On the other hand, alignment parameters do not change over the tracks' full set and can be labelled as global parameters.

3.2.1 Alignment parametrisation

Every vertex sensor provides hit measurement for each passing charged track. The hits are measured in its local coordinate system (Figure 3.1). In the local sensor frame, coordinates u, v coordinates correspond to shorter, respectively longer edge of the sensor and w coordinate is perpendicular to the plane spanned by these two coordinates. However, the tracks are reconstructed in the Belle II global laboratory system.
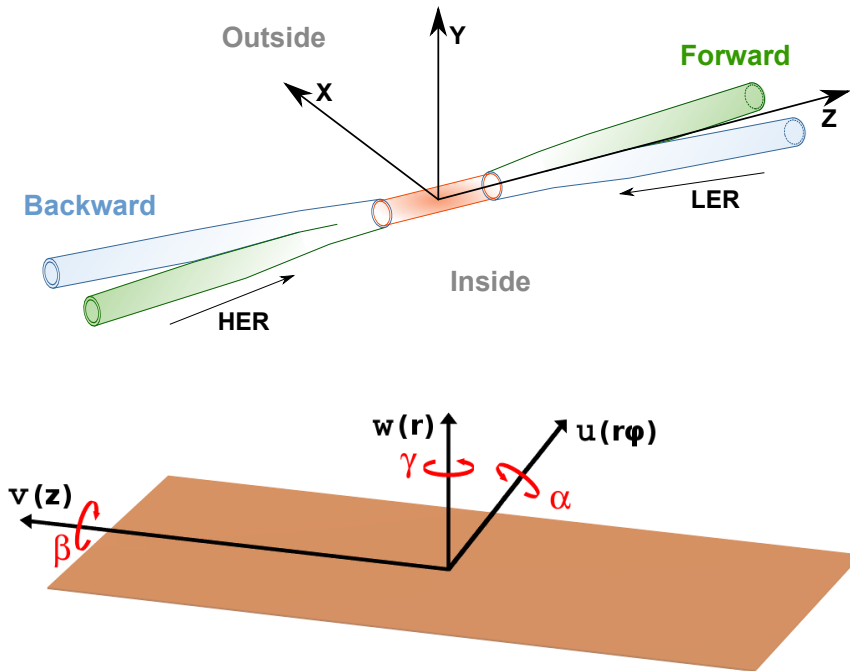

Figure 3.1: The global Belle II (top) and the silicon sensor local (bottom) coordinate systems [6]

Each hit measurement is transformed from the local into the global system. The vector associated with the hit measurement can be introduced as $\mathbf{q} = (u, v, w)$ and the association of this hit with a track can be expressed as $\mathbf{r} = (x, y, z)$.

The relation between both expressions of the hit can be easily represented by the following transformation formula [42]:

$$\mathbf{r} = \mathbf{R}^{\mathrm{T}}\mathbf{q} + \mathbf{r}_0, \tag{3.4}$$

where vector $\mathbf{r_0} = (x_0, y_0, z_0)$ describes the center position of the sensor in the global system and $\mathbf{R}$ is a rotation matrix. In the alignment procedure, corrections to sensors' center position $\Delta\mathbf{q} = (\Delta u, \Delta v, \Delta w)$ and initial rotation matrix $\Delta\mathbf{R}$ are calculated. The transformation relation Eq. (3.4) then turns into:

$$\mathbf{r} = \mathbf{R}^{\mathrm{T}}\Delta\mathbf{R}(\mathbf{q} + \Delta\mathbf{q}) + \mathbf{r}_0. \tag{3.5}$$

The rotation correction $\Delta\mathbf{R} = \mathbf{R}_\gamma\mathbf{R}_\beta\mathbf{R}_\alpha$ is expressed as a product of small rotations $\mathbf{R}_\alpha$, $\mathbf{R}_\beta$ and $\mathbf{R}_\gamma$ and $\Delta\alpha$, $\Delta\beta$, $\Delta\gamma$ about the u-axis, the new v-axis and new w-axis (Figure 3.1), respectively. The alignment correction vector is composed of $\delta\boldsymbol{a}$ observed translation corrections to the center of the sensor and rotation angle corrections $\mathbf{a} = (\Delta u, \Delta v, \Delta w, \Delta\alpha, \Delta\beta, \Delta\gamma)^T$. In case of sensor surface deformation, the local alignment correction associated with perpendicular axis to the sensor plane must be parametrised as a function of the remaining local coordinates $\Delta\mathrm{w}(\mathrm{u}, \mathrm{v})$ (Figure 3.2). Using suitable surface parametrisation (in Appendix A) the alignment parameters $\mathbf{a}$ can be extended using surface deformation parameters: quadratic (P_{20}, P_{11}, P_{02}), cubic $(P_{30}, P_{21}, P_{12}, P_{03})$ and quartic $(P_{40}, P_{31}, P_{22}, P_{13}, P_{04})$. To eliminate higher level of sensor deformation, addition of an adequate group of parameters to the alignment procedure is required [39, 43, 44].

Hierarchical structure of the Belle II detector requires additional alignment parameters for each construction level. Silicon-based sensors, the first level of hierarchy, form larger structures called ladders (Figures 1.9, 1.13 and 1.17), the second level of hierarchy. Each of them can be parametrised by six alignment parameters, three of which describe shifts and other three are associated with rotations. Together these ladders form layers, however, vertex detector is divided into four halves (Figures 1.18 and 1.19), the third hierarchy level. Additional 6 alignment parameters are associated with each half-shell, three describing shifts and three rotations. The total number of alignment parameters per each level of hierarchy, all detectable surface deformation cases and their total sum can be found in the Table 3.1 [40].

	Ladders	Halves	Sensor parameters	Total
Number	65	4	$6 \times 212 = 1272$	1686
Parameters	6	6	$9 \times 212 = 1908$	2322
Per hierarchy	390	24	$13 \times 212 = 2756$	3170
			$18 \times 212 = 3816$	4230

Table 3.1: Number of the vertex detector parameters: for ladder's and half-shell's levels (left); for all sensor surface deformation cases with total sum over all hierarchy levels (right)
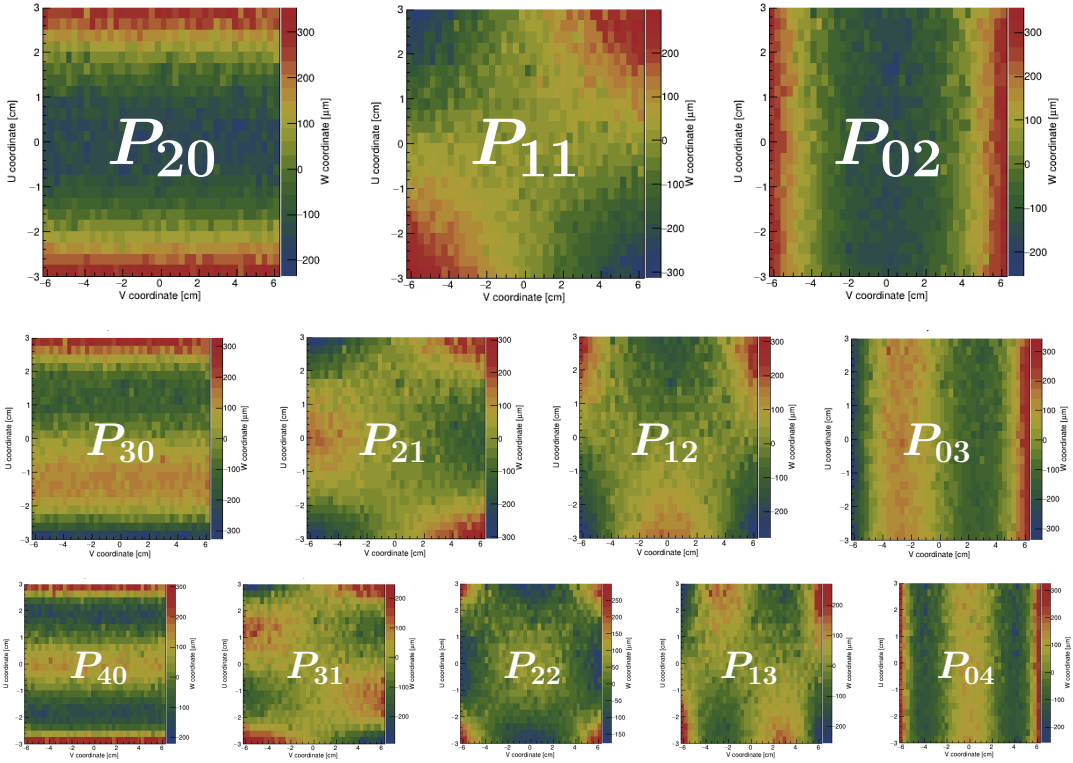
Figure 3.2: Vertex alignment surface parameters: quadratic (top line), cubic (center line), quartic (bottom line)

3.2.2 Track parametrisation

In the alignment procedure, the local track parameters are required to minimize the χ^2 function in Eq. (3.3). A charged particle in vacuum with a constant magnetic field can be parametrized as a helix with five parameters. Due to energy loss in the detector's material, the track's momentum is reduced. On the other hand, the multiple scattering changes the direction and position of the passing track. The general broken lines (GBL) method is implemented to provide a fast global track refit applying the description of multiple scattering to an initial trajectory. A material bulk can be substituted by a thick scatterer changing direction and displacing the track direction. The thick scatterer can be divided into two thin scatterers to locally linearise track model when the track propagation in the material can be explained as changing directions between scatterers or measuring planes. However, the linearization requires iterative fitting. In the local coordinate system, a track can be parametrized by a group of slopes and offsets $(q/p, \frac{du}{dw}, \frac{dv}{dw}, u, v)$, where q/p is inverse momentum [45].

3.3 Misalignment

The alignment procedure is used for determination of real corrections to the silicon sensors' position during data taking. To test and develop the procedure, the Monte Carlo simulation studies are performed. The studies are based on the implementation of realistic initial misplacement of silicon sensors. Initial misalignments are generated and studied in two different ways: as random and

as systematic misalignment [40, 46].

3.3.1 Random misalignment

Random misalignment is generated using the zero-mean normal distribution for each silicon sensor rotations and shifts. Based on Monte Carlo studies the alignment procedure converges to final residual misalignment (the difference between initial misalignment and determined alignment) with range about 5 μm for shifts and 0.1 mrad for rotations. The studies of the random misalignment report about the negligible effect on physical quantities for misalignments in ranges smaller than about 5 μm for shifts and 0.1 mrad for rotations [46].

3.3.2 Systematic misalignment

Coherent movements of the individual sensors poorly controlled within the minimization procedure define the systematic misalignment (Table 3.3). Their recognition and elimination is a major problem because their presence does not affect χ^2-function. These movements are called χ^2 invariant or weak modes. Uncontrolled weak modes can affect the result of the alignment procedure and measurements provided by the misaligned detector. Using Monte Carlo simulations, their effects on physical quantities can be determined and studied. The most sensitive procedure to find most of the weak modes can be used to monitor and control them. Projection of the weak modes into local sensor systems and weak modes visualization can be found in Appendix B.
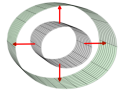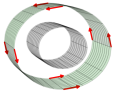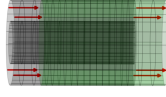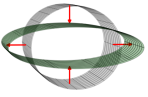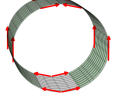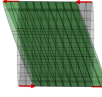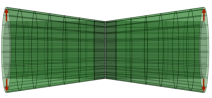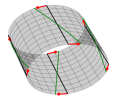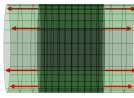
	Δr	$r\Delta\phi$	Δz
r	**Radial expansion** $\Delta r = c_{scale} \cdot r$	**Curl** $r\Delta\phi = c_{scale} \cdot r + c_0$	**Telescope** $\Delta z = c_{scale} \cdot r$
ϕ	**Elliptical expansion** $\Delta r = c_{scale} \cdot \cos(2\phi) \cdot r$	**Clamshell** $\Delta\phi = c_{scale} \cdot \cos(\phi)$	**Skew** $\Delta z = c_{scale} \cdot \cos(\phi)$
z	**Bowing** $\Delta r = c_{scale} \cdot |z|$	**Twist** $r\Delta\phi = c_{scale} \cdot z$	**Z expansion** $\Delta z = c_{scale} \cdot z$

Figure 3.3: Weak modes of the vertex detector: Coherent movements of individual sensors, which can be parametrized by displacements in global coordinates (columns) depending on the location of the sensor (rows). Each cell of the table shows the name of the weak mode (top), its parametrization (middle) and schematic illustration (bottom).

3.4 Monitoring vertex detector alignment

We developed a tool for monitoring vertex detector alignment. The algorithm can be divided into two independent parts: collection and analysis. The collection part is written as a basf2 `Python` module with the possibility to be implemented into a steering file. The collection algorithm can be applied to cosmic tracks either inside or outside of the magnetic field or collision tracks in the magnetic field. In the collection stage, the algorithm provides a fast check of detector reconstruction and tracking results such as [43, 47, 48]:

- Occupancy of vertex detector sensors

- Number of vertex detector hits in track

- χ^2/NDF: χ^2 probability over number of degrees freedom for tracks

- Number of hits in layer per event

Moreover, this algorithm also searches for important quantities such as positions of hits, unbiased hit-to-track residuals, slopes of track in a sensor and sensor characterisation for each hit. Finally, the selected data are stored in a `ROOT` file. The analysis algorithm consists of two independent sections each serving a different purpose: monitoring of vertex detector alignment parameters and χ^2 invariant modes.

3.4.1 Monitoring vertex alignment parameters

Monitoring alignment parameters can be done in different ways. One of the useful methods is monitoring the quality of data reconstructed per each sensor. We are looking at several quantities in order to obtain a bigger and clearer picture of the precision of alignment parameters. First, the crucial information is presented by two dimensional "hit map" plot showing how often which part of a sensor is hit by tracks. This tells us about the functionality of the readout system, possible failures during reconstruction procedure and effects of the trigger system. A standard method used for validation and monitoring of alignment procedure uses the unbiased hit-to-track residual distributions. We can estimate two dimensional u and v residual distribution for each sensor. It is valuable when checking the correct position of the sensor, quality of fitting and estimation needed correction.

The sensor surface deformation can be monitored and validated using residual distribution corresponding to the w coordinate. Based on measurements in the u and v coordinates, the w residual should be estimated by extrapolating these measurements. To determine small surface deformations one can use the following formulas [39]:

$$r_w = \frac{r_u}{\tan \alpha_u} \quad or \quad r_w = \frac{r_v}{\tan \alpha_v}, \tag{3.6}$$

where $r_{u,v,w}$ are residuals and $\tan \alpha_{u,v}$ are slopes of a track in a sensor. Estimation of the w residual can be explained in three steps (Figure 3.4). We are starting from the two-dimensional measurement of the hit position on a sensor surface. The sensor's surface is divided into a matrix with 30 columns and 18 rows. Averaged w residual is estimated in each cell of the matrix using all hits in the cell

and applying formulas (3.6). Each contribution to averaged value is weighted by squared slopes of track in a sensor. The estimation is done for both measurements.
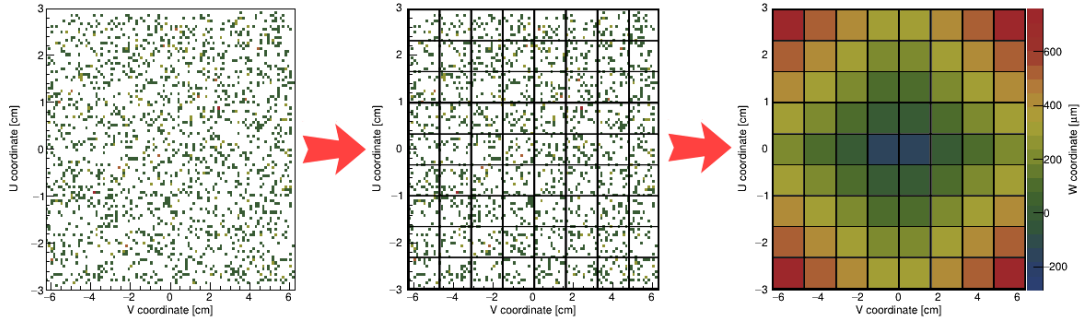
Figure 3.4: Illustration for w residual estimation: hit map (left), matrix creation (center) and visualisation of averaged w residual (right) [49]

For monitoring purposes, the alignment parameters can be estimated using residuals plots. The u and v shifts can be determined from residual distributions as the means of the distributions depending on direction. The other alignment parameters can be estimated from w residual distribution, where they are extracted from two-dimensional surface fit (Appendix A). According to the alignment parameters visualisation, γ parameter can not be estimated exactly. This angle is neglected in our monitoring procedure. The monitoring procedure is able to estimate other alignment parameters very well, but not with required precision for the alignment algorithm. The monitoring tool is used as a qualitative tool to inform experts about troubles or defects in vertex detector alignment.

The tool can also be used for a small statistic sample in which case the alignment parameters extraction procedure has to be performed only once. On the other hand, the tool can process large statistic samples divided into files depending on, e.g. run number and recognize alignment parameters per each sensor in each file. The monitored alignment parameters can be plotted as a function of run number or time in the so-called time-dependent alignment parameters monitoring plots.

3.4.2 Monitoring χ^2 invariant modes

The systematic misalignment of the silicon vertex detectors was studied several times in previous experiments (e.g. LHC experiments [50]). Several techniques have been developed. Some methods monitor weak modes using physical quantities as mass, vertex position or efficiency, but other techniques use methods based on pure tracking information. In this thesis, the tracking method based on measuring residual difference using a pair of hits in neighbouring sensors [51] is used. Using this technique, all topographical different tracks can be used (cosmic and collision samples).

The core of this method is based on finding a pair of hits from overlapping areas of the vertex detector (Figure 3.5). Overlapping hits from tracks are filtered from
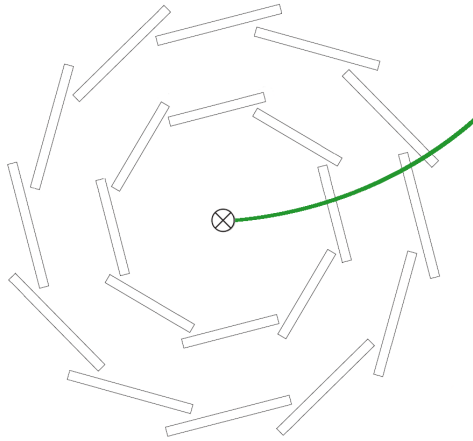
Figure 3.5: A track passing through overlapping area (second layer) of vertex detector

other hits and studied. In our studies, pairs of overlapping hits are classified based on two different criteria : pairs of hits with the same and different sensor positions in ladders (Figure 3.6). The sensitivity of both categories is different. The first category, pairs with the same position of the sensors in ladders, detects geometrical issues in the r and ϕ directions, but the second category is more useful for studying effects in the z direction.
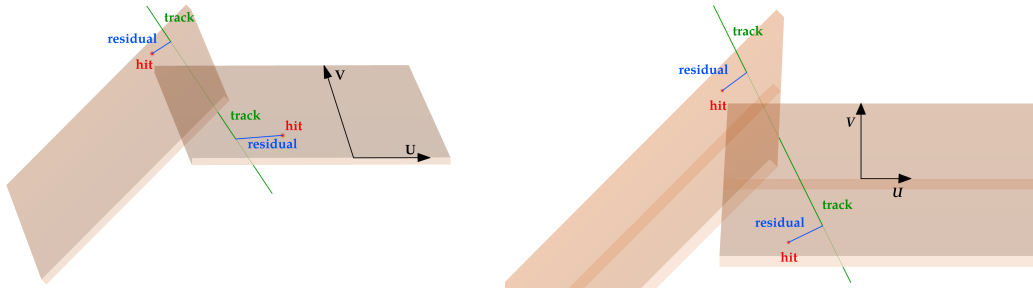
Figure 3.6: Illustration of the pair of overlapping hits with same (left) and different (right) sensor number

The monitoring tool at the collection level can distinguish between overlapping situations. To keep the information, the storing procedure is completed according to one of the three scenarios:

1) Overlapping hits in sensors with same positions in ladder

2) Overlapping hits in sensors with different positions in ladder

3) Hits from non-overlapping area

The most sensitive quantity to geometry changes is the difference between unbiased residuals of hit pairs from overlapping areas. Due to measuring residuals

in two independent directions (u and v), we measure two independent values of difference for a single pair of hits, which can be shown as two-dimensional distribution. Thanks to two pair categories, two two-dimensional distributions and an additional two-dimensional distribution filled by standard residuals for non-paired hits can be studied. Fortunately, the vertex detector geometry can be studied depending on hierarchy levels (as a function of halves, layers ladders and sensors).

4. Belle II detector operation

After KEKB and Belle detector were shut down and uninstalled, the KEK complex started preparations for the upgrade into SuperKEKB, Belle II respectively. As was mentioned in Chapter 1, several upgrades were performed and new tools were developed. In this chapter, we will explain the individual steps of operation of the accelerator and the detector needed to achieve first beam injections into the storage rings, first collision observations and the world highest luminosity record.

4.1 The SuperKEKB operation

The SuperKEKB beam commissioning consisted of three phases (Figure 4.1) [52]:

1) Phase 1: Accelerator commissioning without the Belle II detector

2) Phase 2: Partial Belle II detector commissioning

3) Phase 3: Complete Belle II detector commissioning
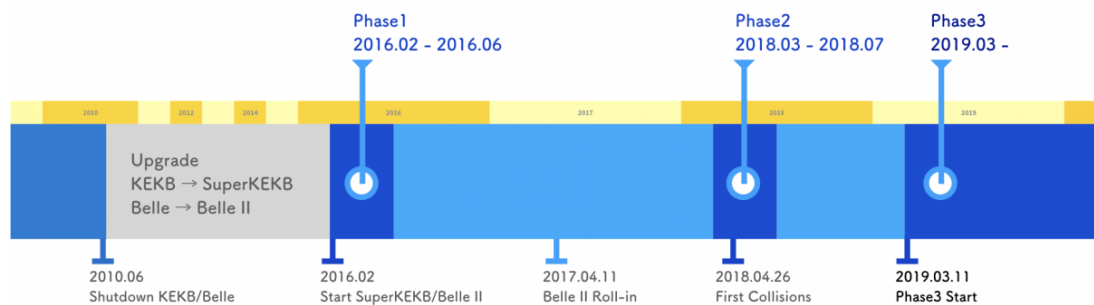
Figure 4.1: Timeline of the path from KEKB to SuperKEKB [53]

In 2016 the Phase 1 was commissioned without the focusing magnets (QCS) or the detector. The collision was not performed. During Phase 1 accelerator hardware components were turned on, beam operation software tools were developed and applied; optics, vacuum scrubbing and other machine components studies were conducted. The important study of the accelerator beam background was also performed using a test detector named BEAST II (Beam Exorcisms for A Stable Belle II experiment). It was installed for verification of safe conditions for the installation of the Belle II detector and validation of the background simulations [54].

The damping ring, the final focusing system and the Belle II detector with beam background detector system were installed during a long shutdown between Phase 1 and Phase 2. The Phase 2 commissioning was started on the 19th of March 2018 and finished on the 17th of July. The non-collision optics was replaced by collision optics, and the Belle II detector observed the first collision event on

the 26$^{\text{th}}$ of April. In Phase 2 the beta functions in the IP were squeezed from $\{\beta_x^*, \beta_y^*\} = \{400, 81\}$ mm to $\{200, 3\}$ mm for HER and from $\{384, 48.6\}$ mm down to $\{200, 3\}$ mm for LER. The maximum beam current was 860 mA in the LER and 800 mA in the HER, respectively. The peak luminosity of 5.55×10^{33} cm^{-2}s^{-1} was achieved. The history of beam currents and luminosity in the Phase 2 is shown in Figure 4.2 [55].

Figure 4.2: History of beam currents for HER (top) and LER (center) and peak luminosity (bottom) in the Phase 2 [55]

Before the Phase 3 started the beam background detector had been replaced by full vertex detector. It was installed in December 2018. The belle II detector has been running since Phase 3 started at the beginning of 2019. The accelerator operation was paused due to a fire accident in April 2019, Summer and Winter shutdowns and some smaller temporary pauses for maintaining the detector and accelerator happen every two weeks. The accelerator group performs several investigations and studies to improve collisions and accelerator characteristics. The squeezing of beta functions in the interaction region had continued and the record values are $\{\beta_x^*, \beta_y^*\} = \{60, 0.8\}$ mm for both rings from July 1$^{\text{st}}$ 2020. For both rings, the crab waist scheme has been used since spring 2020. The progress in tuning of machine parameters resulted into the world's highest 2.40 $\times 10^{34}$ cm^{-2}s^{-1} luminosity achieved on 21$^{\text{th}}$ June 2020 [56]. Again the history of beam currents and luminosity for the Phase 3 can be found in Figure 4.3.

4.2   Beam backgrounds of SuperKEKB

The beam background means background particles generated by the accelerator. The particles can be produced by single-beam processes: synchrotron radiation, Touschek scattering, beam-gas scattering and beam-dust scattering. The injection of the beams into the storage ring can produce background events such as Bhabha scattering, multi-lepton and multi-photon events. There is also a possibility of luminosity related background production, for example, electromagnetic
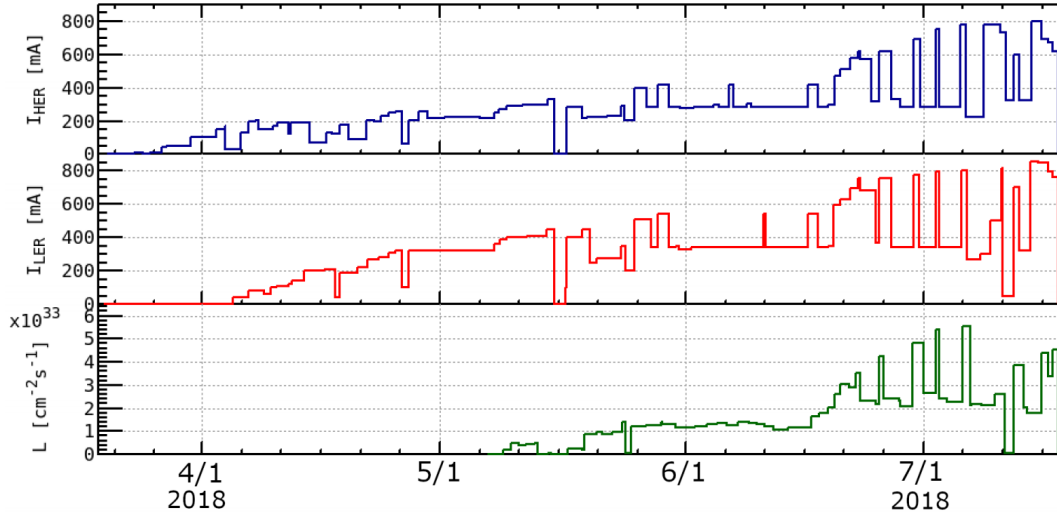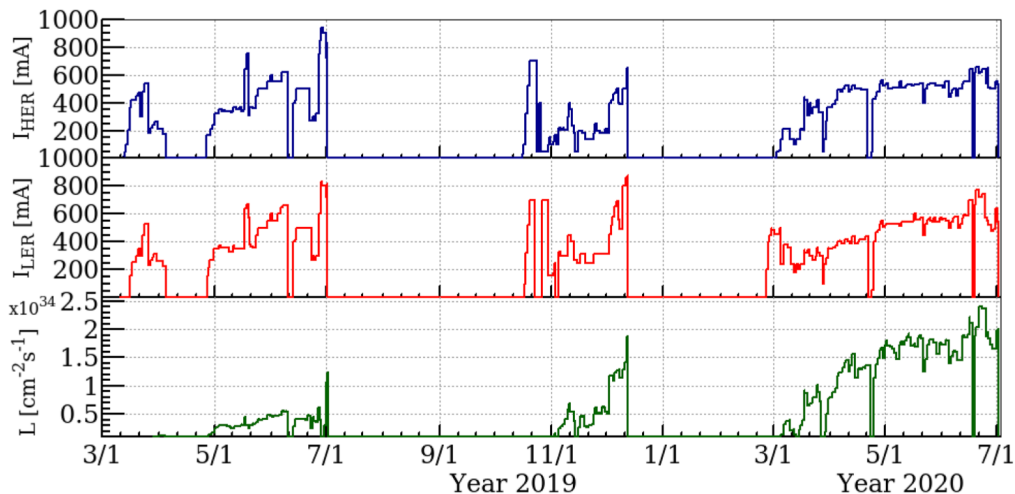
Figure 4.3: History of beam currents for HER (top) and LER (center) and peak luminosity (bottom) in the Phase 3 [57]

shower after passing through the final focusing magnets, neutrons produced in the interaction of Bhabha's photon and iron atoms in the magnets, two-photon processes and low momentum electron-positron pairs production [54, 55].

During the Phase 2, the beam background measurement observed higher background levels than expected, with LER storage background being around five times the size of the HER one and with HER injection background always higher than LER one. In the Phase 3 beam background reduction was achieved by implementing additional new collimators, replacement of destroyed collimators, moving some collimators in rings of SuperKEKB and vacuum scrubbing.

4.3   The Belle II operation

The Belle II detector was rolled-in to the collision point on the 11$^{\text{th}}$ of April 2017 [58]. Prior to the Phase 2, partial Belle II detector was installed. The vertex detector was replaced by beam background detector system combined with one ladder in every layer of the final silicon detector. The detailed geometry and alignment studies related to Phase 2 vertex detector are discussed in Chapter 5. In 2018 the Belle II detector collected Phase 2 data sample at the energy corresponding to the $\Upsilon(4S)$ resonance. The integrated luminosity of the data sample is about 500 pb^{-1}, where the measurement was provided using Bhabha and $\gamma\gamma$ events [59].

After Phase 2 the beam background detector system was replaced by the full vertex detector. The vertex detector is composed of full strip detector and partial pixel detector (Figure 4.4), called *Phase 3 early*. The Phase 3 early pixel detector is composed of ten ladders, eight of which form the first layer and two
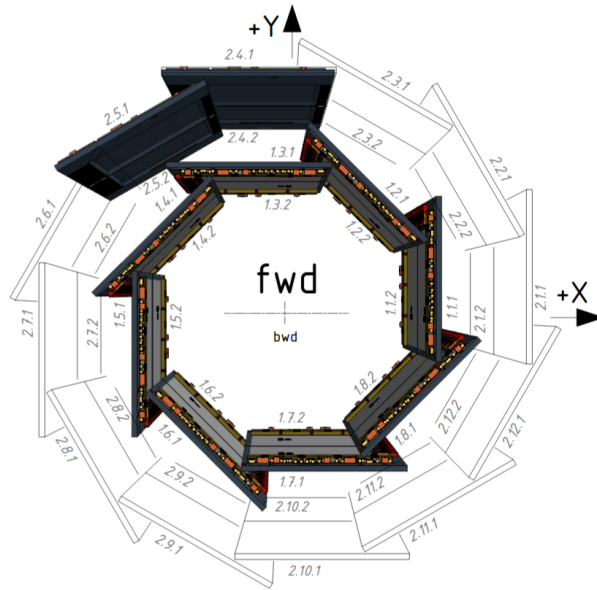
Figure 4.4: Overview of Phase 3 early pixel detector [60]
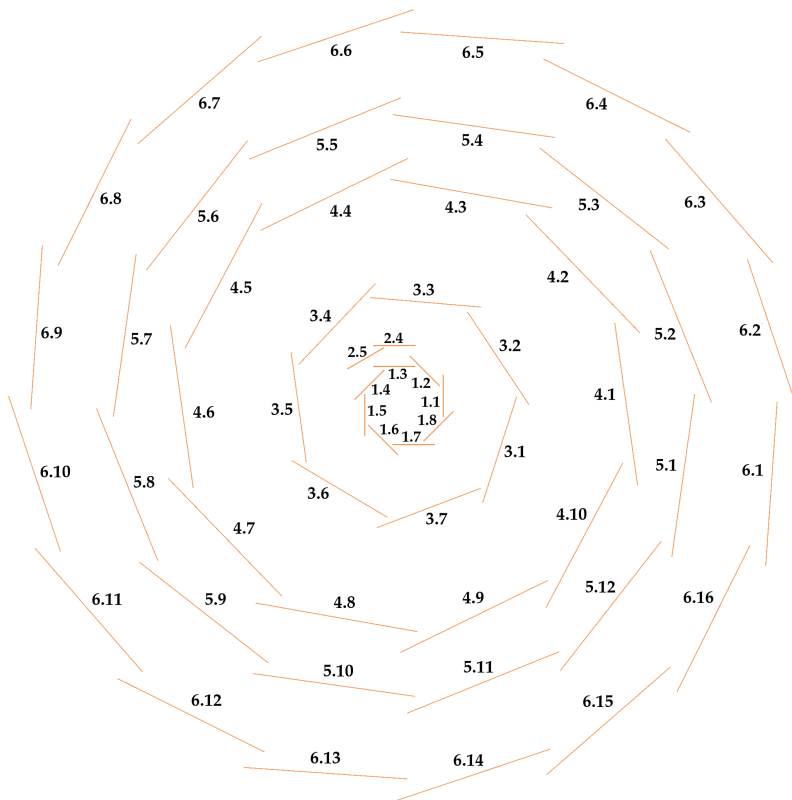
Figure 4.5: Ladder numbering of vertex detector for phase 3 early geometry

ladders are installed in the second layer. Considering the design of Phase 3 early pixel detector, the Figure 1.16 can be updated to Phase 3 early version as can be found in Figure 4.5. For clarification, the vertex detector with full pixel de-
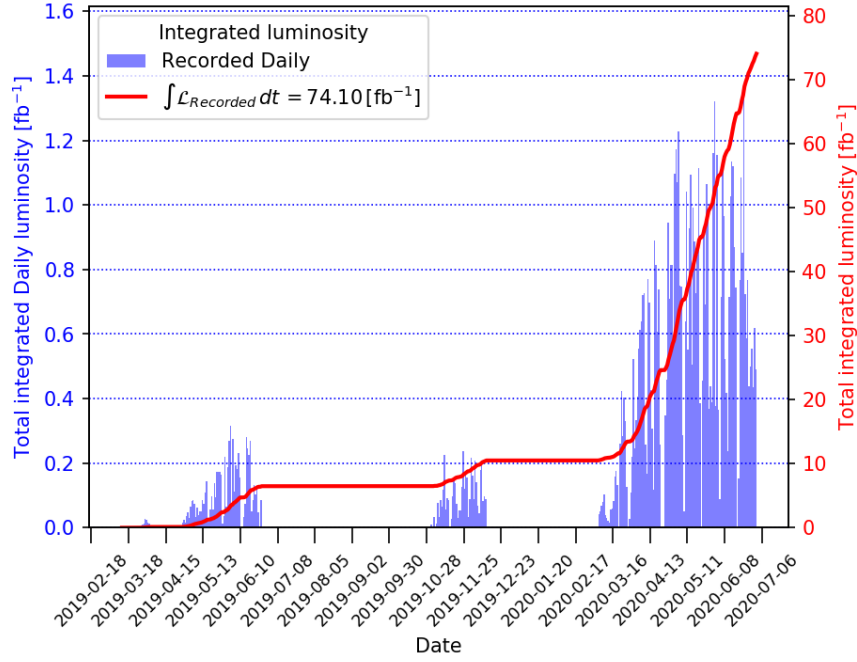
Figure 4.6: History of integrated luminosity during Phase 3 [61]

tector is labelled *Phase 3*, and it is used for some dedicated Monte Carlo studies. Before installation, two special data taking rounds took place: standalone SVD and combined PXD-SVD commissioning runs, which are studied and discussed in Chapter 6. Since the vertex detector assembly, only nineteen-pixel sensors have been operating; the 1.3.2 sensor has never been operated [60, 62, 63, 64].

In December 2018 the vertex detector was installed in the center of the Belle II detector. After installation, some studies were repeated, and they are discussed in Chapter 7. The Belle II detector started collecting data sample corresponding to the $\Upsilon(4S)$ resonance on the 11th of March 2019. The integrated luminosity of the data sample collected before June 2020 is about 74.10 fb^{-1} with 10% off-resonance data sample. The history of Phase 3 integrated luminosity can be found in Figure 4.6. In summary, the Belle II data taking periods and experiment numbers can be found in Table 4.1.

Year	2018											
Month	01	02	03	04	05	06	07	08	09	10	11	12
Label			Phase 2				VXD Commissioning					
Experiment	1	2	3				4					
Year	2019											
Month	01	02	03	04	05	06	07	08	09	10	11	12
Label			Phase 3							Phase 3		
Experiment	5	6	7		8		9			10		
Year	2020											
Month	01	02	03	04	05	06	07	08	09	10	11	12
Label			Phase 3							Phase 3		
Experiment	11		12				13			14		

Table 4.1: The Belle II data taking periods and experiment numbers

5. Vertex detector in Phase 2

During Phase 2, the vertex detector was composed of the associated background detector: PLUME, CLAWS and FANGS sensors and one ladder per each layer of pixel and strip detectors. It was labelled as the *Phase 2 vertex detector* and its design is introduced in Figure 5.1, and the number of sensors can be found in Table 5.1. The ladders are installed in a row along the x axis. The outer ladders perfectly covered inner layers, what allowed for measurement of horizontal tracks with a high number of hits in the vertex detector. In other words, we expect no or very few vertical tracks with a hit in the vertex detector.
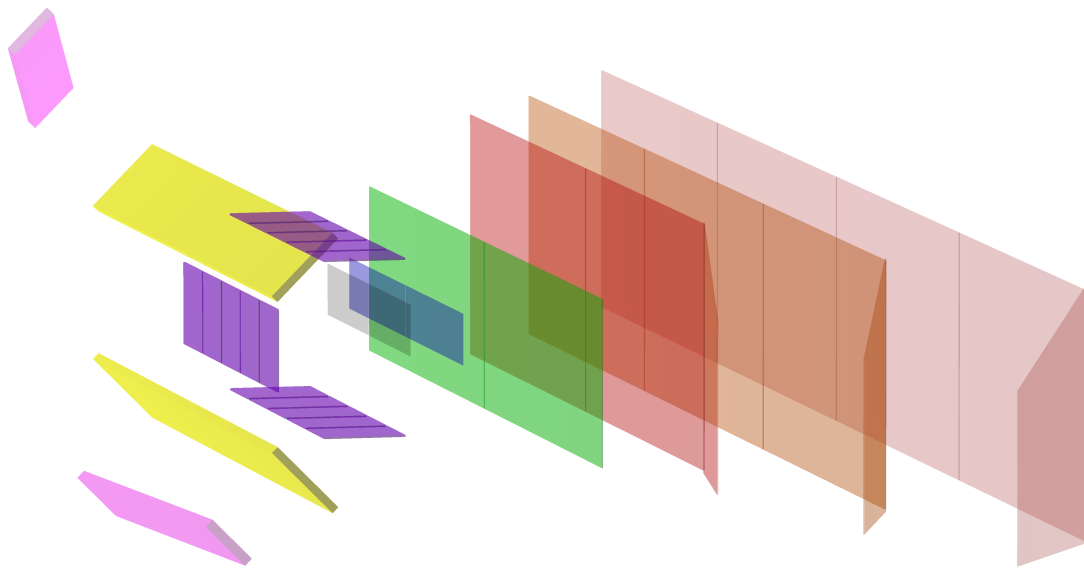
Figure 5.1: Geometry of Phase 2 vertex detector: PLUME (pink), FANGS (yellow) and CLAWS (violet) background sensors and one ladder per layer of pixel and strip detector, where colors are associated with number of layers and Table 5.1

	Radius [mm]	Sensors
PXD Layer 1	14	2
PXD Layer 2	22	2
SVD Layer 3	39	2
SVD Layer 4	80	3
SVD Layer 5	104	4
SVD Layer 6	135	5
Total		18

Table 5.1: Number of sensors in layer or ladders in Phase 2 vertex detector

5.1 Track reconstruction in Phase 2

From the geometry of the Phase 2 vertex detector, two χ^2 invariant modes can be spotted clearly: x (w) direction and β angle. To be able to provide sensitive alignment studies, the χ^2 invariant modes must be eliminated. Our alignment algorithm can use rich track samples, or additional constraints can be applied. The collection of rich track samples can be problematic because the vertex detector can reconstruct horizontal collision tracks only (Figure 5.2). The cosmic tracks with vertical orientation can be difficultly reconstructed in basf2 software framework. In the Belle II tracking approach, the reconstruction of a cosmic track with one or two SVD hits is possible, but a cosmic track with single PXD hit without SVD hits is impossible. The PXD hits can be found using SVD tracks only. In order to be able to reconstruct cosmic tracks passing through the vertex detector additional software extensions should be developed and tracking studies performed. Using cosmic and collision tracks, alignment parameters were determined. The final alignment validation studies were provided using collision tracks.
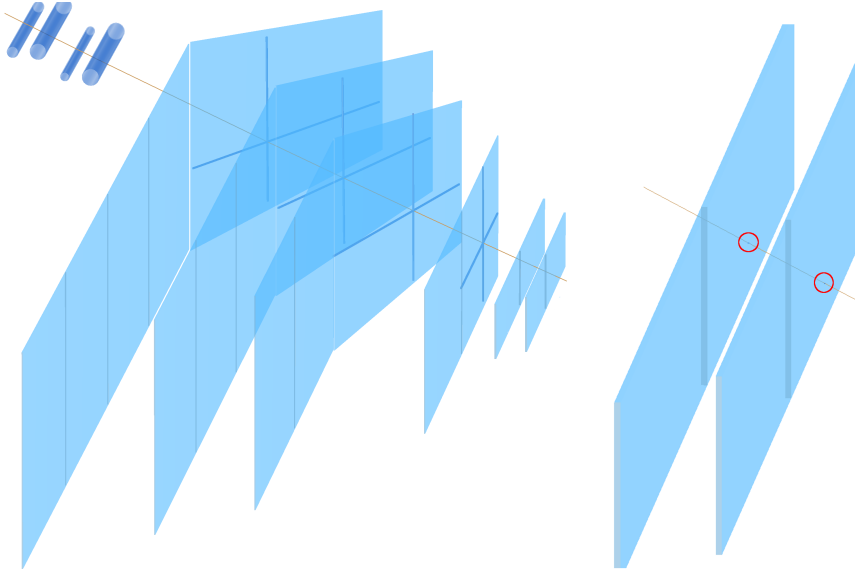
Figure 5.2: Collision track (orange) passing through the vertex detector (light blue) with reconstructed CDC hits (dark blue), SVD (dark blue) and PXD (dark blue in red circles) clusters

5.1.1 Cosmic tracks in the vertex detector

The Belle II track finding approach does not support extrapolation of the CDC tracks to the PXD volume for adding a PXD hit to a track. The PXD hits are read from RoIs only, which are extrapolated from the orientation of SVD tracks. For connecting inner detectors with the outer detector, the combinatorial Kalman filter (CKF) is used. The CDC-SVD filter can find single SVD hit on a cosmic track composed by two CDC tracks (upper and lower parts). Due to the central

position of the vertex detector, the CDC track parts associated with vertex detector hit(s) can be populated by 50 to 60 CDC hits. The CDC-PXD filter was not developed until Phase 2, and special requirements had to be met: elimination of RoI using SVD tracks, decrease the number of PXD hits per event as much as possible and tune developed track finding techniques to identify correct cosmic PXD hit on the track.

Firstly, the Monte Carlo studies related to finding PXD hits on cosmic track were provided. The CDC-SVD CKF technique was tuned for high efficiency in finding SVD hits. The CDC-PXD CKF technique was developed in order to find hits in pixel detector. Due to cosmic events being relatively clean, the pre-scaled RoIs were implemented in the Phase 2 HLT. These track finding conditions were applied in first cosmic data taking runs to prove the correct functionality of CDC-PXD CKF. First experiences reported about high occupancy of events with PXD hits and additional hot spots masking procedure for pixel sensors was required. After having processing the cosmic data offline, the first cosmic tracks with the vertex detector hits were observed. A cosmic track passing through an SVD sensor is illustrated in Figure 5.3, and a PXD hit in a cosmic track is reported in Figure 5.4.
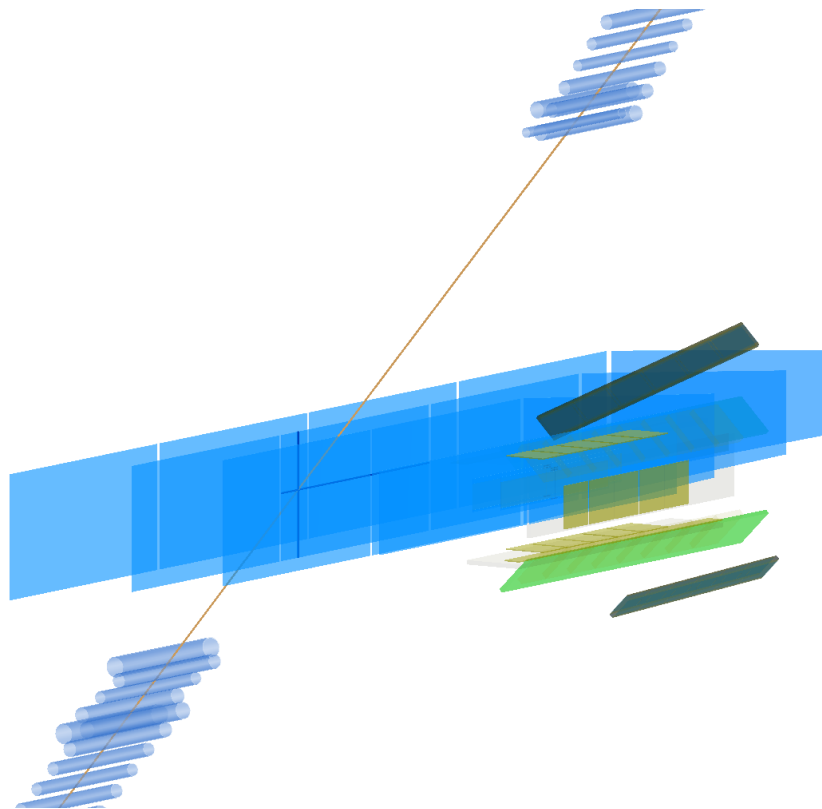
Figure 5.3: Cosmic track (orange) passing through the Phase 2 strip detector (light blue) with reconstructed SVD clusters (dark blue) and the CDC hits (dark blue); the background detectors (green) are shown too
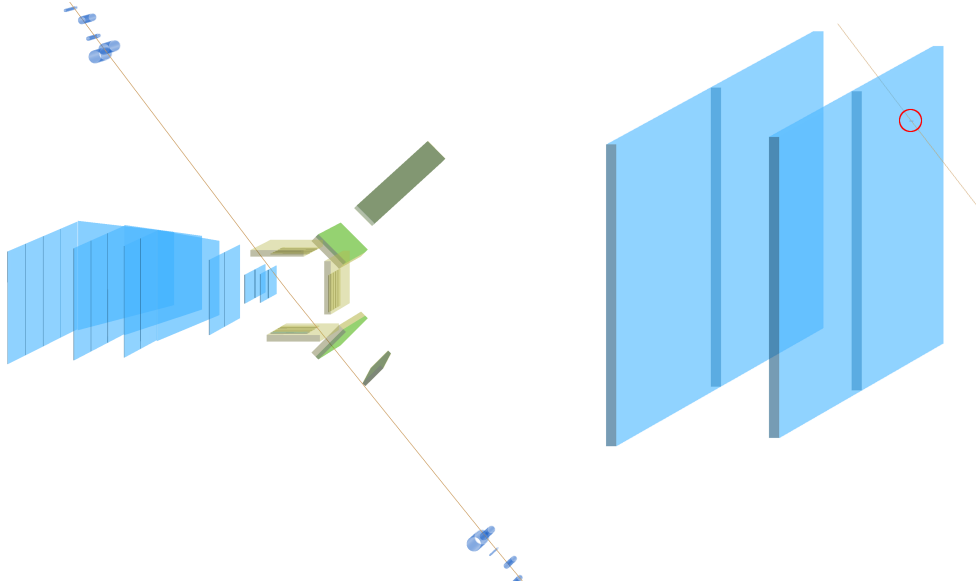
Figure 5.4: Cosmic track (orange) passing through the Phase 2 pixel detector (light blue) with reconstructed SVD clusters (dark blue) and the CDC hits (dark blue); the background detectors (green) are shown too

5.2 Data samples

The Monte Carlo studies had been performed before the first data was processed. To produce simulated cosmic samples, we used the CRY cosmic generator with a global box large enough, the volume of the keep box was proportionally equivalent to the one of the CDC and the same applies to the accept box with respect to the VXD volume. The geographical and time properties were set according to the position of the detector and time in Japan when cosmic data taking was planned. The collision data was generated by standard Belle II event generator for $\Upsilon(4S)$ data sample. The cosmic and collision tracks are reconstructed using the Phase 2 geometry. For the cosmic track, one requires at least one VXD hit, and for collisions, we expect at least three hits.

The cosmic Monte Carlo sample is composed of 30 thousand cosmic tracks passing through the VXD sensors, where about 86 % of them are tracks with single VXD hit, 10 % are with a pair of VXD hits, 3 % with three VXD hits and other possibilities form less than 1 % (Figure 5.5). On average the strip sensors have a 10 times higher probability of detecting a cosmic track than the pixel sensors. For alignment studies, 90 thousand collision tracks were simulated.

The cosmic and collision data was taken during experiments 2 and 3. The run 2 was dedicated to collecting cosmic data without using a solenoidal magnet and the focusing system (QCS). In run 3, the cosmic and collision data was collected using a solenoidal magnet and the QCS. For alignment purposes, the 70 thousand cosmic and collision tracks were collected. In collected data the cosmic tracks are populated with similar statistical probability as a simulated sample: 73 % cosmic tracks with single VXD hit, 19 % tracks with double hits in the VXD, 7 % for
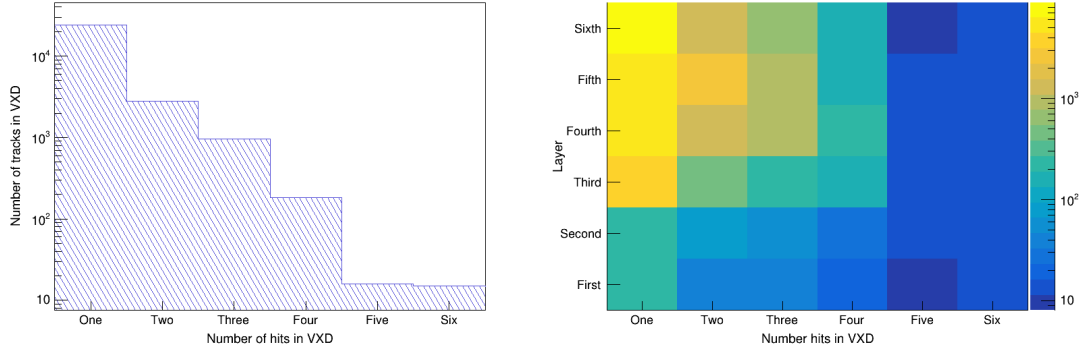
Figure 5.5: Number of VXD hits in cosmic track for Monte Carlo simulation: one dimensional distribution (left) and function of VXD layers (right)

three VXD hits and less than 2 % for other cosmic tracks.

The alignment monitoring studies were performed using the full sample of collected collision data. The data was processed to investigate and validate the alignment parameters. Afterwards, the time-dependent monitoring of alignment parameters for a chosen combination of alignment parameters was performed.

5.3 Vertex detector alignment studies

To check the optimal alignment strategy, the Monte Carlo studies was provided before the data taking. After the first data was available, the alignment studies with rigid body parameters were carried out, and the alignment constants were determined. During the data taking in 2018, the alignment results were monitored. Several months after finishing the data collection, the surface parameters were implemented in reconstruction software, and surface deformation of the vertex detector sensors was estimated. The final alignment studies to investigate the number of necessary alignment parameters and monitor them were done. In all alignment studies, no constraint was used, but the central drift chamber was used as a reference.

5.3.1 Monte Carlo studies

To estimate systematic and statistical errors, we provide three similar alignment studies with different combinations of samples: cosmic sample, collision sample and a mixture of them. We processed prepared simulated tracks and using outputs of Millepede II algorithm we estimated the errors. The results are summarized in Table 5.2. For vertical cosmic tracks, the errors dominate for local u (vertical y axis) and β parameters for all sensors. For horizontal collision tracks the largest discrepancy was observed for local w (horizontal x axis) shift and β angle. For the mixture of samples, same parameters as in the cosmic data sample showed matching highest values. The cosmic tracks with less occupation of VXD hits have more significant effect than collision tracks with high occupancy of VXD hits. From the study, one can clearly see the size of samples has no crucial effect

on a precision of the alignment procedure, but the track topography is more significant.

Sample		Cosmic		Collision		Mixture	
Sensors		Pixel	Strip	Pixel	Strip	Pixel	Strip
Systematic	Shifts [μm]	20.0	20.0	50.0	50.0	17.0	16.0
error	Rotations [mrad]	1.5	0.6	1.5	0.4	0.4	0.2
Statistic	Shifts [μm]	4.0	4.0	17.0	28.0	3.0	3.0
error	Rotations [mrad]	0.7	0.1	2.0	0.4	0.3	0.1

Table 5.2: Statistic and systematic errors for different alignment samples

5.3.2 Rigid body alignment tests

After collecting and reconstructing the cosmic and collision samples, the vertex detector alignment could be determined. The vertex detector alignment procedure was performed to determine rigid body parameters as the first step. The resulting alignment values are shown and discussed in Appendix C.

After determining alignment constants, the validation procedure was performed to verify the correctness of alignment parameters. Resulting validation plots can be found in Figure 5.6. The validation report about the effect of alignment on unbiased residual distribution in u and v directions. For pixel sensors, we observed residual distributions with means close to zero and standard deviations about 20 - 50 μm. The strip sensors residual distributions were obtained, their means were close to zeros and the standard deviations were about 50 - 100 μm.

In pixel sensors, we can not recognize any surface deformation; residuals in w direction projected onto the plane of sensors are flat and closed to zero, what is in agreement with our expectations. However, the projected residuals report about potential surface deformation for some strip sensors. The validation plots for strip sensors inform about maxima on edges and sides and minimum in the center of sensors. The scale of deformation is about 400 - 500 μm. In comparison with the definition of alignment parameters in Figure 3.2 we see these are formed by a linear combination of P_{02} and P_{20} parameters.

Historically, this was the first measurement of sensor surface deformations using the Belle II vertex detector. However, the first observation of the surface deformations was not enough to expand the Belle II reconstruction software using the surface parameters due to low quality of installed silicon sensors and possible bugs in developed validation software tools. After the next experiences from VXD Commissioning (Section 6) and positive effect of elimination procedure on the precision of measurement, the alignment studies were repeated for elimination surface deformations of silicon sensors using the Phase 2 datasets.
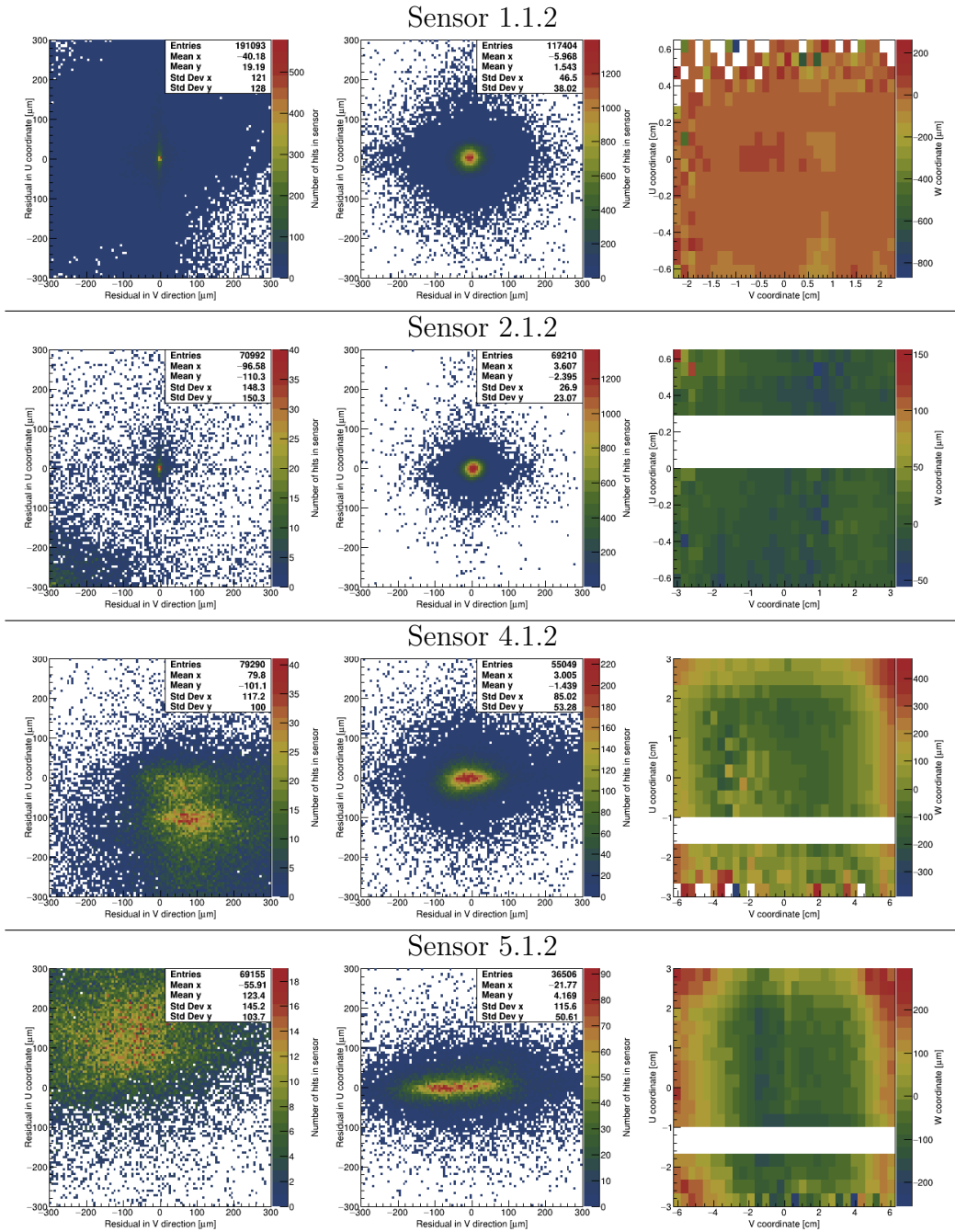
Figure 5.6: Validation of rigid body alignment for vertex sensors: residual distributions for u and v parameters before alignment (left), after alignment (center) and w residual (right) after alignment; improvements coming from alignment can be seen in differences between left and center columns; empty (white) areas in right column are masked areas of sensors; low occupancy can be identified as areas with large fluctuation of averaged values on sides of sensors in right column

5.3.3 Estimation of surface deformation of vertex sensors

Based on our previous experience and from the VXD Commissioning, additional alignment study was important to approximate sensors surface deformations before Phase 3 data taking periods. Because of that, sophisticated alignment studies and tests were performed. To check and estimate real surface deformation,

the alignment surface parameters were implemented and studied level by level. Firstly, we combined and determined rigid and quadratic surface parameters (P_{20}, P_{11}, P_{02}) and provided validation of alignment. Then we combined rigid, quadratic and cubic $(P_{30}, P_{21}, P_{12}, P_{03})$ parameters and repeat validation algorithm to check the results. The resulting values of alignment algorithms can be found in Appendix C. According to w residuals projected to sensor surfaces in Figure 5.7 extensions improve residual distributions and decrease discrepancy for data. In high occupied areas of 4.1.2 sensor, the residual distribution looks flat and close to zero for quadratic distribution. The cubic option has no crucial effect, and it is not required in this sensor. In sensor 5.1.2 the surface is flatter for the cubic option than for quadratic. The cubic surface parameter P_{03} can be identified and determined using the alignment procedure.
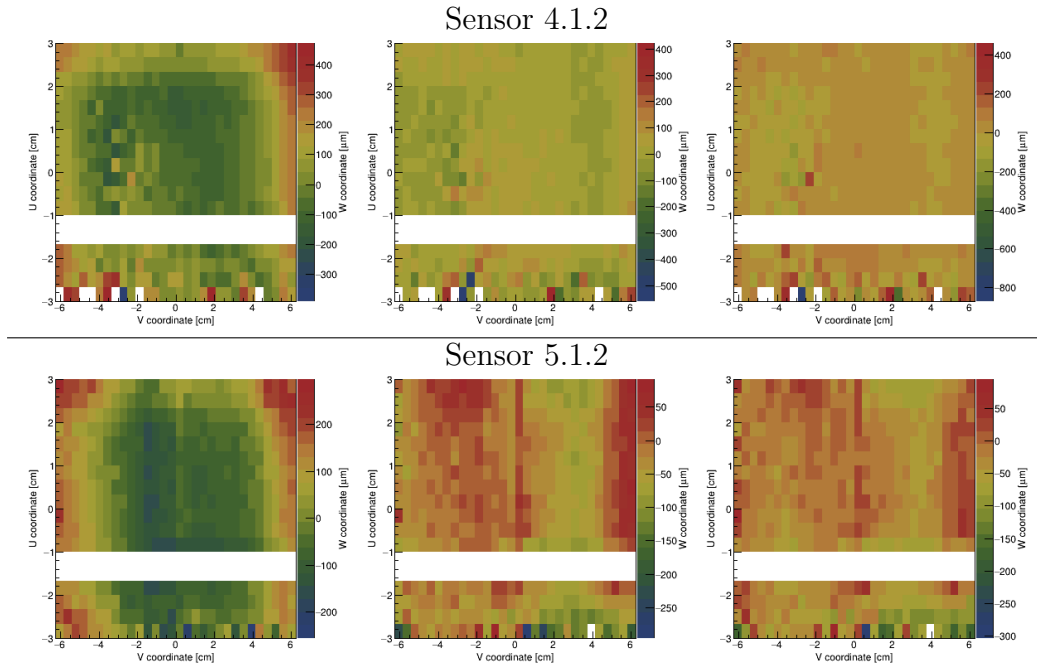
Figure 5.7: Validation of surface alignment for strip sensors: w residual distribution projected onto the surface of strip sensors for rigid body (left), quartic (center) and cubic (right) alignment parameters; white areas are masked

5.3.4 Alignment parameters monitoring depends on time

The alignment procedure determining rigid body and quadratic surface parameters was sufficient for several sensors. To get better alignment, we iterated the procedure one more time. These final alignment constants were used for processing the full Phase 2 data. The processed data was divided according to runs. In each run, the alignment parameters were extracted for each sensor. The values were plotted to report about time-dependent validation of alignment parameters. The monitoring plots of sensor 1.1.2, 2.1.2, 4.1.2 and 5.1.2 are plotted in Figures 5.8, 5.9, 5.10 and 5.11, respectively. From monitoring plots we can observe, the parameters were close to zero. The monitoring values fluctuated in the range $\pm$ 10 μm. For the sensor 5.1.2, fluctuation of P_{03} parameter is shifted about 20 μm.

Figure 5.8: Time dependent validation of sensor 1.1.2 alignment parameters: shift (first line), rotation (second line), quadratic (third line) and cubic (fourth line) surface parameters; the units of alignment parameter axes are μm.
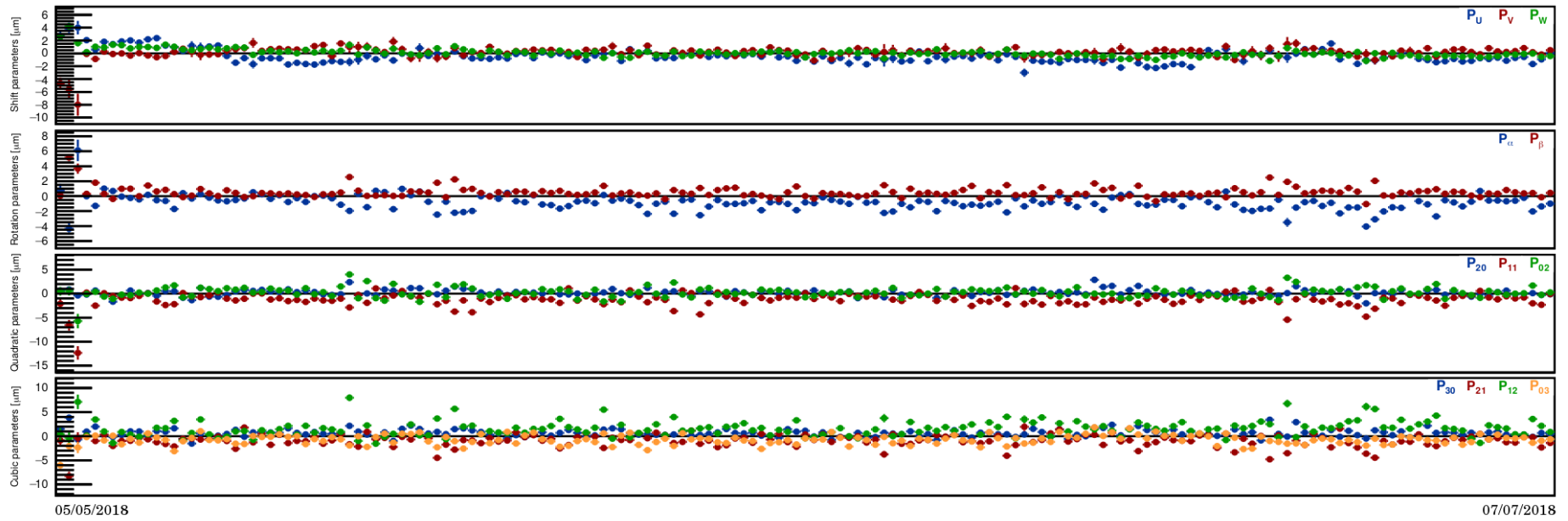
Figure 5.9: Time dependent validation of sensor 2.1.2 alignment parameters: shift (first line), rotation (second line), quadratic (third line) and cubic (fourth line) surface parameters; the units of alignment parameter axes are μm.
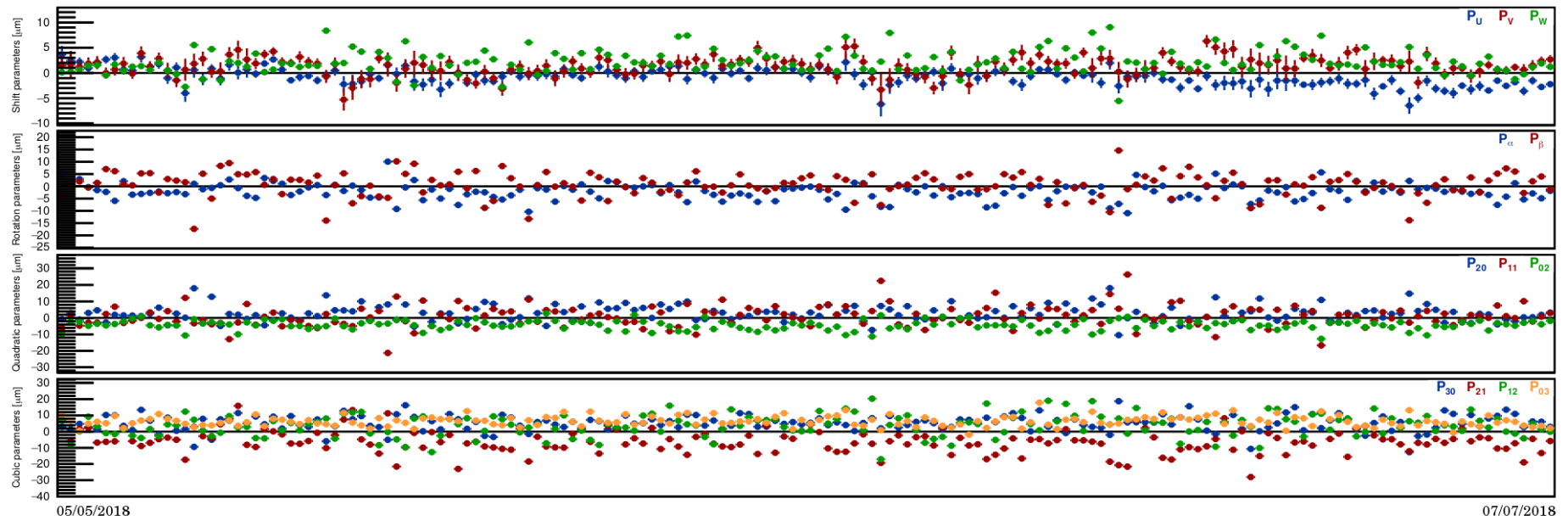
Figure 5.10: Time dependent validation of sensor 4.1.2 alignment parameters: shift (first line), rotation (second line), quadratic (third line) and cubic (fourth line) surface parameters; the units of alignment parameter axes are μm.
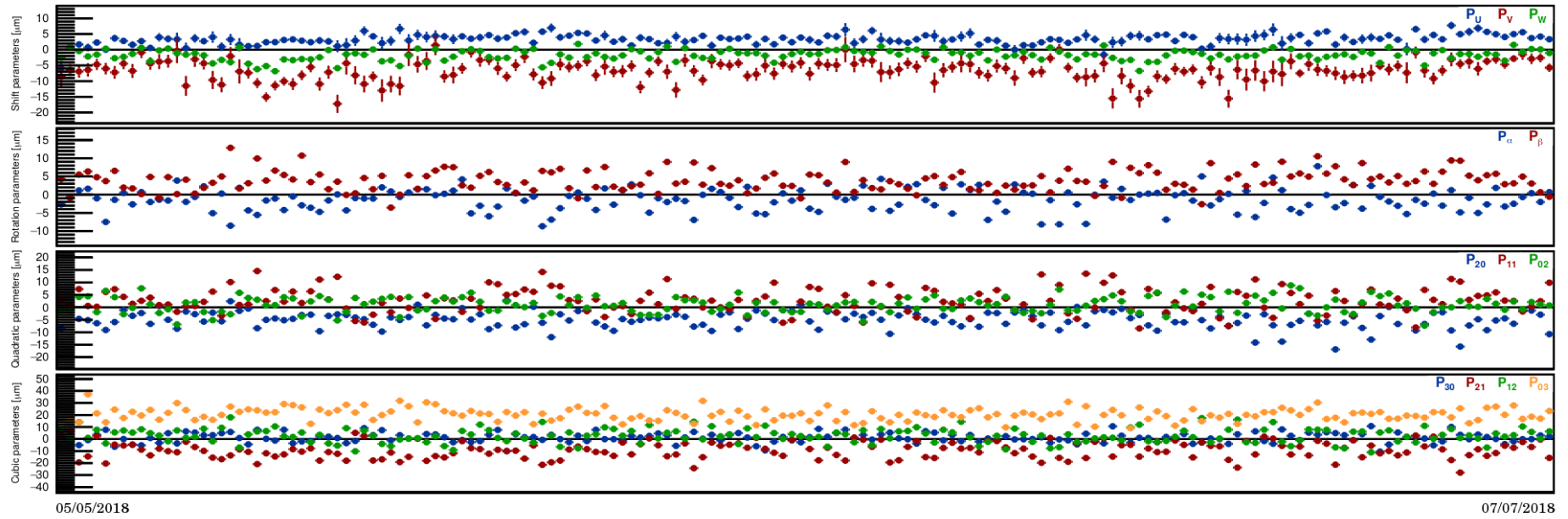
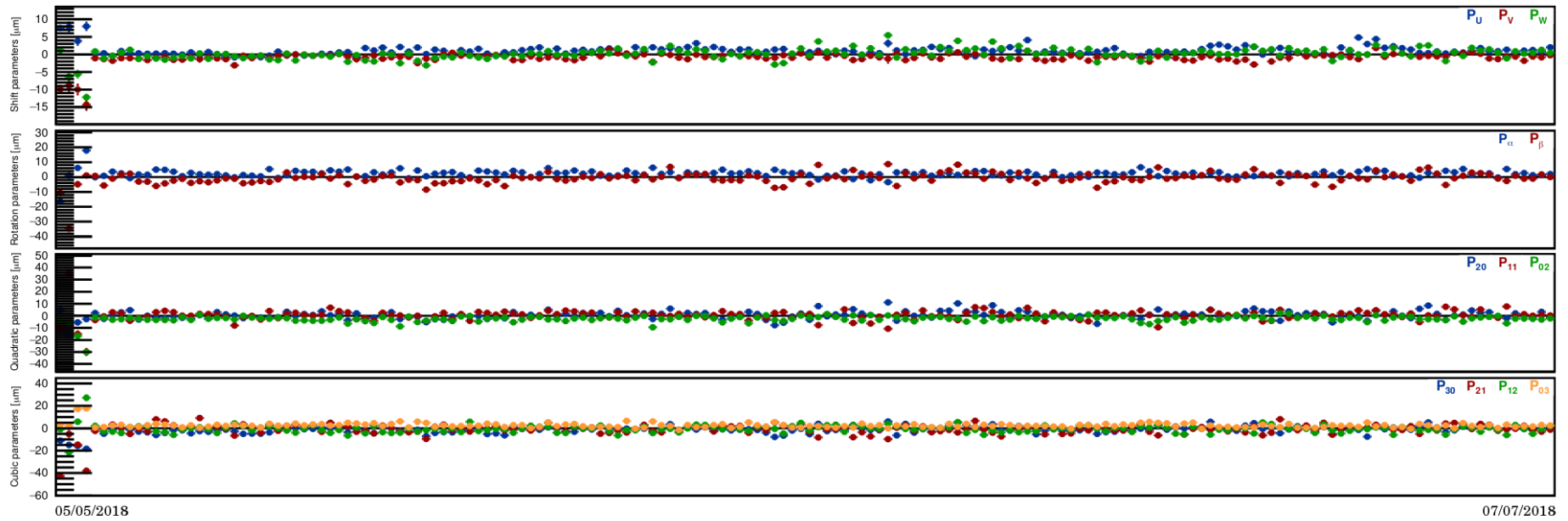Figure 5.11: Time dependent validation of sensor 5.1.2 alignment parameters: shift (first line), rotation (second line), quadratic (third line) and cubic (fourth line) surface parameters; the units of alignment parameter axes are μm.

6. Vertex detector commissioning

In February 2018 strip ladders were assembled into the first SVD-half. The half was moved into a storage box. The assembly of the second SVD-half was completed in July and it was also moved into the second storage box. The storage boxes were built from aluminium panels and frames to ensure light-shielding, device protection, and a stable dry environment. The halves were cooled using -20 C° stream of coolant. Two plastic scintillator bars were installed: a larger bar on the roof of the box and a smaller under a storage table. The illustration of the triggers and halves setup can be found in Figures 6.1 and 6.2. To test the operation, data acquisition system, calibration and track reconstruction algorithms, cosmic rays were measured by SVD-halves in SVD standalone commissioning data taking periods.
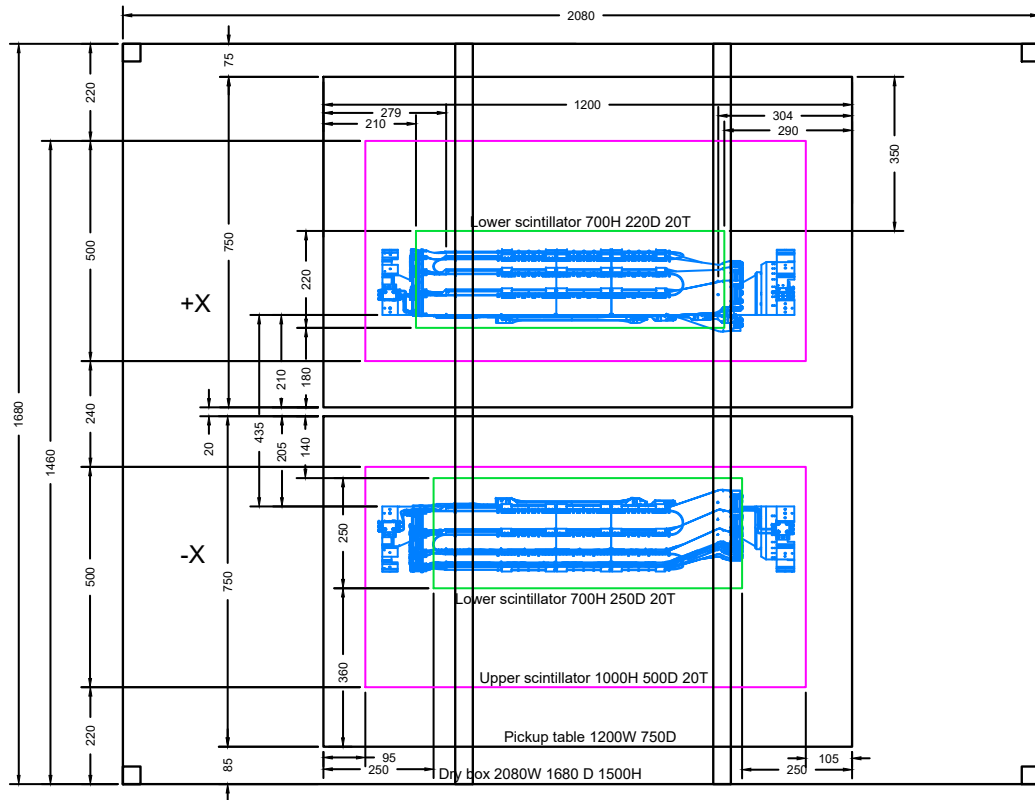
Figure 6.1: SVD standalone commissioning geometry in XZ plane: the upper trigger counter (pink), the lower trigger counter (green) and the halves of the strip detector (blue). Distance values are in milimiters. [65]

In October 2018 the pixel detector was finished. As mentioned in the Section 4 only one half of the ladders were mounted. All ladders from the first layer and two ladders from the second layer were implemented. The partial pixel detector was coupled with SVD-halves. The scintillating counters covered the finished
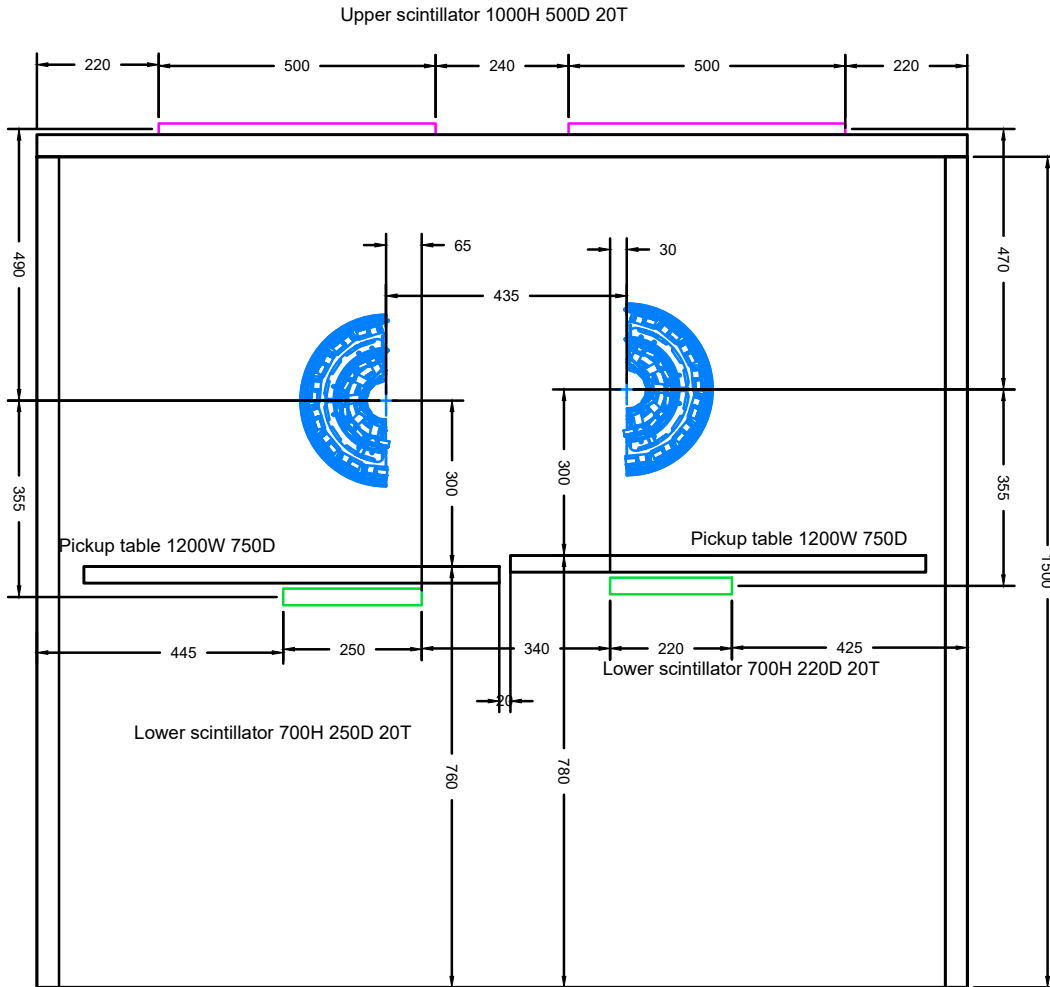
Figure 6.2: SVD standalone commissioning geometry in XY plane: the upper trigger counter (pink), the lower trigger counter (green) and the halves of the strip detector (blue). Distance values are in milimiters. [65]

vertex detector in order to perform combined measurement of cosmic rays. Combined data acquisition system, combined track reconstruction, pixel and strip detector calibration algorithms were tested. Based on past experience with the SVD-halves, a sophisticated trigger system was used. The main trigger system composed of six plastic scintillating bars at the top and six bars at the bottom. To expand vertical trigger efficiency, four additional triggers were installed. One of them was implemented into the top forward side and another one into the bottom forward side. The next pair of triggers was installed at the backward side. Two large plastic scintillating bars from SVD standalone commissioning were added on the right and left side to detect mostly horizontal cosmic rays. The trigger setup is illustrated in Figure 6.3.
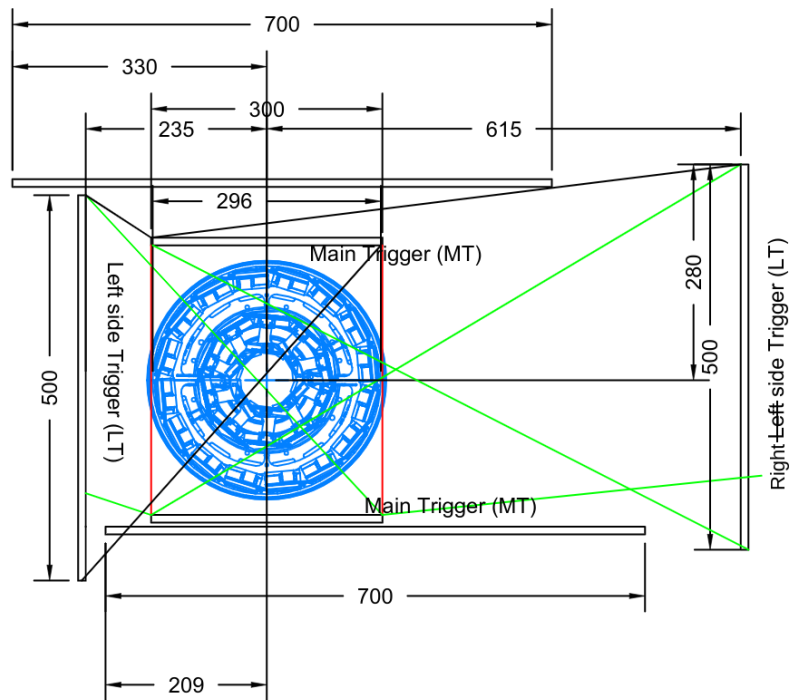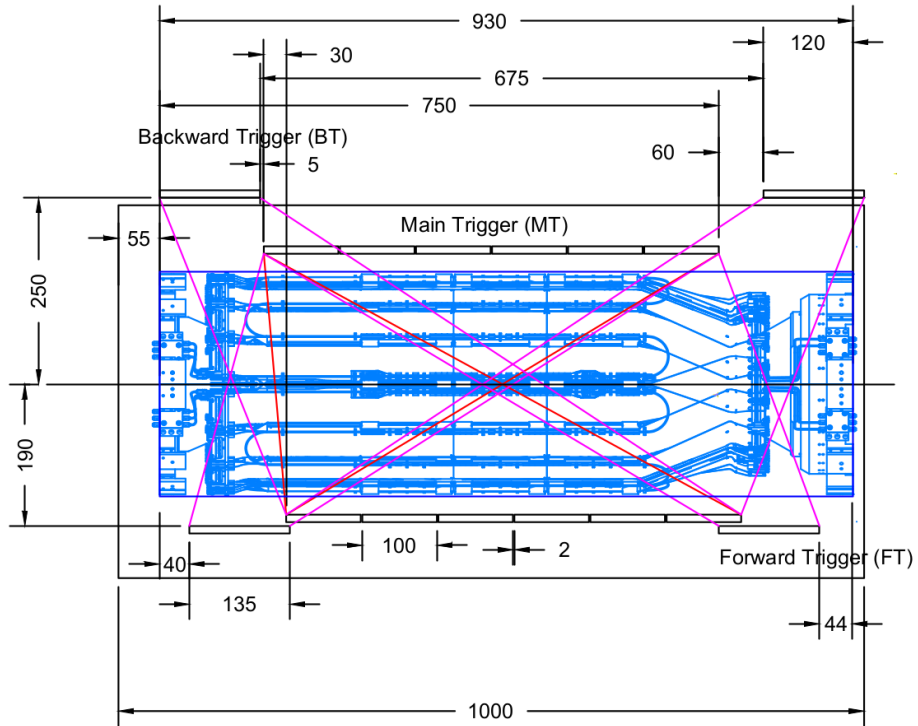
Figure 6.3: Combined PXD-SVD commissioning geometry in XZ plane (top) and XY plane (bottom): the combined vertex detector (blue) and the triggers: six main top scintillators with two additional ones (backward and forward), six main bottom scintillators with two additional ones (backward and forward) and two side triggers (left and right). Distance values are in milimiters. [66]

6.1 Data acquisition

In SVD standalone commissioning cosmic events were triggered by the coincidence of triggers. In combined PXD-SVD commissioning, trigger system requires advanced logic. The trigger system was designed to keep vertical tracks passing through the top and bottom triggers, horizontal tracks producing scintillation signal in the left and right side triggers and tracks detected by by combining signal from one vertical and one horizontal trigger. The trigger logic is summarized in Fig 6.4.
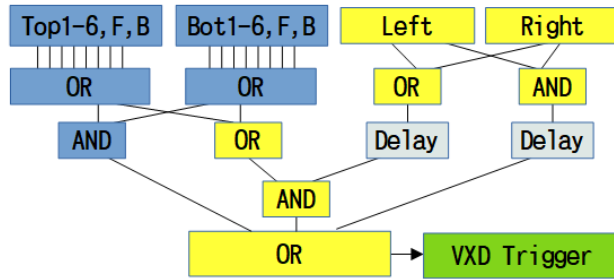
Figure 6.4: Schematic diagram of trigger logic: vertical triggers (blue) are combined together, horizontal triggers (yellow) are combined together and combination of a horizontal and a vertical trigger [67]

For both, the SVD standalone and combined SVD-PXD commissionings, local data acquisition system was developed. After a particle passes through the trigger, data are transferred from detector readout system to the storage server via HLT server. The collected data was formatted and checked. Subsequently, the data was copied from the storage to KEKCC server for offline analysis at the end of each day. In combined PXD-SVD commissioning the data flows in two separate lines (the PXD and SVD chains) into software trigger, where collected information was processed (Figure 6.5). In SVD standalone commissioning the data flows through the SVD chain only.
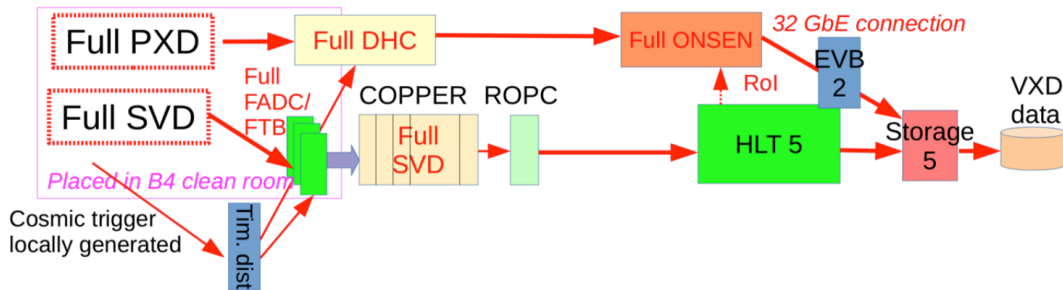
Figure 6.5: VXD commissioning data acquisition system: top line represents the PXD data flow to HLT; bottom line shows the SVD data flow to HLT; after software trigger data are stored on the storage server and then transferred to KEKCC server for analysis [68]

6.2 Cosmic track reconstruction

Data acquisition system delivered raw data onto KEKCC, and the data was unpacked. Using dedicated calibrations, reconstruction of pixel and strip hits was performed. Due to a large number of pixel hits hot spot masking algorithm was applied. Collections of hits were prepared for track finding algorithm.

The trajectory of cosmic rays in an environment without a magnetic field can be described as a straight line. The tracking experts developed a simple tool for putting all hits in an event into an order and filtering them. A seed of a track was found using a technique based on the principal component analysis approach. This approach assumes that all hits in the vertex (strip) detector are a part of the track and removes SpacePoints from the track candidate until a maximal χ^2 value for the track is reached. Inputs for the tool are a minimal number of SpacePoints in the track, a maximal number of removed SpacePoints from the track candidate until it rejects the event completely. The deterministic annealing filter (DAF) created the final track candidate fit. The reconstructed track and its fit result candidate were stored. The cosmic tracks passing through the SVD halves, Pat and Mat, are shown in Figure 6.6, and cosmic track passing through the full vertex detector can be found in Figure 6.7.
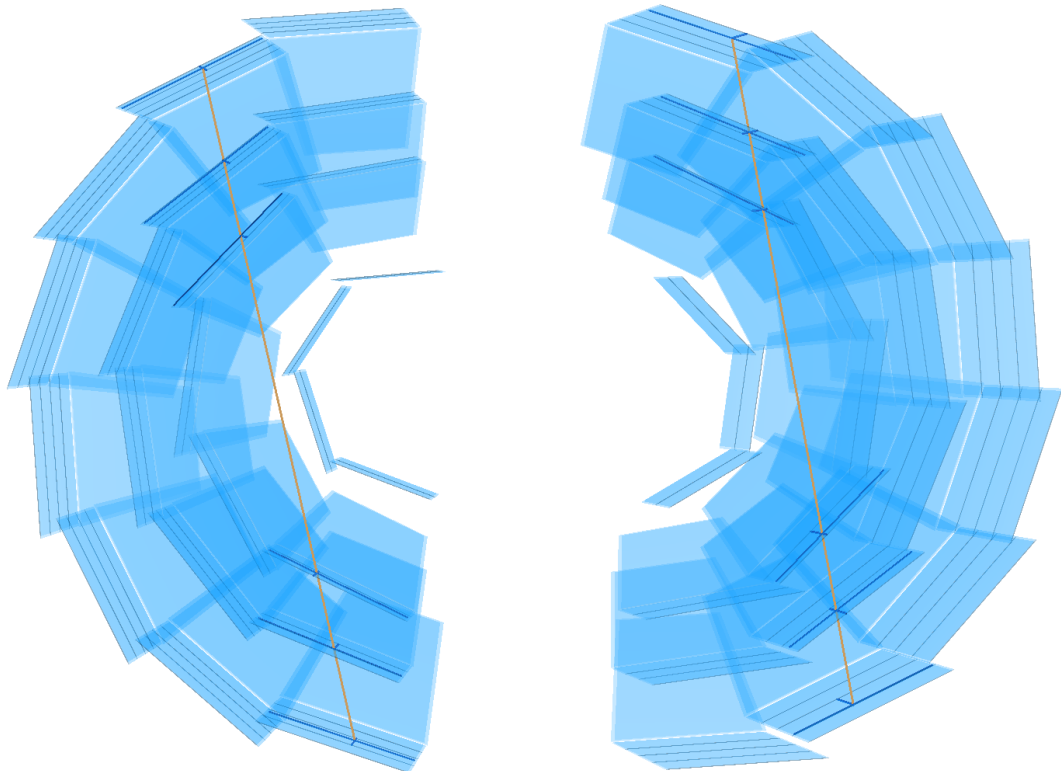
Figure 6.6: Cosmic tracks (orange) passing through Pat (left, light blue) and Mat (right, light blue) with reconstructed SVD clusters (dark blue)
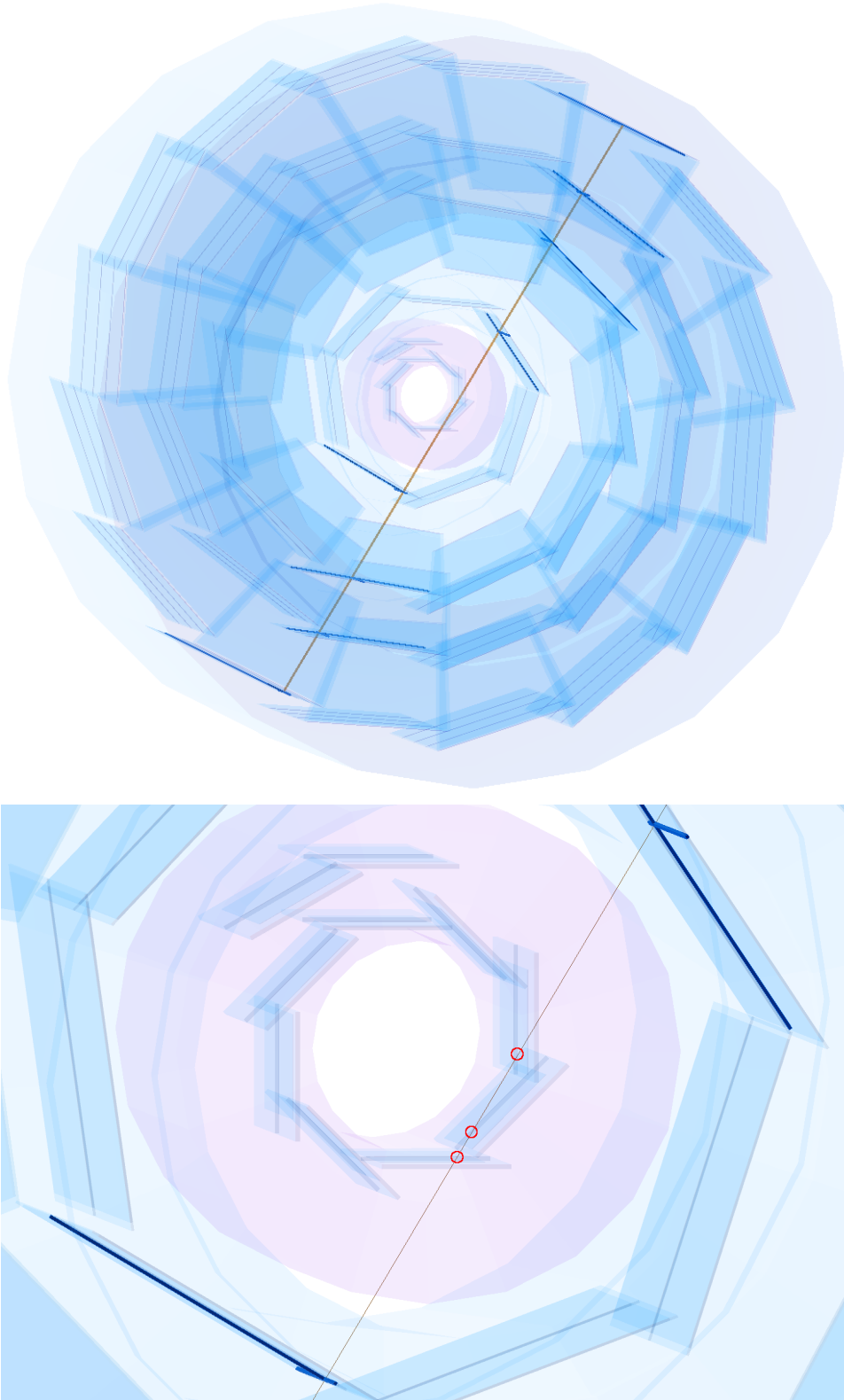
Figure 6.7: Cosmic track (orange) passing through the vertex detector (light blue) with reconstructed SVD clusters (dark blue) and PXD clusters in red circles; detail of the partial pixel detector (bottom) composed of eight ladders in the first layer and two ladders in the second layer

6.3 Data samples

During the VXD commissioning three different samples were processed: a simulated sample for PXD-SVD combined commissioning, a data sample of SVD standalone commissioning and a data sample of PXD-SVD combined commissioning.

The Monte Carlo simulation was done using CRY cosmic generator with a big enough global box, the keep and accept boxes were the same size as the VXD volume. The global geographical and time properties were set according to the data taking plans. No special trigger settings were required, at least one simulated hit in SVD was required at the simulation level. At least three VXD hits should compose the reconstructed track; otherwise, an event was skipped. In the simulated sample, we used about thirty thousand cosmic ray tracks. The Phase 3 early geometry of the vertex detector was used for the production of the simulated sample. The simulated data sample was used to determine whether the estimated alignments were enough, or another iteration was needed.
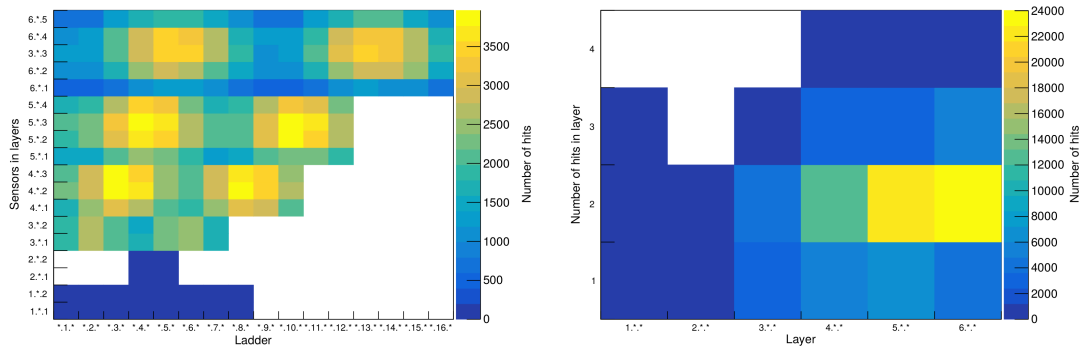
Figure 6.8: Occupancy of sensors (left) and number of hits in a simulated track per layer (right)

In Figure 6.8 occupancy plots for the simulated sample are shown. In the sensor occupancy plot, a characteristic ϕ dependency is shown, where sensors perpendicular to vertical cosmic ray tracks are highly occupied, and parallel sensors to cosmic tracks are occupied less. The first and last sensors in ladders of the outer layers are occupied less because the probability that tracks pass through at least three sensors is lower than in the detector's central part. The second plot, where a number of the VXD hits per track per layer is shown, illustrates that mostly two hits per layer for the detector's outer layers are expected. Three hits per layer are possible when a cosmic track passes through one overlapping area of this layer or three neighbouring sensors. Four hits per layer introduce a case, where a cosmic track passes through two overlapping areas within one layer. One hit per layer is associated with a track, which is not passing through the full detector. Both plots are very useful during the alignment studies to prove alignment quality. From both plots one can see that the occupancy of pixel sensors is rapidly less than that of the strip sensors, and in the second layer ladders 2.3 and 2.4 were used.

At the beginning of the standalone SVD commissioning, data was collected using only one SVD-half, this data was processed, but it was not used in alignment studies. After both SVD-halves were installed into separated storage boxes, about eight hundred thousand cosmic tracks were reconstructed, at least three SVD hits were required per track. In the PXD-SVD combined commissioning the collected data was analysed, and a cut requiring for at least three VXD hits per track was applied. For the alignment studies, more than eight hundred thousand cosmic ray tracks were available.

6.4   Vertex detector alignment studies

Two independent alignment studies were performed. One of them for separated SVD-halves and another for the full vertex detector. The simulated samples are used as a reference for comparing the tracking and reconstruction variables.

6.4.1   SVD standalone comissioning

In the first study, the rigid body alignment parameters were determined for all sensors. The alignment procedure was iterated three times without constraints. The final alignment results can be found in Appendix D. The resulted occupancy plots were similar as for simulated sample. Comparison of occupancy distributions applying no alignment and the latest alignment can be found in Figure 6.9. A similar comparison for the number of hits per track per layer can be found in Figure 6.10. With no alignment corrections applied, the plots report about a disagreement between the simulation and data. After applying the latest alignment, the data sample gives a similar result as the simulation.
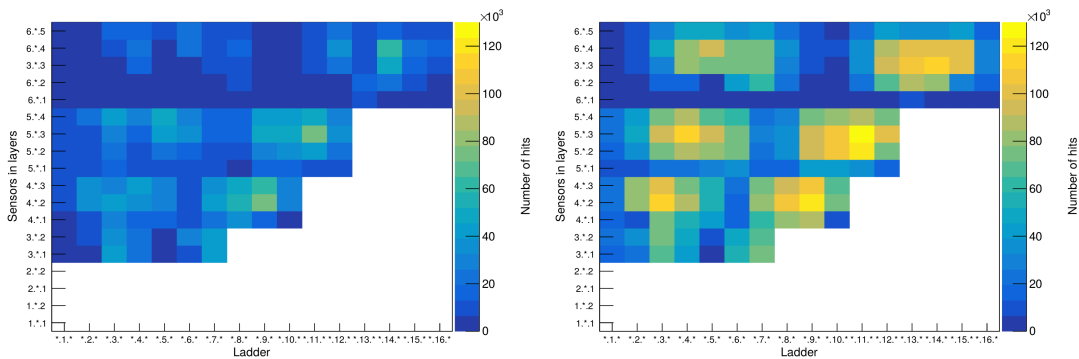
Figure 6.9: Occupancy of sensors in SVD standalone commissioning: before (left) and after (right) applying alignment constants

One half of the ladders with the small ladder number (the top half) in the sixth layer is occupied less than the other half. The forward and backward sensors in the top half of the last layer rarely reconstructed cosmic rays, what can be related to the fact that the top trigger is larger than the bottom trigger. A cosmic ray passing through the top trigger and forward or backward sensor could not hit the
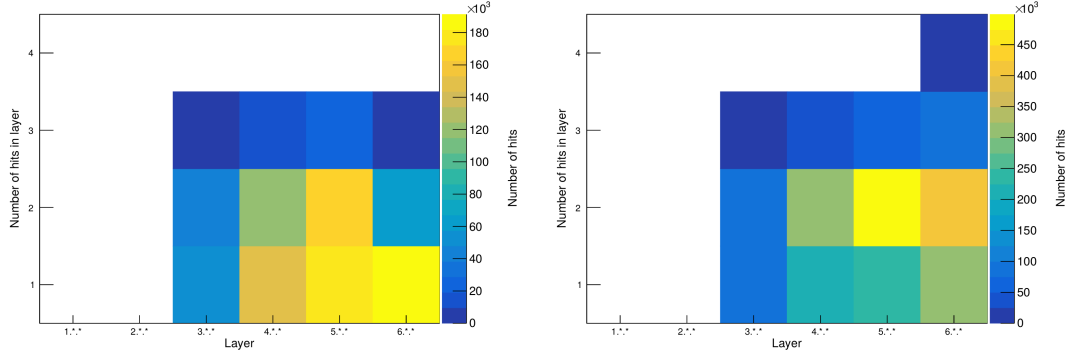
Figure 6.10: Number of hits in tracks per layer in SVD standalone commissioning: before (left) and after (right) applying alignment constants

bottom trigger or has not enough SVD hits.

The number of the VXD hits in tracks (Figure 6.11) indicates the number of VXD tracks doubled by applying the latest alignment corrections. The tracks are more populated, therefore the averaged number of VXD hits is higher. The fit quality distribution such as χ^2 over the number of degrees freedom also significantly improved by applying the latest alignment values. Significant improvements were observed in the residual distributions filled by all recorded SVD hits (Figure 6.12).
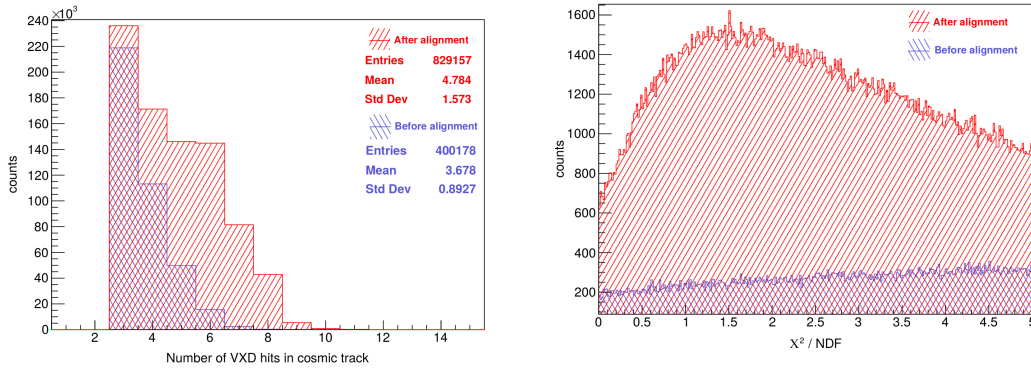
Figure 6.11: Number of hits per track (left) and χ^2 over number of degrees freedom (right) of track during the SVD standalone commissioning

The possibility to identify surface deformation of sensors was tested using the w residual distribution as a function of u and v coordinates of hits. As you can see in Figure 6.13, the quadratic deformation of sensors can be found in some highly occupied sensors.

6.4.2 PXD-SVD combined commissioning

Applying the sophisticated trigger system and collecting highly populated tracks with better precision ensures sufficient conditions for more precise measurements.

73
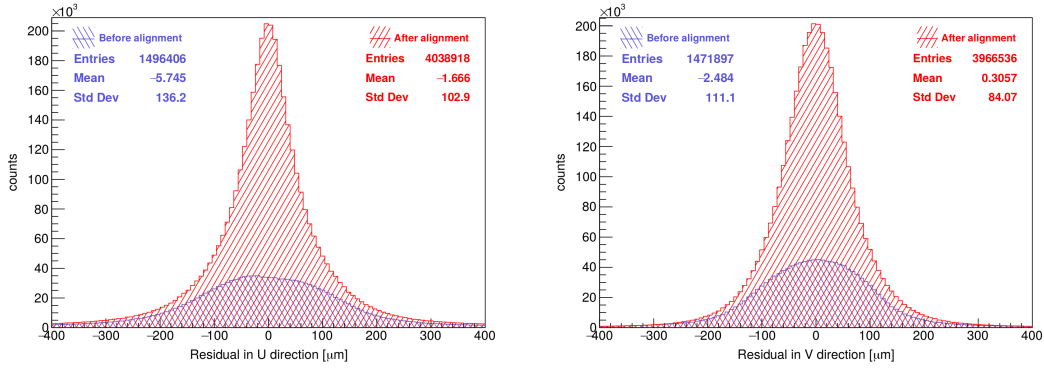
Figure 6.12: Residual distributions for u (left) and v (right) directions in SVD standalone commissioning
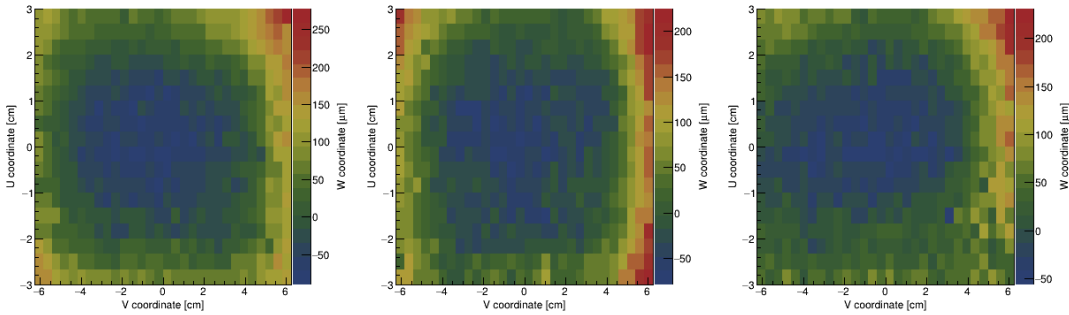
Figure 6.13: Quadratic deformation of sensors in SVD standalone commissioning: w residual distribution as a function of u and v coordinates for 4.2.2 (left), 4.9.2 (center) and 5.9.2 (right) sensors

In the second alignment study, we were focused on a historically first determination of the surface deformation of sensors. Two different alignment scenarios were tested: rigid body scenario and a combination of a rigid body and quadratic sensor surface deformation scenarios. Each alignment scenario was determined using one iteration, and hierarchical constraints between sensors and ladders were applied. More alignment studies and tests were provided using this data [49].

Using the sensor occupancy (Figure 6.14) plots and the number of hits in track per layer (Figure 6.15) plots one could only hardly distinguish between the rigid body and quadratic sensor surface deformation. When comparing with the result of the SVD standalone commissioning, we observed large improvements in the PXD-SVD combined commissioning. The additional triggers significantly improve sensor and ladder occupancy. Both plots show great agreement between data and simulated results.

Looking at the number of the VXD hits in track (Figure 6.16), one can see the effect of adding the quadratic surface deformations to the rigid body parameters in the alignment algorithm is not remarkable. However the χ^2 over the number of degrees of freedom distribution shows a significant difference between these two alignment scenarios, which makes this quantity a useful variable for further
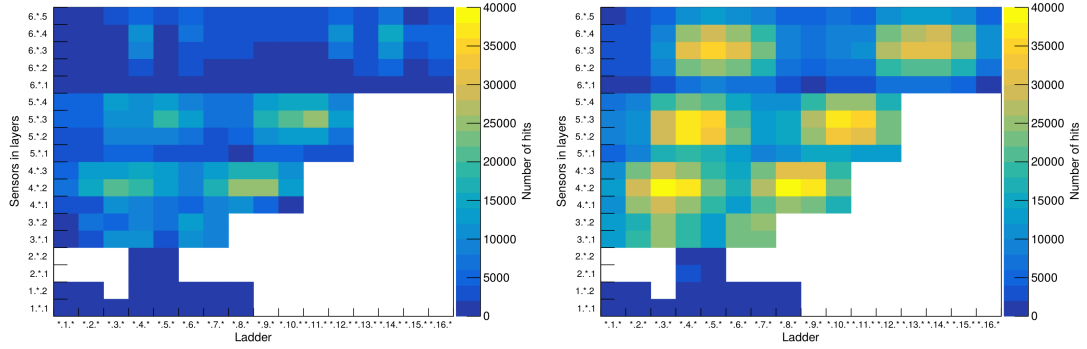
Figure 6.14: Occupancy of sensors in PXD-SVD combined commissioning: before (left) and after (right) applying rigid body and quadratic surface alignment constants
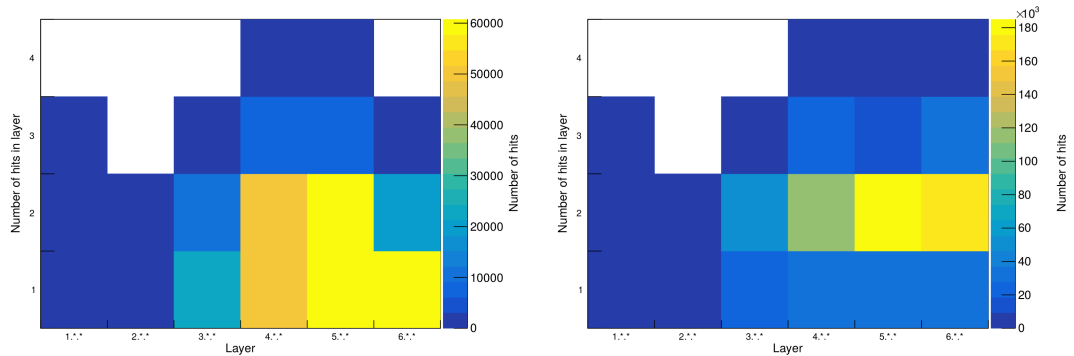
Figure 6.15: Number of hits in tracks per layer in PXD-SVD combined commissioning: before (left) and after (right) applying rigid body and quadratic surface alignment constants

monitoring purposes, which tells us about the quality of deformations description. Residual distributions for hits (Figure 6.17) show small improvement in standard deviation.

6.5 Data and Monte Carlo comparison

Thanks to the CRY generator's ability to approximate the real time elapsed during the generated events, we are able to estimate the simulated cosmic rate. Equivalent measurement was performed with collected data where time was measured between the first and last event, which we processed. Estimated rates for simulated and processed samples are shown in Table 6.1.

The cosmic rate in the pixel detector is estimated precisely, and the results for simulated and measured samples agree. However, the rates of tracks passing through the strip detector for simulated and measured data samples did not agree within this particular measurement. The large difference between samples

75
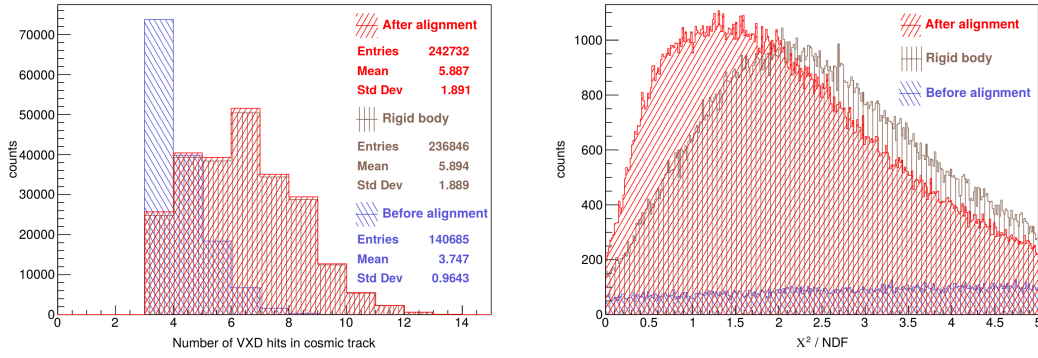
Figure 6.16: Number of VXD hits in track (left) and χ^2 over number of degrees freedom (right) of track in PXD-SVD combined commissioning
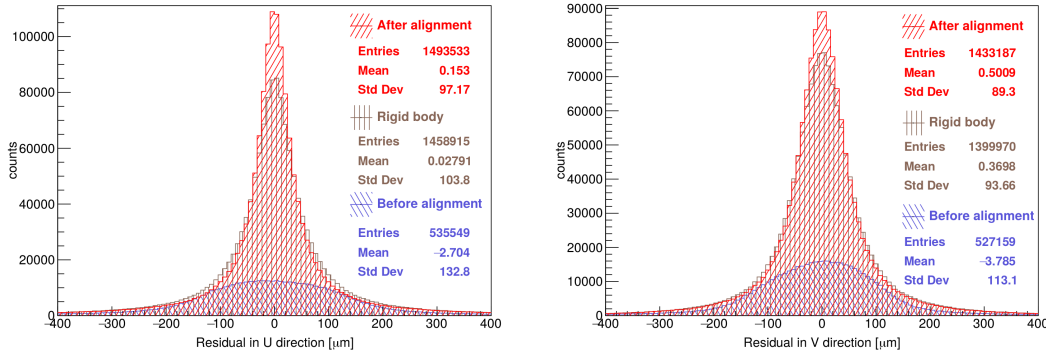
Figure 6.17: Residual distributions for u (left) and v (right) directions in PXD-SVD combined commissioning

| | Monte Carlo simulation | | Real data measurement | |
	Tracks	Rate [Hz]	Tracks	Rate [Hz]
VXD	37 041 ± 192	7.53 ± 0.04	274 500 ± 523	5.26 ± 0.01
SVD only	35 602	7.24 ± 0.04	261 390	5.01 ± 0.01
PXD + SVD	1 439	0.29 ± 0.04	13 110	0.25 ± 0.01
Time [s]	4 920		52 158	

Table 6.1: Comparison between simulated and measured cosmic rate in vertex detector

(about 30 %) originated from the trigger system and worse trigger efficiency for tracks with fewer VXD hits. From the Figure 6.18, this disagreement is obvious. Tracks with the high number of VXD hits are well populated in the measured sample. The tracks with a fewer number of VXD hits are difficult to reconstruct. Sometimes these track candidates passed through one trigger only, and the event was not triggered.
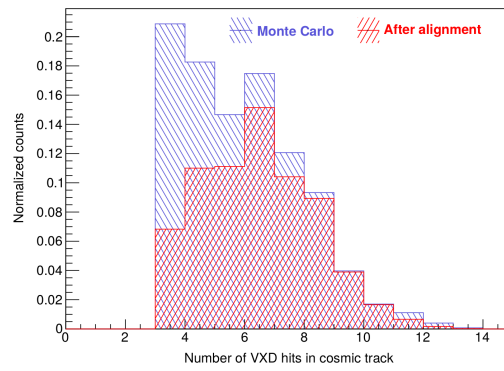
Figure 6.18: Comparison between simulated and measured samples for the number of VXD hits in cosmic track

7. Phase 3 early vertex detector

After installing the vertex detector to the Belle II detector, an alignment procedure was not carried out locally. Cosmic and collision tracks were found and fitted by the standard Belle II track reconstruction procedure. The alignment procedure for the vertex detector was done simultaneously with other subdetectors such as the central drift chamber and K_L^0-muon system. The vertex detector alignment procedure was performed by the alignment group and the alignment constants were published in global tags. Then constants were validated using our validation procedures.

7.1   Surface alignment parameters

During Phase 2 (Section 5) and the VXD commissioning (Section 6), surface deformations of the vertex detector sensors were identified. By applying the quadratic surface deformation parameters, the alignment validation results were improved. The scale of the quadratic surface deformation was observed at 300 μm. At least for one of the Phase 2 vertex sensors the results improved by applying cubic surface parameters. Using higher statistics ($\sim$ millions of cosmic tracks without magnetic field) and better precision (including about a hundred of the CDC hits) we repeated validation studies related to surface deformation of sensors. Firstly, the shift, rotation and quadratic surface parameters were determined and validated. The validation results can be found in Figure 7.1, where the surface monitoring plot for the 4.3.3 sensor illustrates a cubic deformation (parameter P_{12}) of about 50 μm. Extended alignment procedure using cubic parameters was performed, and validation plots suggest successful elimination of their effects.

Surface monitoring plot (Figure 7.1) for the 4.4.2 sensor showed another level of sensor surface deformation, the quartic level. The alignment parameters extracted from the surface monitoring plot can be found in Table 7.1. The P_{04} parameter can be extracted with sufficient precision. The error distribution of the w residual projection onto the sensor's surface is also monitored, and its fit by a constant function can be interpreted as an error of w residual projection. Fitted error value for the 4.4.2 sensor is 9.91 μm. Based on the comparison of the extracted P_{04} parameter and error values, this deformation can be neglected in the alignment procedure.

7.2   Validation χ^2 invariant modes

Once the surface deformations of the silicon sensors are eliminated, we would like to study possible effects of the χ^2 invariant mode on the alignment. Firstly, the physical motivation for the validation and monitoring χ^2 invariant modes is shown. First validation studies were performed using the Monte Carlo simulation to estimate the validation procedure's sensitivity and ability to illustrate observed effects. Finally, the collected data was validated.

Sensor 4.3.3

Sensor 4.4.2
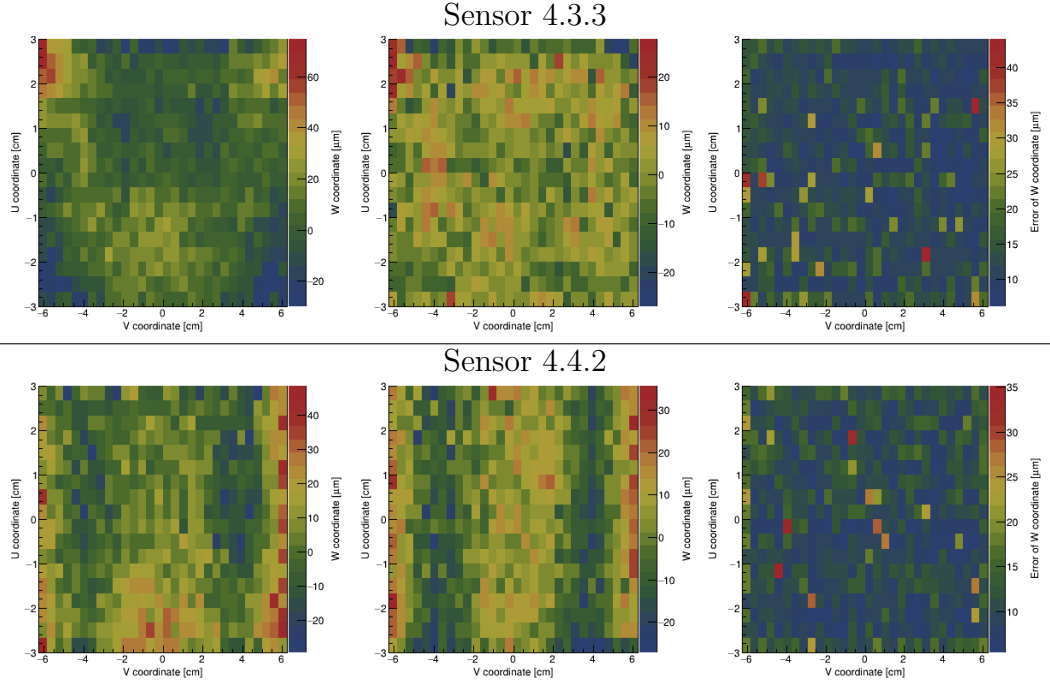
Figure 7.1: Cubic deformation of sensors in the Phase 3 early: w residual distribution as a function of the u and v coordinates for the 4.3.3 (top line) and 4.4.2 (bottom line) sensors after applying shift, rotation and quadratic surface parameters (left), extended by additional cubic parameters (center); projected error of the w residual onto a sensor surface.

P_u	1.06 $\pm$ 0.10 μm	P_α	0.68 $\pm$ 0.17 μm		
P_v	0.25 $\pm$ 0.12 μm	P_β	0.49 $\pm$ 0.14 μm	P_{04}	12.20 $\pm$ 0.32 μm
P_w	0.66 $\pm$ 0.08 μm			P_{13}	2.71 $\pm$ 0.40 μm
		P_{03}	0.02 $\pm$ 0.25 μm	P_{22}	-1.68 $\pm$ 0.45 μm
P_{02}	4.18 $\pm$ 0.23 μm	P_{12}	-0.31 $\pm$ 0.35 μm	P_{31}	-0.77 $\pm$ 0.41 μm
P_{11}	0.18 $\pm$ 0.29 μm	P_{21}	-0.30 $\pm$ 0.36 μm	P_{40}	-1.49 $\pm$ 0.25 μm
P_{20}	-1.14 $\pm$ 0.18 μm	P_{30}	1.71 $\pm$ 0.19 μm		

Table 7.1: Monitoring of the 4.4.2 sensor shift (left top), rotation (center top), quadratic (left bottom), cubic (center bottom) and quartic (right) parameters in Phase 3 early

7.2.1 Physical motivation

Impact of the χ^2 invariant modes on physics is described using the time-dependent CP violation measurement using half a million $B^0 \to J/\psi \ (\mu^+\mu^-) + K_S^0 \ (\pi^+\pi^-)$ events. The study is based on Monte Carlo simulation of the process in ten different Phase 3 vertex detector geometries: the nominal one and nine weak modes. Systematic misalignments were modelled using coherent movements of sensors with maximal value being about 250 μm (Appendix B). The simulation was performed in two steps. In the first step, the dedicated physical generator generated the process, and hits in the vertex detector were simulated. In the second level,

the misalignments were applied, and the simulated sample was reconstructed and analysed. During the analysis, the simple Belle approach with three Gaussian resolution function was implemented. The final fit of CP violation parameters can be found in Figure 7.2, where A_{CP} and S_{CP} variables are shown as a function of systematic misalignment of the vertex detector.
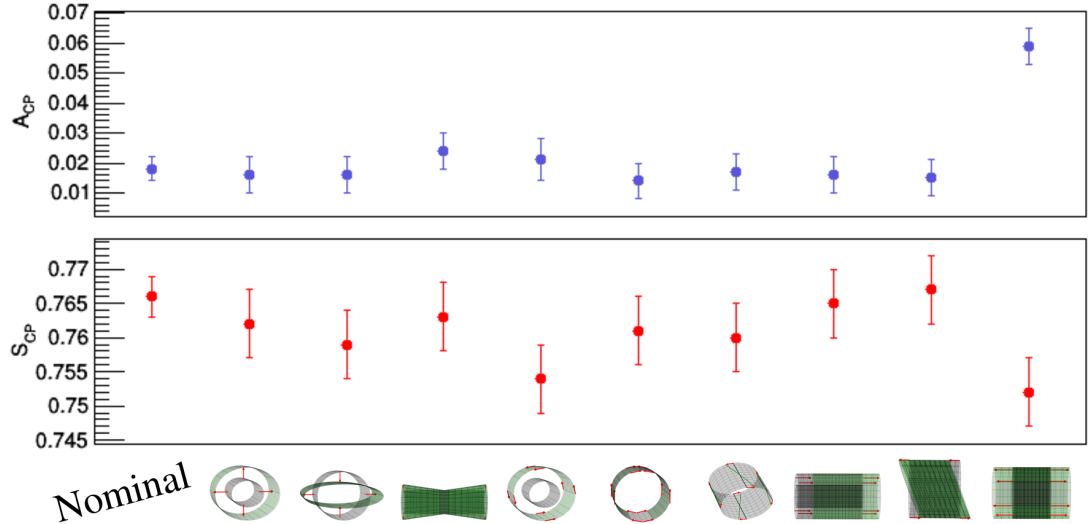
Figure 7.2: Impact of the weak modes on the CP violation measurement: Significant effect on physics can be seen for Z expansion of the vertex detector.

7.2.2 Monte Carlo simulation

The Monte Carlo studies were performed to test usefulness and to clarify the properties of the monitoring tool. The studies were based on universality assessment of the tool and the possibility of identifying the χ^2 invariant modes. The tool universality was checked using different simulated samples: cosmic ray reconstructed without a magnetic field, tracks from a random decay of $\Upsilon(4S)$ resonance and muon pairs produced in the electron-positron scattering. Due to different track properties, their effects on our studies are not negligible. In all samples, multiple scattering effects of tracks can be neglected. For each sample, ten different geometries were processed, and the same simulation procedure was applied. We looked for changes in the difference of residual distributions in overlapping regions or standard residuals for other sensor areas. We generated about 38.5 million cosmic tracks, 12.0 million tracks from $\Upsilon(4S)$ resonance and 18.1 million muon tracks from the process $e^+ + e^- \rightarrow \mu^+ + \mu^-$ (Appendix E), which were validated using our validation tool.

Hit statistics in overlapping area

Before discussing the results, the sensor occupancy was checked. The characteristics of the 4.3 ladder were studied using cosmic sample. The occupancy plots for all hits, overlapping hits from sensors with both, same as well as different, position in a ladder are shown in Figure 7.3. In the cosmic data, the overlapping hits are located in two parallel 1.5 cm wide strips along the longer sides of the

sensor. In Table 7.2 the statistics for each sensor in the 4.3 ladder are presented. About 18 % of sensor hits meet the requirements to be classified as an overlapping hit pair. Most of them (99 %) are from sensors with the same sensor position in the ladder. Double hits from the sensor with the different position in the ladder are infrequent and very high statistics is needed for their detection. Each sample has a different track topography, and overlapping occupancy can slightly vary.
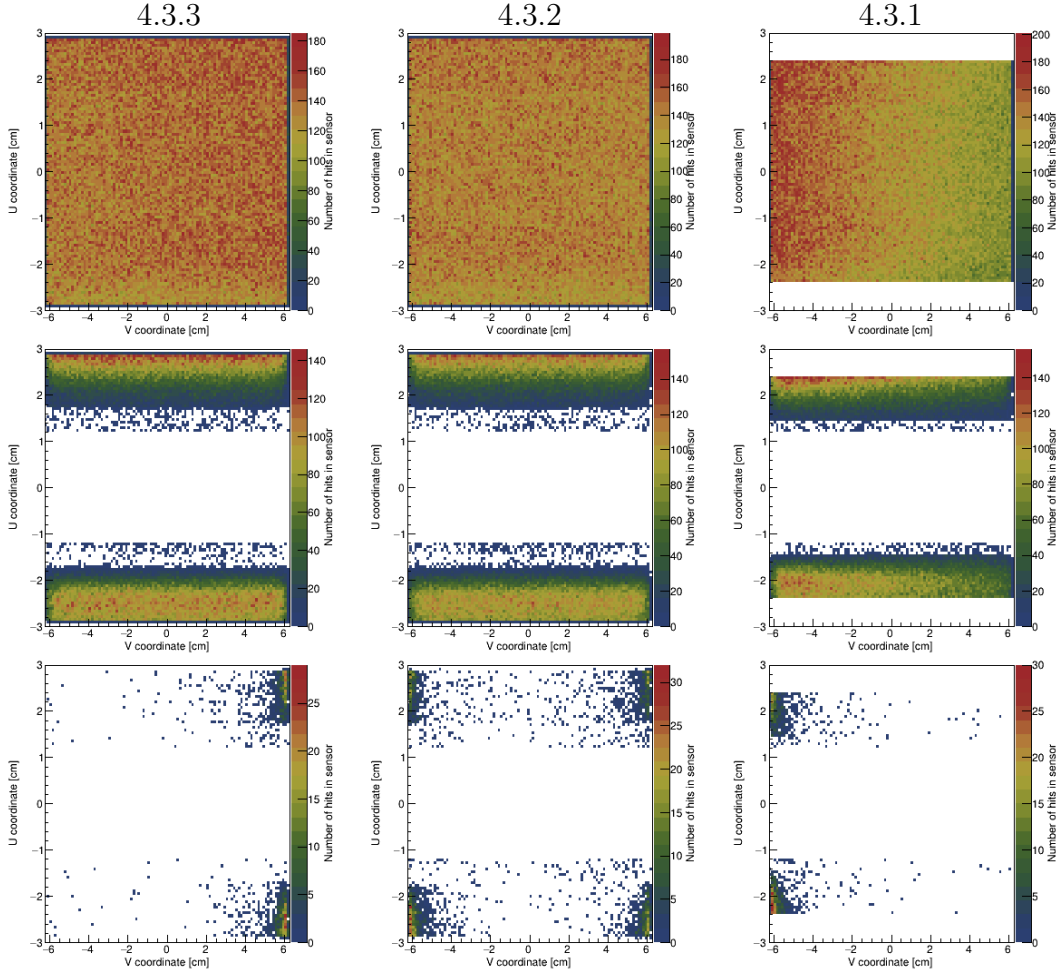
Figure 7.3: Sensor occupancy as a function of number of the overlapping hits in the 4.3 ladder: all hits (top), overlapping hits from sensors with same (center) and different (bottom) position in a ladder

Sensors	All hits [10^6]	All overlaps [10^6]	[%]	Same overlaps [10^3]	[%]	Different overlaps [%]
4.3.1	1.034	0.179	17.31	177	17.16	1 518	0.15
4.3.2	1.328	0.236	17.83	233	17.57	3 467	0.26
4.3.3	1.293	0.233	18.05	321	17.90	1 937	0.15

Table 7.2: Hits statistics in 4.3 ladder overlapping area using cosmic simulated sample
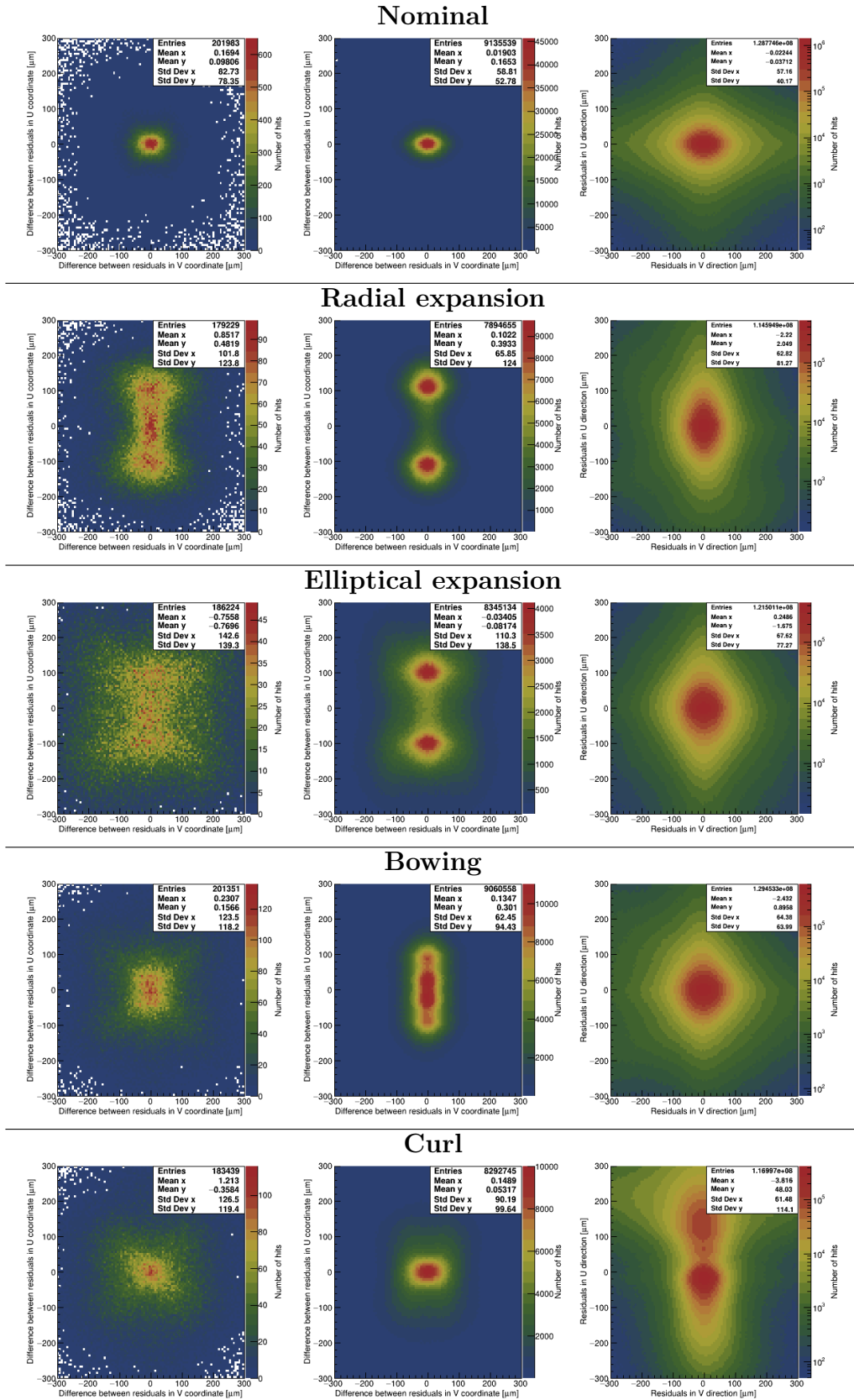
Figure 7.4: Nominal geometry and weak modes validation by simulated cosmic rays: difference distribution for overlapping hits from sensors with different (left) and same (center) position in ladder, residual distribution for other hits (right)
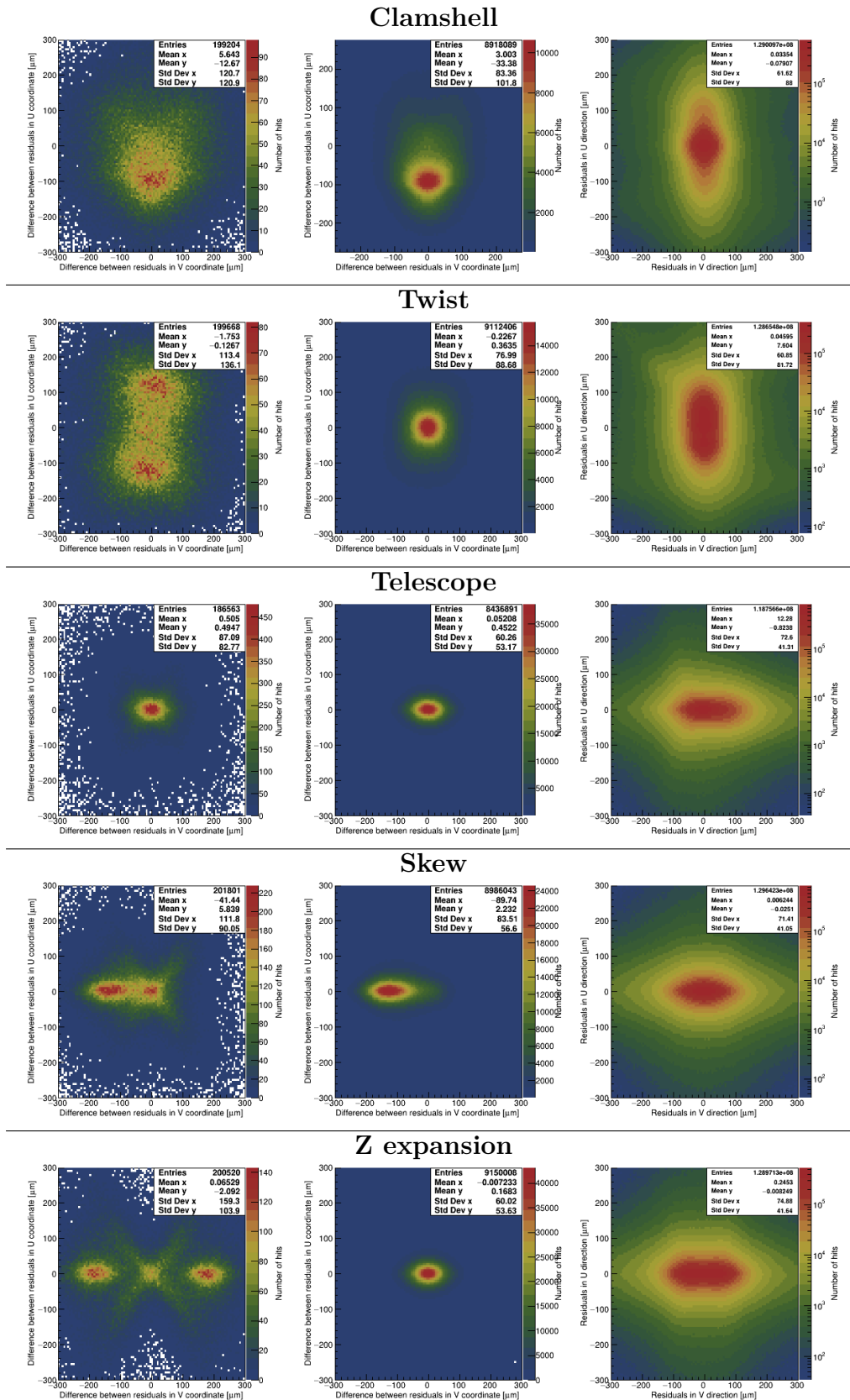
Figure 7.5: Nominal geometry and weak modes validation by simulated cosmic rays: difference distribution for overlapping hits for sensors with different (left) and same (center) position in ladder, residual distribution for other hits (right)

84

Validation results using simulation samples

All simulated samples were studied in the same way, where the validation plots were produced for all weak modes and compared to each other to check for significant differences. For all samples, the results inform about sensitivity to all studied χ^2 invariant modes with small differences among the samples. To illustrate the basic mutually similar monitoring results, the cosmic sample was selected, and its results were shown in Figures 7.4 and 7.5. Results for collision samples can be found in Section E. In these plots, results for all geometry scenarios are shown.

Using monitoring plots for a pair of hits from overlapping areas, we can observe the effect of all χ^2 invariant modes. The residual difference distributions for overlapping hits from sensors with the same position in ladders can help identify the radial (radial, elliptical expansion and bowing) and ϕ (curl, clamshell and twist) modes. However, the difference distributions for overlapping hits from sensors with a different position in ladders are more sensitive to the z modes (skew and z expansion). In the telescope case, using the combination of all monitored distributions one can reliably identify the weak mode.

7.2.3   Experiences with data

In experiments 5 and 6, the vertex detector detected about 4.3 millions of cosmic muon tracks. Collected cosmic data samples were processed and analysed. The observed monitoring result is shown in Figure 7.6. The monitoring using overlapping hits with same sensor positions in layers presents an unexpected result. The studied pattern does not correspond with simulated sample result, and a "snowman" structure was found in the residual difference distribution.
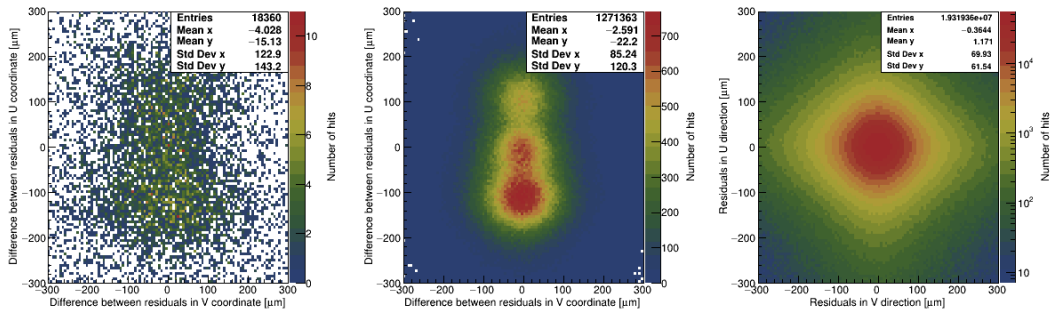
Figure 7.6: Validation result for cosmic data in experiments 5 and 6: difference distribution for overlapping hits from sensors with different (left) and same (center) position in ladder, residual distribution for other hits (right)

One of the advantages of this developed tool is the possibility to look at residual difference distributions as a function of layers (Figure 7.7), sensors (Figure 7.8) or ladders (Figure 7.9). The folllowing study was focused on explaining the observed difference between data and expectations from simulated samples. In principle, we looked at the residual difference distribution for overlapping hits from sensors

with the same position in more details. In each of the plots, we checked the situation in overlapping areas of two neighbouring sensors.
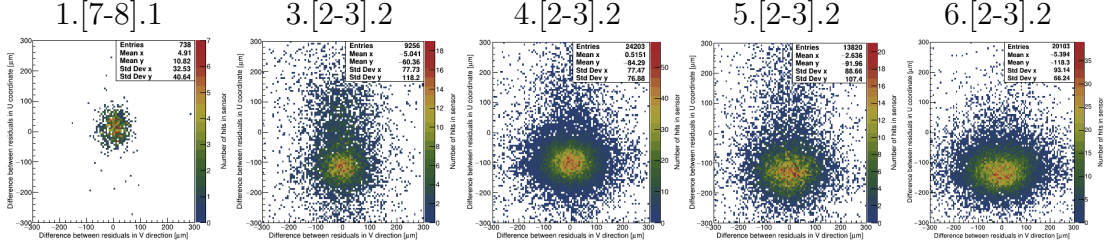
Figure 7.7: Validation result for cosmic data in experiments 5 and 6 in layers: difference distribution for overlapping hits from sensors with same position for the first (left), third (center left), fourth (center), fifth (center right) and sixth (right) layer

In Figure 7.7 a neighbouring sensor pair from each layer was chosen and studied. As can be seen, the first pixel layer is not affected, but the third and remaining higher layers are affected.
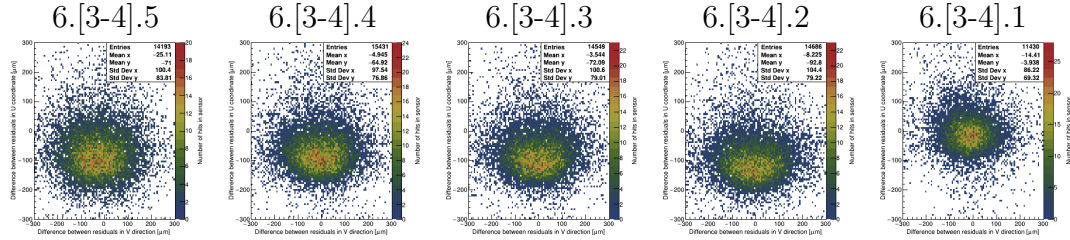
Figure 7.8: Validation result for cosmic data in experiments 5 and 6 in a ladder of the sixth layer: difference distributions for overlapping hits from neighbouring sensors with the same position

Subsequently, we selected two neighbouring highly occupied ladders in the sixth layer and checked residual differences for pairs of hits in their overlapping areas. According to the results shown in Figure 7.8, the first slanted sensors are not affected, but barrel rectangular sensors are affected.

As a last validation check, we looked at the ϕ dependence. One of the rectangular barrel sensors from each ladder of the fourth layer was selected and the residual difference distributions for the neighbouring sensor pairs were monitored. The final pattern (Figure 7.9) was compared with the equivalent situation in the simulated samples. The radial expansion was selected as the best candidate from χ^2 invariant modes was selected (Figure 7.10). Both patterns are similar, but the distributions of the collected sample have opposite sign.

The "snowman" structure in the final validation plot (Figure 7.6) can be interpreted through the contributions of various sensors: the pixel detector and slanted sensor constributions form the central ball of the "snowman", the barrel rectangular strip contributes to the top and bottom ball of the "snowman". According
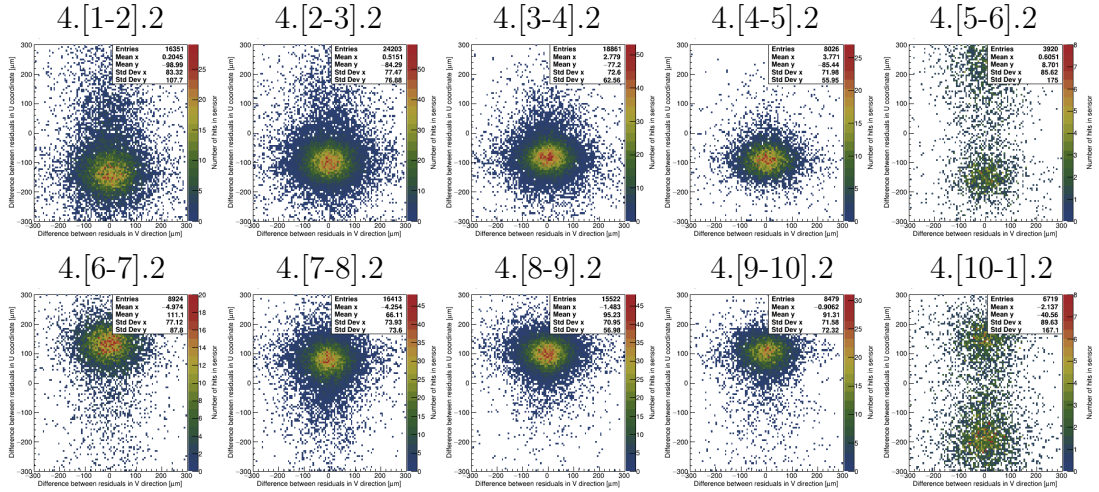
Figure 7.9: Validation result for cosmic data in experiments 5 and 6 in ϕ dependence of fourth layer: difference distribution for overlapping hits from sensors with same position for top half and bottom half of sensors with increasing ladder number from left to right
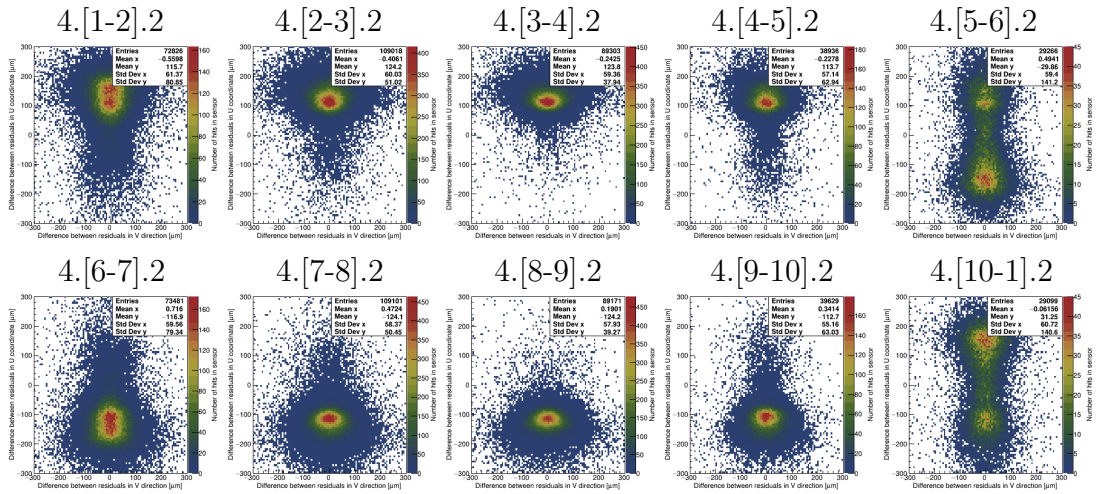
Figure 7.10: Validation result for simulated cosmic rays for radial expansion in ϕ; dependence of the fourth layer: the difference distribution for overlapping hits from sensors with same position from both, the top and the half bottom half of sensors with the ladder number increasing from left to right

to a comparison of collected and simulated samples, the contribution of the barrel strip part of the vertex detector demonstrates same behaviour as the radial expansion with the negative sign (contraction) according to comparison collected and simulated samples.

During the investigation of a problem in the strip detector reconstruction software, the different pattern was caused by different pitch sizes for simulated and collected samples. Once this issue was corrected, the vertex detector was realigned and the study using overlapping hits was repeated in experiment 7 using 4.8 million cosmic tracks. The new result for experiment 7 is shown in Figure 7.11. This result corresponds with expected distributions for the nominal geometry. Applied

corrected pitch values and extrapolated sensor sizes can be found in Table 7.3.

Sensor		Exp 5, 6 [μm]	Exp 7 [μm]	Δ [μm]	Δ [%]
1.1.1	U Pitch	50.0	50.0	0.0	0.0
	V Pitch	60.0	60.0	0.0	0.0
3.1.1	U Pitch	50.2	50.0	0.2	0.3
	V Pitch	160.0	160.0	0.0	0.0
4.1.1	Short U Pitch	50.2	50.0	0.2	0.3
	Long U Pitch	75.0	75.0	0.0	0.0
	V Pitch	239.8	240.0	0.2	0.1
4.1.2	U Pitch	75.2	75.0	0.2	0.2
	V Pitch	240.0	240.0	0.0	0.0

Sensor		Exp 5, 6 [mm]	Exp 7 [mm]	Δ [μm]	Δ [%]
1.1.1	Width	12.50	12.50	0	0.0
	Length	44.80	44.80	0	0.0
3.1.1	Width	38.52	38.40	120	0.3
	Length	122.90	122.88	20	0.0
4.1.1	Short width	38.42	38.40	20	0.3
	Long width	57.59	57.60	10	0.0
	Length	122.76	122.88	120	0.1
4.1.2	Width	57.72	57.60	120	0.2
	Length	122.90	122.88	20	0.0

Table 7.3: Pitch (top) and sensor (bottom) size changes after experiment 6
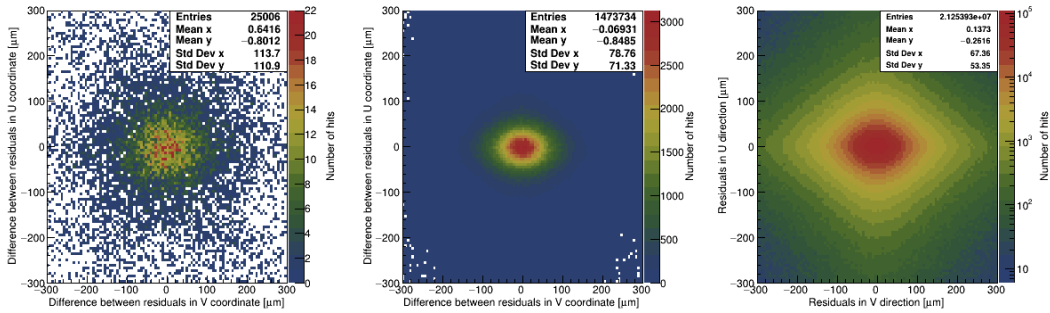
Figure 7.11: Validation result for cosmic data in experiment 7: difference distribution for overlapping hits from sensors with different (left) and same (center) position in the ladder, residual distribution for other hits (right)

From Table 7.3 one can see that the width of the barrel rectangular (e.g. 3.1.1 and 4.1.2) sensors increased after the correction by about 120 μm. For slanted sensors (e.g. 4.1.1), the difference in length turned out to be about 120 μm. Other widths or lengths decreased after the correction by approximately 20 μm after correction. During the minimization process, the alignment algorithm (Millepede

II) converged to a set of alignment constants, which compensated the difference between software and real sensor sizes as a movement of rectangular sensors in the negative radial direction and slanted sensors in z (length) direction. As Monte Carlo studies report, the changes in the z direction can be detected through by rare overlapping hit pairs in sensors with different position in the ladder, and we cannot clarify if they were there. In the validation plot for experiments 5 and 6 (Figure 7.6) the residual difference distributions for barrel rectangular sensors are shifted about 100 μm in the positive or negative direction. In my opinion, the radial contraction of the rectangular barrel sensors is caused by choosing bigger pitch size during reconstruction of hits in strip detector.

7.3 Vertex detector alignment

After checking the vertex detector alignment using our validation tools, it can be confirmed that silicon sensors surface deformation is eliminated and the alignment is not affected any χ^2 invariant mode. In the final step of the alignment procedure only determined sensor parameters and higher hierarchy (ladder and halves) parameters were excluded from the alignment procedure. The values of the final shift and rotation alignment parameters can be found in Figure 7.12 and the final surface deformation parameters in figure 7.13.
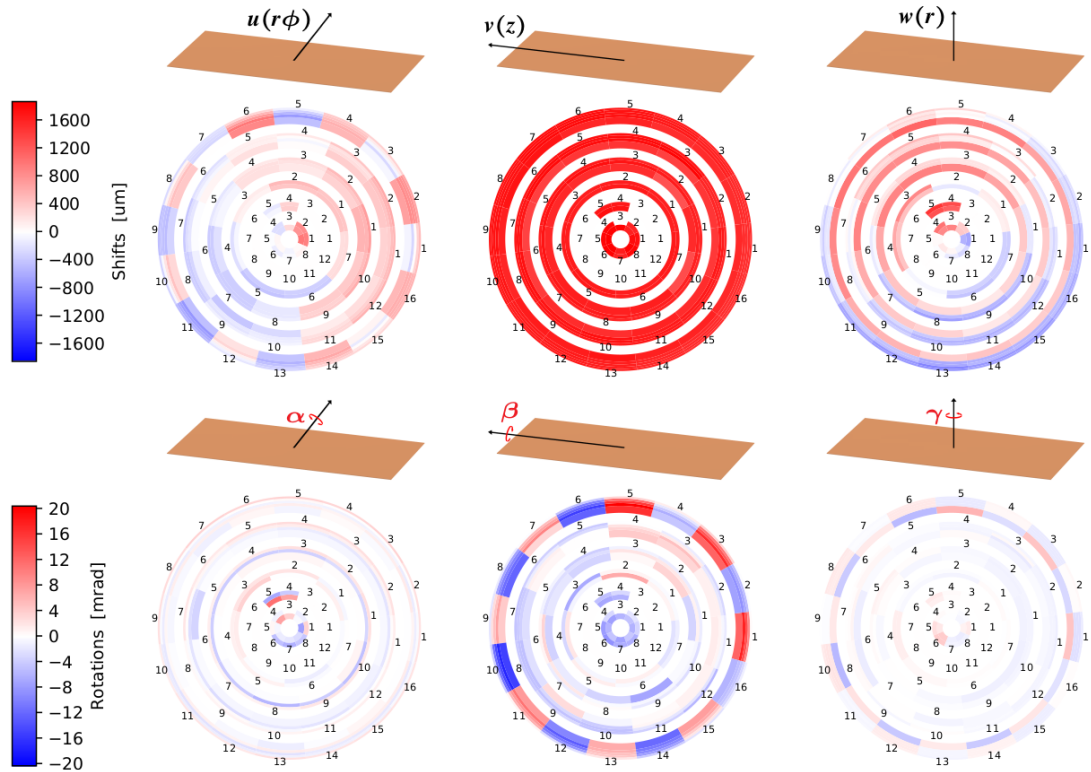
Figure 7.12: Shift and rotation alignment parameters for the vertex detector

In the vertex detector's sixth layer, periodically alternating signs of some alignment parameters can be observed. The most affected parameters are u shifts, β, γ
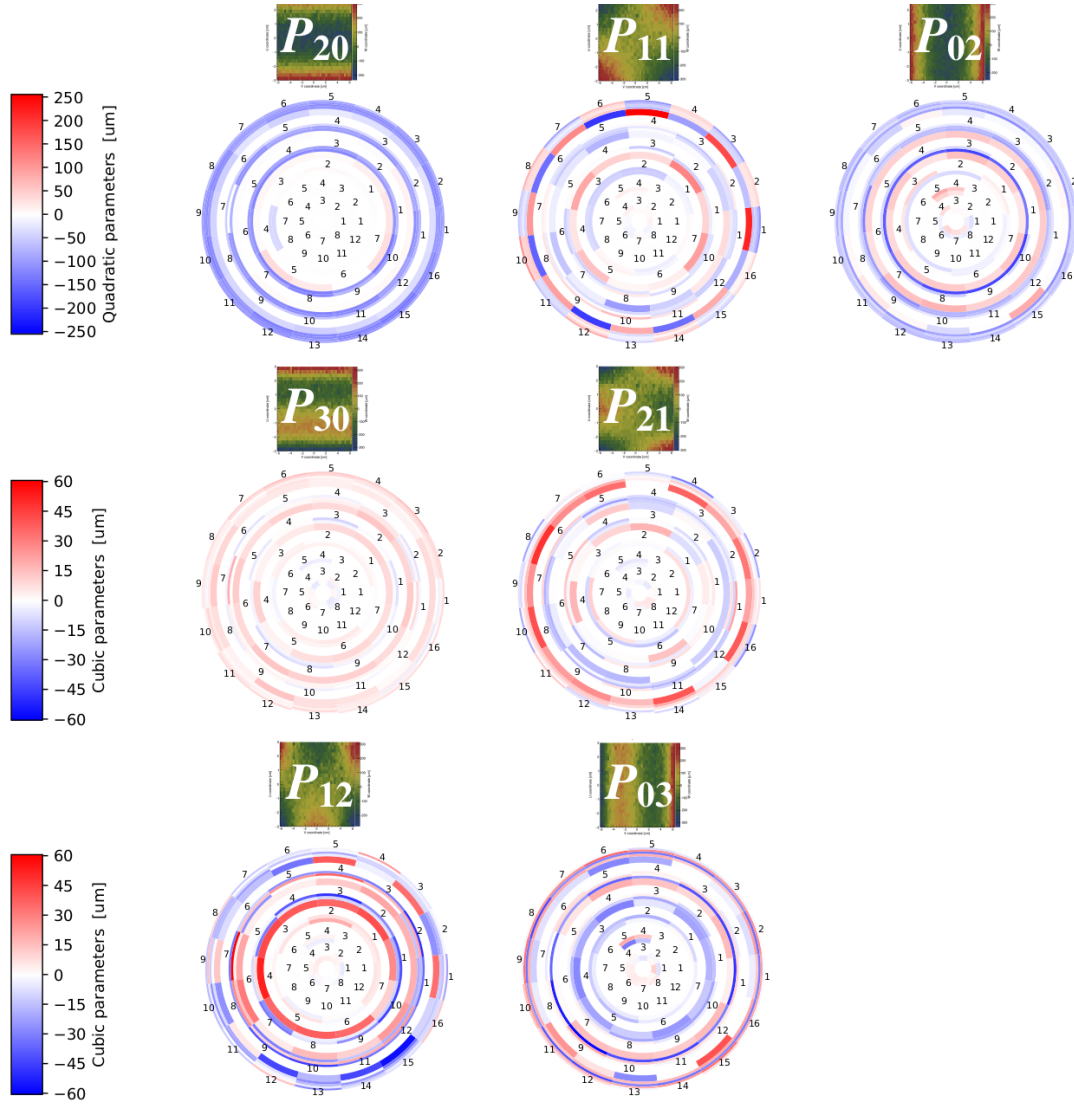
Figure 7.13: Surface deformation alignment parameters for the vertex detector

rotations and P_{11} quadratic surface parameters. The effect is a function of adder number parity and is called the "zebra" effect (Figure 7.14). After discussing this issue with hardware and mounting experts, the zebra effect is appeared after the installation of the cooling pipes, which ended up being slightly different from the designed pipes. In other strip layers, the presence of the clamshell effect was identified thanks to the u shift constants. In the v direction, we observed large movement in the positive direction, which can be interpreted as the vertex detector's movement as a function of position of the reference alignment detector - the CDC, what is the central drift chamber. In the w direction the slanted sensors are shifted due to radial expansion, the bottom barrel strip sensors move closer towards the center of the detector, and the top barrel sensors shift outwards from their nominal position. In terms of rotations, no large effect on alignment was found, except for the sixth layer's zebra effect.

From surface deformation parameters, the large quadratic deformations can be identified. For the large central perpendicular sensors, the combination of P_{20}
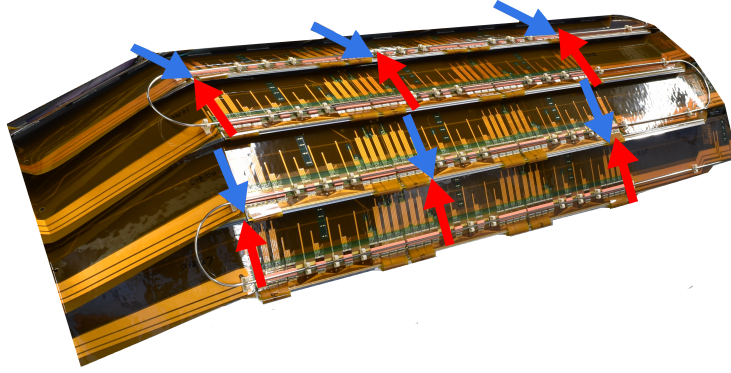
Figure 7.14: The schematic illustration of the zebra effect in the sixth layer

and P_{02} deformation parameters is introduced. The issue is well known from previous experience, and its parametrisation is equivalent to that of the issues observed in Phase 2 (Figure 5.6) and the VXD commissioning (Figure 6.13). The slanted sensors in the sixth layer are mostly deformed due to the zebra effect. Deformation is eliminated using the P_{11} parameter and central sensors in ladders of the sixth layer manifest deformation with opposite sign with respect to the slanted sensors. The cubic deformations can be found mostly in the slanted strip sensors, and many barrel sensors are also affected, yet on a lower scales.

For the pixel detector, the largest displacement with respect to the nominal geometry can be identified in two ladders of the second layer. The combination of w, α, P_{02} and P_{20} parameters represents the main issue of the Phase 3 early pixel detector. The same issue was found during control measurement after assembling the sensors to ladders (Figure 7.15).
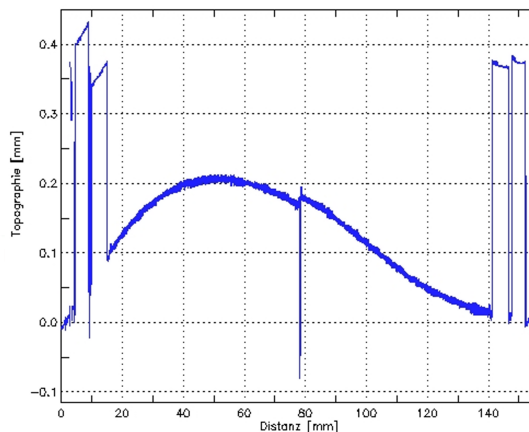
Figure 7.15: Longitudinal shape of the second-layer ladder after assembly [69]

7.4 Monitoring alignment parameters

Once the alignment parameters are determined, their value fluctuations need to be monitored to ensure quality of data collection. The time-dependent monitor-

ing of the parameters needs to be able to make an assessment of how often the alignment procedure should be repeated. Due to low comic rate in the pixel detector, the cosmic ray data taking periods were excluded from this study. However, high rate collision data sample with an average of ten tracks per event produced creates an optimal environment for monitoring and validating alignment parameters for every silicon sensor in the vertex detector.

Collected collision data samples are processed in periods based on experiments. All available runs were processed for the purpose of monitoring twelve alignment parameters per silicon sensor. The alignment parameters were extracted using the monitoring tool and plotted as function of run number. To keep the conditions during our study stable, the initial alignment constants were used as a reference. When an unexpected situation occurs, the resulting changes can be observed in parameter values. Their association with time helps with understanding the cause of their origin. Sometimes the conditions can return to the initial state and the alignment procedure does not have to be repeated. However, irreversible changes in alignment constants can occur, and new alignment constants must be determined. Using monitoring plots, these situations can be identified and discussed with colleagues. Some of these situations are discussed in this chapter. Two sensors were selected to demonstrate the vertex detector sensors' usual behaviour: 4.3.2 and 1.2.2 sensors.

7.4.1 Spring 2019 period

During spring 2019 period, the collected data was formed by the experiments 7 and 8. Experiment 7 started in March and was aborted because of a fire accident in the Linac tunnel in April. It was followed by experiment 8, which started in May and terminated in July. The monitoring results for reference sensors can be found in Figures 7.16 and 7.17.

The fluctuations observed in the alignment parameter values reach about 10 μm. In many sensors, the observed monitoring results were equivalent to those from Phase 2. However, some sensors, mostly in the first layer, delivered unexpected results. Observed changes can be found for 1.5.1 sensor in Figure 7.18 and for 1.6.1 sensor in Figure 7.19.

On the 28th of May, the power supply issue occurred in the focusing magnets and the beams were defocused. It caused irreversible changes in the 1.5.1 sensor alignment parameters determined from the monitoring plots. For the v shift parameter, the amplitude of changes was two or three times higher than the observed range of fluctuations. Rotation and shift alignment parameters started to fluctuate in a range higher than before. In my opinion, the quality of reconstructed data decreased. Unfortunately , the large observed fluctuations were not fixed by machine tuning or new calibration of the sensor. Probably a new set of alignment constants or hardware examination is needed to fix it.

Figure 7.16: Time dependent validation of sensor 1.2.2 alignment parameters: shift (first line), rotation (second line), quadratic (third line) and cubic (fourth line) surface parameters; the unit on the values of alignment parameter axes is μm.

Figure 7.17: Time dependent validation of sensor 4.3.2 alignment parameters: shift (first line), rotation (second line), quadratic (third line) and cubic (fourth line) surface parameters; the unit of the values of alignment parameter axes is μm.

On the 9$^{\text{th}}$ of June a quench of focusing magnets occurred, what again had an effect on some of the sensors in the first layer (e.g. 1.6.1 sensor). Similar behaviour of monitoring alignment parameters was observed for the 1.5.1 sensor after the power supply accident. The amplitude of changes was again four to five times higher than the range of fluctuations. The range of fluctuation for other alignment parameters increased. In this case, after having applied the machine tuning procedures the parameters converged back to the values from before the quench. We can say that the monitoring values were "realigned" back to zeros thanks to external machine procedures.

Figure 7.18: Time-dependent validation of 1.5.1 sensor alignment parameters: shift (first line), rotation (second line), quadratic (third line) and cubic (fourth line) surface parameters; the units of alignment parameter axes are μm.

7.4.2 Autumn 2019 period

During the spring data taking period and the summer shutdown, new upgrades were implemented into the software trigger procedure. One of the upgrades was focused on improving filtering the background tracks with origin outside of the interaction region. This software upgrade resulted in high sensitivity of the alignment monitoring tool.

In autumn 2019, the accelerator was restarted, and the detector collected collision data samples. Subsequently, new alignment parameters for the vertex detector sensors were determined. Using collision data samples, the alignment monitoring

Figure 7.19: Time-dependent validation of the 1.6.1 sensor alignment parameters: shift (first line), rotation (second line), quadratic (third line) and cubic (fourth line) surface parameters; the unit of the values of alignment parameter axes is μm.

procedure for experiment 10 was performed. The final results of validation for full collision collection finished at the end of the year 2019 are shown in Figures 7.20 and 7.21. For both, the reference sensors as well as for most of the other sensors, the expected fluctuation amplitude was kept within 10 μm from the values obtained in previous observations.

Unfortunately, alignment parameters for many sensors in the first layer fluctuated with amplitude larger than the reference sensors usual value. (Figure 7.22). The rotation and surface parameters were fluctuating within the standard $\pm$ 10 μm range from their mean value. The shift parameters were described as a continuous linear function with small fluctuations and they were realigned to their initial values three times during the data taking period. No new alignment parameters were determined during the period. The "realigning jumps" were related to hardware procedures performed during the maintenance days. The maintenance days took place every two weeks. As one can notice, the jumps of amplitudes in the first layer are about 20 to 40 μm depending on a sensor. In particular, a pair of sensors in a ladder of the first layer showed potential shifts in the opposite directions. If this movement really did happen, it could destroy or deform the ladder. The jumps of amplitudes of the sensors of the oppositely oriented ladders were the same up to a sign, what introduced opposite motion for the opposite ladders. For clarification, if the sensors in the top (1.4) ladder would shift towards each other, the sensors of the bottom (1.8) ladder would shift away from each other.
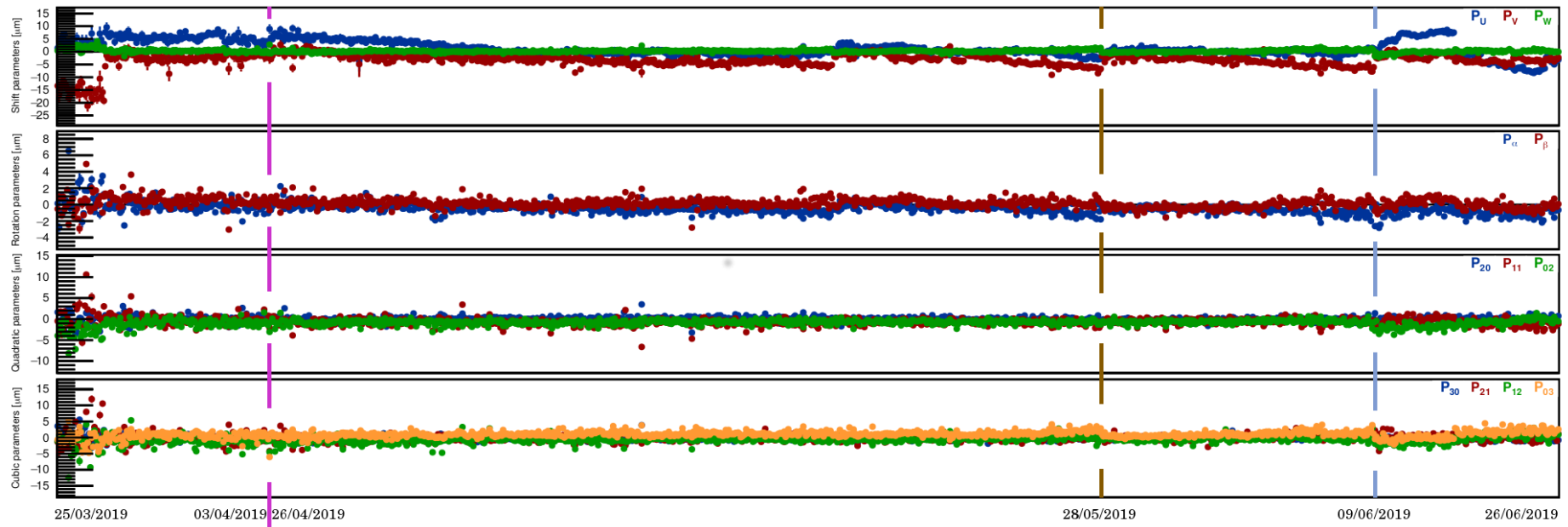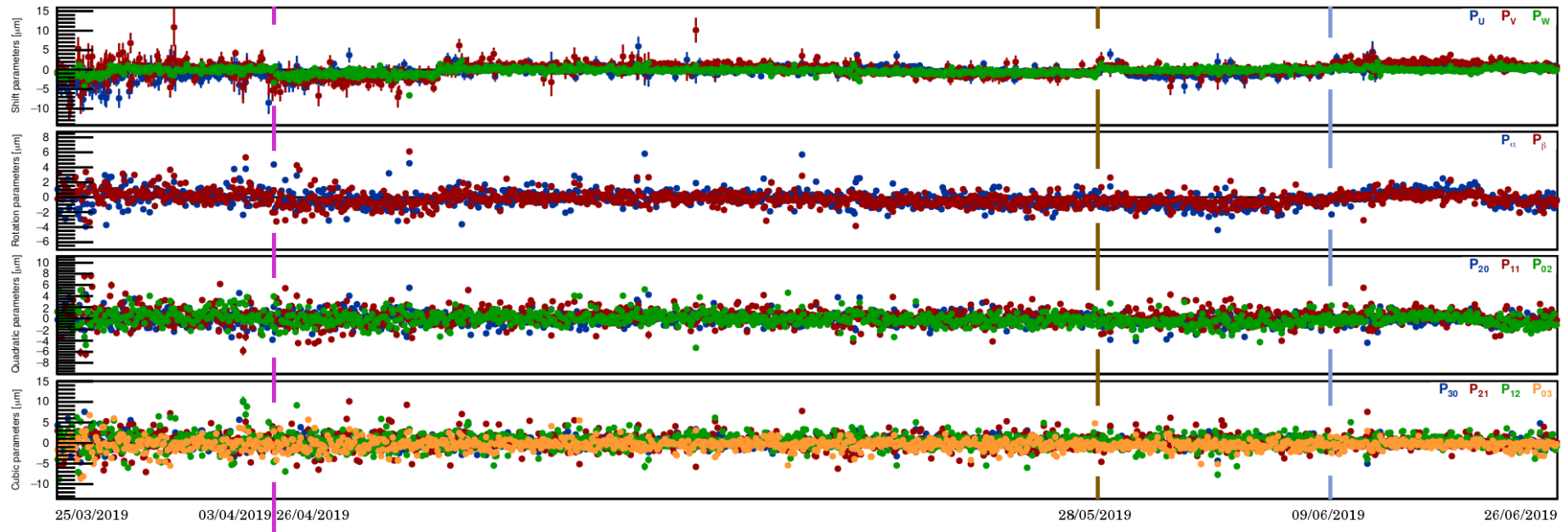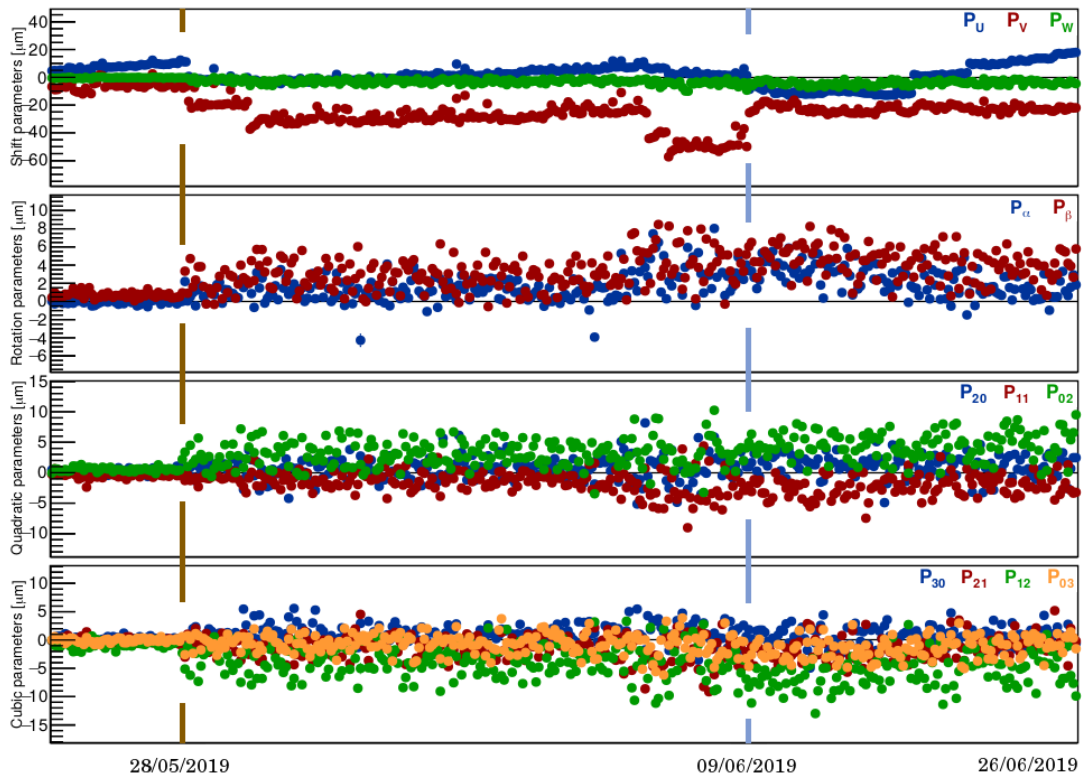
Figure 7.20: Time dependent validation of sensor 1.2.2 alignment parameters: shift (first line), rotation (second line), quadratic (third line) and cubic (fourth line) surface parameters; the unit of the values of alignment parameter axes is μm.
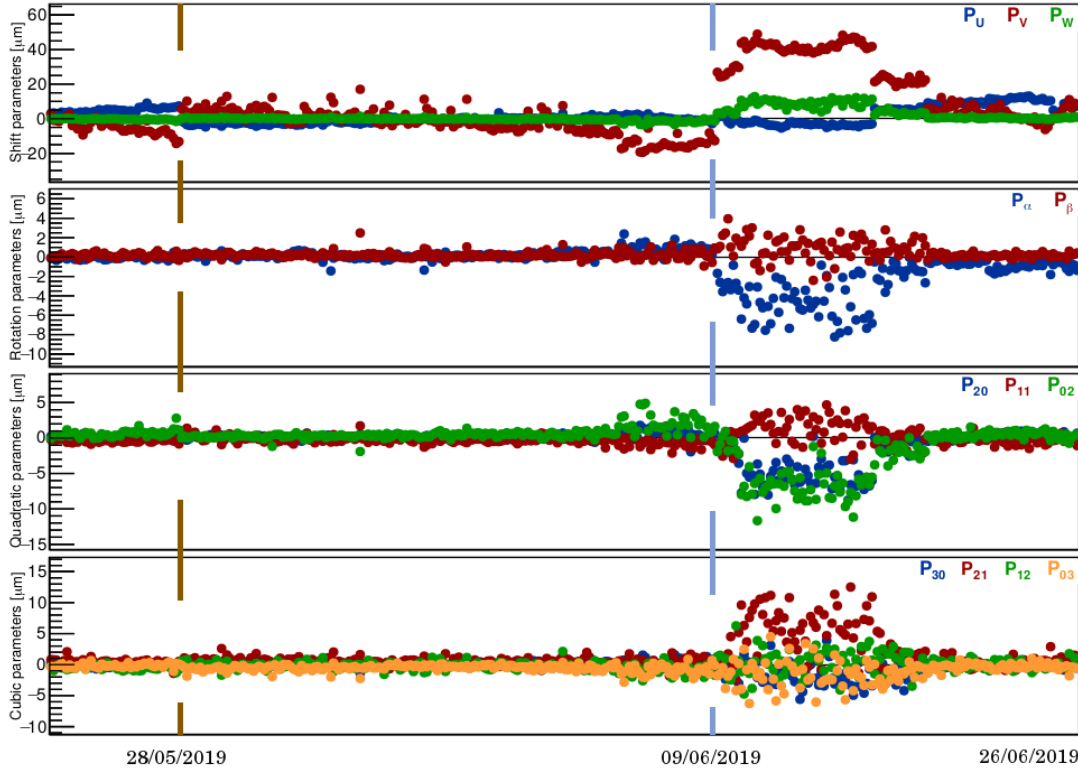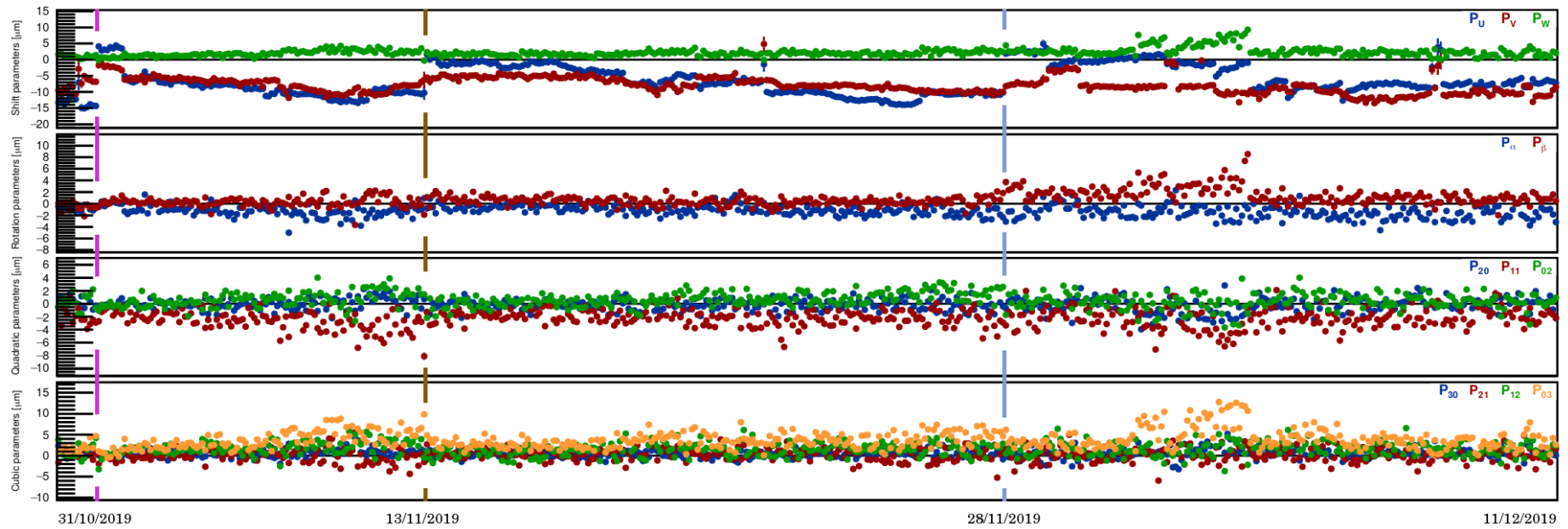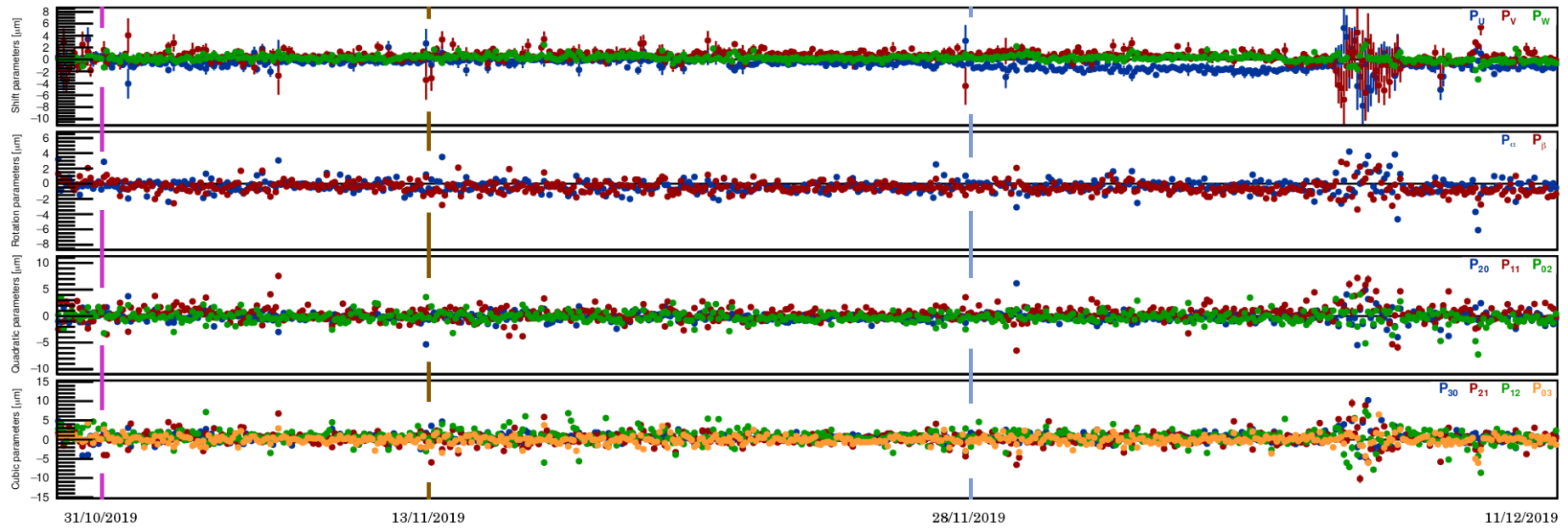
Figure 7.21: Time dependent validation of sensor 4.3.2 alignment parameters: shift (first line), rotation (second line), quadratic (third line) and cubic (fourth line) surface parameters; the unit of the values of alignment parameter axes is μm.
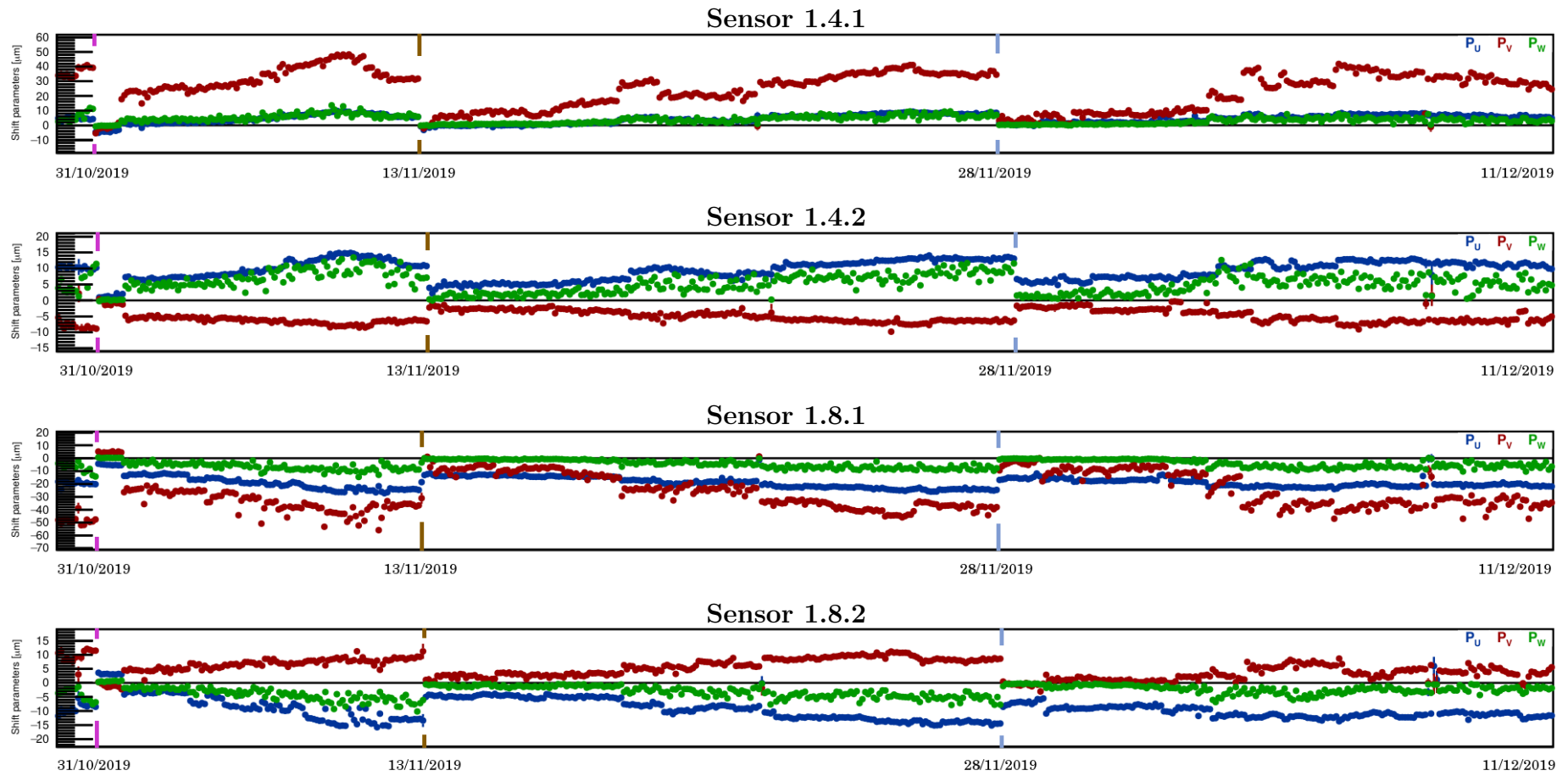
Figure 7.22: Time dependent validation of ladders 1.4 and 1.8 for shift parameters: the unit of the values of alignment parameter axes is μm.

Amplitudes and directions of all sensor jumps in the first layer measured during the maintenance days were projected onto the first layer geometry (Figure 7.23) in order to summarize all possible motions in the layer. The projected directions and amplitudes reported about the vertex detector's relative motion in the vertical direction. Despite this possible motion of the pixel detector being reversible, it could destroy the first layer's ladders and the pixel detector. On the other hand, this motion could be caused by changing conditions of pixel reconstruction and their association into pixel hits. The changes in alignment parameters would then reflect the machine and background conditions. The elimination of this effect could be done by keeping the machine conditions stable during the maintenance days or by applying an advanced run-dependent alignment procedure for the pixel sensors in the first layer.
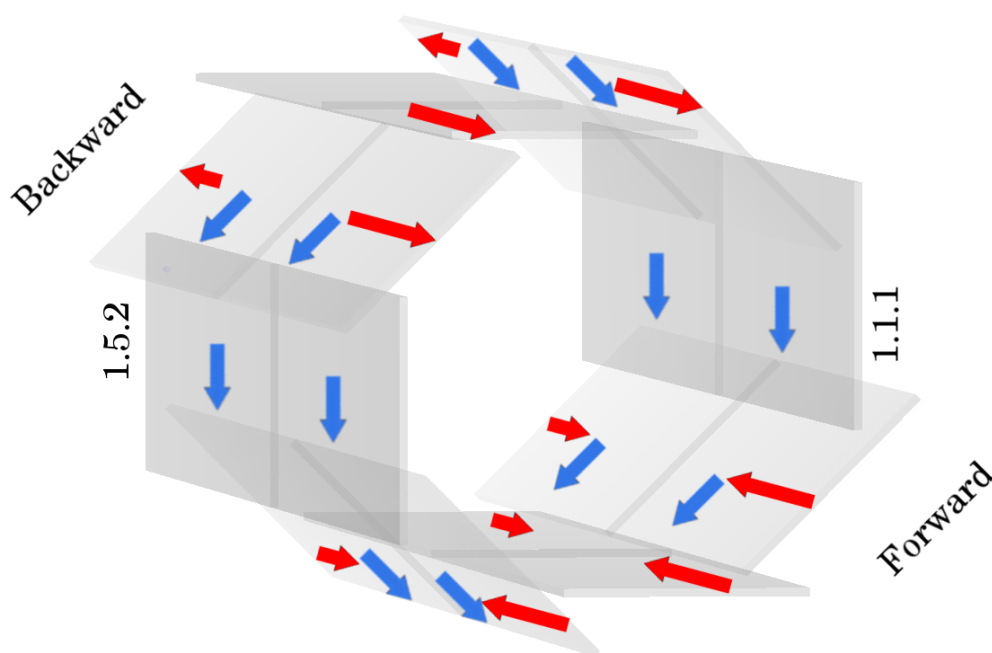
Figure 7.23: Projection of maintenance jumps in validation to first layer: large red arrows correspond with about 40 μm, small red arrows correspond with about 10 μm in the u direction and blue arrows correspond about 20 μm shifts in the v direction.

As can be seen the monitoring values of the v shift for sensors 1.4.1 and 1.8.1 (Figure 7.22) are showing a "teeth" structure after the 28$^{\text{th}}$ of November. In a detailed picture of this special case (Figure 7.24), clear jumps were observed for each day of a week in December, when the beams were aborted right before the day shift (starting at 8:00 am JST) and collisions were restarted after the day shift (at 4:00 pm JST). During day shifts, machine studies for increasing beam currents in the main rings were performed. This teeth structure corresponds with an observation of synchrotron radiation in the first layer of the pixel detector.

On the 18$^{\text{th}}$ of November an earthquake occurred at 8:00 am. It affected monitored alignment parameters, which can be identified for sensor 1.4.1 (Figure 7.22) between the 13$^{\text{th}}$ and the 28$^{\text{th}}$ of November as a jump in the v shift. Afterwards,
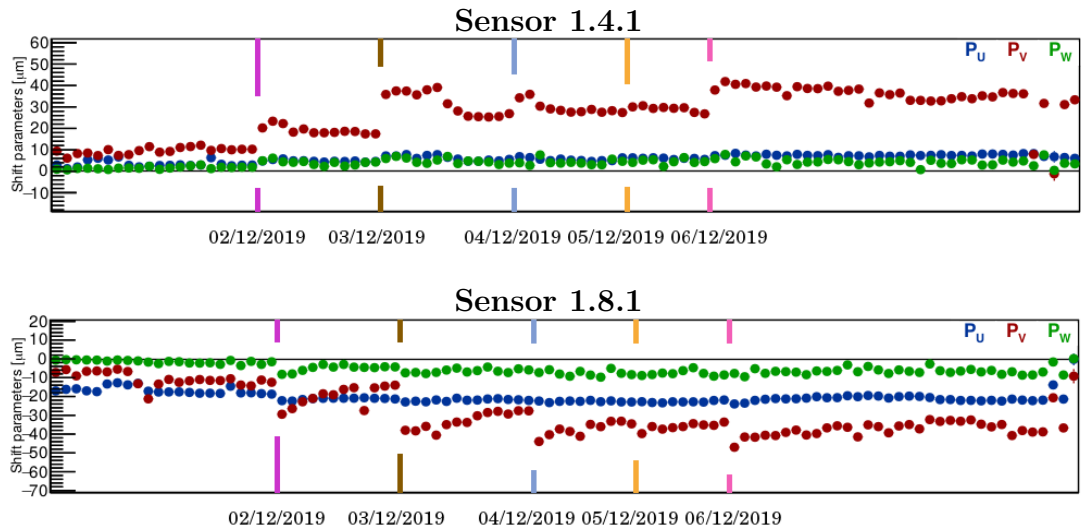
Figure 7.24: The "teeth" structure in shift validation plots: the unit of the values of alignment parameter axes is μm.

the earthquake data was collected. During lunchtime, the beams were aborted, and the machine studies were performed. After restarting the collisions (late afternoon), the v monitoring parameter jumped back to the same values as before the earthquake. Similar observations were made for other sensors, as shown in Figure 7.25. In my interpretation, the alignment parameters reflect any issue or incident which were fixed during the machine tuning procedures or the calibration process of pixel sensors.
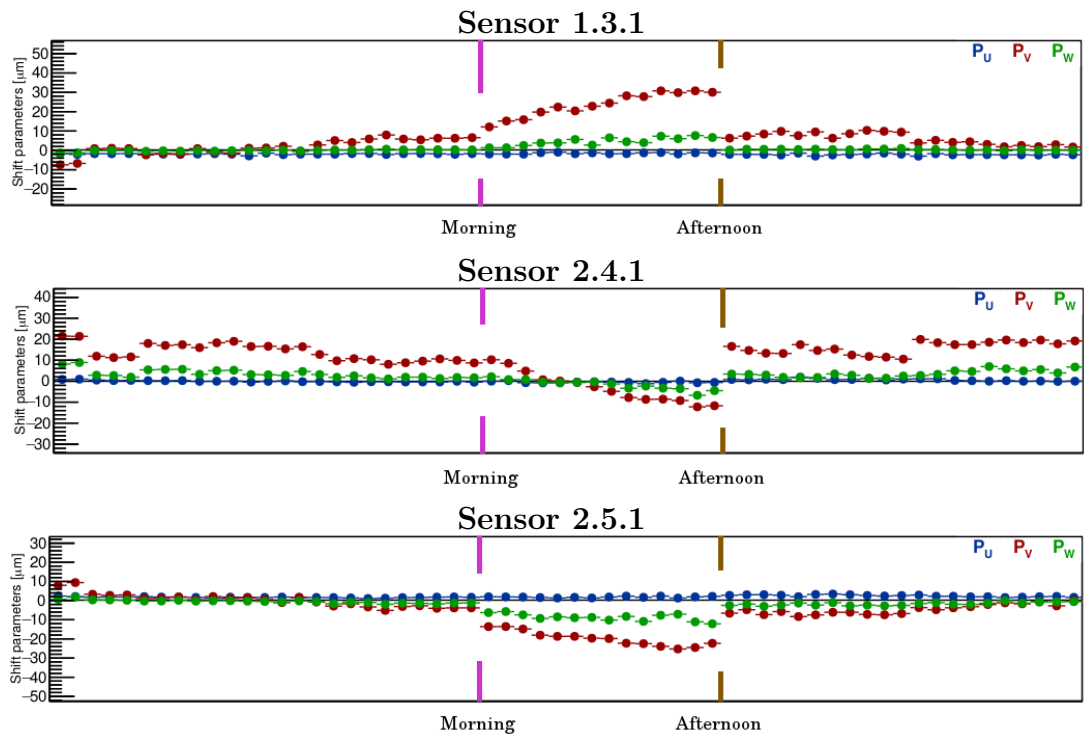
Figure 7.25: Behaviour of pixel sensors after an earthquake on the 18th of November, 2019: The unit of the values of alignment parameter axes is μm.

7.4.3 Spring 2020 period

In spring 2020 the Belle II detector was collecting collision data from the beginning March till the end of June. The alignment procedure was performed using the first cosmic and collision data, and new alignment constants were determined. The alignment monitoring procedure was performed with the data available on the 11$^{\text{th}}$ May. The validation plots for reference sensors are shown in Figures 7.26 and 7.27. Again, the plots report about standard behaviour for most vertex detector sensors where alignment parameters fluctuate within 10 μm range around mean value. During monitoring of sensors in the first layer, the jumps during maintenance days and the teeth structures due to increasing beam currents in main rings were identified again.
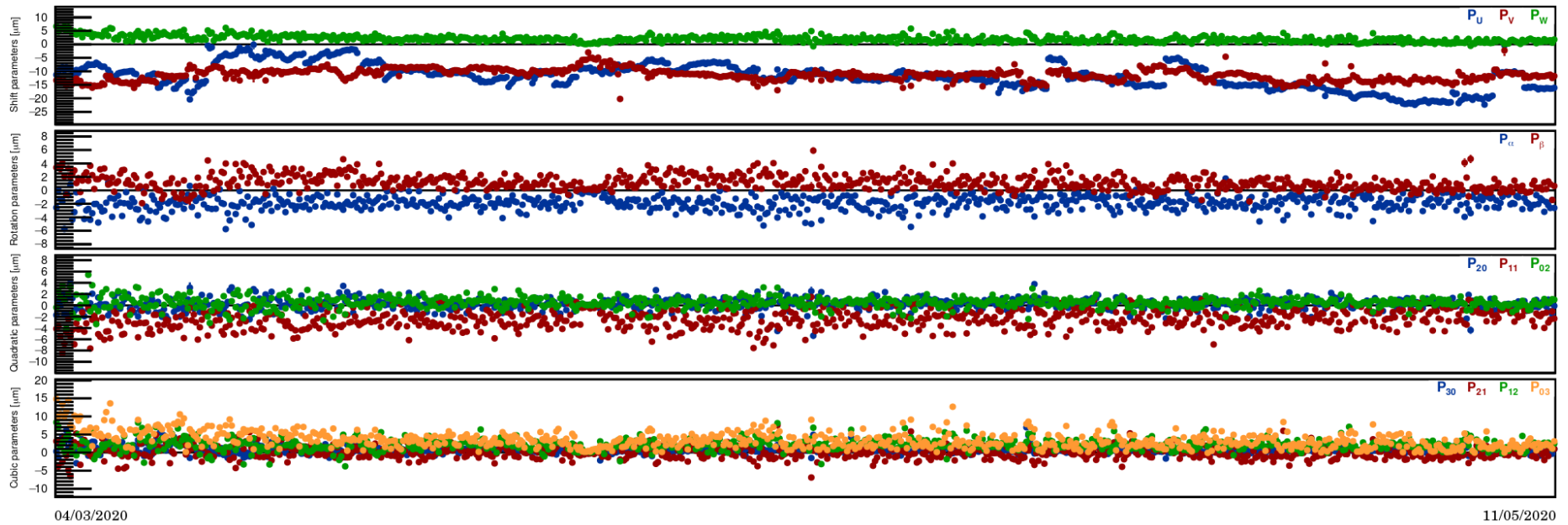
Figure 7.26: Time dependent validation of sensor 1.2.2 alignment parameters: shift (first line), rotation (second line), quadratic (third line) and cubic (fourth line) surface parameters; the unit of the values of alignment parameter axes is μm.
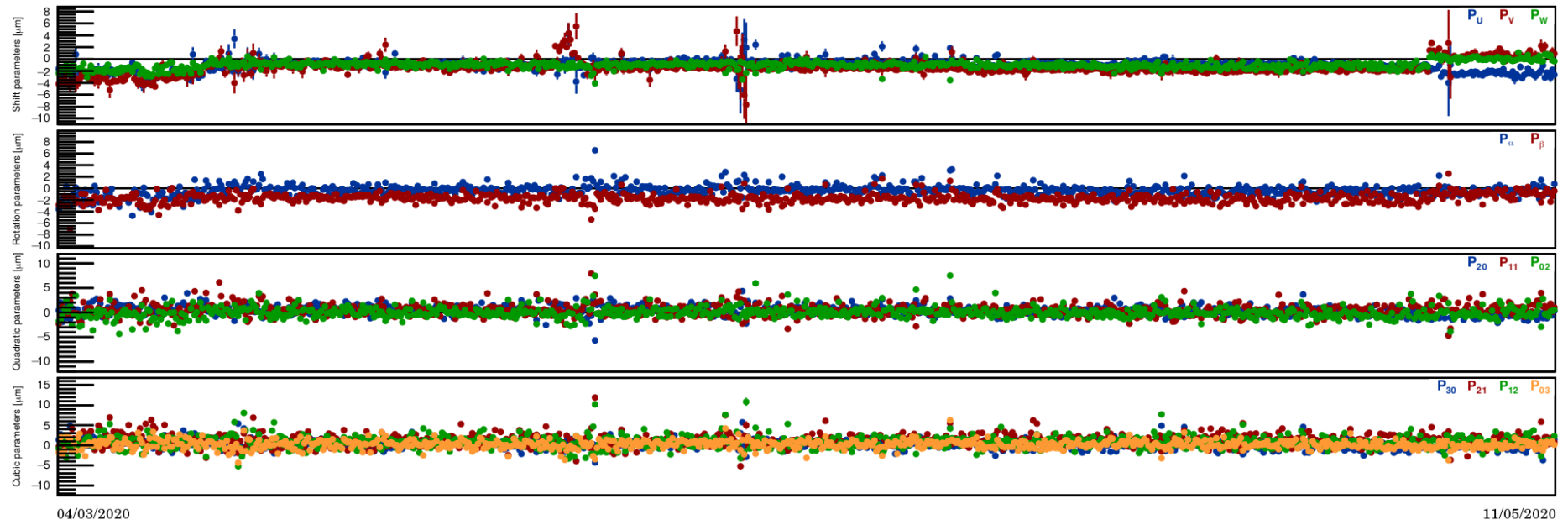
Figure 7.27: Time dependent validation of sensor 4.3.2 alignment parameters: shift (first line), rotation (second line), quadratic (third line) and cubic (fourth line) surface parameters; the unit of the values of alignment parameter axes is μm.

8. Prompt $\sin 2\phi_1$ measurement

With ~ 30 fb^{-1} available, prompt measurement of $\sin 2\phi_1$ was perfomed. The description is based on the text of the internal note [70, 71]. The analysis is kept as simple as possible using following simplifications and assumptions:

- For extracting time dependent CP violating parameter $\sin 2\phi_1$ (S_{f}) only one CP-eigenstate is used,

- For extracting the wrong tag fraction w only one flavour specific mode is used

- Only one flavour tagger quality bin is used, including bias of $\mathcal{O}(3\%)$ on the physics parameters

- The effect of the kinematic approximation is neglected, including bias of $\mathcal{O}(2\%)$ on the physics parameters.

Measuring the CKM parameter $\sin 2\phi_1$ requires complete set of information and understanding of full reconstruction of one of the B^0 mesons, called signal B meson, B$^0_{\mathrm{sig}}$, decaying into a CP-eigenstate $J/\psi K^0_{\mathrm{S}}$ (Figure 8.1). A second partially reconstructed B candidate, called tag B meson, B$^0_{\mathrm{tag}}$ is formed from remaining tracks in the event. Every event can be labelled as positive or negative in terms of flavour by the flavour tagger algorithm which checks whether the tag B is B^0 or $\overline{\mathrm{B}}^0$. The spatial position of both meson vertices is reconstructed to measure the distance $\Delta \ell$ between them [72, 73, 3],

$$\Delta \ell = \ell(B^0_{\mathrm{sig}}) - \ell(B^0_{\mathrm{tag}}), \tag{8.1}$$

where ℓ corresponds to the boost direction axis. The position difference measurement can be equivalently interpreted as the proper time difference $\Delta t_{\mathrm{approx}} \approx \frac{\Delta \ell}{\beta\gamma}$ using the boost $\beta\gamma$ of the $\Upsilon(4S)$ and neglecting the motion of B mesons in the center-of-mass frame.
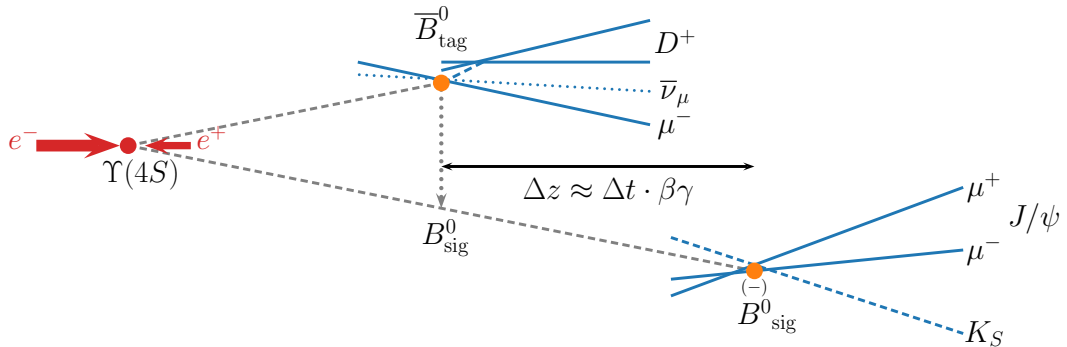
Figure 8.1: Schematic view of a $B^0 \to J/\psi K^0_{\mathrm{S}}$ event[74]

Knowing the angle θ^* between the boost direction and the B$^0_{\mathrm{sig}}$ momentum in the $\Upsilon(4S)$ frame could improve the decay time difference measurement in the following way

$$\Delta t_{\mathrm{rec}} \approx \Delta t_{\mathrm{approx}} - \frac{\beta^* \cos \theta^*}{\beta}(\tau + |\Delta t_{\mathrm{approx}}|) \tag{8.2}$$

where β^* is the velocity of the B in the $\Upsilon(4S)$ rest frame, which approximated value of which is, in the case of Belle II, 0.225 and τ is the B^0 lifetime known from previous measurements. For the purpose of this thesis we define:

- True decay time difference between signal and tagged B mesons $\Delta t_{\mathrm{gen}}(= \tau(B^0_{\mathrm{sig}}) - \tau(B^0_{\mathrm{tag}}))$ accessible in the simulation only

- Approximated decay time difference Δt_{MC} computed according to Eq. (8.2) using the true coordinate ℓ, the true value of the boost and the true value of $\cos\theta^*$. It is also accessible in simulated events only.

- Measured decay time difference Δt_{rec} computed according to Eq. (8.2) using the measured coordinate ℓ from fitted positions of the both vertices and the angle θ^* measured by fitting the B^0 daughters' tracks. This one is accessible in the real data.
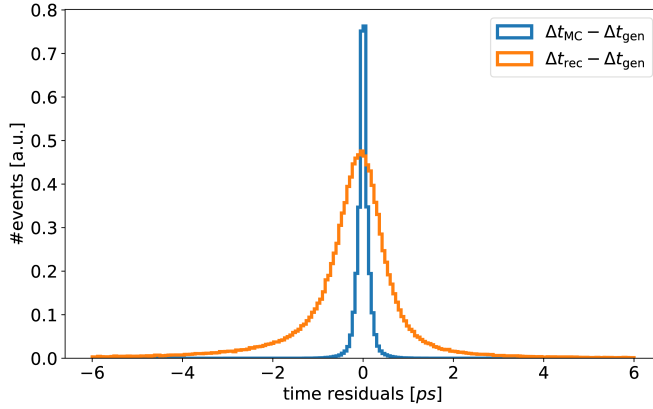
Figure 8.2: Residual Δt distributions for simulated $B^0 \to J/\psi K^0_{\mathrm{S}}$ events

The "kinematic smearing" can be defined as the difference between Δt_{MC} and Δt_{gen}. The residual distributions $\Delta t_{\mathrm{rec}} - \Delta t_{\mathrm{gen}}$ and $\Delta t_{\mathrm{MC}} - \Delta t_{\mathrm{gen}}$ for $B^0 \to J/\psi K^0_{\mathrm{S}}$ simulated events are shown in Figure 8.2. When looking at a comparison of the kinematic and detector smearing effects, one can see that the detector effect dominates. The distributions of positive and negative flavour events as functions of the true decay time difference Δt_{gen} can be expressed:

$$
\begin{aligned}
N^{\pm}(\Delta t_{\mathrm{gen}}) &= N^{\pm} \cdot g^{\pm}(\Delta t_{\mathrm{gen}}) \\
&= N^{\pm} \cdot \frac{e^{\frac{-|\Delta t|}{\tau}}}{4\tau} \{(1 \mp \Delta w) \\
&\quad \pm (1 - 2w) \cdot [S_{\mathrm{f}} \cdot \sin(\Delta m_{\mathrm{d}} \Delta t_{\mathrm{gen}}) - A_{\mathrm{f}} \cdot \cos(\Delta m_{\mathrm{d}} \Delta t_{\mathrm{gen}})]\}
\end{aligned}
\tag{8.3}
$$

where N_+ (N_-) is the number of positive (negative) flavour events, w is the wrong tag fraction, Δw is the difference in wrong tag fraction between a B^0 and a $\overline{B}^0$ tag, τ is the B^0 lifetime, Δm_d is the mixing frequency, $S_{\mathrm{f}} \approx \sin 2\phi_1$ is the time-dependent CP violation parameter and A_f is the direct CP violation parameter. Within our approach, values of the B^0 lifetime τ and the mixing frequency Δm_{d} are fixed and set to the average values obtained from previous

measurements. Additionally, difference in wrong tag fraction Δw and the direct CP violation parameter $A_f \approx 0$ are neglected. Taking into account all mentioned approximations Eq. (8.3) can be simplified to:

$$N^{\pm}(\Delta t_{\text{gen}}) \approx N^{\pm} \cdot \frac{e^{\frac{-|\Delta t|}{\tau}}}{4\tau} \{1 \pm (1 - 2w) \cdot S_{\text{f}} \cdot \sin(\Delta m_{\text{d}} \Delta t_{\text{gen}})\}. \qquad (8.4)$$

Using flavour specific decays $B^0 \to D^{(*)}h$ allows us to extract the tag fraction from data. In these events, the B^0_{tag} flavour and B^0_{tag} decay vertex are determined in the same way as in the case of $B^0 \to J\psi K^0_{\text{S}}$ CP-eigenstate. Based on the B^0_{sig} specific flavour, the events can be separated into two groups based on whether the two B mesons in the event have the same flavour (SF) and opposite flavour (OF) and their distributions of true decay time difference Δt_{gen} can be expressed as:

$$
\begin{aligned}
N^{\text{SF}}(\Delta t_{\text{gen}}) &= N^{\text{SF}} \cdot g^{\text{SF}}(\Delta t_{\text{gen}}) \\
&= N \cdot \frac{e^{\frac{-|\Delta t|}{\tau}}}{4\tau} \left[1 + (1 - 2w)\cos(\Delta m_{\text{d}} \Delta t_{\text{gen}})\right] \\
N^{\text{OF}}(\Delta t_{\text{gen}}) &= N^{\text{OF}} \cdot g^{\text{OF}}(\Delta t_{\text{gen}}) \\
&= N \cdot \frac{e^{\frac{-|\Delta t|}{\tau}}}{4\tau} \left[1 - (1 - 2w)\cos(\Delta m_{\text{d}} \Delta t_{\text{gen}})\right]
\end{aligned}
\qquad (8.5)
$$

The wrong tag fraction can be extracted using the measurement of the N^{SF} and the N^{OF} decay time difference distributions.

8.1 Approximations for the Δt fit

Based on the past measurements of S_{f} provided by BaBar and Belle experiments, this analysis is sub-optimal. There are five main approximations used: the number of studied physical channels is limited, only one flavour tagger quality bin is used, no tag vertex constraint is applied, the two B mesons' motion is the $\Upsilon(4S)$ rest frame is neglected and the resolution is not a conditional probability density function (pdf). All these approximations are explained in the following subsections.

Selection of channels

In the analysis, one CP-eigenstate $B^0 \to J/\psi K^0_{\text{S}}$ and one flavour specific channel $B^0 \to D^- \pi^+$, $D^- \to K^+ \pi^- \pi^-$ are used. The short living kaon K^0_{S} is reconstructed via its decay $K^0_{\text{S}} \to \pi^+ \pi^-$ and the lightest charmonium J/ψ is reconstructed using two leptonic pair modes : $J/\psi \to e^+ e^-$ and $J/\psi \to \mu^+ \mu^-$.

The r bin

In previous experiments, Belle and BaBar, the mixing precision and time dependent measurements were performed in bins of r using Δt fit. The parameter r represents the flavour tagger algorithm quality indicator and its values lie in the range between 0 (no flavour information) and 1 (flavour of B^0_{tag} is determined with quasi certainty). Measurement which uses r bins increases precision, but it

implies technical difficulties (e.g. dependency of the Δt resolution on r, complexity of the Δt fit). The analysis described in this thesis is not binned in r, which introduces a systematic uncertainty in measurement of the wrong tag fraction in simulated events using MC-truth information of about ~ 3 % depending on the signal physics channel.

Constraint for tagged vertexing procedure

Using a constraint on the tag vertex can improve the Δt resolution and enhance the tag vertex reconstruction efficiency by allowing reconstruction of vertices using only one track. In the Belle II vertexing procedure for tagged side three different constraint options can be selected: "No constraint", "IP" and "Tube" constraints. Using the "No constraint" option the procedure reconstructs tagged vertex without any information of the interaction point position. Other options constrain the tagged vertex based on the information about the interaction point, and both options required precise calibration of the position and size of the interaction point. The "IP" option was inherited from the Belle detector. Because of the expectations for the Belle II interaction point, the "Tube" constraint was developed in addition to the Tube constraint. In the "IP" option reconstruction procedure approximates the x and y coordinates of the tagged vertex based on the interaction point characteristics. In the case of large interaction point, the tagged and reconstructed B mesons are expected to be located within the projection of the interaction point onto the xy plane (schematic picture for "IP" option in Fig 8.3). This approximation can be useful during the first years of Belle II operation, when the accelerator creates large interaction point. However, once the size of the interaction point is decreased in the future, the "IP" constraint will no longer be useful. The "Tube" constraint procedure constrains the tagged vertex in a more sophisticated way by approximating the tagged vertex position based on the information about the position of the reconstructed B meson (schematic picture for "Tube" option in Figure 8.3).

Within our analysis, all options were tested in order to choose the best one based on the agreement between data and Monte Carlo. The results obtained using the first data collected (from experiments 7, 8 and 10) can be found in Figure 8.3, where the comparison plots for errors of the x and y coordinates of the tagged vertex are shown. As can be seen, the "IP" and "Tube" options produce the large discrepancies. The observed differences between data and expectations are understood as issues in the calibration of the interaction point. Therefore, the "No constraint" option is used in this analysis.

Kinematic approximation

The described difference between Δt_{gen} and Δt_{MC}, which is a function of the Δt_{gen}, does not let the Δt_{rec} distribution be described solely as a convolution of Eq. (8.3) with resolution function $\mathcal{R}'(\Delta t_{\mathrm{rec}} - \Delta t_{\mathrm{gen}})$. Alternatively Eq. (8.5, 8.3) must be edited to reflect the motion of the B meson

$$
\begin{aligned}
g^{\mathrm{SF/OF}}(\Delta t_{\mathrm{gen}}) &\rightarrow g_{\mathrm{eff}}^{\mathrm{SF/OF}}(\Delta t_{\mathrm{MC}}), \\
g^{\pm}(\Delta t_{\mathrm{gen}}) &\rightarrow g_{\mathrm{eff}}^{\pm}(\Delta t_{\mathrm{MC}})
\end{aligned}
\tag{8.6}
$$

No constraint option
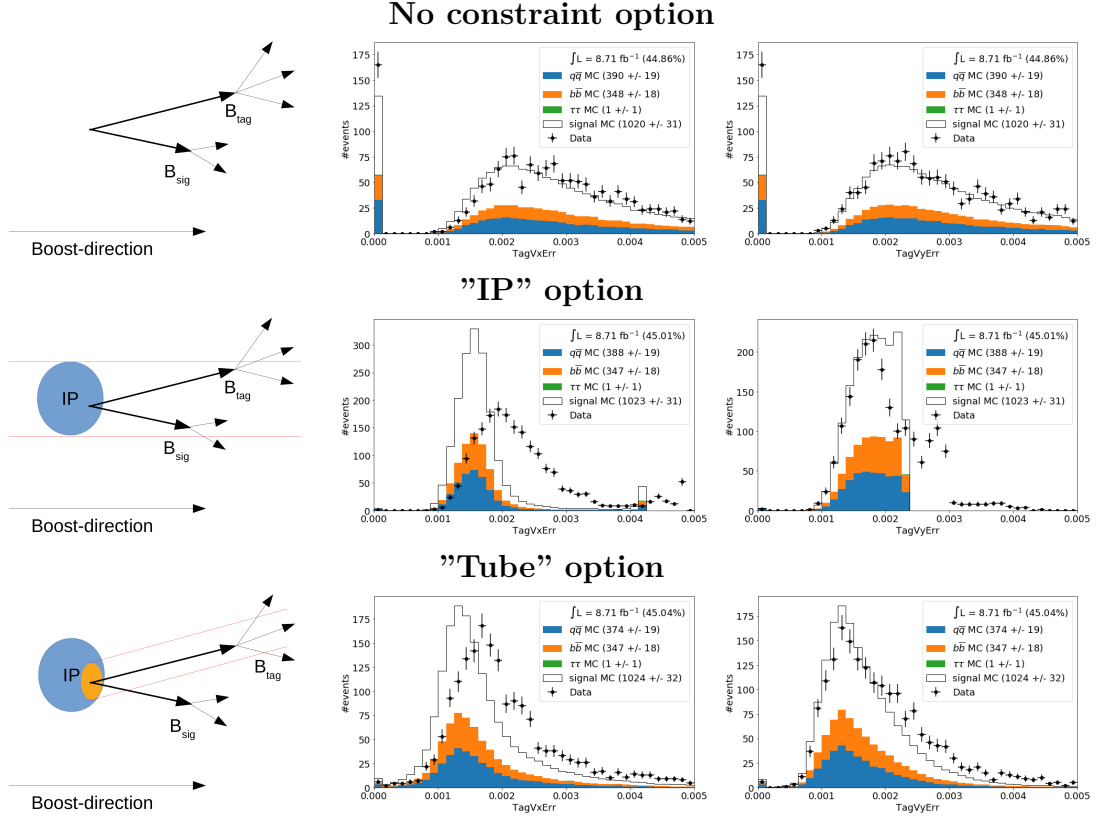

"IP" option

"Tube" option

Figure 8.3: Study of vertexing options for tagging side: comparison of no constraint (top line), "IP" constraint (center line) and "Tube" constraint (line) options; explaining schematic figures (left column), data and Monte Carlo comparison for error of x (central column) and y (right column) coordinate of tagged vertex

where $g_{\mathrm{eff}}^{\mathrm{SF/OF}}$ and $g_{\mathrm{eff}}^{\pm}$ characterize the pdf of Δt_{MC} in $B^0 \to D^- \pi^+$, respectively $B^0 \to J/\psi K_{\mathrm{S}}^0$) decays. In this prompt study, the kinematic smearing is neglected and the following approximations are made:

$$
\begin{aligned}
g_{\mathrm{eff}}^{\mathrm{SF/OF}}(\Delta t_{\mathrm{gen}}) &\approx g^{\mathrm{SF/OF}}(\Delta t_{\mathrm{MC}}), \\
g_{\mathrm{eff}}^{\pm}(\Delta t_{\mathrm{gen}}) &\approx g^{\pm}(\Delta t_{\mathrm{MC}}).
\end{aligned}
\tag{8.7}
$$

Possible effect of this approximation of S_f is studied and its systematic uncertainty is smaller than the statistical one.

Resolution function

The resolution function $\mathcal{R}(\Delta t_{\mathrm{rec}} - \Delta t_{\mathrm{MC}})$ characterizes the residual distribution $\Delta t_{\mathrm{res}} = \Delta t_{\mathrm{rec}} - \Delta t_{\mathrm{MC}}$. The physical parameter Δt_{MC} is independent on the shape of $\mathcal{R}(\Delta t_{\mathrm{rec}} - \Delta t_{\mathrm{MC}})$ and is constant as function of Δt_{MC}. The measured Δt_{rec} distributions, $\mathcal{G}^{\mathrm{SF/OF}}(\Delta t_{\mathrm{rec}})$ and $\mathcal{G}^{\pm}(\Delta t_{\mathrm{rec}})$, are described as a convolution of the resolution function and the physical distributions

$$
\begin{aligned}
\mathcal{G}^{\mathrm{SF/OF}}(\Delta t_{\mathrm{rec}}) &= (g^{\mathrm{SF/OF}} * \mathcal{R})(\Delta t_{\mathrm{rec}}), \\
\mathcal{G}^{\pm}(\Delta t_{\mathrm{rec}}) &= (g^{\pm} * \mathcal{R})(\Delta t_{\mathrm{rec}})
\end{aligned}
\tag{8.8}
$$

The resolution function as a conditional pdf on the uncertainty on Δt_{rec}, Δt_{err} has been introduced in the past analysis. This technique improves statistical precision and minimizes systematic uncertainties. The pull distribution ($\Delta t_{rec} - \Delta t_{MC})/\Delta t_{err}$ (Figure 8.4) changes for different bins of Δt_{err}. The phenomenon can be explained as non-linear dependencies on Δt_{err} or dependencies on other parameters. The source of non-linearities can lie in some issues with calibration of the track parameters, and secondary particles in the B^0_{tag} decay. A correct conditional pdf, which can eliminate this non-linearities, was not developed for this analysis.
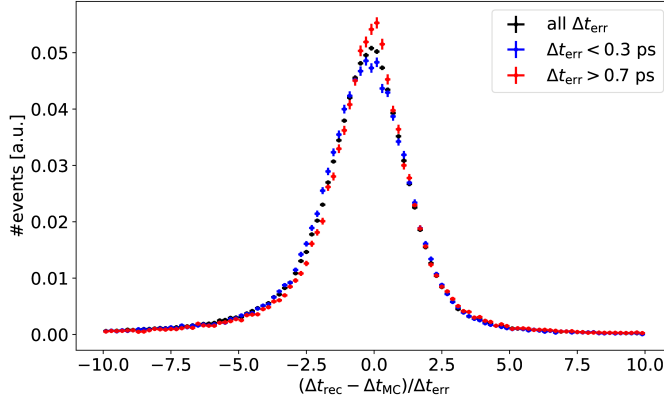

Figure 8.4: Distribution of the Δt_{rec} pull in $B^0 \rightarrow D^- \pi^+$ simulated events: The pull distribution is shown for Δt_{err} values.

In simple terms, one dimensional resolution function is used in this analysis. The resolution function is defined as a sum of Gaussian cores due to the spread of Δt_{gen} and a tail component present due to the smearing because of tracks coming from the decay of secondary particles in the B^0_{tag} decay. The Δt_{err} distribution is divided into 18 bins Δt^i_{err} and the fraction of events in each of the bins f^i_{err} is extracted from a simulation sample. The bin segmentation (Figure 8.5) is the same for all channels. The resolution function consists of a sum of 18 Gaussian distributions with exponential tails, means and width of which are consistent with Δt^i_{err}:

$$\mathcal{R}(\Delta t_{res}) = \sum_i f^i_{err} \cdot \mathcal{R}^i(\Delta t_{res}) \qquad (8.9)$$

with

$$
\begin{aligned}
\mathcal{R}^i(\Delta t_{res}) = {} & (1 - r_{tail}) \cdot G(\Delta t_{res}, \mu \cdot \Delta t^i_{err}, \sigma \cdot \Delta t^i_{err}) \\
& + r_{tail} \cdot r_R \cdot G(\Delta t_{res}, \mu \cdot \Delta t^i_{err}, \sigma \cdot \Delta t^i_{err}) * \exp_R(-c_R \cdot \Delta t_{res}/\Delta t^i_{err}) \\
& + r_{tail} \cdot (1 - r_R) \cdot G(\Delta t_{res}, \mu \cdot \Delta t^i_{err}, \sigma \cdot \Delta t^i_{err}) * \exp_L(c_L \cdot \Delta t_{res}/\Delta t^i_{err})
\end{aligned}
$$
$$(8.10)$$

where

- $G(\Delta t_{res}, \mu \cdot \Delta t^i_{err}, \sigma \cdot \Delta t^i_{err})$ is the normalised Gaussian function of mean $\mu \cdot \Delta t^i_{err}$ and width $\sigma \cdot \Delta t^i_{err}$);

- $\exp_R(-c_R \cdot \Delta t_{res}/\Delta t^i_{err}) = c_R e^{-c_R \cdot \Delta t_{res}}$ when $\Delta t_{res} > 0$; 0 otherwise

- $\exp_{\mathrm{L}}(-c_{\mathrm{L}} \cdot \Delta t_{\mathrm{res}}/\Delta t^{\mathrm{i}}_{\mathrm{err}}) = c_{\mathrm{L}} e^{c_{\mathrm{L}} \cdot \Delta t_{\mathrm{res}}}$ when $\Delta t_{\mathrm{res}} > 0$; 0 otherwise

- r_{tail} is the fraction of events contributing to the tails of the distribution;

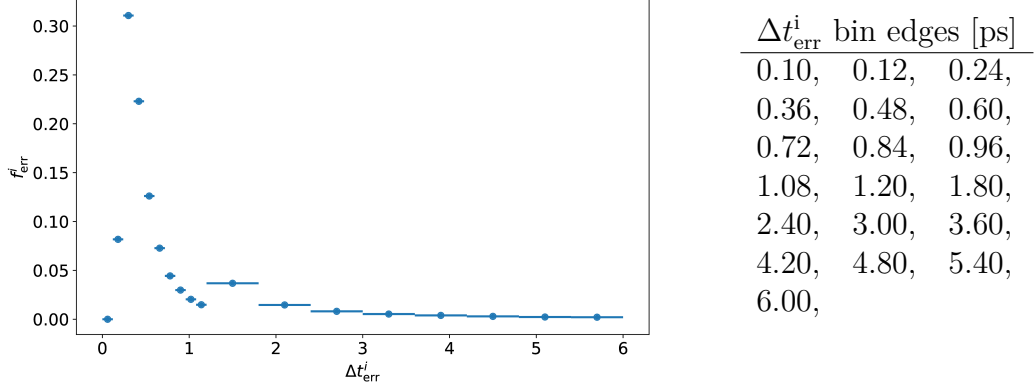- r_{R} is the fraction of events in the tails that contribute to the right tail.

$\Delta t^{\mathrm{i}}_{\mathrm{err}}$ bin edges [ps]		
0.10,	0.12,	0.24,
0.36,	0.48,	0.60,
0.72,	0.84,	0.96,
1.08,	1.20,	1.80,
2.40,	3.00,	3.60,
4.20,	4.80,	5.40,
6.00,		

Figure 8.5: Description of 18 bins of $\Delta t^{\mathrm{i}}_{\mathrm{err}}$ for the resolution function: fraction of $B^0 \to D^- \pi^+$ events (left) and corresponding $\Delta t^{\mathrm{i}}_{\mathrm{err}}$ bin edges.

This resolution function can be parametrised by six free parameters in total: μ, σ, c_{L}, c_{R}, r_{tail} and r_{R}. All these six parameters and the fractions $f^{\mathrm{i}}_{\mathrm{res}}$ are extract from a fit to the Δt_{res} distribution. The parameter values are extracted from the simulation fit and fixed for the real data fit. To eliminate discrepancies in Δt resolution function between the real data and the simulation additional two parameters, the mean Δ_μ and width s_σ, can be introduced. All modes are scaled and shifted by these two parameters

$$\text{simulation} \to \text{real data}$$
$$\sigma \to s_\sigma \cdot \sigma \qquad (8.11)$$
$$\mu \to \mu + \Delta_\mu.$$

To interpret real data, the signal $B^0 \to D^- \pi^+$ Δt_{rec} distribution is fitted with

$$\mathcal{G}^{\mathrm{SF/OF}}(\Delta t_{\mathrm{rec}}; w, \Delta_\mu, s_\sigma) = (g^{\mathrm{SF/OF}} * \mathcal{R})(\Delta t_{\mathrm{rec}}; w, \Delta_\mu, s_\sigma), \qquad (8.12)$$

and the $B^0 \to J/\psi K_{\mathrm{S}}$ Δt_{rec} distribution with

$$\mathcal{G}^{\pm}(\Delta t_{\mathrm{rec}}; S_f, \Delta_\mu, s_\sigma) = (g^{\pm} * \mathcal{R})(\Delta t_{\mathrm{rec}}; S_{\mathrm{f}}, \Delta_\mu, s_\sigma), \qquad (8.13)$$

where all the parameters listed after the semi-column are free floating. Assuming agreement between the data and the simulation in the Δt_{err} distributions, other parameters of the resolution function and fractions of events in bins are fixed to the values extracted from the simulated events. The resolution functions $\mathcal{R}$ and the physical distributions $g^{\mathrm{SF/OF}}$, $g^{\pm}$ are convoluted analytically. The convolution depends on the computation and implementation in python software (`scipy.wolz` function) [75, 76].

8.2 Background and $m_{\rm bc}$ fits

After applying the selection requirements some background events remain and must be taken into account when performing the $\Delta t_{\rm rec}$ fit. To distinguish between signal and background, the beam energy-constraint mass, $m_{\rm bc}$, is used and defined as

$$m_{\rm bc} = \sqrt{\left(E^*_{\rm beam}\right)^2 - \left(p^*_{\rm B}\right)^2}, \tag{8.14}$$

where $E^*_{\rm beam}$ is the energy of the beam and $p^*_{\rm B}$ the momentum of the B candidate in the $\Upsilon(4S)$ frame. This physics quantity shows a distinct peak for fully reconstructed B decays and it has continuum-like shape for background events. By applying selection to $m_{\rm bc}$ we can select two regions,

- for $5.27 < m_{\rm bc} < 5.29$ GeV, the signal region covers $> 99.9\,\%$ of the correctly reconstructed signal events;

- for $5.20 < m_{\rm bc} < 5.27$ GeV, the background region is populated by background events.

Thanks to the selection in this analysis, the purities of the $B^0 \to J/\psi K^0_{\rm S}$ and $B^0 \to D^- \pi^+$ modes in the signal region can be expected to be $\sim 94\,\%$ and $\sim 75\,\%$. With 30 fb^{-1} of data, this signals approximately 10 and 350 background events for each of the channels, respectively.

For the $B^0 \to D^- \pi^+$ mode the background events can be divided into two categories: $q\bar{q}$ and $b\bar{b}$. Most of the tracks in $q\bar{q}$ events come from the interaction point and the $q\bar{q}$ $\Delta t_{\rm rec}$ distribution is narrower than the $b\bar{b}$ $\Delta t_{\rm rec}$ distribution. For $B^0 \to J/\psi K^0_{\rm S}$ mode only the $q\bar{q}$ background events are significant.

Another component, called self-cross-feed, describing events where the signal B candidate is a mixture of the tracks from signal and tagged B meson, is made up of less than 1 % of the signal for all studied modes. This component is not extracted from the fit, but it is associated with the rest of the background. The final fit used for determination of $S_{\rm f}$ is a two dimensional fit dependent on $m_{\rm bc}$; $\Delta t_{\rm rec}$.

8.3 Simulation samples

The samples from the thirteen Belle II official simulation campaign (MC13a) were chosen as the simulation samples, and all of them were processed in the summer of 2020. At the time, it was the latest available Monte Carlo simulated campaign. The simulation samples can be divided into to the signal and background samples. The signal simulated samples are reconstructed for each channel separately, details of which can be found in Table 8.1. For CP-eigenstate channels, we processed signal samples with and without CP violation set at the generator level.

The simulated background samples are separated into parts: continuum, $b\bar{b}$ background and τ pair events. The continuum sample has four components: $u\bar{u}$, $d\bar{d}$, $c\bar{c}$ and $s\bar{s}$. The background samples were simulated in five independent batches. Each of them represents 100 fb^{-1}. In total, background of 500 fb^{-1} was processed.

channel	occupancy	events	
$B^0 \to J/\psi\ (\mu^+\mu^-) + K_S^0\ (\pi^+\pi^-)$	100 %	$1 \cdot 10^6$	
$B^0 \to J/\psi\ (e^+e^-) + K_S^0\ (\pi^+\pi^-)$	100 %	$1 \cdot 10^6$	
$B^0 \to J/\psi\ (\mu^+\mu^-) + K_S^0\ (\pi^+\pi^-)$	100 %	$1 \cdot 10^6$	$C\!\!\!/P\!\!\!/$
$B^0 \to J/\psi\ (e^+e^-) + K_S^0\ (\pi^+\pi^-)$	100 %	$1 \cdot 10^6$	$C\!\!\!/P\!\!\!/$
$B^0 \to \pi^\pm + D^\mp(K^\pm\pi^\mp\pi^\mp)$	50 %	$2 \cdot 10^6$	

Table 8.1: Signal Monte Carlo samples in this study: channel occupancies of generated decay files, number of generated events and specific conditions for some channels

8.4   Data samples

In the summer of 2020, the data samples were processed and analysed. The data was taken in separate blocks in 2019 and 2020. The data samples corresponding to the the 2019 data taking period are experiments 7, 8 and 10. The data from the experiment 12 was collected in spring and summer 2020. The integrated luminosity corresponding to each of the experiments can be found in Table 8.2. Only that fraction of data from experiment 12 which was collected before the 11$^{\text{th}}$ of May 2020 was processed and analysed, instead of the full set of collected data (in experiment 12).

Experiment	7	8	10	12	Total
Luminosity [fb^{-1}]	0.42	4.60	3.74	25.82	34.58

Table 8.2: Integrated luminosity of analysed data for each of the experiments

8.5   Reconstruction and selection

This section describes all the selection requirements applied to the channels used in this analysis and it is subdivided into two parts. First, the skimming requirements for filtering `DSTs` to produce `Root` tuples are described. Second, the requirements applied in order to further suppress the background and get rid of events of unsatisfactory quality for the Δt_{rec} fit are presented.

8.5.1   Skimming pre-selection

The algorithm developed to reconstruct B mesons from tracks and produce `Root` tuples for analysis is written in a Python steering file. The algorithm takes ($\mu^\pm$, $\pi^\pm$, $K^\pm$) as input, combines them into composite particles (J/ψ, K_S^0, $D^\pm$) and finally reconstructs the B mesons. The tagged B-meson candidates are also reconstructed using relevant information.

Selection of tracks

The tracks are loaded from the standard container of tracks using selection criteria shown in Table 8.3. The impact parameters, $d_r < 0.5$ cm and $|d_z| < 3$ cm are also applied to the tag tracks. No criteria are applied for the $\pi^\pm_{K_S^0}$ candidates.

type	d_{r} [cm]	d_{z} [cm]	thetaInCDCAcceptance	particleID
$\mu^{\pm}$	$d_{\mathrm{r}} < 0.5$	$|d_{\mathrm{z}}| < 3$	✅	
$e^{\pm}$	$d_{\mathrm{r}} < 0.5$	$|d_{\mathrm{z}}| < 3$	✅	
$K^{\pm}$	$d_{\mathrm{r}} < 0.5$	$|d_{\mathrm{z}}| < 3$	✅	kaonID > 0.01
$\pi^{\pm}$	$d_{\mathrm{r}} < 0.5$	$|d_{\mathrm{z}}| < 3$	✅	
$\pi^{\pm}_{K^0_{\mathrm{S}}}$				

Table 8.3: Selection criteria for tracks

Composite particles reconstruction

Composite particles are reconstructed using selected tracks. Details of the selection applied to composite particles can be found in Table 8.4. For reconstructed J/ψ particles at least on lepton with leptonID higher than 1 % is required. The K^0_{S} candidate is reconstructed from V0 candidate or combination of two charged tracks.

channel	daughter particles	mass [GeV]
$J/\psi(e^+e^-)$	$e^+ + e^-$	(2.80, 3.40)
$J/\psi(\mu^+\mu^-)$	$\mu^+ + \mu^-$	(2.80, 3.40)
$D^{\mp}(K^{\pm}\pi^{\mp}\pi^{\mp})$	$K^{\pm} + \pi^{\mp} + \pi^{\mp}$	(1.84, 1.90)
$K^0_{\mathrm{S}}(\pi^+\pi^-)$	stdKshorts$(\pi^+_{K^0_{\mathrm{S}}}\pi^-_{K^0_{\mathrm{S}}})$	(0.45, 0.55)

Table 8.4: Selection criteria for composite particles

B meson reconstruction

The B-meson candidates are reconstructed using a combination of several composite particles or composite particles and selected tracks. The signal vertex is fitted without any pointing constraint for the vertex fit; the same fitting procedure was performed for the tagged B candidate. The track fit parameters were updated after the vertex fit. Additional conditions are applied, which are described in Table 8.5 together with final efficiencies for signal simulated samples.

channel	m_{bc} [GeV]	ΔE [GeV]	ε [%]
$B^0[J/\psi(\mu^+\mu^-)K^0_{\mathrm{S}}(\pi^+\pi^-)]$	(5.2, 5.3)	$|\Delta E| < 0.3$	54.9
$B^0[J/\psi(e^+e^-)K^0_{\mathrm{S}}(\pi^+\pi^-)]$	(5.2, 5.3)	$|\Delta E| < 0.3$	33.2
$B^0[\pi^{\pm}\ D^{\mp}(K^{\pm}\pi^{\mp}\pi^{\mp})]$	(5.2, 5.3)	$|\Delta E| < 0.3$	53.4

Table 8.5: Selection criteria and skimming efficiency for the reconstructed B mesons

8.5.2   Analysis selection

After the data and simulation samples are skimmed and background is reduced, one additionally also precisely removes background and events with an insufficient vertex or poor flavour tagger information.

For the $B^0 \to D^- \pi^+$ channel (Table 8.6), selection criteria for D^- mass and particle identification of the kaon $\mathrm{ID_K}(K^+) > 0.4$ are applied. Combinatorial background and partially reconstructed B decays are reduced by the $|\Delta E| < 0.05$ GeV cut. Peaking background coming from $B^- \to D^- K^+$ is eliminated using the kaon hypothesis requirement applied to the pion from the B $\mathrm{ID_K}(\pi_B) < 0.5$. Thanks to ΔE and $\mathrm{ID_K}$ cuts, the branching fraction of $B^0 \to D^- K^+$ (~ 7 %) is reduced to ~ 1.5 %.

$\boldsymbol{B^0[\pi_B^\pm\ D^\mp(K^\pm\pi^\mp\pi^\mp)]}$	
$|\Delta E| < 0.05$ GeV	$\mathrm{ID_K}(\pi_B) < 0.5$
$m(D^\mp) \in (1.844, 1.894)$ GeV	$\mathrm{ID_K}(K^\pm) > 0.4$

Table 8.6: Analysis selection requirements for $B^0 \to \pi^+ D^-$ events

For the $B^0 \to J/\psi(\ell\ell)K_S^0$ channels (Table 8.7), combinatorial background events are eliminated using a cut on the radial distance of the K_S^0, $d_\mathrm{r}(K_S)$. Selection criteria for mass of J/ψ and K_S^0 particles are also applied. Due to the existence of peaking background from $B^0 \to \eta_c(\pi^+\pi^-)K_S^0$ and $B^0 \to D^-(K_S^0\pi^-)\pi^+$, one requires the di-lepton mass veto with a lepton to pion mass hypothesis to meet the following condition: $m_{\ell\to\pi}(\ell\ell) > 3.05$ GeV and $K_S^0\ell$ mass with a lepton to pion hypothesis to fulfill: $m_{\ell^\pm\to\pi^\pm}(K_S^0\ell^\pm) \notin 1.85 - 1.89$ GeV.

For $J/\psi(\mu^+\mu^-)$ channel, the combinatorial background and partially reconstructed B decays are eliminated by the $|\Delta E| < 0.05$ GeV cut. However, for the $B^0 \to J/\psi(e^+e^-)$ channel, an additional physical quantity is considered and constrained by the J/ψ-mass constraint ΔE_ctr with requirement $|\Delta E_\mathrm{crt}| < 0.05$ GeV applied. For both channels, at least one lepton of pair with its particle identification hypothesis $\mathrm{ID}_\mu(\mu) > 0.2$, $\mathrm{ID}_e(e^-) > 0.2$ is required.

$\boldsymbol{B^0[J/\psi(\ell^+\ell^-)K_S^0(\pi^+\pi^-)]}$	
$m_{\mu\to\pi}(\ell\ell) > 3.05$ GeV	$m(\pi\pi) \in (0.47, 0.53)$ GeV
$d_\mathrm{r}(K_S^0) > 0.6$ cm	$m_{\mu^\pm\to\pi^\pm}(K_S^0\ell^\pm) \notin (1.85, 1.89)$ GeV

$\boldsymbol{J/\psi(\mu^+\mu^-)}$		
$|\Delta E| < 0.05$ GeV	$m(\mu\mu) \in (3.00, 3.15)$ GeV	$\mathrm{ID}_\mu(\mu^+)$ or $\mathrm{ID}_\mu(\mu^-) > 0.2$

$\boldsymbol{J/\psi(e^+e^-)}$		
$|\Delta E_\mathrm{ctr}| < 0.04$ GeV	$m(ee) \in (2.90, 3.15)$ GeV	$\mathrm{ID}_e(e^+)$ or $\mathrm{ID}_e(e^-) > 0.2$

Table 8.7: Analysis selection requirements for $B^0 \to J/\psi K_S^0$ events: selection criteria for both $B^0 \to J/\psi K_S^0$ events (top table), for special criteria for $J/\psi(\mu^+\mu^-)$ (middle table) and $J/\psi(e^+e^-)$ (bottom table) particles

Due to the presence of daughter particles in $B^0\overline{B}^0$ events are distributed spherically and continuum events are high momentum jet-like, the background events

can be suppressed. For all channels (Table 8.8), the Fox–Wolfram moment $R_2 < 0.4$ cut is applied to remove background. To exclude wrongly fitted vertices, one requires the p-value of the signal and tag sides to be $p - \text{val(tag)} > 1\%$ and $p - \text{val(sig)} > -1$. To select events with high flavour tagger quality, the criterion of $|q \cdot r_{\text{FBDT}}| > 0.2$ is requested. $0.1 < \Delta t_{\text{err}} < 6.0$ ps is required in order to eliminate cases with large uncertainty of Δt_{rec} and failures in computation of Δt_{err}.

All channels	
$R_2 < 0.4$	$p-\text{val(tag)} > 1\%$
$|q \cdot r_{\text{FBDT}}| > 0.2$	$p-\text{val(sig)} > -1$
$\Delta t_{\text{err}} \in (0.1, 6.0)$ ps	

Table 8.8: Analysis selection requirements for all channels

8.6 Fit shapes from the simulation samples

In this section the m_{bc} and Δt shapes are introduced. The distribution shapes are fitted to simulated samples and extracted parameters are stored. Later the shapes are used to fit the data.

8.6.1 The m_{bc} shapes

Studied simulated sample is split into three different categories: signal, $b\bar{b}$ and continuum background. The percentage representation for each of the categories is extracted from the fit of the m_{bc} distribution. At the beginning, a simulated sample of each category is fitted separately with a probability density function (pdf) to establish a shape describing the category. To check the correctness of the shapes, the simulated sample is fitted using fixed values of all shape parameters obtained from the previous iteration. Only parameters determining yields of each category are free floating. Fitted category yields are compared and juxtaposed with the Monte Carlo expectations.

Fits for $B^0 \to D^- \pi^+$ events

In this section the pdfs used for fitting all categories of the $B^0 \to D^- \pi^+$ mode are introduced. Then a fit of the simulated sample is discussed. Crystal Ball function with following parametrisation is chosen as the describing shape of the signal m_{bc} distribution:

$$\text{CB}(x, \alpha, n, \overline{x}, \sigma) = N \cdot \begin{cases} e^{-\frac{(x-\overline{x})^2}{2\sigma^2}}, & \text{for } x > -\beta, \\ \left(\frac{n}{\alpha}\right)^n \cdot e^{-\frac{\alpha^2}{2}} \cdot \left(\frac{n}{|\alpha|} - |\alpha| - \frac{(x-\overline{x})^2}{2\sigma^2}\right)^{-n} & \text{for } x \leq -\beta \end{cases} \quad (8.15)$$

where N is a normalisation constant.

As a shape describing the continuum background category, an Argus function is selected with parametrisation for $0 < x < 1$ being:

$$\mathrm{Ar}(x, \chi, x_0, m_0) = \frac{\chi^3}{\sqrt{2\pi}\Psi(\chi)} \frac{(x - x_0)}{m_0} \sqrt{1 - \frac{(x - x_0)^2}{m_0^2}} e^{-\frac{\chi^2}{2}\left(1 - \frac{(x - x_0)^2}{m_0^2}\right)} \quad (8.16)$$

where $\Psi(\chi) = \Phi(\chi) - \chi\phi(\chi) - 1/2$ with Φ are cumulative distribution functions of the standard normal distribution and ϕ is the probability distribution of the standard normal distribution.

As the shape expressing $b\bar{b}$ background m_{bc} distribution, the sum of an Argus and Crystal Ball functions with the free floating fraction f_{CB} is used:

$$f(x, f_{\mathrm{CB}}) = (1 - f_{\mathrm{CB}}) \cdot \mathrm{Ar} + f_{\mathrm{CB}} \cdot \mathrm{CB}. \quad (8.17)$$

The final fit of the simulated sample is shown in Figure 8.6, where the shape parameters of each category are fixed to the values obtained by fitting all categories separately using functions defined above (Table 8.9). The value of the continuum to the $b\bar{b}$ background fraction is well known from the Monte Carlo truth matching and it is fixed. Eventually, parameters describing signal and total background yields are set free floating in the final fit. Fitted yields and true values from the Monte Carlo truth matching agree within one sigma.

	Signal	**Continuum**	**$b\bar{b}$ background**
α	2.705 ± 0.049		0.675 ± 0.094
n	9.2 ± 1.3		1.105 ± 0.045
$\overline{x}$	$5.27955 \pm 5.1 \cdot 10^{-6}$		5.27968 ± 0.00017
σ	$0.0025667 \pm 3.8 \cdot 10^{-6}$		0.00477 ± 0.00019
χ		6.617 ± 0.080	8.69 ± 0.67
x_0		$-0.000149 \pm 2.9 \cdot 10^{-5}$	-0.00017 ± 0.00025
m_0		$5.28994 \pm 8.7 \cdot 10^{-6}$	5.28983 ± 0.00025
f_{CB}			0.66 ± 0.10

Table 8.9: Fitted values for $B^0 \rightarrow D^-\pi^+$ pdfs; the units of $\overline{x}, \sigma, x_0$ and m_0 quantities are GeV; the shapes of fitted pdfs can be found in Appendix G

The m_{bc} shapes for SF and OF sample

Additional checks of m_{bc} shapes for all categories of simulated $B^0 \rightarrow D^-\pi^+$ SF and OF were performed. Comparison between the SF and OF m_{bc} shapes does not introduce any additional problem. However, the fraction of $b\bar{b}/(b\bar{b} + q\bar{q})$ reports about difference between SF and OF samples, where as the value of the fraction for SF is 0.4805 ± 0.0067 and 0.5220 ± 0.0025 for OF, respectively.

Fits for $B^0 \rightarrow J/\psi(\mu^+\mu^-)K_{\mathrm{S}}^0$ events

In this section the fitting pdfs for all categories of the $B^0 \rightarrow J/\psi(\mu^+\mu^-)K_{\mathrm{S}}^0$ mode are described. Then, the fit of the simulated sample is discussed. As a shape describing signal distribution, the Crystal Ball function is applied. Since only
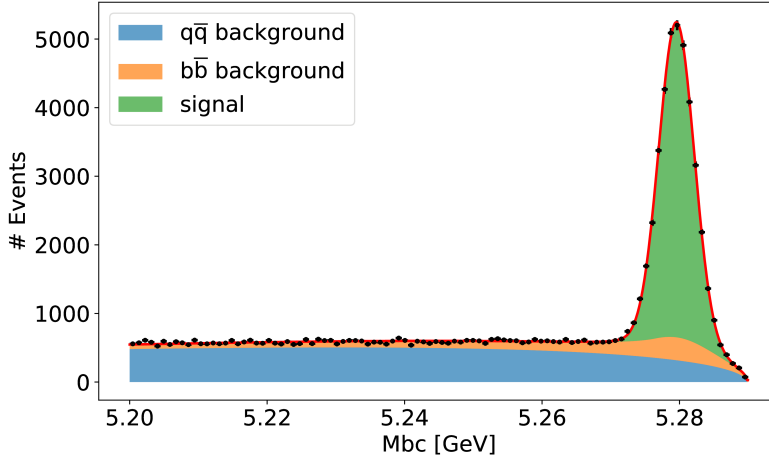
	Fitted	Expected
Signal	32860 ± 210	32800
Background	56850 ± 260	56910

Figure 8.6: Fit of the m_{bc} distribution for $B^0 \to D^- \pi^+$ candidates from 500 fb^{-1} simulation sample (black dots) in top picture with corresponding free fit parameters (bottom table).

a small number of $b\bar{b}$ background events can be found around true B mass ($\sim$ 2 % of signal), the $b\bar{b}$ and continuum backgrounds can be merged into a single category, simply put - background, where the Crystal Ball function is replaced by Gaussian:

$$\text{G}(x, \overline{x}, \sigma) = \frac{1}{\sigma\sqrt{2\pi}} e^{-\frac{1}{2}\frac{(x-\overline{x})^2}{\sigma^2}}, \tag{8.18}$$

with final sum of pdfs:

$$f(x, f_{\text{G}}) = (1 - f_{\text{G}}) \cdot \text{Ar} + f_{\text{G}} \cdot \text{G}. \tag{8.19}$$

	Signal	**Background**
α	3.819 ± 0.039	
n	$1.0214 \pm 1.1 \cdot 10^{-5}$	
$\overline{x}$ [GeV]	$5.27953 \pm 4.6 \cdot 10^{-6}$	5.27771 ± 0.00090
σ [GeV]	$0.0025806 \pm 3.3 \cdot 10^{-6}$	0.0034 ± 0.0010
χ		6.52 ± 0.81
x_0 [GeV]		0.00008 ± 0.00059
m_0 [GeV]		5.29037 ± 0.00059
f_{G}		0.0220 ± 0.0059

Table 8.10: Fitted values for the $B^0 \to J/\psi(\mu^+\mu^-)K_S^0$ pdfs; the shapes of fitted pdfs can be found in Appendix G

The final fit of the simulated sample is shown in Figure 8.7, where shape parameters for each category are fixed and set to the values obtained by fitting all categories separated using functions defined above (Table 8.10). As a last step, parameters describing the signal and background yields are set free floating in the final fit. Fitted yields and true values from the Monte Carlo truth matching agree within one sigma.
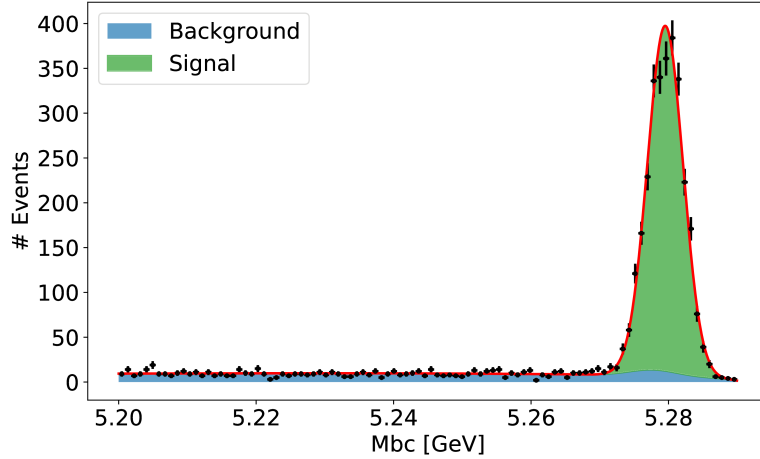
	Fitted	Expected
Signal	2770 ± 54	2784
Background	926 ± 33	912

Figure 8.7: Fit of m_{bc} distribution of $B^0 \to J/\psi(\mu^+\mu^-)K_{\mathrm{S}}^0$ candidates from 500 fb^{-1} simulation sample (black dots) in top picture with corresponding free fit parameters (bottom table).

Fits for $B^0 \to J/\psi(e^+e^-)K_{\mathrm{S}}^0$ events

In this section the pdfs used for fitting all categories of the $B^0 \to J/\psi(e^+e^-)K_{\mathrm{S}}^0$ mode are explained and a fit of the simulated sample is discussed. As a shape describing signal distribution a Crystal Ball function was chosen. The $b\bar{b}$ and continuum backgrounds is merged into single category, where the Crystal Ball function is replaced by Gaussian and summed with Argus function to give the final sum, Eq. (8.19), similar as for the $B^0 \to J/\psi(\mu^+\mu^-)K_{\mathrm{S}}^0$ mode.

	Signal	Background
α	$2.150 \quad \pm \quad 0.039$	
n	$5.99 \quad \pm \, 0.48 \cdot 10^{-5}$	
$\bar{x}$ [GeV]	$5.27955 \pm 6.9 \cdot 10^{-6}$	5.27992 ± 0.00062
σ [GeV]	$0.002680 \pm 5.5 \cdot 10^{-6}$	0.00244 ± 0.00063
χ		$7.04 \quad \pm \quad 0.52$
x_0 [GeV]		-0.00015 ± 0.00015
m_0 [GeV]		5.28985 ± 0.00016
f_{G}		$0.0181 \quad \pm \quad 0.0042$

Table 8.11: Fitted values for $B^0 \to J/\psi(e^+e^-)K_{\mathrm{S}}^0$ pdfs; the shapes of fitted pdfs can be found in Appendix G

The final fit of the simulated sample is shown in Figure 8.8, where the values of shape parameters corresponding to each category are fixed and set to values obtained by fitting all categories separated using functions defined above (Table 8.11). As a last step, parameters describing signal and background yields are free floating in the final fit. Fitted yields and true values from Monte Carlo truth matching agree within one sigma.
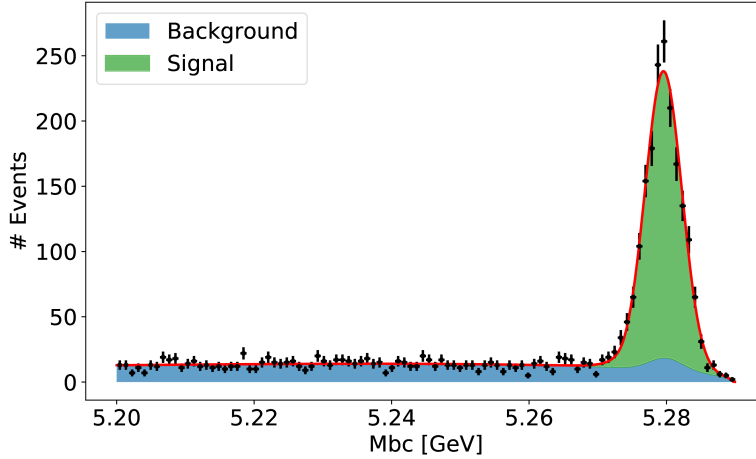
	Fitted	Expected
Signal	1649 ± 44	1658
Background	1298 ± 39	1289

Figure 8.8: Fit of the m_{bc} distribution for $B^0 \to J/\psi(e^+e^-)K_S^0$ candidates from 500 fb^{-1} simulation sample (black dots) in the top picture with corresponding values of free parameters(bottom table).

8.6.2 The Δt_{rec} shapes

In this section the parameters of the Δt_{rec} shapes are determined using signal and background simulation samples for $B^0 \to J/\psi K_S^0$ and $B^0 \to D^-\pi^+$ modes.

8.6.3 The $B^0 \to J/\psi K_S^0$ signal resolution function

The signal Δt_{rec} residual distributions are fitted with the resolution function given by Eq. (8.10). The result of the fit is illustrated in Figure 8.9, where values of the fitted parameters can be found. Presented results are separated into two groups: the $J/\psi(\mu^+\mu^-)$ and $J/\psi(e^+e^-)$ modes. The fit looks good, but some discrepancies can be found, e.g. right tails. Even though the signal simulation sample is three times orders of magnitude bigger than expected for 30 fb^{-1} of data, it looks good enough to be used in analysis. Looking at the fitted parameter values, one can see that the width of the Gaussian core is larger than 1.0, which can be cause by the imperfect calibration of uncertainty on the track parameters and the displacement of the secondary particles from the B_{tag}^0.

8.6.4 The $B^0 \to J/\psi K_S^0$ background Δt_{rec} shape

The background Δt_{rec} residual distributions are studied using the 500 fb^{-1} simulation sample, where selected events are not generated as signal events. An effect of the $b\bar{b}$ background events can be introduced by the finite effective lifetime, however, the occupancy of these events in 500 fb^{-1} simulation sample is very low. In the resolution function, the effect of the effective lifetime of the background events is neglected. The fit of such low number of events with a sum of 18 Gaussian functions can be excessive. To check validity of the resolution functions, the fit of the real data events in the m_{bc} sideband region can be performed. It can be checked whether the shape used to fit the m_{bc} signal region can also describe the

μ	-0.1484 ± 0.0077
σ	1.3539 ± 0.0076
c_{R}	0.2867 ± 0.0097
c_{L}	0.2847 ± 0.0048
r_{tail}	0.2819 ± 0.0063
r_{R}	0.2749 ± 0.0088

μ	-0.155 ± 0.011
σ	1.360 ± 0.011
c_{R}	0.301 ± 0.013
c_{L}	0.2865 ± 0.0068
r_{tail}	0.2864 ± 0.0090
r_{R}	0.287 ± 0.012
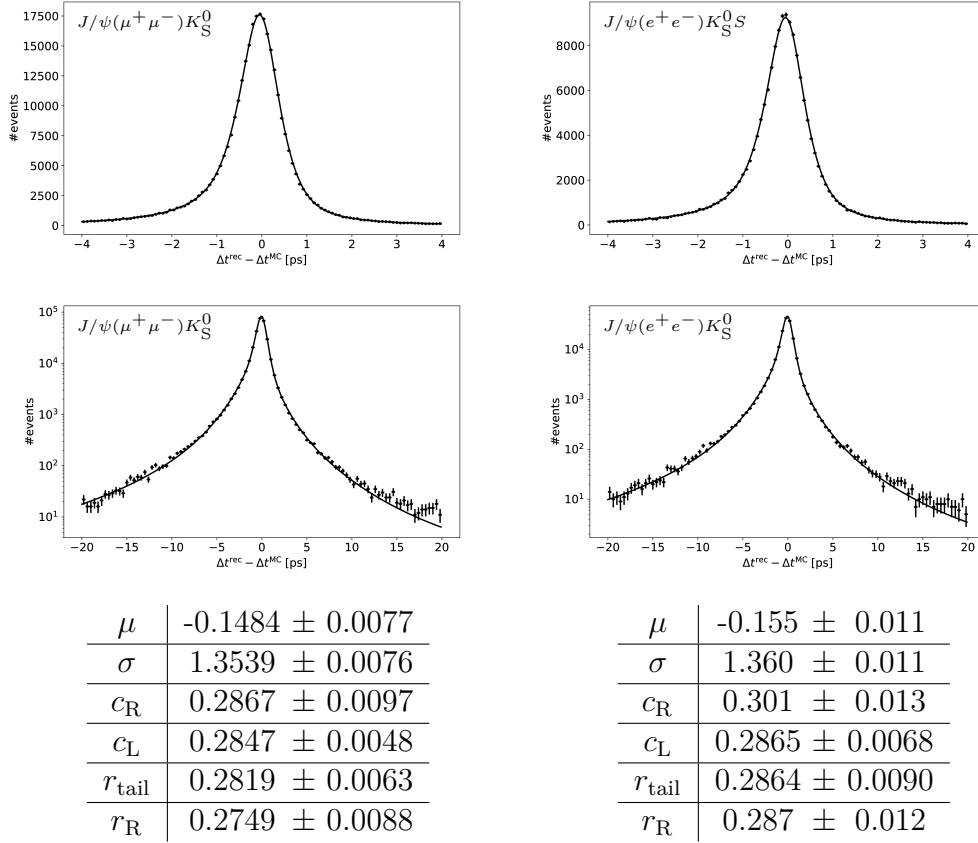
Figure 8.9: The fit of Δt_{rec} residuals for $B^0 \to J/\psi K_{\mathrm{S}}^0$ signal simulation sample for $J/\psi(\mu^+\mu^-)$ (left) and $J/\psi(e^+e^-)$ (right): The fit function is drawn in solid line on top of the data points shown with error bars in linear (top) and logarithmic (center) scales. Obtained shape parameters are listed in the bottom row.

distribution of sideband events. Due to a smaller number of background events, the Δt_{rec} fit is conducted once for all four background cases: negative or positive B_{tag}^0 flavour in the m_{bc} sideband and signal regions. The result of the fit is shown in Figure 8.10. No difference in shape is observed among all background cases.When comparing signal and background shapes of the Δt_{rec} residual distributions, one notices that the values of the σ and r_{tail} parameters are higher for background samples, which can be caused by widened distribution by a finite lifetime discussed above.

8.6.5 The $B^0 \to D^-\pi^+$ signal resolution function

The signal Δt_{rec} residual distributions are fitted with the resolution function given by Eq. (8.10). The result of the fit is illustrated in Figure 8.11, where values of the fitted parameters can be found. The fit is not perfect, however it looks satisfactory enough to be used in analysis, even when taking into account the signal simulation sample being two orders of magnitude higher than expected in 30 fb^{-1} of data. Fitted values of μ and σ parameters are similar to the values determined for resolution functions of the $B^0 \to J/\psi K_{\mathrm{S}}^0$ modes in Figure 8.9. Because not all events are being binned in bins of the flavour tagger equality indicator r, the resolution functions for SF and OF events differ. The reason for this is that B_{tag}^0s
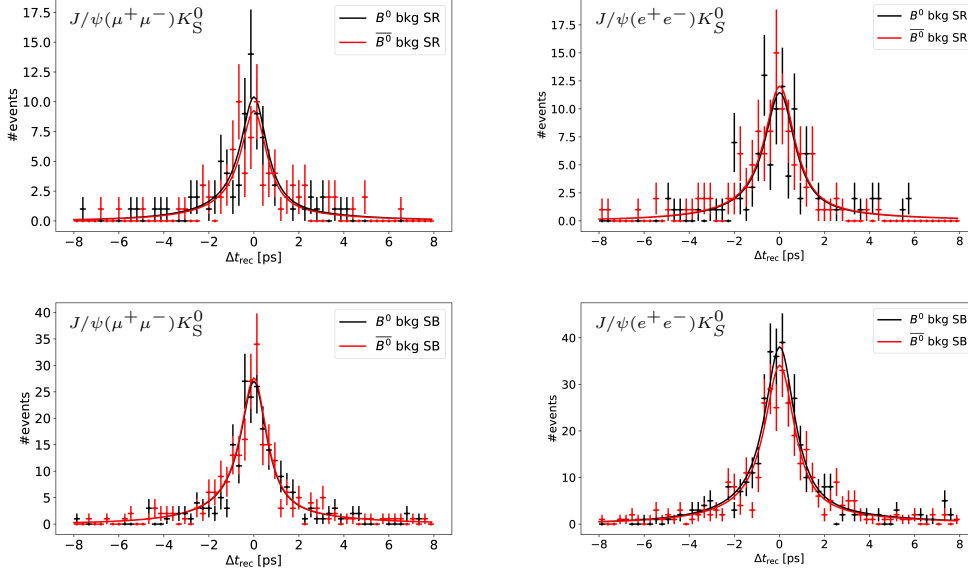
μ	0.16 ± 0.20
σ	1.88 ± 0.20
c_{R}	0.101 ± 0.034
c_{L}	0.209 ± 0.053
r_{tail}	0.430 ± 0.091
r_{R}	0.424 ± 0.087

μ	0.13 ± 0.24
σ	1.49 ± 0.26
c_{R}	0.154 ± 0.043
c_{L}	0.268 ± 0.069
r_{tail}	0.52 ± 0.14
r_{R}	0.395 ± 0.092

Figure 8.10: The fit to Δt_{rec} residuals for $B^0 \to J/\psi K_{\mathrm{S}}^0$ background simulation samples for $J/\psi(\mu^+\mu^-)$ (left) and $J/\psi(e^+e^-)$ (right): The fit functions for $\overline{B}^0_{\mathrm{tag}}$ (**black**) and B^0_{tag} (red) are drawn in the solid lines over the data points shown with error bars for the signal region (top) and the sideband region (center). Obtained shape parameters are listed in the bottom row.

with a large wrong tag probability and large uncertainty in the vertex position coming from tracks are reconstructed using tracks with poor quality. Because the SF sample is less populated than the OF sample, the effect of poorly reconstructed tag vertex on the SF residuals is higher. The Δt_{err} distribution and the residual distribution for SF and OF simulated events are shown in Figure 8.12. The resolution function is fitted to the residual distribution. The values of resolution function parameters are fixed to the ones found in Figure 8.11, but the fractions f_{err}^i are determined from the SF ans OF samples individually. The OF and SF residual distributions report about good agreement without any update of the resolution shape parameters. Moreover, the residual shapes of SF and OF events look similar. A large systematic uncertainty can be expected since a large difference between the OF and SF residuals is combined with data/simulation disagreement in the flavour output result.

8.6.6   The $B^0 \to D^-\pi^+$ background Δt_{rec} shape

The background Δt_{rec} residual distributions are studied using the 500 fb^{-1} simulation sample, where selected events are not generated as signal events. The resolution function shapes of the $q\bar{q}$ and $b\bar{b}$ background categories are determined

μ	-0.1351 ± 0.0089	c_{R}	0.271 ± 0.014	r_{tail}	0.248 ± 0.078
σ	1.3504 ± 0.0088	c_{L}	0.3051 ± 0.0069	r_{R}	0.238 ± 0.012
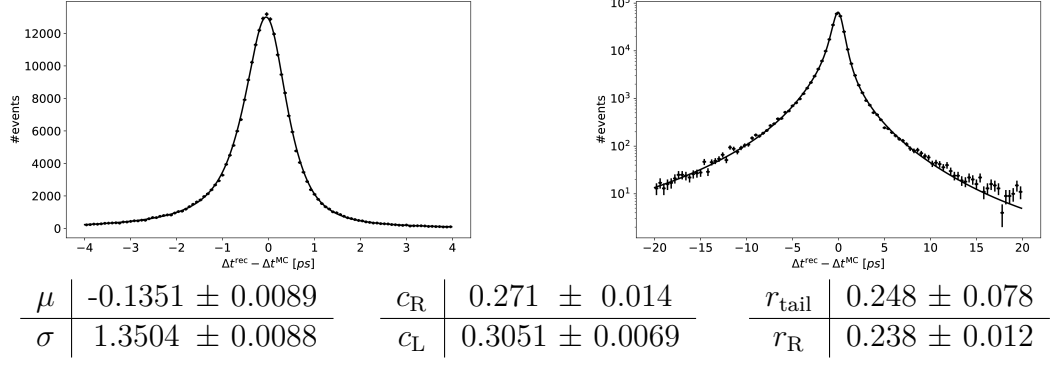
Figure 8.11: The fit of Δt_{rec} residuals for $B^0 \to D^- \pi^+$ signal simulation sample: The fit function is drawn in in solid line over the data points shown with error bars in linear (top left) and logarithmic (top right) scales. Obtained shape parameters are shown at the bottom.
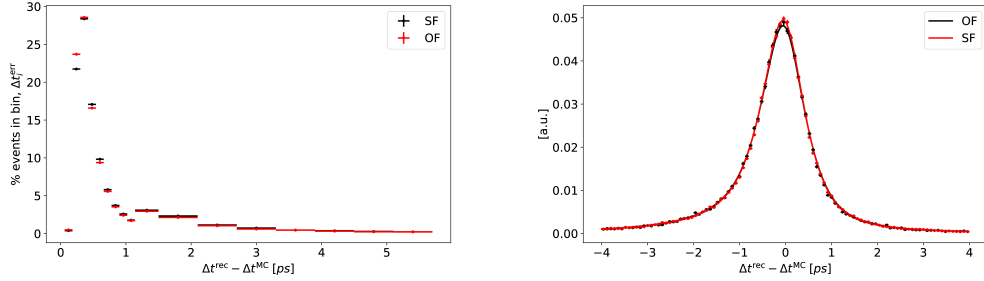
Figure 8.12: Fraction of simulated SF (**black**) and OF (red) $B^0 \to D^- \pi^+$ events in bins $\Delta t^i_{\mathrm{err}}$ (left) and residual distribution (right) for the same events with resolution function (solid lines)

using different functions. The resolution function fit of the $q\bar{q}$ background is performed without any extensions. The Δt_{rec} shapes for OF and SF events are fitted in the m_{bc} sideband and signal regions simultaneously. To take into account statistical size of samples, resolution function shapes look very similar in all studied background regions and the fits can be found in Figure 8.13.

In comparison with $q\bar{q}$, the resolution function for $b\bar{b}$ background should be extended due to the distribution being wider in the m_{bc} signal region than in the sideband. This is well known, because the peaking background in the signal region is influenced by effective lifetime. However, the peaking background in the sideband is influenced by shorter effective lifetime due to being a mixture of tag and signal tracks. Therefore, the Δt_{rec} resolution function is determined in the sideband and signal regions independently. The fit was performed in two steps. Firstly, the SF and OF events are merged to one sample and the lifetime distribution is fitted with an exponential decay with effective free-floating lifetime τ_{eff} convoluted with the resolution functions

$$e^{\tau_{\mathrm{eff}}} * \mathcal{R}. \tag{8.20}$$

All values of all resolution function parameters are free-floating in that fit, but value of the σ parameters is fixed to 1.35 [77], in other case the fit would diverge.

123

μ	0.027 ± 0.039	c_{R}	0.142 ± 0.029	r_{tail}	0.185 ± 0.025
σ	1.358 ± 0.043	c_{L}	0.150 ± 0.029	r_{R}	0.466 ± 0.050
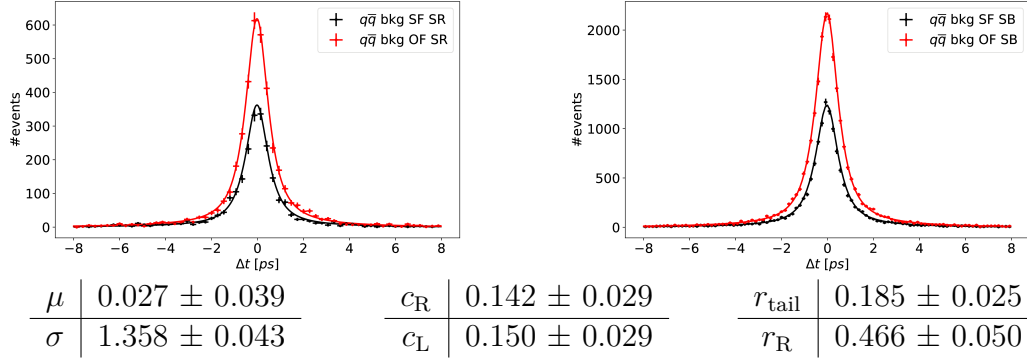
Figure 8.13: The fit of Δt_{rec} residuals for $B^0 \to D^- \pi^+$ $q\bar{q}$ background simulation sample for SF (**black**) and OF (red): The fit function is shown drawn in the solid line on top of the data points shown with black bars in signal (top left) and sideband (top right) regions. Obtained shape parameters are shown at the bottom.

Secondly, the Δt_{rec} resolution function for the OF ans SF are determined simultaneously with the shape of Eq. (8.8). In the second fit, values of the lifetime and resolution function parameters are fixed and set to the values found in the previous fit, but values of w and Δm_{d} are free floating. Values of parameters obtained from both fits can be found in Figure 8.14.

μ	-0.159 ± 0.070		μ	-0.188 ± 0.29
σ	$1.35 \pm$ fixed		σ	$1.35 \pm$ fixed
c_{R}	0.0060 ± 0.0017		c_{R}	0.0084 ± 0.0019
c_{L}	0.167 ± 0.016		c_{L}	0.179 ± 0.013
f_{tail}	0.157 ± 0.010		f_{tail}	0.168 ± 0.011
f_{R}	0.427 ± 0.028		f_{R}	0.482 ± 0.025
τ_{eff}	1.546 ± 0.040		τ_{eff}	1.377 ± 0.038
w	0.360 ± 0.012		w	0.42569 ± 0.00013
Δm_{eff}	0.420 ± 0.028		Δm_{eff}	0.02544 ± 0.00033
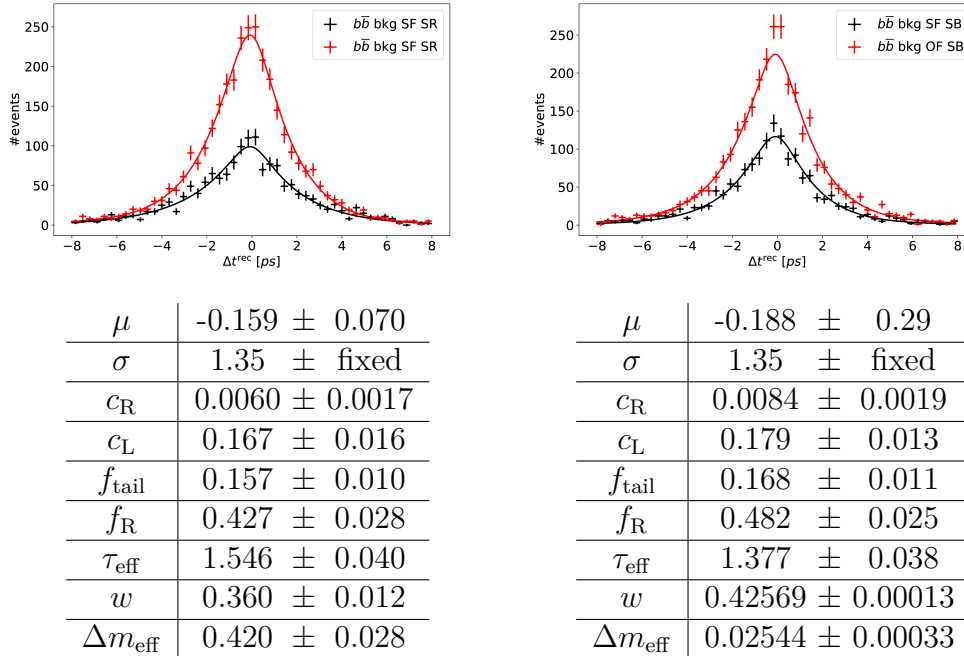
Figure 8.14: The fit of Δt_{rec} residuals for $B^0 \to D^- \pi^+$ $b\bar{b}$ background simulation sample for SF (**black**) and OF (red): The fit function is shown with the solid line on top of the data points shown with error bars in signal (top left) and sideband (top right) regions. Obtained shape parameters are shown at the bottom.

8.6.7 Combined fit strategy

In order to extract the physical parameters, all samples are simultaneously fitted by an extended maximum likelihood fit. The final fit is a two dimensional m_{bc}; Δt_{rec} fit in the m_{bc} signal region and one dimensional fit in the m_{bc} sideband. For the purpose of minimisation, a final function $\mathcal{H}_{\mathrm{tot}}$ can be defined:

$$\mathcal{H}_{\mathrm{tot}} = \sum_{\mathrm{c}} -2 \left[H_{\mathrm{c}} + \log\left(N_{\mathrm{sig}}^{\mathrm{c}} + N_{\mathrm{bkg}}^{\mathrm{c}} \right) \right] \qquad (8.21)$$

where $N_{\mathrm{sig}}^{\mathrm{c}}$ and $N_{\mathrm{bkg}}^{\mathrm{c}}$ are signal and background yields for the channel c (c runs over $B^0 \to J/\psi K_{\mathrm{S}}^0$ + and -, and $B^0 \to D^- \pi^+$ SF and OF). The function H_{c} is a log likelihood that takes the data events i characterized by their coordinates $\Delta t_{\mathrm{rec}}^{\mathrm{i}}$; m_{bc} as an input

$$
\begin{aligned}
H_{\mathrm{c}} = \sum_{\mathrm{i} \in \mathrm{c, SR}} \log &\left[N_{\mathrm{sig}}^{\mathrm{c}} \cdot f_{\mathrm{sig}}^{\mathrm{SR}} \cdot \mathcal{G}(\Delta t_{\mathrm{rec}}^{\mathrm{i}}; w(S_{\mathrm{f}}), s_{\Delta t}, \Delta_{\Delta t}) \cdot h_{\mathrm{sig}}^{\mathrm{c}}(m_{\mathrm{bc}}^{\mathrm{i}}; s_{m_{\mathrm{bc}}}, \Delta_{m_{\mathrm{bc}}}) \right. \\
&\left. + N_{\mathrm{bkg}}^{\mathrm{c}} \cdot f_{\mathrm{bkg}}^{\mathrm{SR}} \cdot \mathcal{G}(\Delta t_{\mathrm{rec}}^{\mathrm{i}}; w(S_{\mathrm{f}}), s_{\Delta t}, \Delta_{\Delta t}) \cdot h_{\mathrm{bkg}}^{\mathrm{c}}(m_{\mathrm{bc}}^{\mathrm{i}}; s_{m_{\mathrm{bc}}}, \Delta_{m_{\mathrm{bc}}}) \right] \\
\sum_{\mathrm{i} \in \mathrm{c, SB}} \log &\left[N_{\mathrm{sig}}^{\mathrm{c}} \cdot (1 - f_{\mathrm{sig}}^{\mathrm{SR}}) \cdot h_{\mathrm{sig}}^{\mathrm{c}}(m_{\mathrm{bc}}^{\mathrm{i}}; s_{m_{\mathrm{bc}}}, \Delta_{m_{\mathrm{bc}}}) \right. \\
&\left. + N_{\mathrm{bkg}}^{\mathrm{c}} \cdot (1 - f_{\mathrm{bkg}}^{\mathrm{SR}}) \cdot h_{\mathrm{bkg}}^{\mathrm{c}}(m_{\mathrm{bc}}^{\mathrm{i}}; s_{m_{\mathrm{bc}}}, \Delta_{m_{\mathrm{bc}}}) \right]
\end{aligned}
$$
$$(8.22)$$

where

- the superscript SR and SB indicates a quality relative to the signal and sideband, respectively, regions;

- $\mathcal{G}_{\mathrm{sig}}^{c}$ and $\mathcal{G}_{\mathrm{bkg}}^{c}$ are the signal and background, respectively, Δt_{rec} shapes for channel c;

- h_{sig} and h_{bkg} denote the signal and background m_{bc} shapes, respectively;

- f_{sig}^{SR} and $f_{\mathrm{bkg}}^{\mathrm{SR}}$ are the fraction of signal and background, respectively, events forming to the signal region. Values of these parameters are not free, but they are computed from the integral of h_{sig} or h_{bkg} over the adequate m_{bc} range.

8.7 Checks of the fit using simulated events

In this section the developed fitting procedure is tested using simulated samples. The tests are done using signal simulated samples, simulated sample corresponding to a luminosity of 500 fb^{-1}, stability fits and lifetime fit.

8.7.1 Checks of the Δt_{rec} fit using simulated signal events

Firstly, the Δt_{rec} distributions for $B^0 \to J/\psi K_{\mathrm{S}}^0$ and $B^0 \to D^- \pi^+$ are fitted separately using the large signal simulated samples. The fitted functions are derived as a convolution of physics distribution with the resolution function introduced in

the previous section for each channel. The results of the fit with determined values of the parameters are shown in Figure 8.15 for $B^0 \to D^- \pi^+$ and in Figure 8.16 for $B^0 \to J/\psi K_S^0$. The fitted values can be compared with their MC-truth values:

$$S_{\mathrm{f}}^{\mathrm{truth}} = 0.695; \quad w_{J/\psi K_S^0}^{\mathrm{truth}} = 19.22\%; \quad w_{D^- \pi^+}^{\mathrm{truth}} = 20.12\%. \tag{8.23}$$

In the fit of the Δt_{rec} distribution of $B^0 \to J/\psi K_S^0$ mode, the wrong tag fraction w parameter is fixed to the MC-truth value. When comparing the determined and the generated values of the S_{f}, one can see both values correspond very well. In $B^0 \to D^- \pi^+$ mode, the estimated wrong tag fraction w is larger by 3 %. Systematic uncertainty from kinematic approximation is about 1.4 % and the expected values of $\Delta_{\Delta t_{\mathrm{rec}}}$ and $s_{\Delta t_{\mathrm{rec}}}$ are not equal to determined values. This can be caused by imperfections of the resolution function.

	Value	Error
$\Delta_{\Delta t_{\mathrm{rec}}}$	0.015	0.0082
$s_{\Delta t_{\mathrm{rec}}}$	0.9230	0.0064
w	0.2077	0.0020
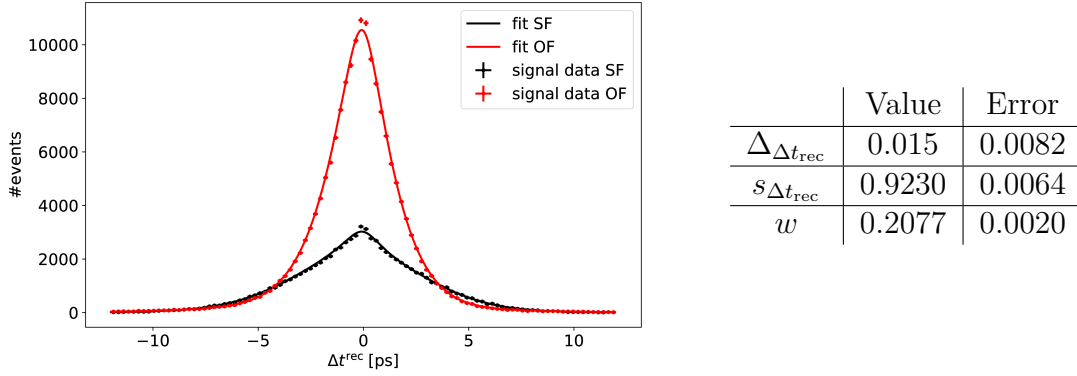
Figure 8.15: The Δt_{rec} distribution (left) for signal $B^0 \to D^- \pi^+$ SF (**black**) and OF (red) simulated events: The fit function is shown with the solid line on top of the data points shown with error bars. Obtained shape parameters are shown on the right.

$\Delta_{\Delta t_{\mathrm{rec}}}$	0.0139 ± 0.0083
$s_{\Delta t_{\mathrm{rec}}}$	0.9581 ± 0.0069
S_{f}	0.6941 ± 0.0060

$\Delta_{\Delta t_{\mathrm{rec}}}$	0.0123 ± 0.0112
$s_{\Delta t_{\mathrm{rec}}}$	0.9531 ± 0.0092
S_{f}	0.6951 ± 0.0080
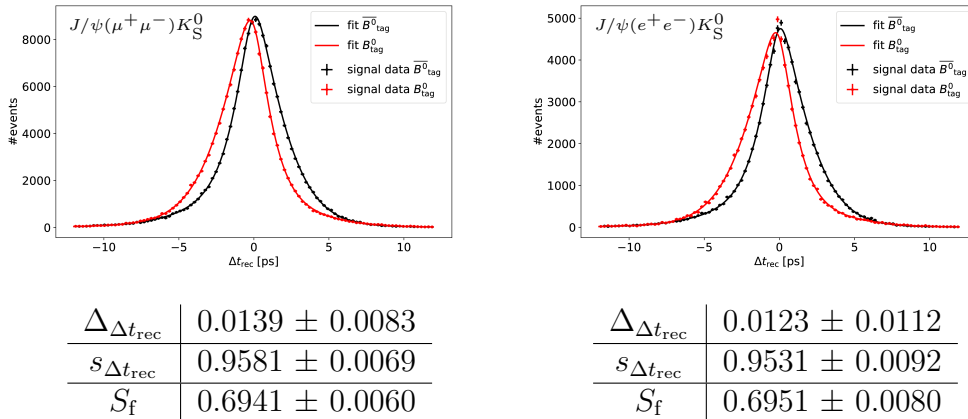
Figure 8.16: The Δt_{rec} distribution for signal $B^0 \to J/\psi(\mu^+ \mu^-) K_S^0$ (top left) and $B^0 \to J/\psi(e^+ e^-) K_S^0$ (top right) $\overline{B}_{\mathrm{tag}}^0$ (**black**) and B_{tag}^0 (red) simulated events: The fit function is shown with the solid line on top of the data points shown with error bars. Obtained shape parameters are shown in the bottom row.

8.7.2 Checks of the $m_{\rm bc}$; $\Delta t_{\rm rec}$ fit using simulated sample

The simultaneous combined fit is tested using simulated sample corresponding to a luminosity of 500 fb^{-1} (Figure 8.17). Also, the fitted function is described as a convolution of physics distribution with resolution function. The determined values of the parameters and their errors from the minimisation are shown in Table 8.12. The physics parameter $S_{\rm f}$ differs from its generated value about 1.0 standard deviation, which can be caused by the difference between the wrong tag fractions in the $B^0 \to D^-\pi^+$ and $B^0 \to J/\psi K_{\rm S}^0$ modes.

$N_{\rm sig}^+\{J/\psi(\mu^+\mu^-)K_{\rm S}^0\}$	1408 ± 39
$N_{\rm sig}^-\{J/\psi(\mu^+\mu^-)K_{\rm S}^0\}$	1355 ± 38
$N_{\rm bkg}^+\{J/\psi(\mu^+\mu^-)K_{\rm S}^0\}$	461 ± 24
$N_{\rm bkg}^-\{J/\psi(\mu^+\mu^-)K_{\rm S}^0\}$	452 ± 23
$N_{\rm sig}^+\{J/\psi(e^+e^-)K_{\rm S}^0\}$	845 ± 31
$N_{\rm sig}^-\{J/\psi(e^+e^-)K_{\rm S}^0\}$	800 ± 30
$N_{\rm bkg}^+\{J/\psi(e^+e^-)K_{\rm S}^0\}$	641 ± 28
$N_{\rm bkg}^-\{J/\psi(e^+e^-)K_{\rm S}^0\}$	576 ± 26

$N_{\rm sig}^{\rm SF}\{D^-\pi^+\}$	10560 ± 120
$N_{\rm sig}^{\rm OF}\{D^-\pi^+\}$	22380 ± 170
$N_{\rm bkg}^{\rm SF}\{D^-\pi^+\}$	20340 ± 150
$N_{\rm bkg}^{\rm OF}\{D^-\pi^+\}$	36700 ± 210
w	0.2078 ± 0.0062
$S_{\rm f}$	0.749 ± 0.055
$\Delta_{\Delta t_{\rm rec}}$	0.009 ± 0.017
$s_{\Delta t_{\rm rec}}$	0.975 ± 0.015
$\Delta_{m_{\rm bc}}$ [GeV]	-0.005 ± 0.013

Table 8.12: Combined fit results using simulation sample corresponding with 500 fb^{-1}

8.7.3 Stability of the fit: studies with pseudo-experiments

The developed fit method needs to be validated and the precision of the physics parameters needs to be approximated. For such a purpose, a set of pseudo-experiments is used as an additional sample for testing the fit. Instead of generating pseudo-experiments in close proximity of the pdf shapes to check the bias introduced by the effect of the kinematic approximation and imperfections in the fit, they are generated by bootstrapping the large statistics simulation samples. By Poisson-oscillating the expected yields in 30 fb^{-1} of the Belle II data, the number of the events in each pseudo-dataset is achieved.

Toy studies with $B^0 \to J/\psi K_{\rm S}^0$, $B^0 \to D^-\pi^+$ simultaneous fit

To test the complete complex $m_{\rm bc}$; $\Delta t_{\rm rec}$ model for fitting the real data, a set of 1000 pseudo-datasets formed by $B^0 \to J/\psi K_{\rm S}^0$ and $B^0 \to D^-\pi^+$ events was generated. Observed pull distributions for physics parameters $S_{\rm f}$ and w are found in Figure 8.18. In addition, the distributions were fitted by a Gaussian function. For physics parameter $S_{\rm f}$, no serious bias was observed, however, the statistical uncertainty of the physics parameter w is affect up to ~ 10 %. The source of this bias is kinematic approximation. The statistical significance of the observation of time-dependent CP violation $S_{\rm f}/{\rm err}(S_{\rm f})$ is determined for all these pseudo-datasets and the distribution of significance can be found in Figure 8.19 with an average of ~ 3.1 standard deviations.
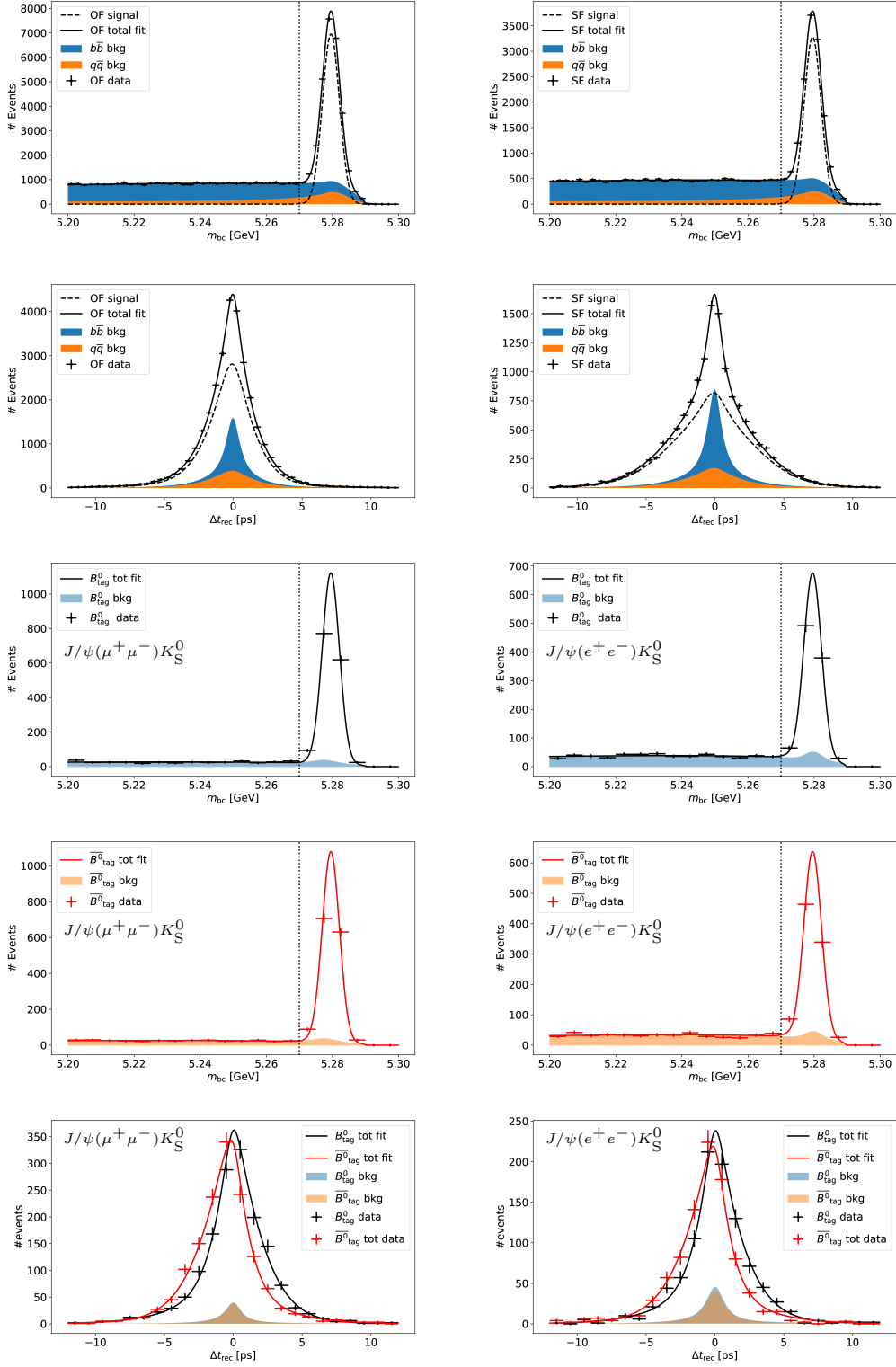
Figure 8.17: Combined fit of S_{f} and w using simulation sample corresponding to 500 fb^{-1}: The two lines represent m_{bc} (first line) and Δt_{rec} distribution (second line) fits for SF (left) and OF (right) of $B^0 \to D^- \pi^+$. Next three lines represent m_{bc} fits for $\overline{B}^0_{\mathrm{tag}}$ (third line), B^0_{tag} (fourth line) and Δt_{rec} (fifth line) fits of $B^0 \to J/\psi(\mu\mu)K^0_{\mathrm{S}}$ (left) and $B^0 \to J/\psi(ee)K^0_{\mathrm{S}}$ (right) channels.

128
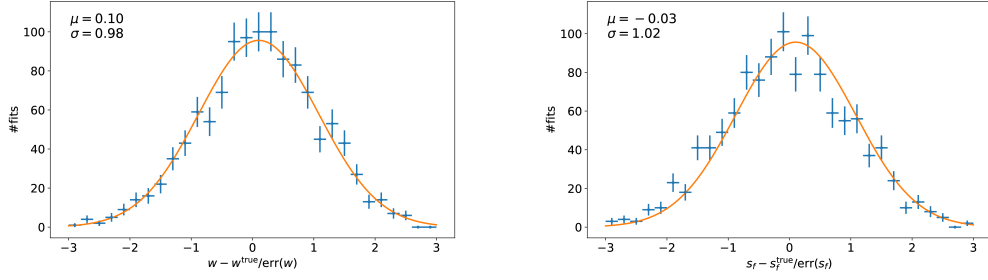
Figure 8.18: Pull distribution of the parameters w (left) and S_{f} (right) fit for 1000 complete fits of the $m_{\mathrm{bc}}; \Delta t_{\mathrm{rec}}$ distributions in 1000 pseudo-datasets corresponding to 30 fb^{-1} of $B^0 \to D^-\pi^+$ and $B^0 \to J/\psi K_{\mathrm{S}}^0$ data. The pull distributions are fitted with a Gaussian curve (orange).
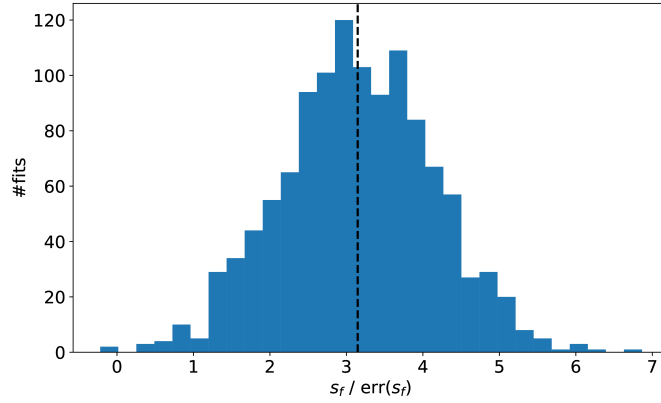
Figure 8.19: Expected statistical significance of observations of TDCPV computed for 1000 pseudo-data sets. The back doted line indicates the mean of the distribution.

Toy studies with $B^0 \to D^-\pi^+$ mixing fit

To test the ability to determine Δm_{d}, similar toy studies were done using $B^0 \to D^-\pi^+$ events only (Figure 8.20). In this case, the physics parameter Δm_{d} is free-floating, however no difference was observed in the pull on the w physics parameter in comparison with the case when the Δm_{d} parameter was fixed. Otherwise, a large shift of the physics parameter Δm_{d} corresponding to ~ 25 % of its statistical uncertainty was observed. Due to the kinematic approximation, an average value of the fit is $\Delta m_{\mathrm{d}} \approx 0.514~ps^{-1}$ affected by 1.5 % bias from the generated value $\Delta m_{\mathrm{d}}^{\mathrm{gen}} = 0.5065~ps^{-1}$. Another toy studies leaving physics parameters $\tau, \Delta m_{\mathrm{d}}, w$ free to float results in an unstable fit with multiple minima.

8.7.4 Lifetime fit

The last check performed on simulated samples was determination of the lifetime τ of neutral B meson using $B^0 \to D^-\pi^+$ events. The signal shape is described by an exponential $e^{-|\Delta t|/\tau}$ convoluted with the resolution function. The scale and shift parameters are free-floating to absorb possible discrepancies between
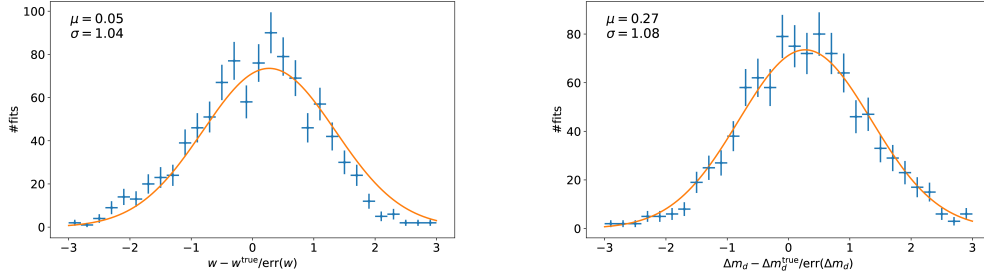
Figure 8.20: Pull distribution of fit parameters w (left) and Δm_{d} (right) for 1000 complete fits to the $m_{\mathrm{bc}};\Delta t_{\mathrm{rec}}$ distributions in 1000 pseudo-datasets corresponding to 30 fb^{-1} of $B^0 \to D^-\pi^+$ and $B^0 \to J/\psi K_S^0$ data. The pull distributions are fitted with a Gaussian curve (orange).
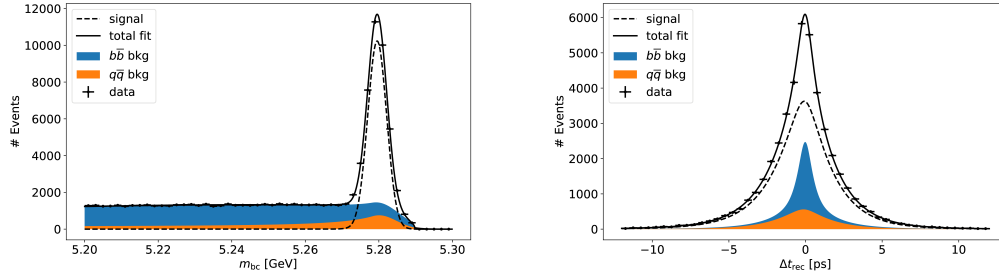
signal	32840	$\pm$	210
background	24550	$\pm$	190
$\Delta_{\Delta t}$	0.006	$\pm$	0.011
$s_{\Delta t}$	1.040	$\pm$	0.078
$\Delta_{m_{\mathrm{bc}}}$	$-1.2 \cdot 10^{-5}$	$\pm$	$1.7 \cdot 10^{-5}$
τ	1.511	$\pm$	0.036

Figure 8.21: Combined fit of m_{bc} (top left);Δt_{rec} (top right) of lifetime using 500 fb^{-1} simulation sample with corresponding free fit parameters (bottom table).

the simulation and the real data. The background is described by a zero lifetime shape for the continuum component and another shape with non-zero effective lifetime for the $b\bar{b}$ component. The fraction of the $b\bar{b}$ events is fixed from the simulation. To check the fit procedure, the fit is performed using 500 fb^{-1} inclusive simulation sample, and the result is shown in Figure 8.21.

8.8 Cross-checks using the data

In this section, the developed fitting procedure is additionally tested on the real data samples. Fit of the Δt_{rec} distribution in sideband, fit of the m_{bc} shape, lifetime fit, comparison between data and Monte Carlo simulation are explained.

8.8.1 Fit to the Δt_{rec} distribution in sideband

To check the compatibility of the developed fitting model on the real data, the Δt_{rec} distribution of the $B^0 \to D^- \pi^+$ candidates in the m_{bc} sideband is used. Performed fit can be found in Figure 8.22 and determined values and errors of the fit parameters can be found in a table below the fit. According to the results, the $s_{\Delta t}$ parameter can be neglected for simulated and real data samples, however the $\Delta_{\Delta t}$ parameter is inevitable.

N^{SF}	1104 ± 33
N^{OF}	2095 ± 46
$\Delta_{\Delta t}$	0.085 ± 0.040
$s_{\Delta t}$	1.025 ± 0.032
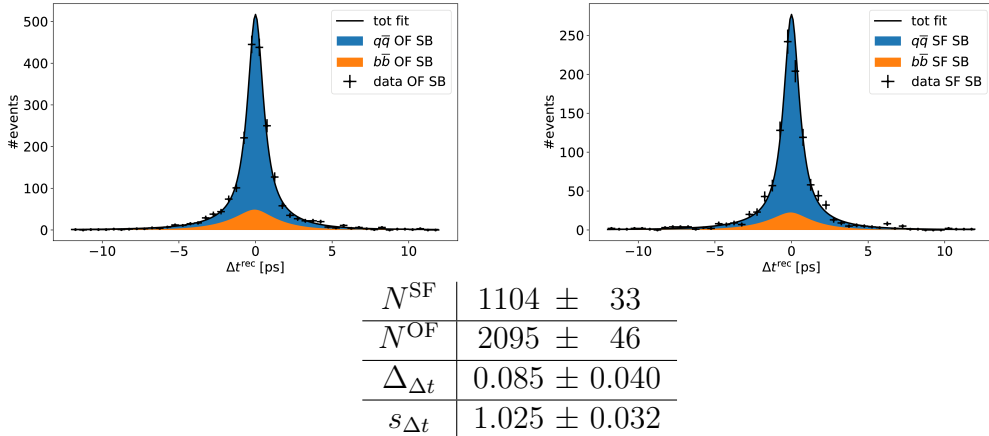
Figure 8.22: Fit of Δt_{rec} distribution for SF and OF using sideband data (black dots) in top pictures with corresponding free fit parameters (bottom table).

8.8.2 Data and Monte Carlo comparison

Data and Monte Carlo comparison of distributions of several variables can be found in Figures 8.23 for $B^0 \to J/\psi(\mu^+\mu^-)K_S^0$ and 8.24 for $B^0 \to J/\psi(e^+e^-)K_S^0$ and 8.25 for $B^0 \to \pi^+ D^-$. Following variables are: checked in the comparison

- difference between the vertex coordinates of the reconstructed B meson ($\{x,y,z\}^{\mathrm{reco}}$) and tagged B meson ($\{x,y,z\}^{\mathrm{tag}}$) or the interaction point ($\{x,y,z\}^{\mathrm{IP}}$),

- errors of the vertex coordinates of reconstructed and tagged B mesons ($\delta\{x,y,z\}^{\mathrm{reco,tag}}$),

- error of the Δt_{reco} distribution,

- masses of $J/\psi, D^-$ particles

- number of fitted tracks associated with the tagged B meson, quality of vertexing tagged side (χ^2_{tag}) and probability of correct identification of flavour of tagged B meson (FBDT qrCombined).

With the statistical precision available, the data and Monte Carlo comparison shows perfect agreement. In particular, the Δt_{err} data and simulated distributions agree well, which justifies that no conditional PDF is used for the reconstructed signal B vertex and the beam spot. This is expected as the beam spot size is not

properly described in the minimum. This justifies the decision not to use any constraint based on the beam spot is used to fit the signal or tag vertex in the analysis.
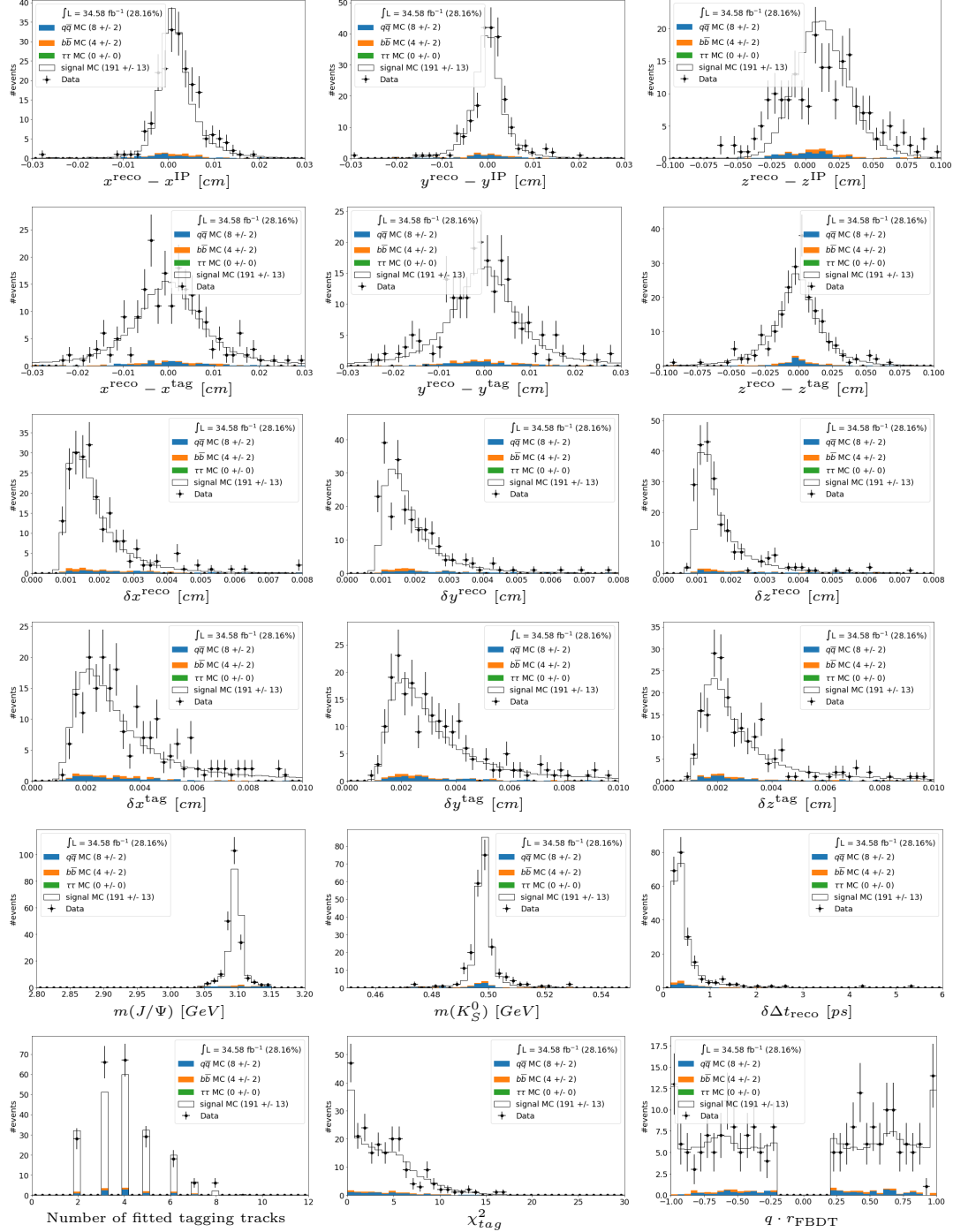
Figure 8.23: Monte Carlo and data distributions for masses, vertexing variables of reconstructed or tagged sides and flavour tagger variables using channel $B^0 \rightarrow J/\psi(\mu^+\mu^-)K_S^0$
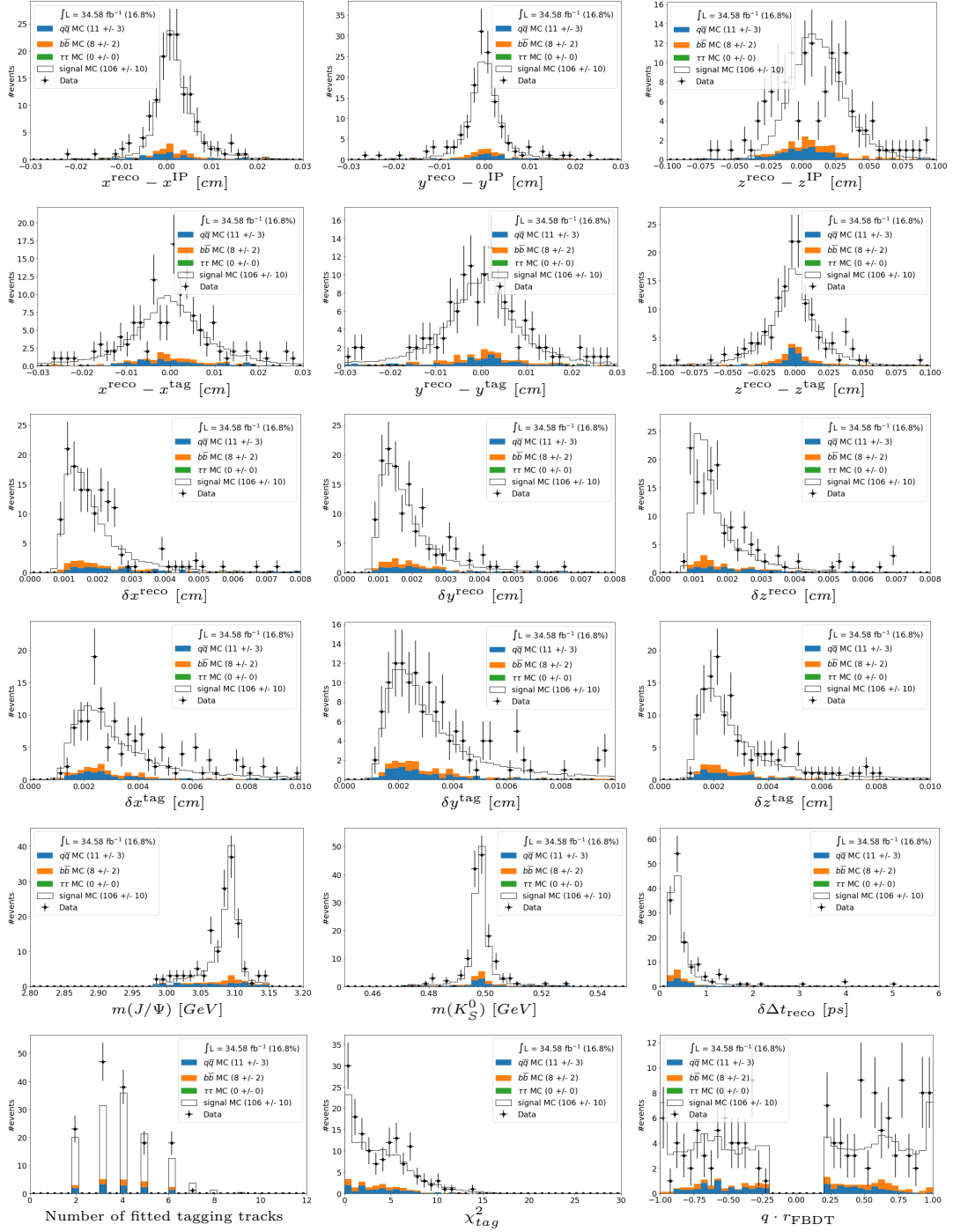
Figure 8.24: Monte Carlo and data distributions for masses, vertexing variables of reconstructed or tagged sides and flavour tagger variables using channel $B^0 \rightarrow J/\psi(e^+e^-)K_S^0$

8.8.3 Fit to the m_{bc} shape in real data

The fits of the m_{bc} for studied simulated physics modes are defined in previous sections and the same fits are applied to the real data as the next check. All shape parameters of the fits are fixed, yield parameters of the the fits are free-floating and additional $\Delta_{m_{\mathrm{bc}}}$ and $s_{m_{\mathrm{bc}}}$ parameters are applied to compensate the energy shift and differences of the detector resolution between data and Monte Carlo

133
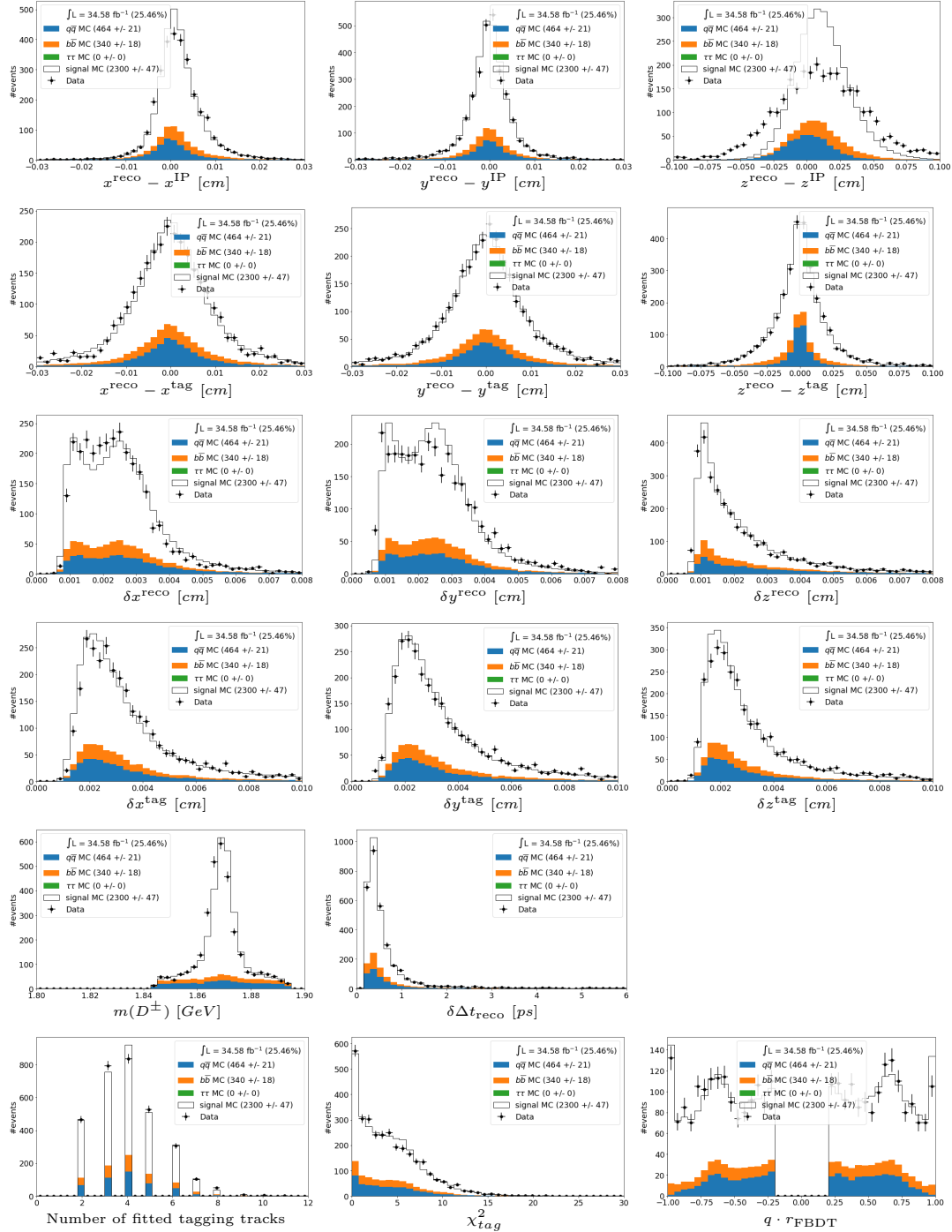
Figure 8.25: Monte Carlo and data distributions for masses, vertexing variables of reconstructed or tagged sides and flavour tagger variables using channel $B^0 \to \pi^+ D^-$

simulation. The fits, their results and expectations from scaling Monte Carlo events to the data luminosity can be found in Figures 8.26, 8.27 and 8.28.

8.8.4 Lifetime fit

As the last check, the combined fit of m_{bc}; Δt_{rec} for B^0 lifetime using $B^0 \to \pi^+ D^-$ channels was done. The fit result can be found in Fiureg 8.29 and the fitted
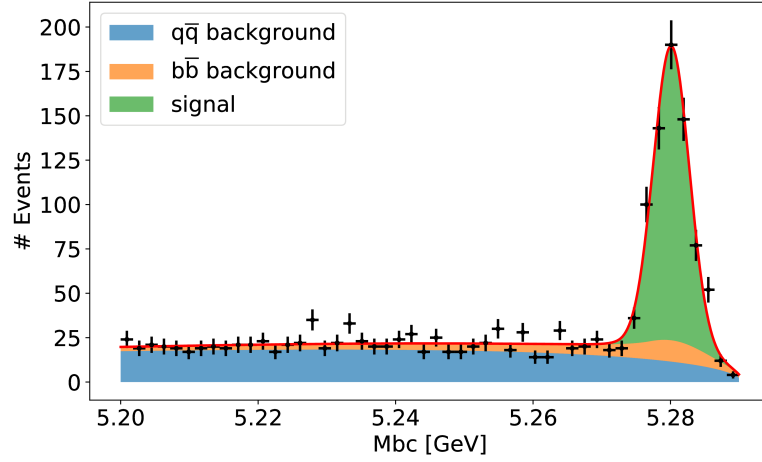
	Fitted		Expected
Signal	2271 $\pm$	56	2289
Background	4101 $\pm$	71	3936
$\Delta_{m_{\mathrm{bc}}}$ [GeV]	$2 \cdot 10^{-6} \pm 60 \cdot 10^{-6}$		
$s_{m_{\mathrm{bc}}}$	0.995 $\pm$	0.022	

Figure 8.26: Fit of m_{bc} distribution for $B^0 \to D^- \pi^+$ candidates from data (black dots) in top picture with corresponding free fit parameters (bottom table).
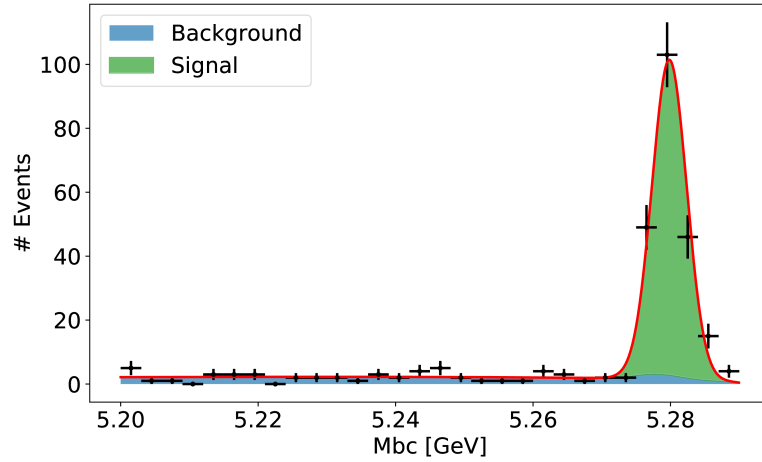
	Fitted		Expected
Signal	207 $\pm$	15	193
Background	64.0 $\pm$	8.9	63.1
$\Delta_{m_{\mathrm{bc}}}$ [MeV]	0.31 $\pm$ 0.18		
$s_{m_{\mathrm{bc}}}$	0.973 $\pm$ 0.059		

Figure 8.27: Fit of m_{bc} distribution for $B^0 \to J/\psi(\mu^+\mu^-)K_{\mathrm{S}}^0$ candidates from data (black dots) in top picture with corresponding free fit parameters (bottom table).

lifetime τ is in agreement with the world average (1.519 ± 0.007) ps [77]. For further fits the lifetime is fixed at the world average.
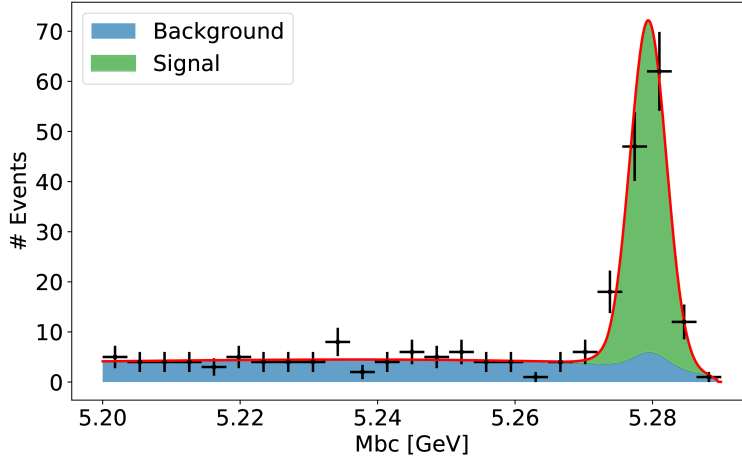
	Fitted	Expected
Signal	123 $\pm$ 12	115
Background	104 $\pm$ 11	89
$\Delta_{m_{\mathrm{bc}}}$ [MeV]	-0.19 $\pm$ 0.25	
$s_{m_{\mathrm{bc}}}$	0.991 $\pm$ 0.083	

Figure 8.28: Fit of m_{bc} distribution for $B^0 \rightarrow J/\psi(e^+e^-)K_S^0$ candidates from data (black dots) in top picture with corresponding free fit parameters (bottom table).

signal	2263	$\pm$	55
background	1643	$\pm$	50
$\Delta_{\Delta t}$	0.112	$\pm$	0.040
$s_{\Delta t}$	1.048	$\pm$	0.033
$\Delta_{m_{\mathrm{bc}}}$ [GeV]	$-0.8 \cdot 10^{-5}$	$\pm$	$6.4 \cdot 10^{-5}$
τ [ps]	1.41	$\pm$	0.16
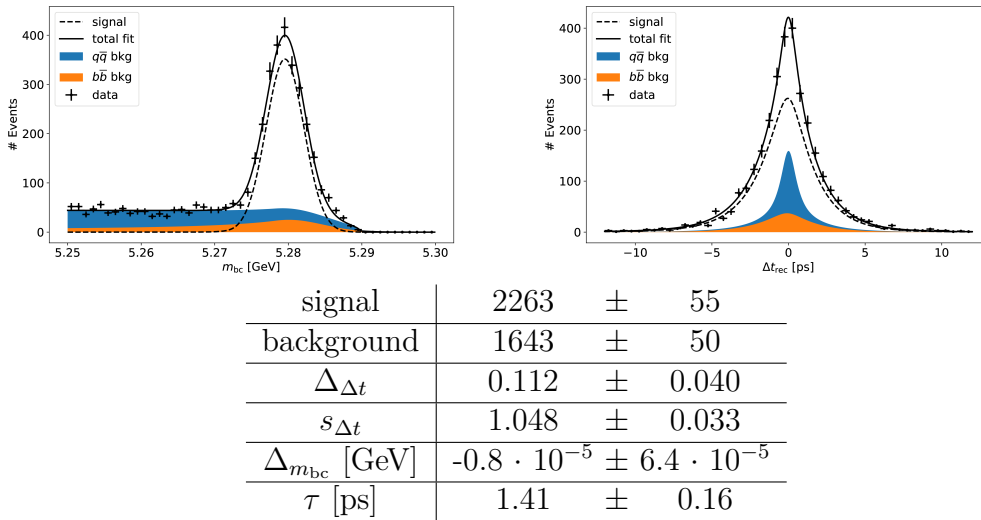
Figure 8.29: Combined fit m_{bc} (top left);Δt_{rec} (top right) for lifetime measurement using 34.6 fb^{-1} of data with corresponding free fit parameters (bottom table).

8.9 Systematic uncertainties

In this section, the systematic uncertainties of the time-dependent CP violation and mixing measurements are discussed. Firstly, several components are explained and their contributions are introduced, then final uncertainties are summed up.

8.9.1 Difference in dilution factor

The simulation shows a 3 % difference in the dilution factor $(1 - 2w)$ between the $B^0 \to D^+\pi^-$ and $B^0 \to J/\psi K_{\mathrm{S}}^0$ modes. This difference is identified with a systematic uncertainty of S_{f}.

8.9.2 Systematics from background

In the nominal fit, the background Δt shape is fixed to that obtained from the simulation. The scale factor s_{bkg} and the shift factor Δ_{bkg} are fixed and their values are set to the ones obtained from the fit of the Δt shape in the m_{bc} sideband. The parameters S_{f} and Δm_{d} are re-extracted by scaling and shifting the background shape in the signal region by alternating the $s_{\mathrm{bkg}}, \Delta_{\mathrm{bkg}}$ and $s_{\mathrm{bkg}}^{-1}, -\Delta_{\mathrm{bkg}}$ options. The largest difference with respect to the nominal value is set as a systematic uncertainty of S_{f} and Δm_{d}.

The fit is repeated by doubling and then setting to zero the peaking background component in the $B^0 \to J/\psi K_{\mathrm{S}}^0$ background m_{bc} shape. The largest deviation of S_f from its nominal value is assigned as a systematic uncertainty.

The fit is repeated with increasing and decreasing the fraction of $b\bar{b}$ background in the $B \to D^-\pi^+$ background Δt and m_{bc} shape by 50 %. The largest difference with respect to the nominal value of S_{f} and Δm_{d} is set as a systematic uncertainty.

8.9.3 Resolution function

In the nominal fit, the resolution function's tail is not scaled by the $s_{\Delta t}$ factor. The fit is re-run while allowing the tail component to be scaled by the same factor as the core. The difference between the Δm_{d} and S_{f} values obtained from this fit with respect to the nominal one is summed up as a systematic uncertainty.

The fraction of the events in the tail of the resolution function is alternatively increased and decreased by 50 %. The difference between the Δm_{d} and S_{f} values obtained by the fit with respect to the nominal one is set as a systematic uncertainty.

8.9.4 Kinematic approximation

The systematic uncertainty coming from the kinematic approximation is determined by fitting the Δt_{MC} distribution of simulated signal events using the physical distribution characterizing the Δt_{gen} distribution. This way, the size of the bias by which the kinematic approximation would affect the physics parameters within an ideal detector resolution is calculated. This method is not perfect, because the kinematic approximation bias can be absorbed by the resolution function parameters. The result of the fit of the Δt_{MC} distribution using the $B^0 \to J/\psi(\mu^+\mu^-)K_{\mathrm{S}}^0$ and $B^0 \to D^-\pi^+$ modes can be found in Figure 8.30. The value determined by the fit for w is 1.4 % greater than the expected generated value. This observation explains the bias of about 10 % in the studies using pseudo-datasets. Also this corresponds to bias of 1 % on the dilution factor

$(1 - 2w).$

w	0.2040 ± 0.0016
$\Delta m_{\mathrm{d}} \ [ps^{-1}]$	0.5153 ± 0.0026
S_{f}	0.7007 ± 0.0046
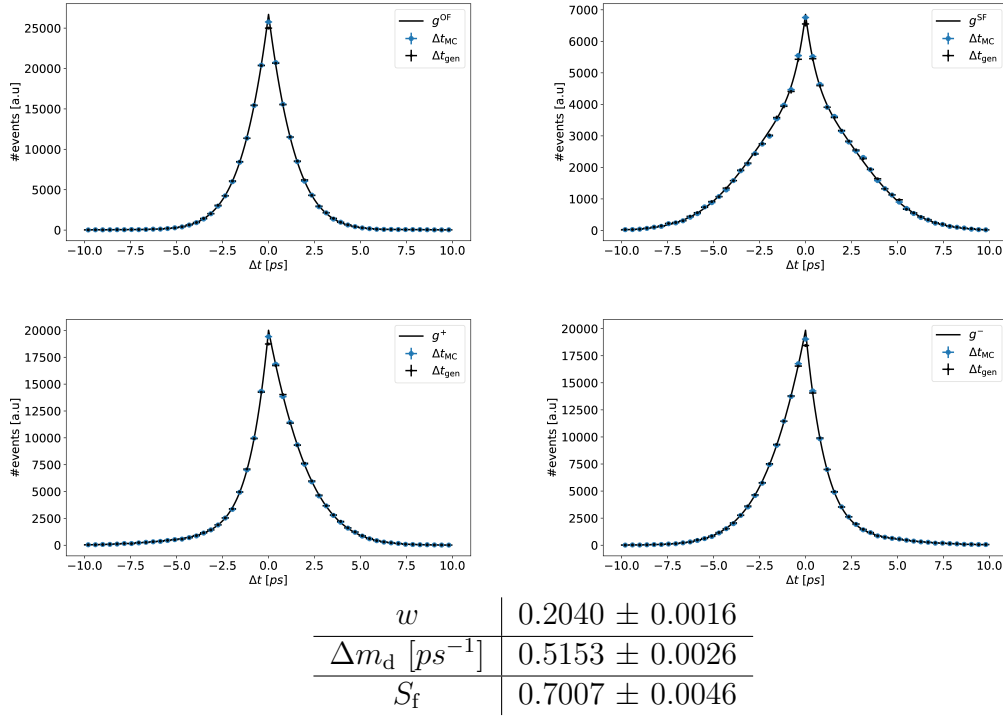
Figure 8.30: Fits of Δt_{MC} distribution for $B^0 \to D^- \pi^+$ OF (top left), SF (top right), $B^0 \to J/\psi(\mu\mu)K_{\mathrm{S}}^0$ with B^0 tag (center left) and $\overline{B}^0$ (center right) events with free floating shape parameters and their values and uncertainties found by the fits.

The bias due to the kinematic approximation for the $B^0 \to D^- \pi^+$ channel is obtained by fitting the Δt_{rec} distribution and looking at how the w and Δm_{d} deviate from their generated values. These deviations are summed up to form the systematic uncertainty on Δm_{d} and propagated to S_{f}.

The bias due to the kinematic approximation for the $B^0 \to J/\psi K_{\mathrm{S}}^0$ channels is obtained by fitting the Δt_{rec} distribution and looking at how much S_{f} deviates from its nominal value.

Observed bias in the toy studies for measurement of Δm_{d} can be related to the difference in the wrong tag fraction Δw between B^0 and $\overline{B}^0$ or the kinematic approximation. To understand this bias, a fit of the Δm_{d} using control channel $B^0 \to D^- \pi^+$ which takes into account Δw is carried out. Therefore, it is a simultaneous fit of four samples, one sample for each flavour of the B_{sig}^0 and B_{tag}^0. The Δt_{gen} and Δt_{MC} distributions are fitted to factorise out the detector effects and focus on the impact of Δw and the kinematic approximation. The results of this fit with different configurations are shown in Table 8.13. It can be seen that neglecting the wrong tag fraction has no impact on Δm_{d}. However, the impact of the kinematic approximation is 2.2 %. The kinematic approximation also induces a 2.6 % impact on w, 1.3 % if Δm_{d} is fixed in the fit.

	Δm_{d} [ps^{-1}]	w [%]	Δw [%]
MC truth	0.5067	20.12	-0.70
fit to Δt_{gen} (Δw free)	0.5078 ± 0.0026	20.04 ± 0.16	-0.28 ± 0.47
fit to Δt_{gen} (Δw fixed)	0.5078 ± 0.0026	20.04 ± 0.16	0.00
fit to Δt_{MC} (Δw fixed)	0.5078 ± 0.0026	20.57 ± 0.16	0.00
fit to Δt_{MC} (Δw, Δm_{d} fixed)	0.5067	20.30 ± 0.14	0.00

Table 8.13: Investigation of bias in the toy studies for measurement Δm_{d}

It is checked explicitly with toys that the bias on Δm_{d} is significantly reduced when correcting the true value of Δm_{d} for kinematic approximation. The pull distribution for Δm_{d} is shown in Figure 8.31. The remaining bias of 8 % of the statistical uncertainty can be attributed to remaining bias due to the fit shape itself.
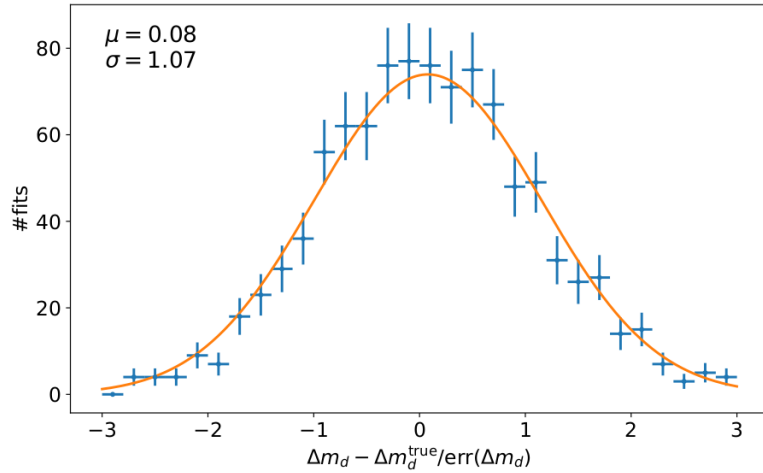
Figure 8.31: Pull distribution of fit Δm_{d} parameter for 1000 complete fits of the m_{bc};Δt_{rec} distributions in 1000 pseudo-datasets corresponding to 30 fb^{-1} of $B^0 \rightarrow D^- \pi^+$ and $B^0 \rightarrow J/\psi K_{\mathrm{S}}^0$ data. The pull distributions are fitted with a Gaussian curve (orange).

8.9.5 VXD alignment

To estimate the systematic uncertainty related to the VXD misalignment, 100 000 events are simulated per each studied mode using the relevant software version. The tracking and reconstruction of these simulated events is performed twice, once using nominal VXD geometry and once using the misalignment estimated by the alignment group. The misalignment was generated to reflect the fluctuation of alignment parameters over the course of two days.

The signal resolution function is extracted using the sample with the nominal alignment. This resolution function is then used to perform the fit to extract S_{f} on both samples with nominal and misaligned geometry. The values found for S_f are shown in Table 8.14. The values of S_{f} for both geometries are statistically

compatible with each other, and compatible with the value found by fitting the centrally produced $B^0 \to J/\psi K_S^0$ simulation sample (Figure 8.16). The 2.6 % difference in S_f between the nominal and misaligned geometry is summed up and forms a systematic uncertainty.

		Nominal	Misalignment	$\delta_{\text{syst}}^{\text{VXD}}$
$B^0 \to J/\psi \; (\mu^+\mu^-) + K_S^0 \; (\pi^+\pi^-)$	S_f	0.687 ± 0.019	0.702 ± 0.019	0.016
$B^0 \to J/\psi \; (e^+e^-) + K_S^0 \; (\pi^+\pi^-)$	S_f	0.672 ± 0.025	0.642 ± 0.024	0.031
$B^0 \to \pi^\pm + D^\mp (K^\pm \pi^\mp \pi^\mp)$	w	0.200 ± 0.006	0.204 ± 0.006	0.004

Table 8.14: Results of the misalignment studies for each channel

8.9.6   Final systematic uncertainty

The statistical uncertainty and the background fraction and the wrong tag fraction are propagated to the S_f and Δm_d automatically by the fit. The systematic uncertainty related to the difference in wrong tag fraction Δw for these channels was shown to be negligible. All other systematic uncertainties are shown in Table 8.15. The combined systematic uncertainty is obtained by summing each source squared.

Source	$\delta \; \Delta m_d$ [%]	$\delta \; S_f$ [%]
Difference in dilution factor		+ 2.9
Background scales	- 0.2	- 0.3
Peaking background for $J/\psi K_S^0$		- 2.7
Peaking background for $D^-\pi^+$	+ 0.03	- 2.1
Tail resolution function scale	+ 1.2	+ 0.6
Tail resolution function fraction	+ 1.4	+ 0.4
Kinematic approximation w, Δm_d	+ 1.2	
Kinematic approximation S_f		- 0.9
VXD alignment	+ 0.4	+ 2.0
Total	2.3	5.1

Table 8.15: Final systematic uncertainty

8.10   Combined fit using data

For the mixing frequency measurement, two dimensional fit of the m_{bc} and Δt_{rec} distributions for $B^0 \to \pi^+ D^-$ mode in the real data sample is done. The Figure 8.32 with Table 8.16 show results of this fit.

One of the fitted parameters is the mixing frequency Δm_d, with its uncertainties it can be expressed as:

$$\Delta m_d = (0.531 \pm 0.046 \; (\text{stat.}) \pm 0.013 \; (\text{syst.})) \; \text{ps}^{-1} \qquad (8.24)$$

that agrees very well with the world average $\Delta m_d = (0.5065 \pm 0.0019) \; \text{ps}^{-1}$ [77]. Additionally, the same fitting procedure with the value of the mixing frequency
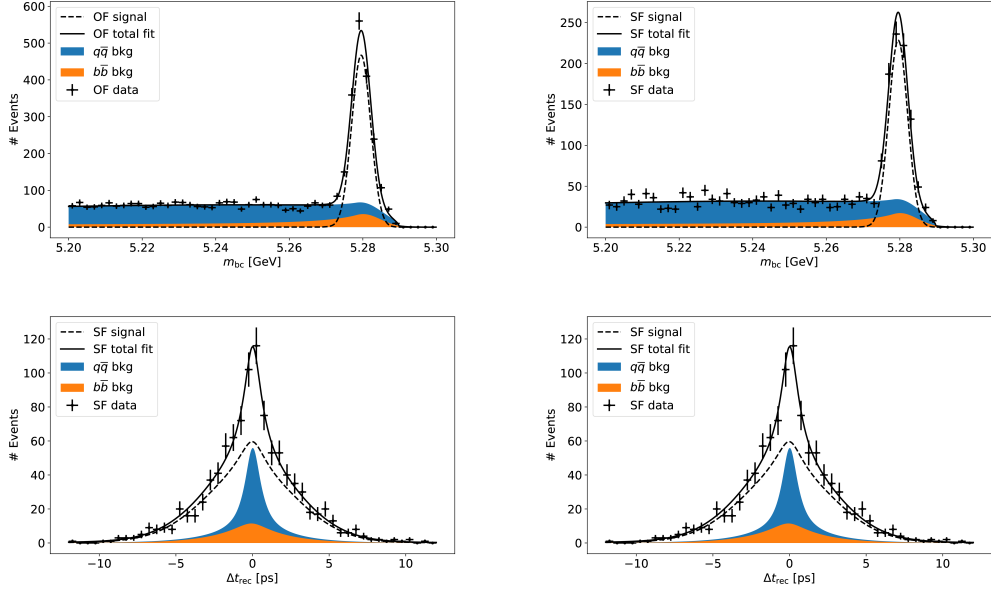
Figure 8.32: Combined fit results of the m_{bc}; Δt_{rec} fit for determination of the mixing frequency using 34.6 fb^{-1} of data: The lines represent m_{bc} (first line) and Δt_{rec} distribution (second line) fits for SF (left) and OF (right) of $B^0 \to D^- \pi^+$.

$N_{\text{sig}}^{\text{SF}}\{D^-\pi^+\}$	736 ± 31
$N_{\text{sig}}^{\text{OF}}\{D^-\pi^+\}$	1503 ± 44
$N_{\text{bkg}}^{\text{SF}}\{D^-\pi^+\}$	1365 ± 40
$N_{\text{bkg}}^{\text{OF}}\{D^-\pi^+\}$	2613 ± 55

w	0.212	$\pm$	0.023
Δm_{d} [ps^{-1}]	0.531	$\pm$	0.046
$\Delta_{\Delta t_{\text{rec}}}$	0.20	$\pm$	0.10
$s_{\Delta t_{\text{rec}}}$	0.82	$\pm$	0.10
$\Delta_{m_{\text{bc}}}$ [GeV]	$-0.3 \cdot 10^{-5}$	$\pm$	$6.4 \cdot 10^{-5}$

Table 8.16: Combined fit results for mixing using 34.6 fb^{-1} of data

fixed at the world average was performed to determine the wrong tag fraction w. The observed value of this parameter is $w = (20.9 \pm 2.2)$ %, what agrees very well with the expected generated value from simulation sample $w = 20.0$ %.

For the time-dependent CP violation measurement, the value of the mixing frequency Δm_{d} was also fixed at the world average. Two dimensional fit of the m_{bc} and Δt_{rec} distributions for $B^0 \to J/\psi K_S^0$ and $B^0 \to \pi^+ D^-$ modes in the real data is done. The Figure 8.33 with Table 8.17 show results of this fit.

One of the determined parameters is the time-dependent CP violation parameter $S_{\text{f}} \approx \sin 2\phi_1$, with its uncertainties it can be expressed as:

$$\sin 2\phi_1 = 0.55 \pm 0.21 \text{ (stat.)} \pm 0.04 \text{ (syst.)}, \tag{8.25}$$

which agrees well with the world average $S_{\text{f}} \approx 0.691 \pm 0.017$ [77]. When taking into account only the statistical uncertainty, this observed value differs from 0 by 2.71 standard deviations.

The asymmetry between the number of events with opposite flavour and same

141

$N_{\text{sig}}^{+}\{J/\psi(\mu^{+}\mu^{-})K_{\text{S}}^{0}\}$	106	$\pm$	11
$N_{\text{sig}}^{-}\{J/\psi(\mu^{+}\mu^{-})K_{\text{S}}^{0}\}$	100	$\pm$	10
$N_{\text{bkg}}^{+}\{J/\psi(\mu^{+}\mu^{-})K_{\text{S}}^{0}\}$	31	$\pm$	6
$N_{\text{bkg}}^{-}\{J/\psi(\mu^{+}\mu^{-})K_{\text{S}}^{0}\}$	29	$\pm$	6
$N_{\text{sig}}^{+}\{J/\psi(e^{+}e^{-})K_{\text{S}}^{0}\}$	72	$\pm$	9
$N_{\text{sig}}^{-}\{J/\psi(e^{+}e^{-})K_{\text{S}}^{0}\}$	50	$\pm$	8
$N_{\text{bkg}}^{+}\{J/\psi(e^{+}e^{-})K_{\text{S}}^{0}\}$	51	$\pm$	8
$N_{\text{bkg}}^{-}\{J/\psi(e^{+}e^{-})K_{\text{S}}^{0}\}$	46	$\pm$	7

$N_{\text{sig}}^{\text{SF}}\{D^{-}\pi^{+}\}$	737	$\pm$	31
$N_{\text{sig}}^{\text{OF}}\{D^{-}\pi^{+}\}$	1503	$\pm$	44
$N_{\text{bkg}}^{\text{SF}}\{D^{-}\pi^{+}\}$	1364	$\pm$	41
$N_{\text{bkg}}^{\text{OF}}\{D^{-}\pi^{+}\}$	2611	$\pm$	55
w	0.209	$\pm$	0.022
S_{f}	0.55	$\pm$	0.21
$\Delta_{\Delta t_{\text{rec}}}$	0.182	$\pm$	0.095
$s_{\Delta t_{\text{rec}}}$	0.782	$\pm$	0.086
$\Delta_{m_{\text{bc}}}$ [GeV]	$1.7\cdot10^{-5}$	$\pm$	$5.9\cdot10^{-5}$

Table 8.17: Combined fit results of $m_{\text{bc}};\Delta t_{\text{rec}}$ of CP violation using 34.6 fb^{-1} of data

flavour for $B^{0}\rightarrow\pi^{+}D^{-}$ channel or asymmetry between the number of events with B^{0} tag and $\overline{B}^{0}$ tag for $J/\psi K_{\text{S}}^{0}$ channel can be found in Appendix H.
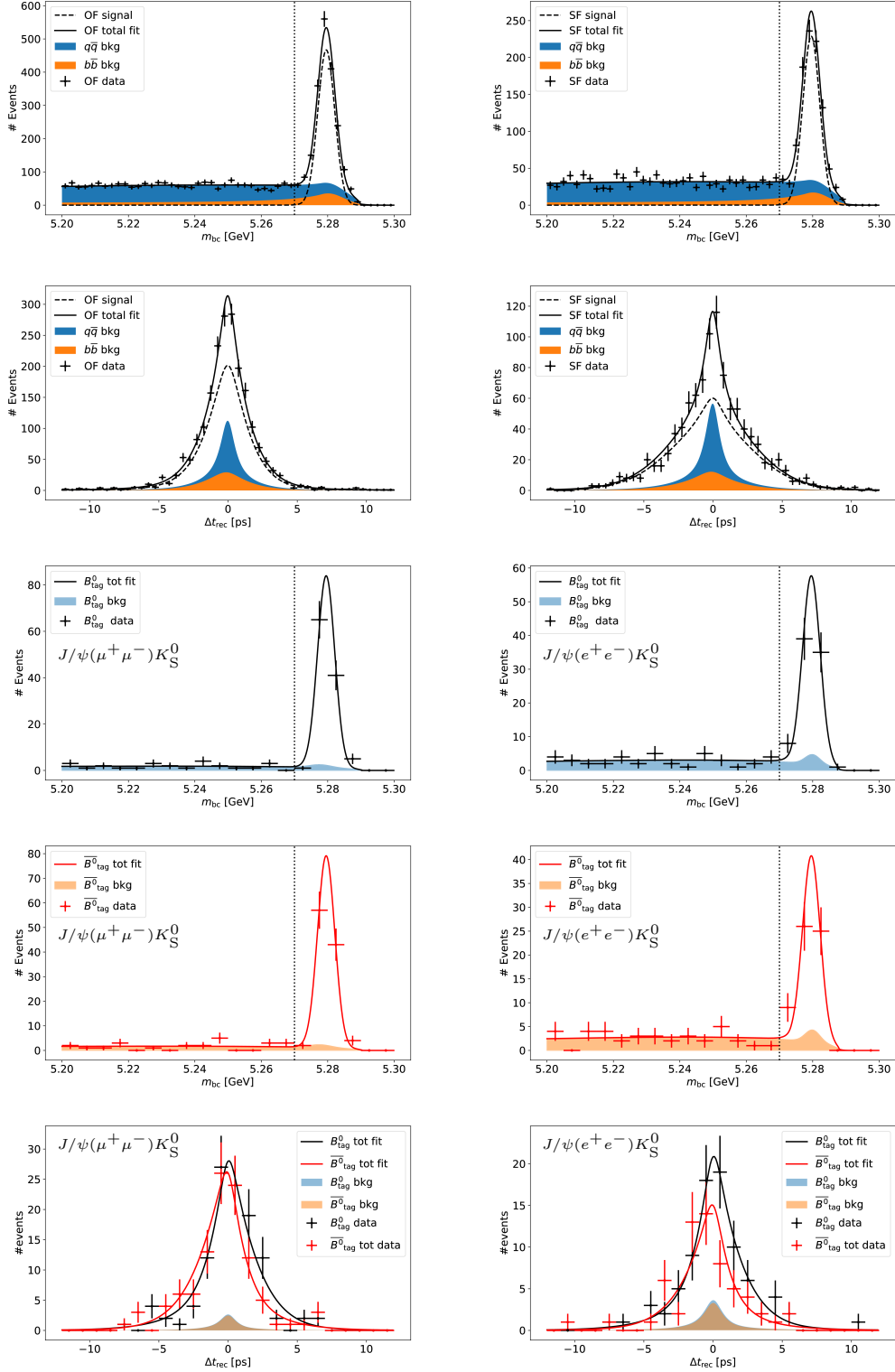
Figure 8.33: Combined fit m_{bc}; Δt_{rec} of CP violation using 34.6 fb^{-1} of data: The two lines represent m_{bc} (first line) and Δt_{rec} distribution (second line) fits for SF (left) and OF (right) of $B^0 \to D^- \pi^+$. Next three lines represent m_{bc} fits for $\overline{B}^0_{\text{tag}}$ (third line), B^0_{tag} (fourth line) and Δt_{rec} (fifth line) fits of $B^0 \to J/\psi(\mu\mu)K^0_{\text{S}}$ (left) and $B^0 \to J/\psi(ee)K^0_{\text{S}}$ (right) channels.

Summary

In this thesis, I presented

- alignment studies for the Belle II vertex detector, in particular validation procedures for identifying and monitoring silicon sensor surface deformations and χ^2 invariant modes of the vertex detector,

- first measurements of $B^0 - \overline{B}^0$ mixing, and

- time-dependent CP violation measurement using the data sample collected by the Belle II experiment.

The analysis part presents prompt $\sin 2\phi_1$ and mixing frequency $\Delta m_{\rm d}$ measurements using first 34.6 fb^{-1} data sample.

Among the alignment validation procedures developed by the author, the algorithm that estimates silicon sensor surface deformations occupies a special position. The procedure was successfully applied several times during Belle II operation. We identified quadratic, cubic and quartic (in terms of Legendre expansion) sensor surface deformations (Tab 9.1). Based on the results of this study, Belle II reconstruction and alignment procedures were expanded using the sensor surface alignment parameters. Quartic parameters were not determined using the alignment procedure since the extracted values were at the level of measurement error (the smallest error $\sim 10~\mu$m). When sensor deformations were taken into account in track reconstruction, monitoring plots showed that no residual sensor deformation left. However, the number of alignment parameters increased to 13 parameters per sensor (including shift and rotation parameters).

Level	Parameters	Scale [μm]	Monitoring	Alignment
Quadratic	P_{20}, P_{11}, P_{02}	~ 300	✅	✅
Cubic	$P_{30}, P_{21}, P_{12}, P_{03}$	~ 60	✅	✅
Quartic	$P_{40}, P_{31}, P_{22}, P_{13}, P_{04}$	~ 10	✅	

Table 9.1: The discovery of sensor surface deformations and their elimination by alignment

The monitoring tool allows to extract alignment parameters for monitoring purpose, and most of the parameters were studied as a function of time. The vertex detector alignment parameters fluctuate in the range of $\pm 10~\mu m$ about aligned values. Several change-points in parameters were identified and described during data taking periods.

The second validation procedure was focused on investigating χ^2 invariant modes of the vertex detector. Monte Carlo studies indicate that the tool is sensitive and universal in identification of weak modes. All available data samples were processed, and the results were compared with simulation. The comparison showed unexpected discrepancies. A detailed investigation identified large rectangular strip sensors as the source of the discrepancy, and the problem was a slightly

incorrect pitch size setting in their geometry model implementation. This was easy to fix. Our experience confirms that the validation tool is sensitive enough to detect even small deviations from designed geometry.

The physical analysis using the first Belle II data sample demonstrates the perfect performance of the vertex detector. The final results report an excellent agreement between measurement and the world averaged values. The statistical and systematic errors can be decreased using precise analysis tools and larger data samples in further analyses. In the coming years, we expect to increase statistics (Figure 9.1) to about a thousand times more than was studied in this thesis.
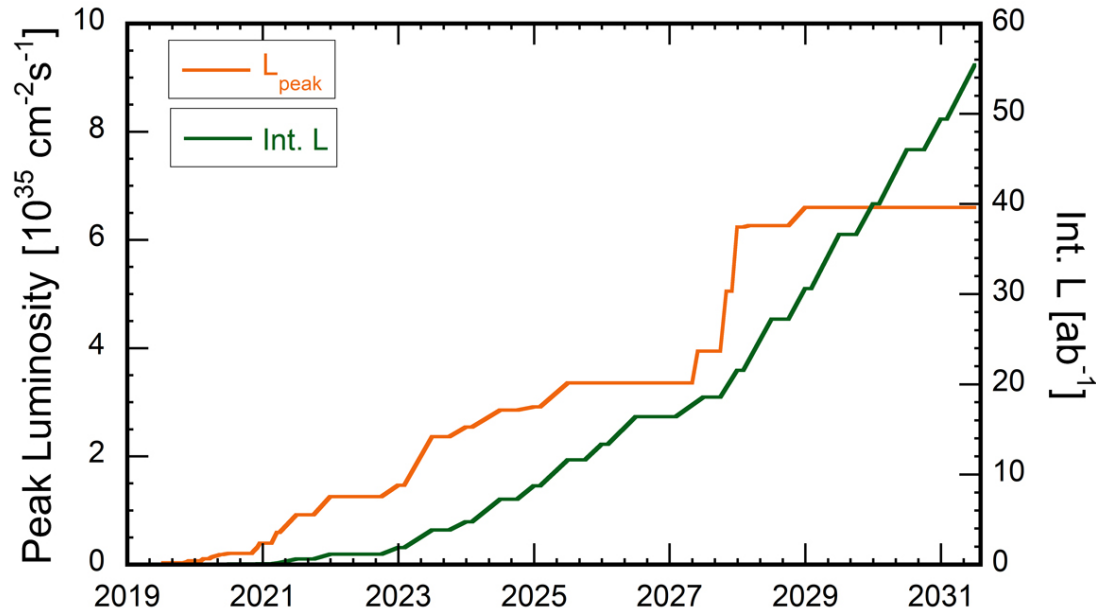
Figure 9.1: Projection of integrated (green) and peak (orange) luminosities for the SuperKEKB accelerator [78]

Physics analysis results prove the readiness and high quality of the vertex detector alignment procedure. Using limited statistics we are able to understand and eliminate all relevant issues and set optimal alignment strategy to deal with the equivalent results from other experiments. With increasing integrated luminosity and expanding physical processes in time-dependent CP violation analysis, the alignment procedure can provide more precise detector geometry and possible defects can be identified. In parallel to author's monitoring and validation procedures, additional performance and detector studies are ongoing to spot any inconsistencies so that the current alignment procedure can be further improved. A necessary step in the development of the alignment procedure is to make it more precise in time to deal with quickly changing accelerator or detector conditions. Precision of alignment can also be increased once enough data are available to include quartic surface deformation parameters.

The Belle II detector was rolled in the current position in April 2017. In the next year, the detector observed the first collisions. In December 2018, the partial

vertex detector was installed. In the next one and a half year, the SuperKEKB accelerator achieved the world's highest luminosity, and the Belle II collaboration published the first CP violation and $B^0 - \overline{B}^0$ mixing measurements with the agreement with the world averages. The Belle II detector and the SuperKEKB collider have so far held all promises to probe the Standard Model limits precisely, and they are on a good track to discover the Physics beyond the Standard Model.

Bibliography

[1] A. Buras. "CP violation in electroweak interactions". In: *Scholarpedia* 10.8 (2015). revision #151973, p. 11418. DOI: 10.4249/scholarpedia.11418.

[2] R. G. Sachs. "CP Violation in K^0 Decays". In: *Phys. Rev. Lett.* 13 (8 Aug. 1964), pp. 286–288. DOI: 10.1103/PhysRevLett.13.286.

[3] K. Abe et al. "Observation of Large CP Violation in the Neutral B Meson System". In: *Physical Review Letters* 87.9 (Aug. 2001). ISSN: 1079-7114. URL: http://dx.ysrevlett.87.091802.

[4] A. J. Bevan et al. "The Physics of the B Factories". In: *The European Physical Journal C* 74.11 (Nov. 2014). ISSN: 1434-6052. DOI: 10.1140/epjc/s10052-014-3026-9. URL: http://dx.doi.org/10.1140/epjc/s10052-014-3026-9.

[5] SuperB Collaboration et al. *SuperB Technical Design Report*. 2013. arXiv: 1306.5655 [physics.ins-det].

[6] T. Abe et al. *Belle II Technical Design Report*. 2010. arXiv: 1011.0352 [physics.ins-det].

[7] E Kou et al. "The Belle II Physics Book". In: *Progress of Theoretical and Experimental Physics* 2019.12 (Dec. 2019). ISSN: 2050-3911. DOI: 10.1093/ptep/ptz106.

[8] HIGH ENERGY ACCELERATOR RESEARCH ORGANIZATION. *A Search for New Physics - The Belle II Experiment*. Youtube. 2014. URL: https://youtu.be/nGCrrgXSEOk.

[9] Y. Ohnishi et al. "Accelerator design at SuperKEKB". In: *Progress of Theoretical and Experimental Physics* 2013.3 (Mar. 2013). 03A011. ISSN: 2050-3911. DOI: 10.1093/ptep/pts083.

[10] K. Akai et al. "SuperKEKB collider". In: *Nuclear Instruments and Methods in Physics Research Section A: Accelerators, Spectrometers, Detectors and Associated Equipment* 907 (Nov. 2018), pp. 188–199. ISSN: 0168-9002. DOI: 10.1016/j.nima.2018.08.017.

[11] K. Kanazawa. *Superkekb mechanical assembly at IR*. 2018. URL: https://indico.cern.ch/event/694811/contributions/2863863/attachments/1596200/2528272/Superkekb_mechanical_asembly_at_IR_kanazawa.pdf (visited on 04/15/2021).

[12] H.-G. Moser. "The Belle II DEPFET pixel detector". In: *Nuclear Instruments and Methods in Physics Research Section A: Accelerators, Spectrometers, Detectors and Associated Equipment* 831 (2016), pp. 85–87. ISSN: 0168-9002. DOI: https://doi.org/10.1016/j.nima.2016.02.078.

[13] Alexander Baehr et al. *DEPFET detectors for direct detection of MeV Dark Matter particles*. 2017. arXiv: 1706.08666 [physics.ins-det].

[14] I. Dourki et al. "Characterization and optimization of a thin direct electron detector for fast imaging applications". In: *JINST* 12.03 (2017), p. C03047. DOI: 10.1088/1748-0221/12/03/C03047.

[15] D. E. Pereira. "DEPFET active pixel sensors for the vertex detector of the Belle-II experiment". In: *Journal of Instrumentation* 9.03 (Mar. 2014), pp. C03004–C03004. DOI: 10.1088/1748-0221/9/03/c03004.

[16] F. Lutticke. *The Belle II pixel detector status and performance*. 2018. URL: https://indico.cern.ch/event/669866/contributions/3234980/attachments/1767984/2871445/Pixel2018_Luetticke.pdf (visited on 04/15/2021).

[17] C. Koffmane et al. *BELLE II Inner Pixel Detector*. URL: https://indico.cern.ch/event/710050/contributions/3161621/attachments/1739043/2813582/Vertex2018_BelleII_PXD_Koffmane.pdf (visited on 04/15/2021).

[18] H. Ye et al. "Commissioning and performance of the Belle II pixel detector". In: *Nuclear Instruments and Methods in Physics Research Section A: Accelerators, Spectrometers, Detectors and Associated Equipment* 987 (2021), p. 164875. ISSN: 0168-9002. DOI: https://doi.org/10.1016/j.nima.2020.164875.

[19] K. R. Nakamura et al. "The Design, Construction, Operation and Performance of the Belle II Silicon Vertex Detector". unpublished.

[20] K. R. Nakamura et al. "The Belle II SVD detector". In: *PoS* Vertex2016 (2017), p. 012. DOI: 10.22323/1.287.0012.

[21] G. Rizzo et al. "The Belle II Silicon Vertex Detector: Performance and Operational Experience in the first year of data taking". unpublished.

[22] A. Moll et al. "The vertex detector numbering scheme". unpublished.

[23] T.V. Dong et al. "Calibration and alignment of the Belle II central drift chamber". In: *Nuclear Instruments and Methods in Physics Research Section A: Accelerators, Spectrometers, Detectors and Associated Equipment* 930 (2019), pp. 132–141. ISSN: 0168-9002. DOI: https://doi.org/10.1016/j.nima.2019.03.072.

[24] U. Tamponi. *The TOP counter of Belle II: status and first results*. 2018. arXiv: 1811.04532 [hep-ex].

[25] D. Kotchetkov et al. "Front-end electronic readout system for the Belle II imaging Time-Of-Propagation detector". In: *Nuclear Instruments and Methods in Physics Research Section A: Accelerators, Spectrometers, Detectors and Associated Equipment* 941 (Oct. 2019), p. 162342. ISSN: 0168-9002. DOI: 10.1016/j.nima.2019.162342.

[26] S. Tamechika et al. "Development of alignment algorithm for Belle II Aerogel RICH counter". In: *Nuclear Instruments and Methods in Physics Research Section A: Accelerators, Spectrometers, Detectors and Associated Equipment* 952 (2020), p. 162337. ISSN: 0168-9002. DOI: https://doi.org/10.1016/j.nima.2019.162337.

[27] B. Shwartz et al. "Electromagnetic calorimeter of the Belle II detector". In: *Journal of Physics: Conference Series* 928 (Nov. 2017), p. 012021. DOI: 10.1088/1742-6596/928/1/012021.

[28] G. de Marino. "D^0 Lifetime Measurement with Belle II Early Data". MA thesis. University of Pisa, 2019.

[29]   T. Aushev et al. "A scintillator based endcap K_L^0 and muon detector for the Belle II experiment". In: *Nuclear Instruments and Methods in Physics Research Section A: Accelerators, Spectrometers, Detectors and Associated Equipment* 789 (June 2015), pp. 134–142. ISSN: 0168-9002. DOI: `10.1016/j.nima.2015.03.060`.

[30]   Ch. Li. "The data acquisition and trigger system of the Belle II experiment". In: *PoS* EPS-HEP2015 (2016), p. 258. DOI: `10.22323/1.234.0258`.

[31]   T. Kuhr et al. "The Belle II Core Software". In: *Computing and Software for Big Science* 3.1 (Nov. 2018). ISSN: 2510-2044. DOI: `10.1007/s41781-018-0017-9`.

[32]   Ch. Pulvermacher. "Analysis software and Full Event Interpretation fot the Belle II Experiment". PhD thesis. Karlsruher Instituts für Technologie, 2015.

[33]   D. Y. Kim. *Software and Physics Simulation at Belle II*. 2015. arXiv: `1510.09008 [physics.ins-det]`.

[34]   C. A. Hagmann et al. "Monte Carlo Simulation of Proton-induced Cosimc Ray Cascades in the Atmosphere". In: (Mar. 2007). DOI: `10.2172/902609`.

[35]   M. Hohlmann et al. "GEANT4 Simulation of a Cosmic Ray Muon Tomography System With Micro-Pattern Gas Detectors for the Detection of High-Z Materials". In: *IEEE Transactions on Nuclear Science* 56.3 (June 2009), pp. 1356–1363. ISSN: 0018-9499. DOI: `10.1109/tns.2009.2016197`.

[36]   E. D. Niner. "Observation of Electron Neutrino Appearance in the NuMI Beam with the NOvA Experiment". PhD thesis. Indiana U., 2015. DOI: `10.2172/1221353`.

[37]   E. A. Navarrete et al. "Cosmic Ray Interactions in Shielding Materials". In: (Sept. 2011). DOI: `10.2172/1025678`.

[39]   M. Stoye. "Calibration and Alignment of the CMS Silicon Tracking Detector". PhD thesis. 2007.

[40]   T. Bilka. "Simulation and analysis of tests of Belle II vertex detector sensors". M.S. thesis. Charles University, 2014.

[41]   V. Blobel et al. "A New Method for the High-Precision Alignment of Track Detectors". In: (Sept. 2002).

[42]   V. Karimaki et al. "Sensor alignment by tracks". In: *eConf* C0303241 (2003), TULT008. arXiv: `physics/0306034`.

[45]   C. Kleinwort. "General broken lines as advanced track fitting method". In: *Nuclear Instruments and Methods in Physics Research Section A: Accelerators, Spectrometers, Detectors and Associated Equipment* 673 (May 2012), pp. 107–110. ISSN: 0168-9002. DOI: `10.1016/j.nima.2012.01.024`.

[46]   J. Kandra. "Simulation of Belle II physics events and performance tests of reconstruction software". M.S. thesis. Charles University, 2016.

[49]   L. Kapitanova. "Cosmic ray study in the Belle II silicon detector". Bachelor thesis. Charles University, 2019.

[50] S. Blusk et al., eds. *Proceedings, first LHC Detector Alignment Workshop, CERN, Geneva, Switzerland, 4-6 September 2006*. CERN Yellow Reports: Conference Proceedings. 2007. DOI: `10.5170/CERN-2007-004`.

[51] F. Heinemann. "Robust Track Based Alignment of the ATLAS Silicon Detectors and Assessing Parton Distribution Uncertainties in Drell-Yan Processes". PhD thesis. 2007.

[52] Yoshihiro Funakoshi et al. "Beam Commissioning of SuperKEKB". In: *7th International Particle Accelerator Conference*. June 2016. DOI: `10.18429/JACoW-IPAC2016-TUOBA01`.

[53] HIGH ENERGY ACCELERATOR RESEARCH ORGANIZATION. *Timeline from KEKB to SuperKEKB*. URL: `https://www.kek.jp/en/newsroom/attic/20190311_superkekb_timeline_en.png` (visited on 04/15/2021).

[54] P.M. Lewis et al. "First measurements of beam backgrounds at SuperKEKB". In: *Nuclear Instruments and Methods in Physics Research Section A: Accelerators, Spectrometers, Detectors and Associated Equipment* 914 (2019), pp. 69–144. ISSN: 0168-9002. DOI: `https://doi.org/10.1016/j.nima.2018.05.071`.

[55] O. Yukiyoshi. *Highlights from SuperKEKB Phase 2 Commissioning*. 2019. arXiv: `1904.10236 [physics.acc-ph]`.

[56] HIGH ENERGY ACCELERATOR RESEARCH ORGANIZATION. *Luminosity History*. URL: `https://www-superkekb.kek.jp/img/SuperKEKB_MachineParameters_2020_07_01.jpg` (visited on 04/15/2021).

[57] HIGH ENERGY ACCELERATOR RESEARCH ORGANIZATION. *Luminosity History*. URL: `https://www-superkekb.kek.jp/img/Histroy_2019-2020.png` (visited on 04/15/2021).

[58] HIGH ENERGY ACCELERATOR RESEARCH ORGANIZATION. *Belle II rolls in*. URL: `https://cerncourier.com/a/belle-ii-rolls-in/` (visited on 04/15/2021).

[59] F. Abudinén et al. "Measurement of the integrated luminosity of the Phase 2 data of the Belle II experiment". In: *Chinese Physics C* 44.2 (Jan. 2020), p. 021001. ISSN: 2058-6132. DOI: `10.1088/1674-1137/44/2/021001`.

[61] The Belle II collaboration. *Belle II Luminosity*. URL: `https://confluence.desy.de/display/BI/Belle+II+Luminosity` (visited on 07/22/2020).

[65] T. Tsuboyama. *Scintillation counters for the half-SVD cosmic ray test*. Confluence page (internal). 2018.

[66] T. Tsuboyama. *Main trigger counters are shifted by 2 cm*. E-Log entry (internal). 2018.

[67] T. Tsuboyama. *Trigger logic update*. E-Log entry (internal). 2018.

[68] K. R. Nakamura. private communication. 2018.

[69] L. Andricek. private communication. 2019.

[70] T. Humair et al. "Prompt $B^0 \rightarrow J/\psi K_S$ analysis". BELLE2-NOTE-PH-2020-038, unpublished.

[71] The Belle II Collaboration. "Prompt measurements of time-dependent CP-violation and mixing". URL: https://docs.belle2.org/record/2024/files/BELLE2-NOTE-PL-2020-11.pdf.

[72] V. I. Chekelian. *The MPI Concept of Time-Dependent Fits at Belle II.* xFitter Workshop. Minsk, Belarus, March 2019.

[73] S. Lacaprara. *First look at time-dependent CP violation using early Belle II data.* 2019. arXiv: 1906.08013 [hep-ex].

[74] T. Humair. private communication. 2021.

[75] T. M. Karbach et al. *Decay time integrals in neutral meson mixing and their efficient evaluation.* 2014. arXiv: 1407.0748 [physics.data-an].

[76] A. Oeftiger et al. "Review of CPU and GPU Faddeeva Implementations". In: *7th International Particle Accelerator Conference.* June 2016. DOI: 10.18429/JACoW-IPAC2016-WEPOY044.

[77] M. Tanabashi et al. "Review of Particle Physics". In: *Phys. Rev. D* 98 (3 Aug. 2018), p. 030001. DOI: 10.1103/PhysRevD.98.030001.

[78] HIGH ENERGY ACCELERATOR RESEARCH ORGANIZATION. *Luminosity projection.* URL: https://www-superkekb.kek.jp/Luminosity_projection.html (visited on 04/15/2021).

[79] Georgia State University. *Legendre Polynomials.* URL: http://hyperphysics.phy-astr.gsu.edu/hbase/Math/legend.html#c1 (visited on 04/15/2021).

[80] Inc. Wikimedia Foundation. *Legendre polynomials.* URL: https://en.wikipedia.org/wiki/Legendre_polynomials (visited on 04/15/2021).

List of Figures

List of Tables

List of publications

Publications written by author

[43]   J. Kandra et al. "Alignment Studies at Belle II Vertex Detector". In: *Acta Phys. Polon. B* 51.6 (2020), pp. 1385–1392. DOI: `10.5506/APhysPolB.51.1385`.

[47]   J. Kandra et al. *B lifetime and $B^0 - \bar{B}^0$ mixing results from early Belle II data*. 2019. arXiv: `1906.08940 [hep-ex]`.

[81]   J. Kandra et al. "Alignment and physics performance of the Belle II vertex detector". In: *PoS* FPCP2017 (2017), p. 053. DOI: `10.22323/1.304.0053`.

Publications partially written by author

[44]   T. Bilka et al. *Calibration and alignment of the Belle II tracker*. 2019. arXiv: `1910.06289 [physics.ins-det]`.

[48]   T. Bilka et al. "Calibration and Alignment Framework for the Belle II detector". In: *Journal of Physics: Conference Series* 1085 (Sept. 2018), p. 032023. DOI: `10.1088/1742-6596/1085/3/032023`. URL: `https://doi.org/10.1088/1742-6596/1085/3/032023`.

Publications co-authored by author

[38]   V. Bertacchi et al. "Track finding at Belle II". In: *Computer Physics Communications* 259 (Feb. 2021), p. 107610. DOI: `10.1016/j.cpc.2020.107610`.

[60]   B. Spruck et al. "Belle II Pixel Detector Commissioning and Operational Experience". In: Mar. 2020, p. 015. DOI: `10.22323/1.373.0015`.

[62]   H. Ye et al. "Commissioning and performance of the Belle II pixel detector". In: *Nucl. Instrum. Meth. A* 987 (2021), p. 164875. DOI: `10.1016/j.nima.2020.164875`.

[63]   F. Abudinen et al. "DEPFET pixel detector in the Belle II experiment". In: *Nucl. Instrum. Meth. A* 936 (2019), pp. 657–659. DOI: `10.1016/j.nima.2018.10.048`.

[64]   B. Paschen et al. "Belle II pixel detector: Performance of final DEPFET modules". In: *Nucl. Instrum. Meth. A* 958 (2020), p. 162222. DOI: `10.1016/j.nima.2019.05.063`.

[82]   A. Paladino et al. "Performance of the Belle II Silicon Vertex Detector". In: Oct. 2020, p. 148. DOI: `10.22323/1.364.0148`.

[83]   P. Kodyš et al. "Data quality monitors of vertex detectors at the start of the Belle II experiment". In: *EPJ Web of Conferences* 245 (Jan. 2020), p. 01035. DOI: `10.1051/epjconf/202024501035`.

[84] T. Bilka et al. "Alignment for the first precision measurements at Belle II". In: *EPJ Web of Conferences* 245 (Jan. 2020), p. 02023. DOI: `10.1051/epjconf/202024502023`.

[85] T. Bilka et al. *Millepede alignment of the Belle 2 sub-detectors after first collisions*. Dec. 2018.

[86] T. Bilka et al. "Alignment and Calibration of the Belle II Detector". In: *EPJ Web of Conferences* 214 (Jan. 2019), p. 01040. DOI: `10.1051/epjconf/201921401040`.

[87] F. Abudinén et al. "Study of $B \to D^{(*)}h$ decays using 62.8 fb^{-1} of Belle II data". In: (Apr. 2021). arXiv: `2104.03628` [`hep-ex`].

[88] H. Tanigawa et al. "Beam background study for the Belle II Silicon Vertex Detector". In: *Nucl. Instrum. Meth. A* 982 (2020), p. 164580. DOI: `10.1016/j.nima.2020.164580`.

[89] F. Abudinén et al. "Measurements of branching fractions and CP-violating charge asymmetries in charmless B decays reconstructed in 2019–2020 Belle II data". In: (Sept. 2020). arXiv: `2009.09452` [`hep-ex`].

[90] F. Abudinén et al. "Measurement of Hadronic Mass Moments M_X^n in $B \to X_c\ell\nu$ Decays at Belle II". In: (Sept. 2020). arXiv: `2009.04493` [`hep-ex`].

[91] F. Abudinén et al. "Measurement of the semileptonic $\bar{B}^0 \to D^{*+}\ell^-\nu_\ell$ branching fraction with fully reconstructed B meson decays and 34.6 fb^{-1} of Belle II data". In: (Aug. 2020). arXiv: `2008.10299` [`hep-ex`].

[92] H. Tanigawa et al. "Performance of the Belle II Silicon Vertex Detector". In: *Nucl. Instrum. Meth. A* 972 (2020), p. 164129. DOI: `10.1016/j.nima.2020.164129`.

[93] F. Abudinén et al. "Exclusive $B^0 \to \pi^-\ell^+\nu_\ell$ Decays with Hadronic Full Event Interpretation Tagging in 34.6 fb^{-1} of Belle II Data". In: (Aug. 2020). arXiv: `2008.08819` [`hep-ex`].

[94] F. Abudinén et al. "Studies of the semileptonic $\bar{B}^0 \to D^{*+}\ell^-\bar{\nu}_\ell$ and $B^- \to D^0\ell^-\bar{\nu}_\ell$ decay processes with 34.6 fb^{-1} of Belle II data". In: (Aug. 2020). arXiv: `2008.07198` [`hep-ex`].

[95] F. Abudinén et al. "A calibration of the Belle II hadronic tag-side reconstruction algorithm with $B \to X\ell\nu$ decays". In: (Aug. 2020). arXiv: `2008.06096` [`hep-ex`].

[96] F. Abudinén et al. "τ lepton mass measurement at Belle II". In: (Aug. 2020). arXiv: `2008.04665` [`hep-ex`].

[97] F. Abudinén et al. "Rediscovery of $B \to \phi K^{(*)}$ decays and measurement of the longitudinal polarization fraction f_L in $B \to \phi K^*$ decays using the Summer 2020 Belle II dataset". In: (Aug. 2020). arXiv: `2008.03873` [`hep-ex`].

[98] F. Abudinén et al. "First flavor tagging calibration using 2019 Belle II data". In: (Aug. 2020). arXiv: `2008.02707` [`hep-ex`].

[99] F. Abudinén et al. "Search for Axion-Like Particles produced in e^+e^- collisions at Belle II". In: *Phys. Rev. Lett.* 125.16 (2020), p. 161806. DOI: `10.1103/PhysRevLett.125.161806`. arXiv: `2007.13071` [`hep-ex`].

[100] F. Abudinén et al. "Charmless B decay reconstruction in 2019 Belle II data". In: (May 2020). arXiv: 2005.13559 [hep-ex].

[101] F. Abudinén et al. "Measurement of the B^0 lifetime using fully reconstructed hadronic decays in the 2019 Belle II dataset". In: (May 2020). arXiv: 2005.07507 [hep-ex].

[102] F. Abudinén et al. "Measurement of the branching fraction $\mathcal{B}(\bar{B}^0 \to D^{*+}\ell^-\bar{\nu}_\ell)$ with early Belle II data". In: (Apr. 2020). arXiv: 2004.09066 [hep-ex].

[103] C. Irmler et al. "Run and slow control system of the Belle II silicon vertex detector". In: *Nucl. Instrum. Meth. A* 958 (2020), p. 162706. DOI: 10.1016/j.nima.2019.162706.

[104] G. Casarosa et al. "Commissioning of the Belle II Silicon Vertex Detector". In: *Nucl. Instrum. Meth. A* 958 (2020), p. 162184. DOI: 10.1016/j.nima.2019.05.025.

[105] R. Thalmeier et al. "Series production testing and commissioning of the Belle II SVD readout system". In: *Nucl. Instrum. Meth. A* 958 (2020), p. 162942. DOI: 10.1016/j.nima.2019.162942.

[106] Christoph Schwanda et al. "Performance of the Belle II Silicon Vertex Detector". In: *PoS* Vertex2019 (2020), p. 014. DOI: 10.22323/1.373.0014.

[107] I. Adachi et al. "Search for an Invisibly Decaying Z' Boson at Belle II in $e^+e^- \to \mu^+\mu^-(e^\pm\mu^\mp)$ Plus Missing Energy Final States". In: *Phys. Rev. Lett.* 124.14 (2020), p. 141801. DOI: 10.1103/PhysRevLett.124.141801. arXiv: 1912.11276 [hep-ex].

[108] P. Kodyš et al. "The Belle II vertex detector integration". In: *Nucl. Instrum. Meth. A* 936 (2019), pp. 616–620. DOI: 10.1016/j.nima.2018.09.003.

[109] R. Thalmeier et al. "The Belle II silicon vertex detector: Assembly and initial results". In: *Nucl. Instrum. Meth. A* 936 (2019), pp. 712–714. DOI: 10.1016/j.nima.2018.08.066.

[110] B. Schwenker et al. "Operational experience and commissioning of the Belle II vertex detector". In: *PoS* VERTEX2018 (2019), p. 006. DOI: 10.22323/1.348.0006.

[111] Richard Thalmeier et al. "Machine learning: hit time finding with a neural network". In: *PoS* TWEPP2018 (2019), p. 065. DOI: 10.22323/1.343.0065.

[112] K. Lalwani et al. "Performance Studies of the Belle II Silicon Vertex Detector". In: *PoS* VERTEX2018 (2019), p. 052. DOI: 10.22323/1.348.0052.

[113] S. Halder et al. "Spatial Resolution of the Belle II Silicon Vertex Detector". In: *PoS* VERTEX2018 (2019), p. 054. DOI: 10.22323/1.348.0054.

[114] H. Aihara et al. "The Silicon Vertex Detector of the Belle II Experiment". In: *PoS* VERTEX2018 (2019), p. 024. DOI: 10.22323/1.348.0024.

[115] P. K. Resmi et al. "Construction and quality assurance of the Belle II Silicon Vertex Detector". In: *PoS* VERTEX2018 (2019), p. 051. DOI: 10.22323/1.348.0051. arXiv: 1901.09549 [physics.ins-det].

[116] K. Lalwani et al. "Performance of the Belle II SVD". In: *Springer Proc. Phys.* 234 (2019), pp. 87–92. DOI: 10.1007/978-3-030-29622-3_11.

[117] T. Bilka et al. "Calibration and Alignment Framework for the Belle II detector". In: *J. Phys. Conf. Ser.* 1085.3 (2018), p. 032023. DOI: 10.1088/1742-6596/1085/3/032023.

[118] W. Altmannshofer et al. "The Belle II Physics Book". In: *PTEP* 2019.12 (2019). [Erratum: PTEP 2020, 029201 (2020)], p. 123C01. DOI: 10.1093/ptep/ptz106. arXiv: 1808.10567 [hep-ex].

[119] S. Bahinipati et al. "Belle II Silicon Vertex Detector (SVD)". In: *Springer Proc. Phys.* 213 (2018), pp. 414–420. DOI: 10.1007/978-981-13-1316-5_78.

[120] Richard Thalmeier et al. "Electronics and Firmware of the Belle II Silicon Vertex Detector Readout System". In: *PoS* TWEPP-17 (2017), p. 109. DOI: 10.22323/1.313.0109.

[121] D. Y. Kim et al. "The simulation library of the Belle II software system". In: *J. Phys. Conf. Ser.* 898.4 (2017), p. 042043. DOI: 10.1088/1742-6596/898/4/042043.

[122] Thomas Lück et al. "Performance studies of the Belle II Silicon Vertex Detector with data taken at the DESY test beam in April 2016". In: *PoS* Vertex2016 (2017), p. 057. DOI: 10.22323/1.287.0057.

[123] D. Dutta et al. "Belle II Silicon Vertex Detector". In: *JINST* 12.02 (2017), p. C02074. DOI: 10.1088/1748-0221/12/02/C02074.

[124] K. Adamczyk et al. "The Belle II silicon vertex detector assembly and mechanics". In: *Nucl. Instrum. Meth. A* 845 (2017), pp. 38–42. DOI: 10.1016/j.nima.2016.03.100.

[125] R. Thalmeier et al. "The Belle II SVD data readout system". In: *Nucl. Instrum. Meth. A* 845 (2017), pp. 633–638. DOI: 10.1016/j.nima.2016.05.104.

[126] Lorenzo Vitale et al. "The Monitoring System of the Belle II Vertex Detector". In: *PoS* Vertex2016 (2017), p. 051. DOI: 10.22323/1.287.0051.

[127] Giacomo Caria et al. "The Software Framework of the Belle II Silicon Vertex Detector and its Development for the 2016 Test-Beam at DESY". In: *PoS* Vertex2016 (2017), p. 060. DOI: 10.22323/1.287.0060.

[128] Antonio Paladino et al. "The Silicon Vertex Detector of the Belle II Experiment". In: *PoS* ICHEP2016 (2016), p. 248. DOI: 10.22323/1.282.0248.

[129] K. H. Kang et al. "A bonding study toward the quality assurance of Belle-II silicon vertex detector modules". In: *Nucl. Instrum. Meth. A* 831 (2016), pp. 213–220. DOI: 10.1016/j.nima.2016.03.075.

[130] K. Adamczyk et al. "The silicon vertex detector of the Belle II experiment". In: *Nucl. Instrum. Meth. A* 824 (2016), pp. 406–410. DOI: 10.1016/j.nima.2015.09.076.

[131] K. Adamczyk et al. "Belle-II VXD radiation monitoring and beam abort with sCVD diamond sensors". In: *Nucl. Instrum. Meth. A* 824 (2016), pp. 480–482. DOI: 10.1016/j.nima.2015.09.007.

[132] K. Adamczyk et al. "Belle II SVD ladder assembly procedure and electrical qualification". In: *Nucl. Instrum. Meth. A* 824 (2016), pp. 381–383. DOI: `10.1016/j.nima.2015.08.067`.

[133] C. Irmler et al. "Construction and test of the first Belle II SVD ladder implementing the origami chip-on-sensor design". In: *JINST* 11.01 (2016), p. C01087. DOI: `10.1088/1748-0221/11/01/C01087`.

[134] R. Thalmeier et al. "EMC studies for the vertex detector of the Belle II experiment". In: *JINST* 11.01 (2016), p. C01044. DOI: `10.1088/1748-0221/11/01/C01044`.

A. Vertex alignment parameters

This appendix contains some technical material on alignment parameters and monitoring procedures described in chapter 3.

We start with Legendre polynomials as the base for the description and monitoring of silicon sensor surface deformations.

Next we show how alignment parameters are visualized to explain how they can be monitored.

The last section introduces a fitting algorithm as the central part of alignment parameters monitoring.

A.1 Legendre polynomials

Legendre polynomials (L_i) are well known as a complete system of orthogonal polynomials that arise in a number of applications in physics and mathematics. The domain of Legendre polynomials is the interval $\langle -1, 1 \rangle$. Their orthogonality means that [79]

$$\int_{-1}^{1} L_i \cdot L_j \sim \delta_{ij} = 0 \text{ for } i \neq j \tag{A.1}$$

and the normalization is $L_i(1) = 1$. The first six Legendre polynomials are

$$\begin{aligned}
L_0(x) &= 1, \\
L_1(x) &= x, \\
L_2(x) &= \frac{1}{2}(3x^2 - 1), \\
L_3(x) &= \frac{1}{2}(5x^3 - 3x), \\
L_4(x) &= \frac{1}{8}(35x^4 - 30x^2 + 3) \\
L_5(x) &= \frac{1}{8}(63x^5 - 70x^3 + 15x)
\end{aligned} \tag{A.2}$$

where the colours of the defining equations correspond to the colours of curves shown in Figure A.1.

We can form a two-dimensional basis of bivariate orthogonal polynomials as a Cartesian product of two Legendre bases. Thus, to describe surface deformation w of a silicon sensor we use a polynomial expansion of the form

$$w(u, v) = \sum_{i,j} P_{ij} \cdot L_i(u) \cdot L_j(v) \tag{A.3}$$

where u and v are sensor local coordinates and the term $L_i(x) \cdot L_j(y)$ is said to
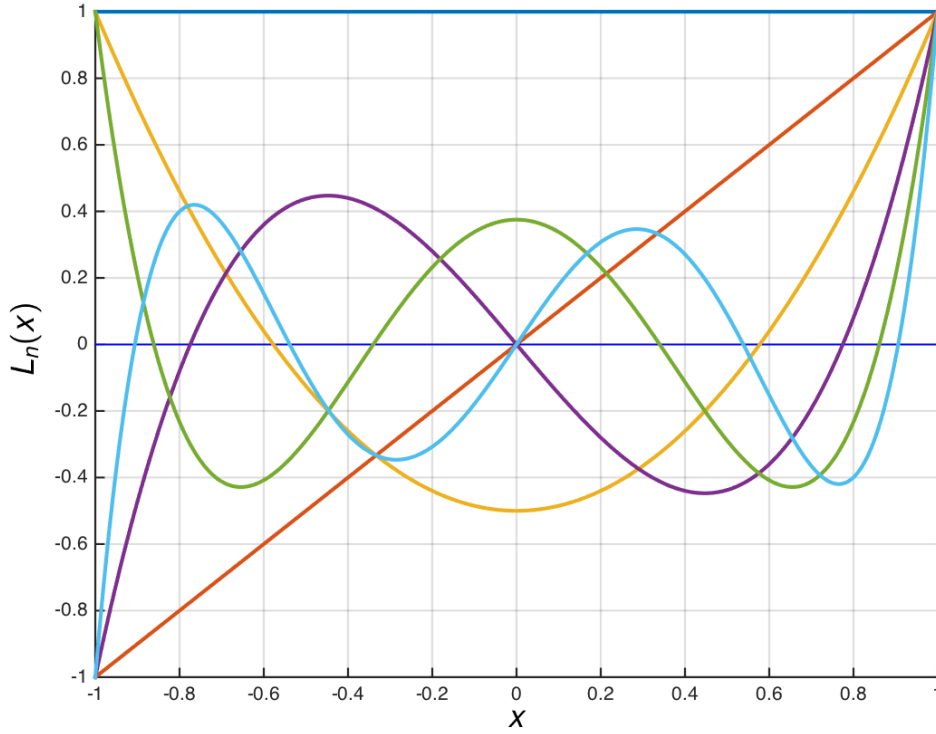
Figure A.1: The first six Legendre polynomials: a constant (dark blue), linear (red), quadratic (orange), cubic (violet), quartic (green), and quintic (light blue) [80]

be of order i + j. The first terms of the polynomial expansion are

$$
\begin{aligned}
w &\sim L_0(u) \cdot L_0(v) & P_{20} &\sim L_2(u) \cdot L_0(v) \\
\alpha &\sim L_1(u) \cdot L_0(v) & P_{11} &\sim L_1(u) \cdot L_1(v) \\
\beta &\sim L_0(u) \cdot L_1(v) & P_{02} &\sim L_0(u) \cdot L_2(v)
\end{aligned}
$$

$$
\begin{aligned}
P_{40} &\sim L_4(u) \cdot L_0(v) & & & (\text{A.4}) \\
P_{31} &\sim L_3(u) \cdot L_1(v) & P_{30} &\sim L_3(u) \cdot L_0(v) \\
P_{22} &\sim L_2(u) \cdot L_2(v) & P_{21} &\sim L_2(u) \cdot L_1(v) \\
P_{13} &\sim L_1(u) \cdot L_3(v) & P_{12} &\sim L_1(u) \cdot L_2(v) \\
P_{04} &\sim L_0(u) \cdot L_4(v) & P_{03} &\sim L_0(u) \cdot L_3(v)
\end{aligned}
$$

Here w, α and β in fact describe a shift along the plane normal and rotations around the u and v axes, respectively; in other words, they describe rigid body displacements of the sensor and hence they are not part of sensor shape expansion. P_{20}, P_{11}, and P_{02} describe quadratic surface deformations, P_{30}, P_{21}, P_{12}, and P_{03} cubic deformation, and finally $P_{40}, P_{31}, P_{22}, P_{13}$ and P_{04}) describe quartic surface deformation. If sensor occupancy is sufficiently uniform along at least one coordinate, the contributions from terms of different orders are independent.

A.2 Visualisation of alignment parameters

The alignment monitoring procedure that we have developed introduces two different plots for monitoring alignment parameters: plots of standard u and v unbiased residuals and projection of u and v residuals onto w using Eq. (3.6) mapped to the sensor surface. The visualisation of alignment parameters (Figures A.2 and A.3) uses the Monte Carlo simulation sample from the VXD Commissioning period (Chapter 6). Strip sensor 4.3.2 sensor was initially misaligned by modifying its alignment parameters, then cosmic tracks were reconstructed, and monitoring procedure applied. We generated 100 μm shifts of sensors in each direction. Each angle was rotated by 10 μrad. To generate surface deformation, 200 μm was set for each parameter.
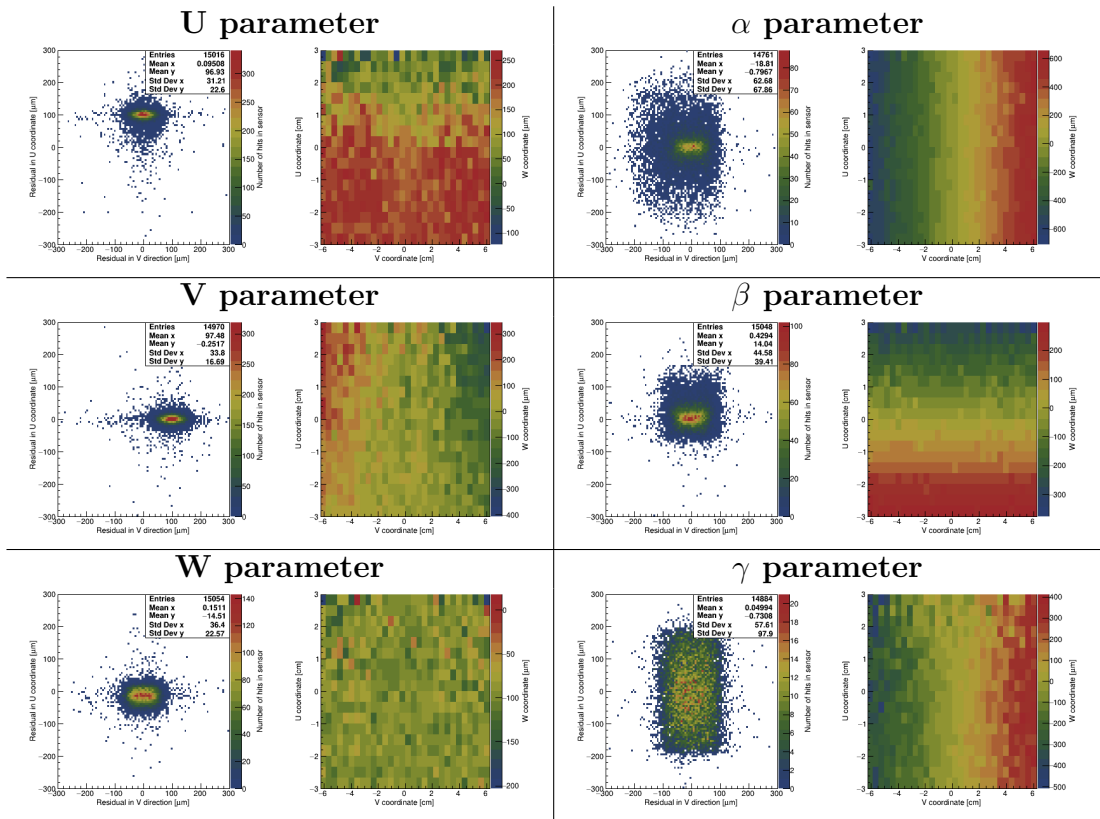
Figure A.2: Visualisation of rigid body parameters of vertex detector sensors: each box is composed of a two dimensional unbiased residual distribution (left) and surface plot of the projected w residual (right)

These plots are a sensitive tool to visualize minor misalignments. The statistical noise in the visualisation plots depend on the statistics of collected hits. The highest observed precision was about 10 μm and it was found using cosmic sample in Chapter 7. According to visualisation plots, the γ angle can not be monitored. The monitoring tool is not suitable or intended for determining alignment parameters, but for easy identification of changes in alignment parameters. The γ angle plots can be removed from the validation procedure to keep only relevant alignment parameters in the monitoring procedure. Visualisation plots are particularly valuable in the monitoring and alignment validation in small data
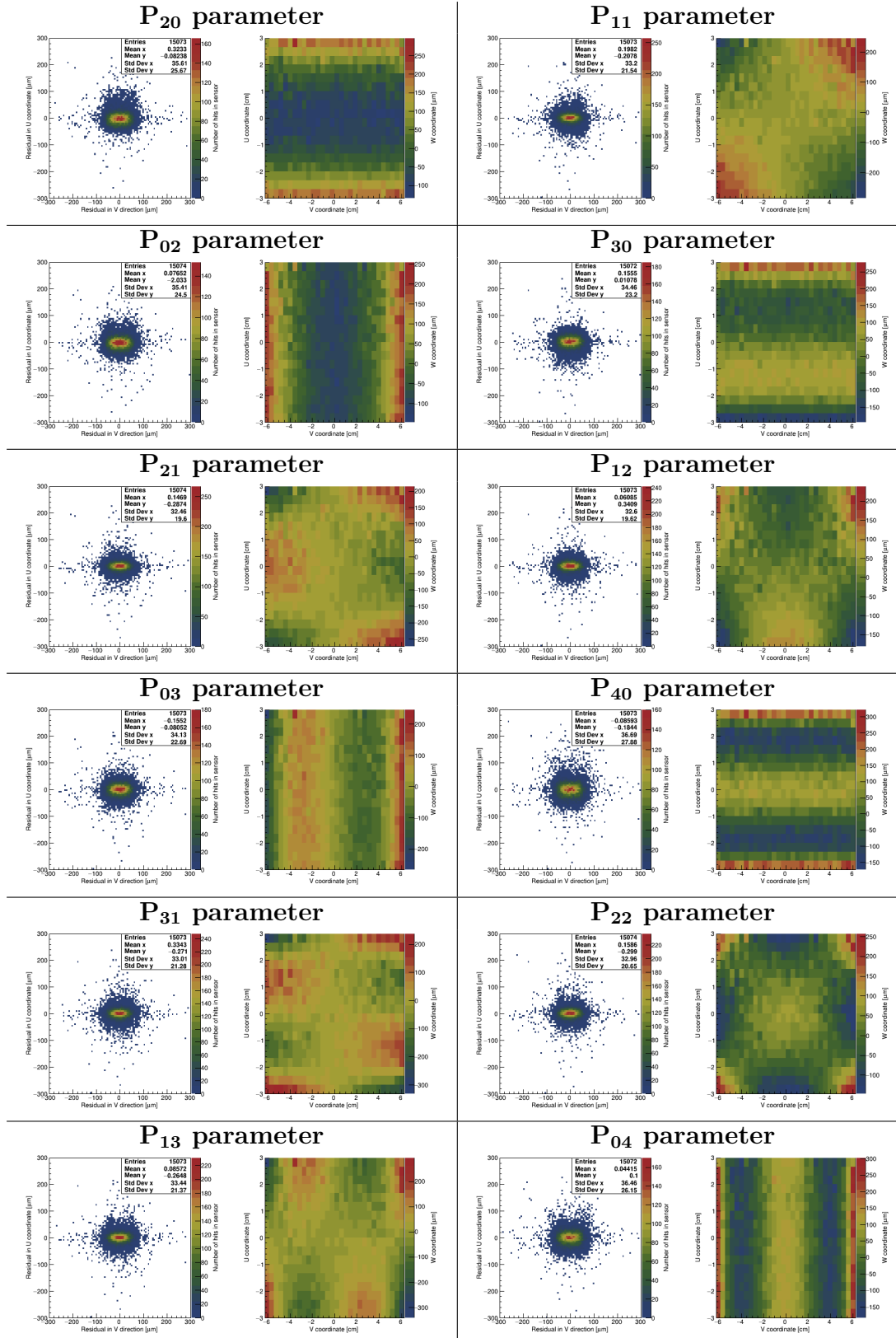
Figure A.3: Visualisation of surface parameters of vertex detector sensors: each box is composed of a two dimensional unbiased residual distribution (left) and surface plot of projected w residual (right)

samples, such as cosmic or small collision samples.

A.3   Extraction of alignment parameters

In big data samples, the monitoring procedure was automated. Alignment parameters were extracted from each monitoring plot. The u and v shifts are extracted as the means of two-dimensional distributions of unbiased residuals for each sensor. Other parameters (except for the γ angle) were extracted from the projected w residual to sensor surface by the fitting function defined as:

$$
\begin{aligned}
w(u,v) = {} & P_W \cdot L_0(u) \cdot L_0(v) + P_\alpha \cdot L_0(u) \cdot L_1(v) + P_\beta \cdot L_1(u) \cdot L_0(v) + \\
& + P_{20} \cdot L_2(u) \cdot L_0(v) + P_{11} \cdot L_1(u) \cdot L_1(v) + P_{02} \cdot L_0(u) \cdot L_2(v) + \\
& + P_{30} \cdot L_3(u) \cdot L_0(v) + P_{21} \cdot L_2(u) \cdot L_1(v) + P_{12} \cdot L_1(u) \cdot L_2(v) + \\
& + P_{03} \cdot L_0(u) \cdot L_3(v).
\end{aligned}
\tag{A.5}
$$

From the plots (Figures A.2 and A.3) we can see that the ranges of u and v coordinates do not correspond to the domain of Legendre polynomials, so the coordinates have to be pre-scaled to interval $\langle -1, 1 \rangle$.

Extracted parameters can be plotted as a function of run or time so that the fluctuations of alignment parameters in time can be studied. The final monitoring plots can be found at the end of Chapters 5 and 7.

B. Generation of weak modes

A special set of plots was created to visualize χ^2 invariant modes for the alignment of the vertex detector using the given data sample. Each weak mode is generated as a coherent movement (a linear combination of changes of alignment parameters) of vertex detector sensors according to the equations in Figure 3.3. Here we show each weak mode in a separate figure: the radial expansion in B.1, elliptical expansion in B.2, bowing in B.3, curl in B.4, clamshell in B.5, twist in B.6, telescope in B.7, skew in B.8, and z expansion in B.9.

Each time it is run, the algorithm that calculates alignment parameters produces a payload that contains corrections of alignment parameters relative to nominal geometry. These are plotted as ringplots in each figure. The generated alignment parameters are projected to the Belle II global coordinate system and shown in a quiver plot, and the schematic plot of each weak mode is also shown in each figure. The arrows in quiver plots represent single sensors; their direction corresponds to the direction of the displacement and their colour encodes its size, the darkest shade meaning maximum displacement. Blue and red shades correspond to negative and positive direction of displacement, respectively. A white arrow means there is no movement for the sensor. The maximal displacement is arbitrarily but practically chosen to be 250 μm.
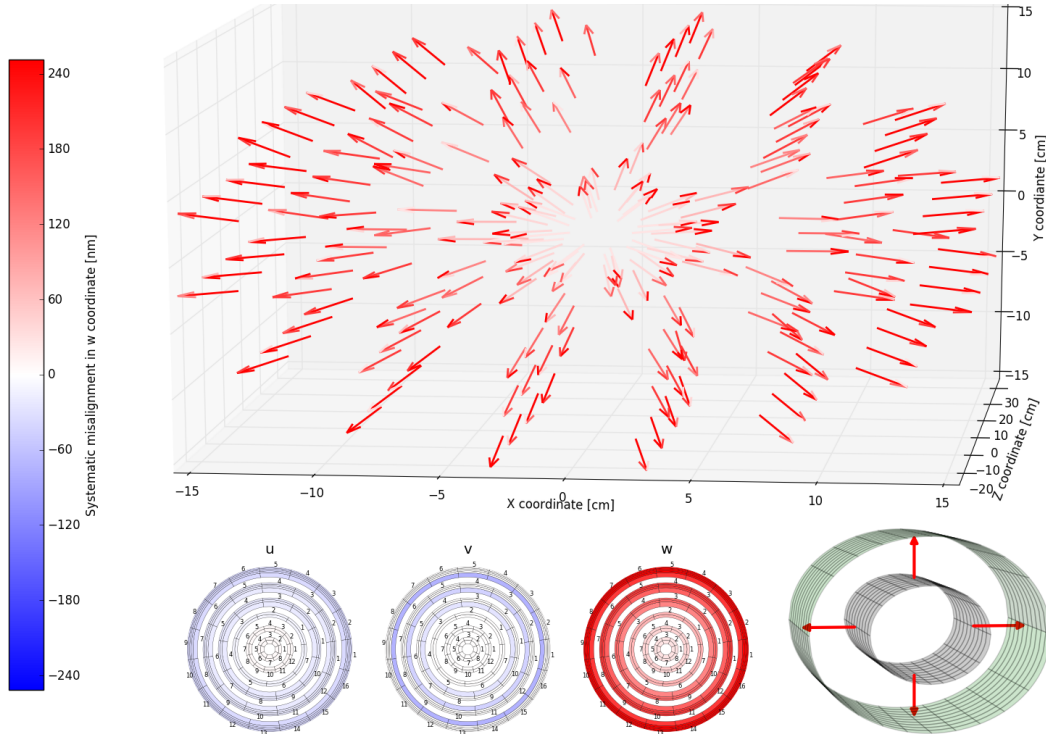
Figure B.1: Generation of radial expansion: Quiver plot (top), ring plots (bottom left) and schematic plot (bottom right)
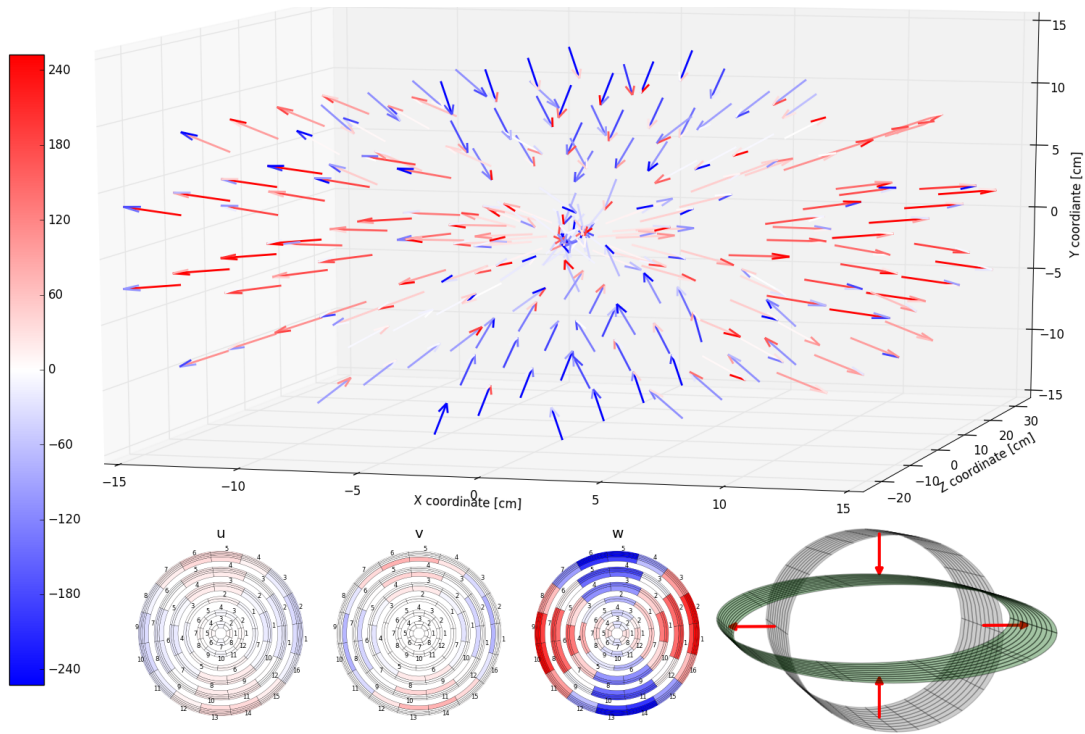
Figure B.2: Generation of elliptical expansion: Quiver plot (top), ring plots (bottom left) and schematic plot (bottom right)
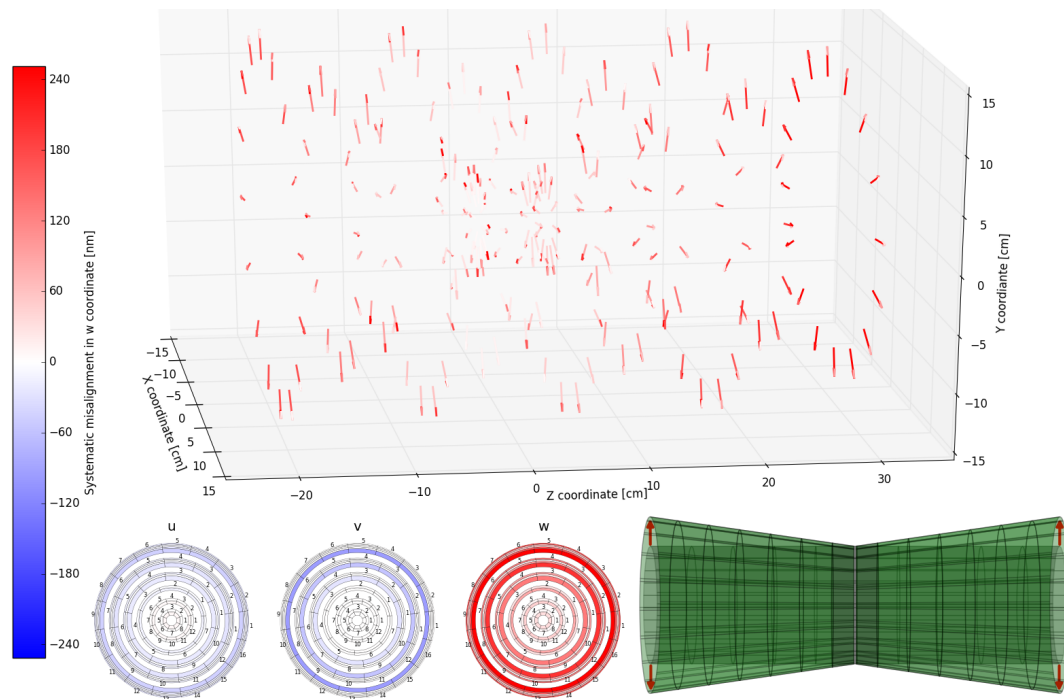
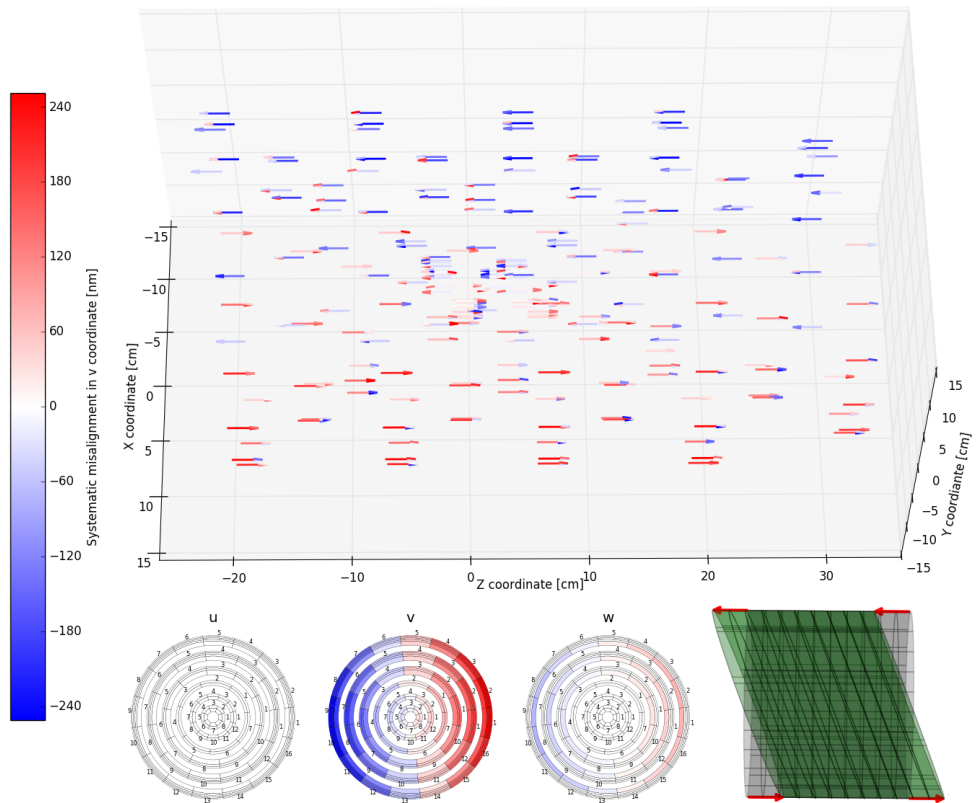Figure B.3: Generation of bowing: Quiver plot (top), ring plots (bottom left) and schematic plot (bottom right)
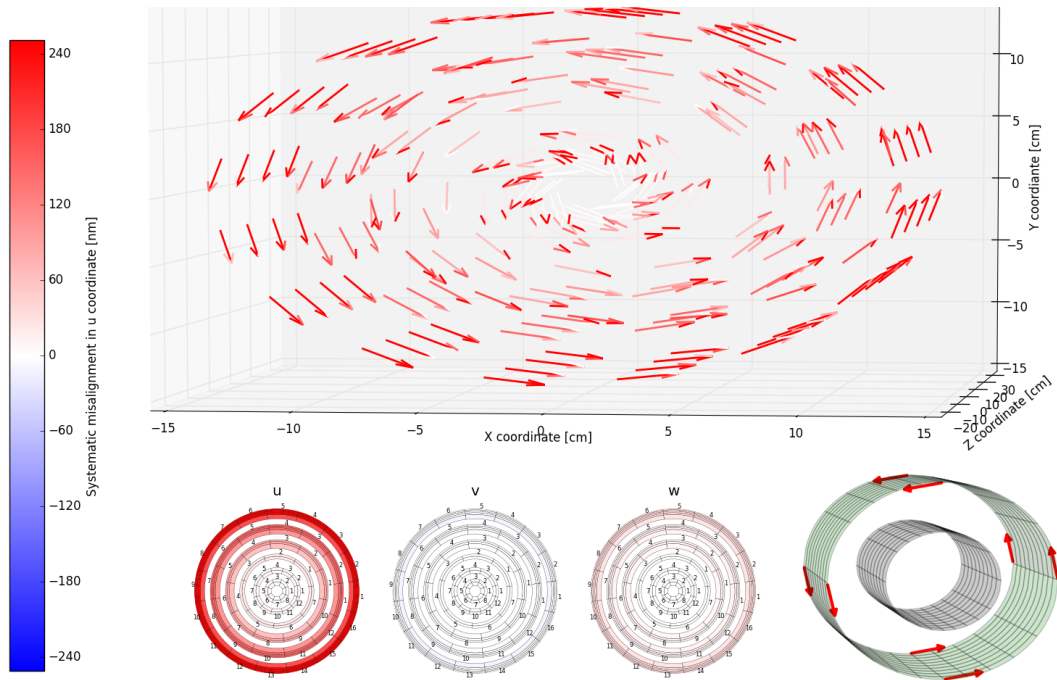
Figure B.4: Generation of curl: Quiver plot (top), ring plots (bottom left) and schematic plot (bottom right)
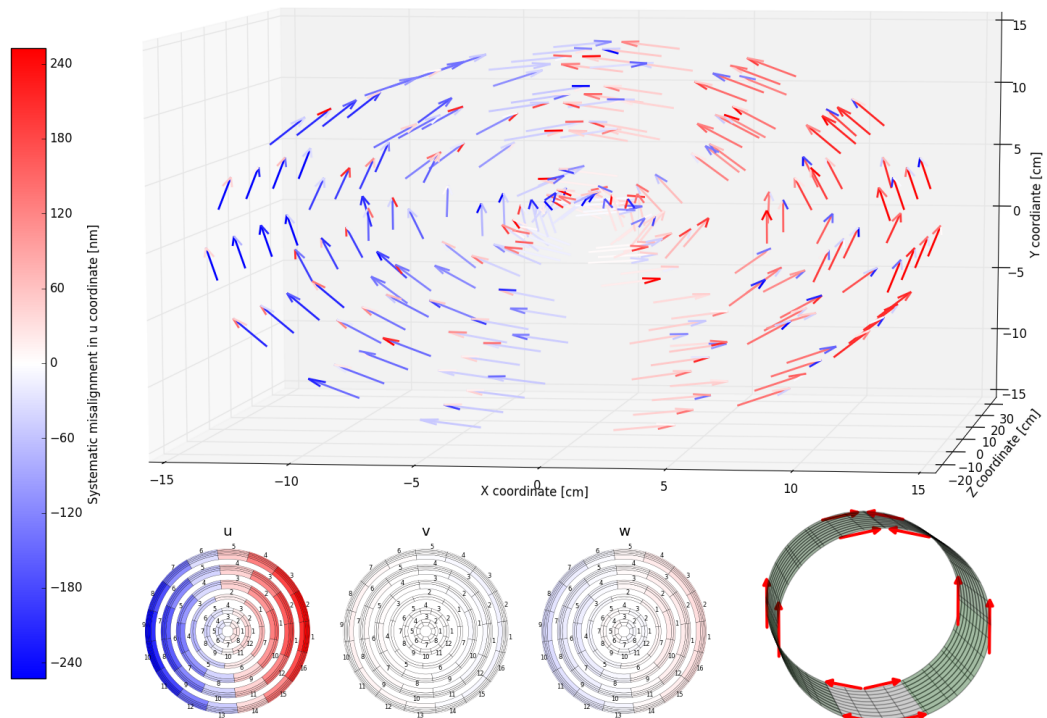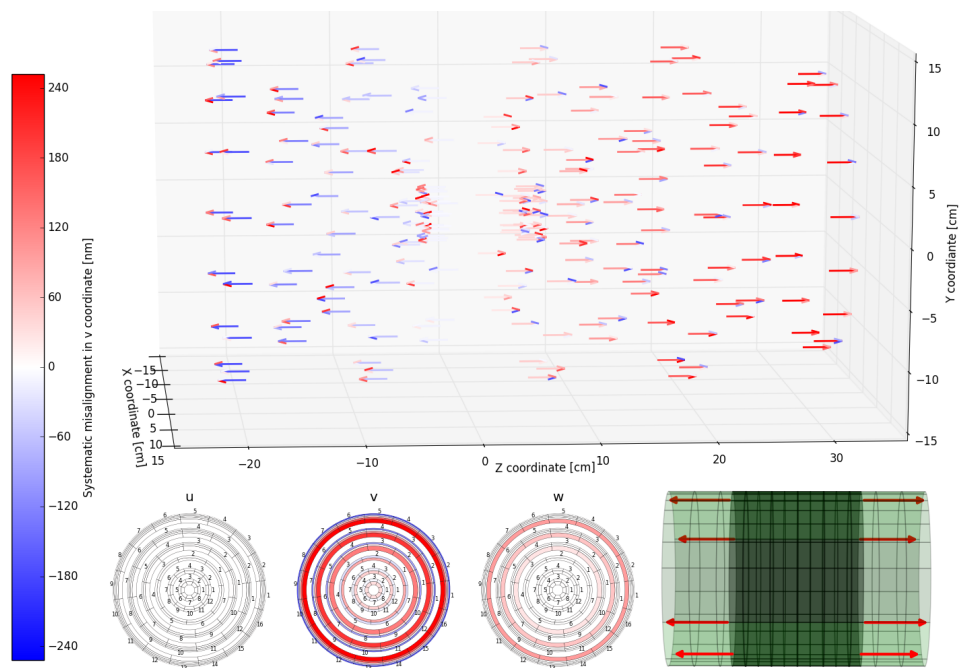

Figure B.5: Generation of clamshell: Quiver plot (top), ring plots (bottom left) and schematic plot (bottom right)
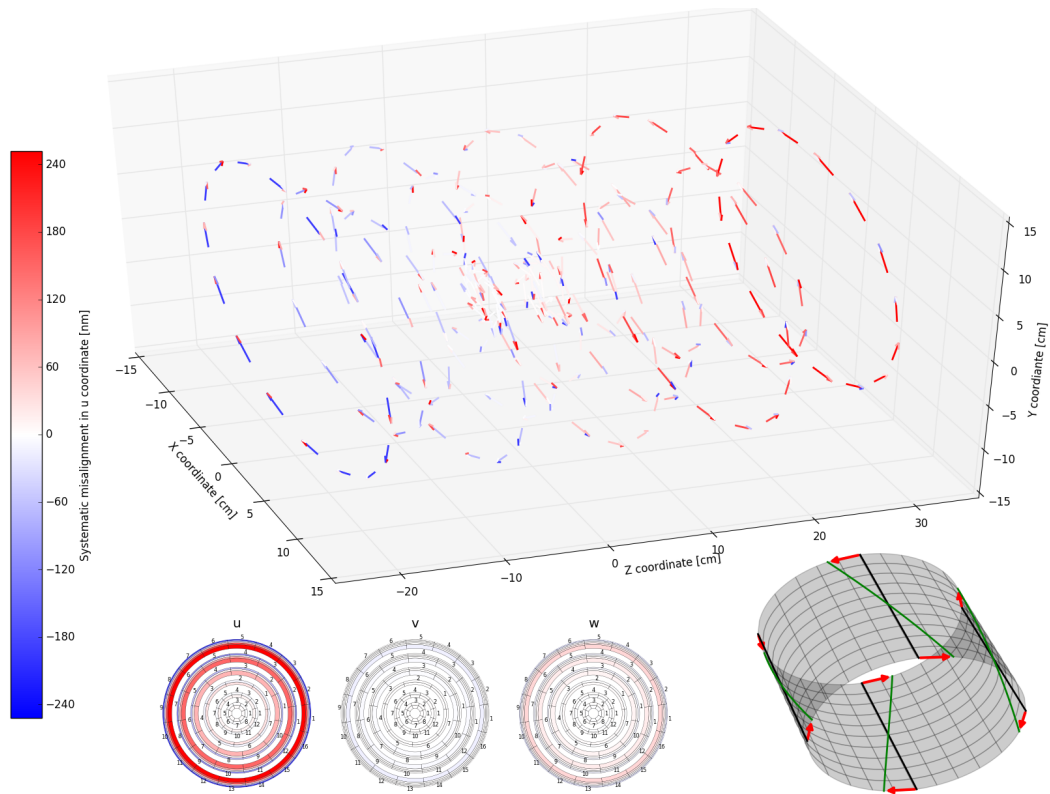
Figure B.6: Generation of twist: Quiver plot (top), ring plots (bottom left) and schematic plot (bottom right)
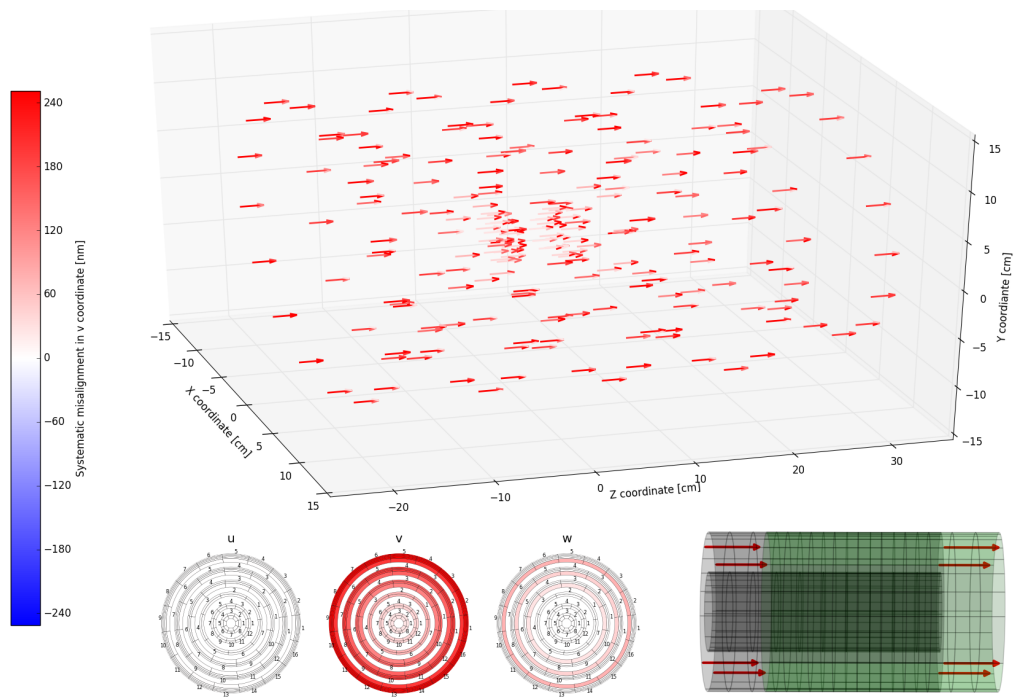
Figure B.7: Generation of telescope: Quiver plot (top), ring plots (bottom left) and schematic plot (bottom right)

176

Figure B.8: Generation of skew: Quiver plot (top), ring plots (bottom left) and schematic plot (bottom right)

Figure B.9: Generation of z expansion: Quiver plot (top), ring plots (bottom left) and schematic plot (bottom right)

C. Phase 2 results

During Phase 2, different vertex detector alignment scenarios were studied. In the beginning, only shift and rotation alignment parameters were determined for each sensor (Figure C.1). For a long time, this alignment was used as a reference for the Phase 2 vertex detector. Using these results, we observed the first sensor surface deformations, and it motivated us to extend the reconstruction software and the alignment procedure by including the surface alignment parameters.
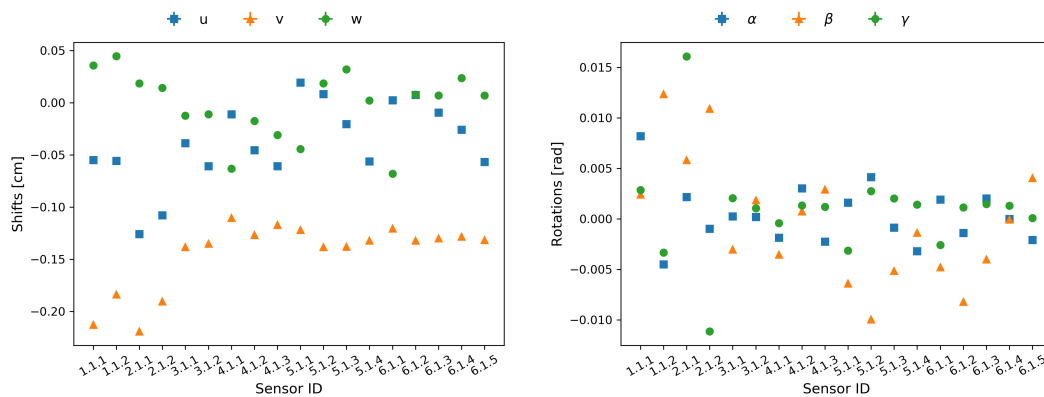
Figure C.1: Alignment results using shift (left) and rotation (right) parameters

Since then, a number of alignment scenarios have been tested - we tried to establish the most practical representation of sensor surface deformation by keeping the lowest meaningful number of terms in the Legendre expansion. So in the first step, we added to the shift and rotation parameters the second order terms of the Legendre expansion, the quadratic surface parameters. The resulting alignment parameters are shown in Figure C.2. Deformations of several sensors were eliminated, and the scale of the quadratic surface deformation is about 100 microns.
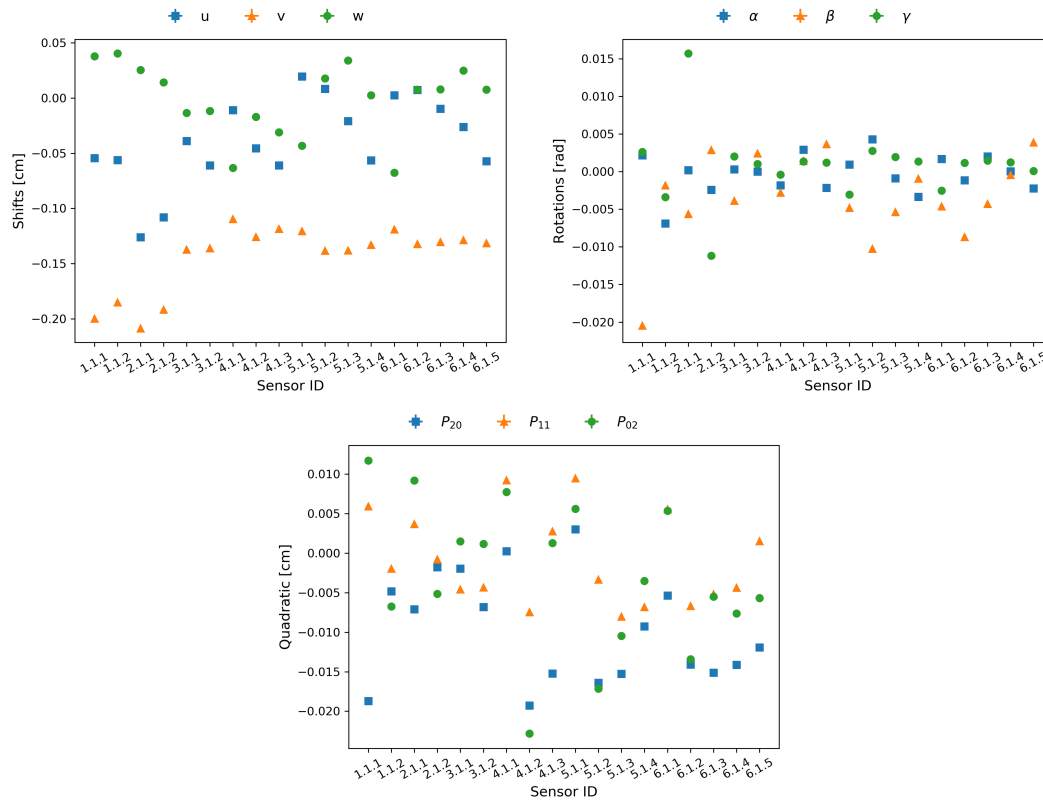
Figure C.2: Alignment results using shift (top left), rotation (top right) and quadratic surface (bottom) parameters

The natural next step was to apply cubic sensor deformations. The result of the alignment procedure can be found in Figure C.3. No visible improvement was observed in the monitoring plots. For the strip sensor 5.2.2, the monitoring plots show a small improvement. For some sensors, unexpected values (on the scale of 100 μm) were observed. Most likely, we did not have enough data in our sample and the problem was ill-conditioned.
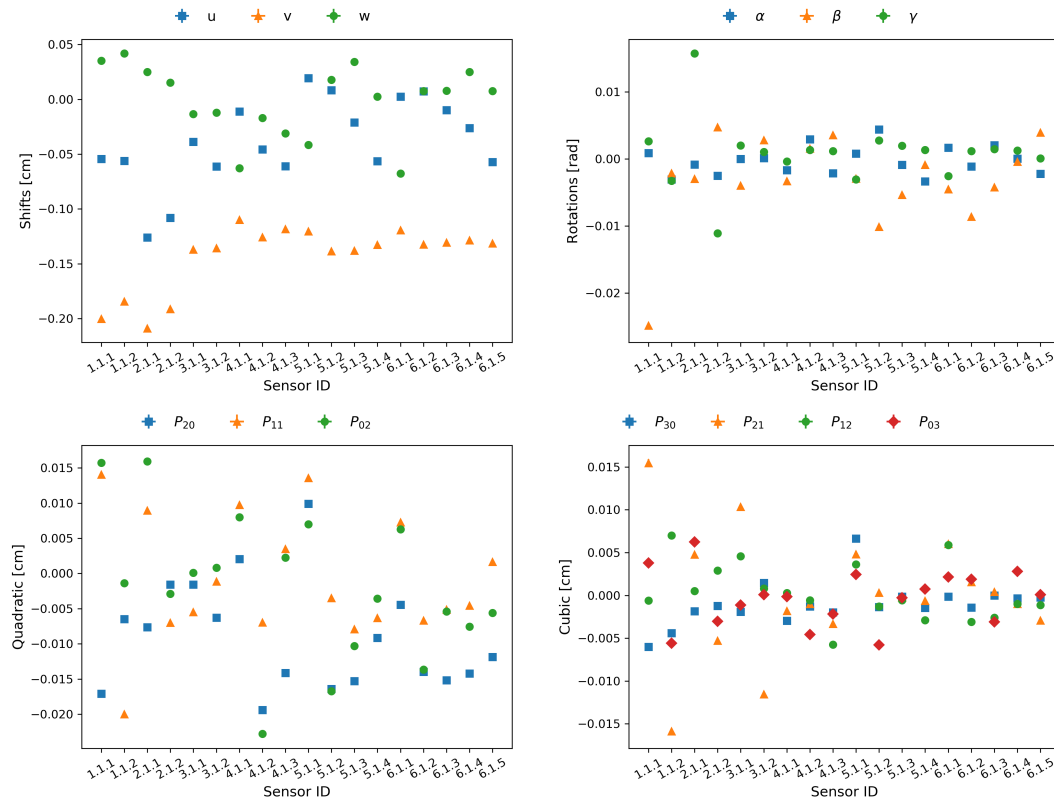
Figure C.3: Alignment results using shift (top left), rotation (top right), quadratic (bottom left) and cubic (bottom right) parameters

The following step was to try the quartic deformations (Figure C.4) and the result shows contributions of quartic deformations in the order of 10 μm. Monitoring plots and alignment results introduce no evidence in support of quartic sensor surface deformations.
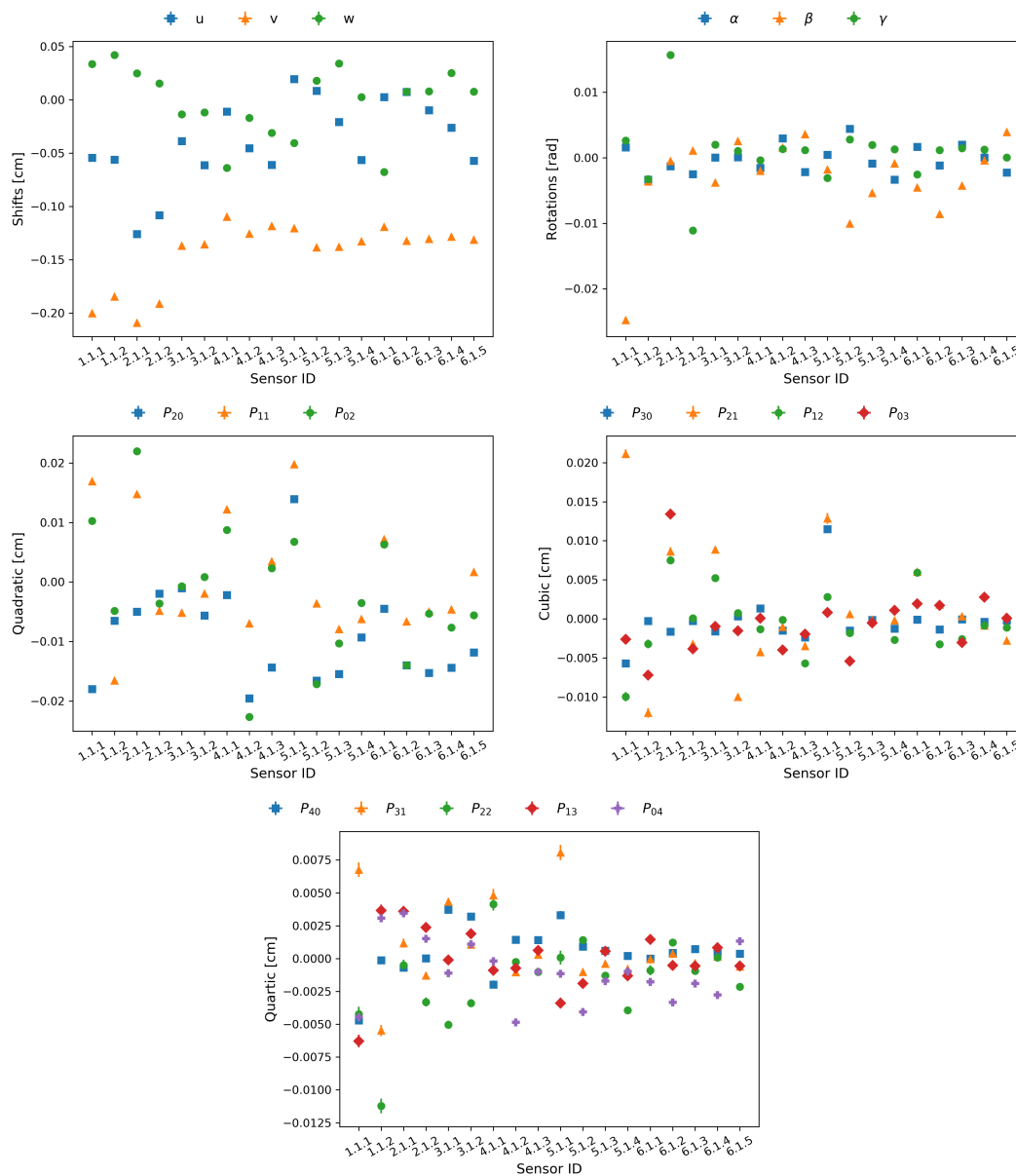
Figure C.4: Alignment results using shift (top left), rotation (top right), quadratic (center left), cubic (center right) and quartic (bottom) parameters

To keep the amount of alignment parameters at a reasonable minimum, we only keep in the alignment procedure only the rigid body and quadratic surface parameters. The observed values of parameters can be found in Figure C.5. Apparently the pixel sensors' parameters diverged, but that does not invalidate other validation plots. The problem with pixel sensors is the low count and low precision of cosmic track extrapolation from the Central Drift Chamber.
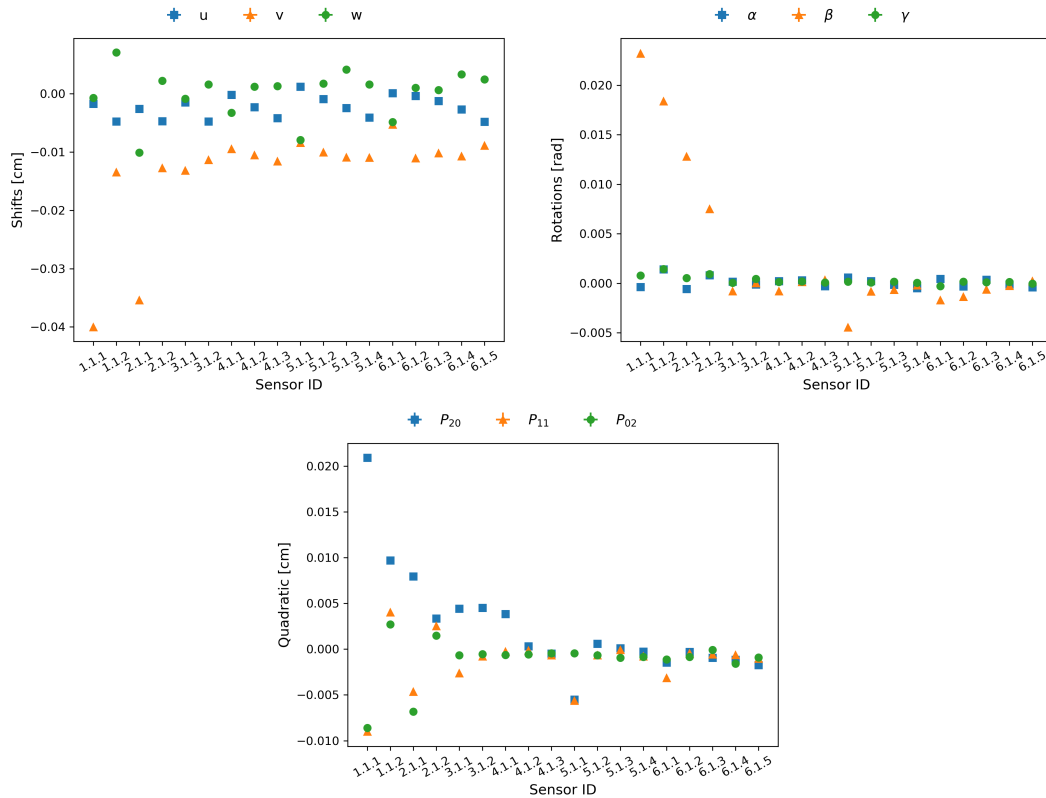
Figure C.5: Results of iterated alignment using shift (top left), rotation (top right) and quadratic (bottom) parameters

D. VXD Commissioning results

In this section we discuss the alignment results during the VXD Commissioning (Chapter 6). The alignment parameters of the vertex detector obtained using the data taken in SVD standalone commissioning campaign is shown in Figure D.1. The alignment procedure was iterated three times, and no constraints were applied. Only the shift and rotation parameters were determined. Large values of parameters in the sixth layer show there is some divergence of the alignment procedure. In this case, the problem was in the simple trigger system, where cosmic tracks coming from forward and backward sides are wrongly triggered. Fortunately, the monitoring tools identified the quadratic deformations of the large rectangular central strip sensors. We repeated our observations from Phase 2.
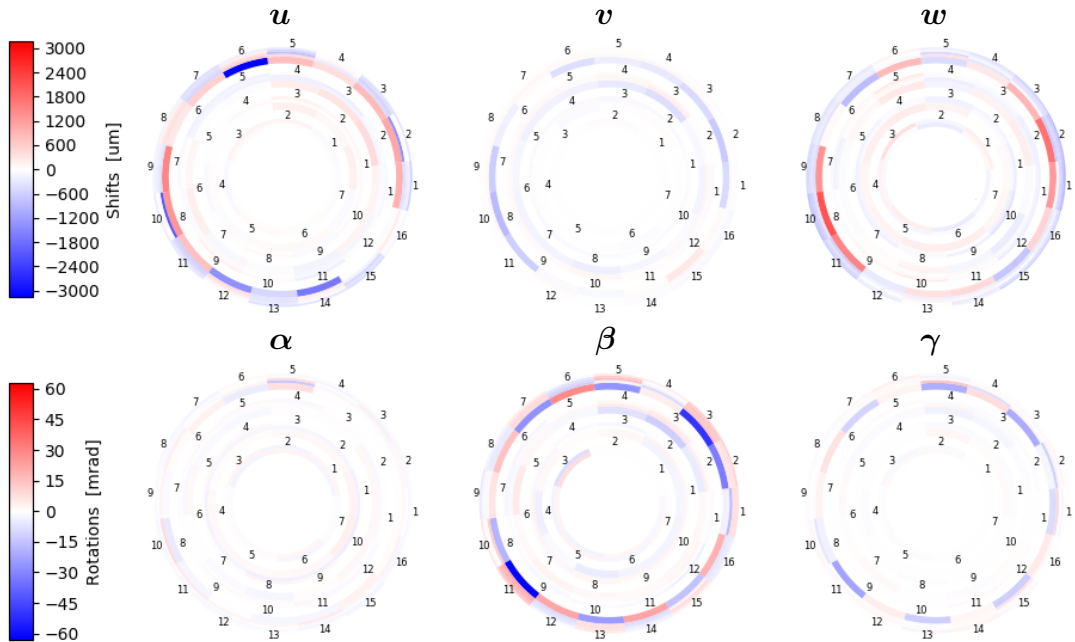
Figure D.1: Alignment results for SVD standalone commissioning

The first alignment corrections in PXD-SVD combined commissioning can be found in Figure D.2, where shift and rotation parameters were calculated using hierarchical constraints between sensor and ladder levels. The alignment procedure was processed only once with no iteration. The alignment corrections are better then in the previous campaign due to a more complex trigger system and higher statistic of cosmic tracks passing through full vertex detector. Using these results, the first observation of the zebra effect in the sixth layer and large deformation of ladders in the second layer was observed. The monitoring procedure shows quadratic deformations in the large central rectangular strip sensors, which motivated us to expand the alignment procedure by including quadratic surface parameters.
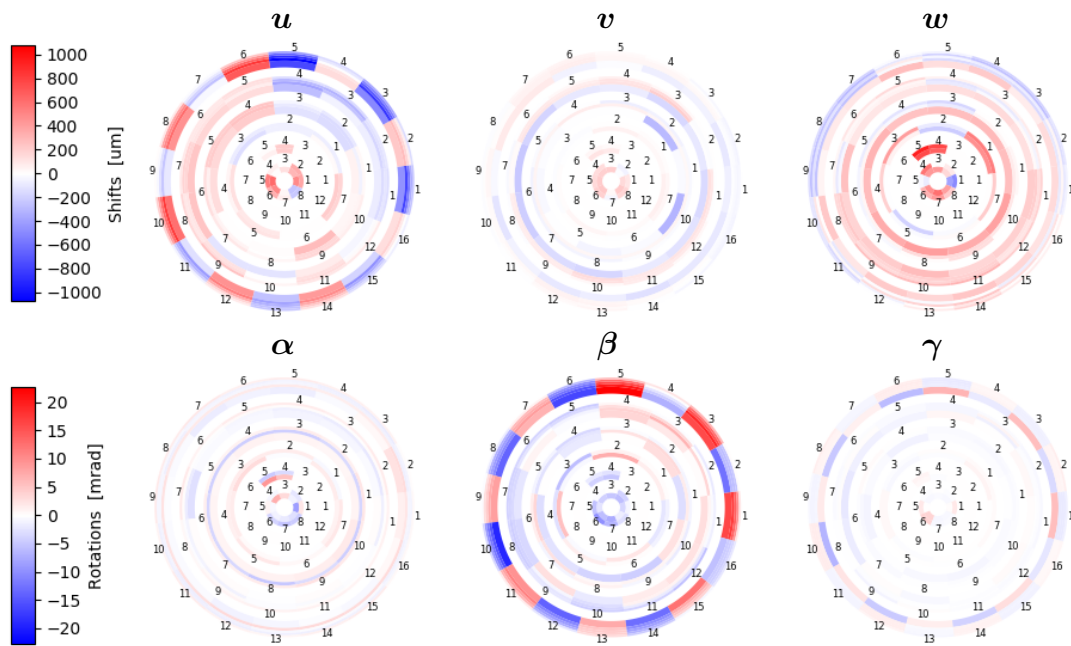
Figure D.2: Alignment results for PXD-SVD combined commissioning

After expanding the reconstruction software and alignment procedure by including the surface sensor parameters, the alignment procedure was repeated. The plots in Figure D.3 show the results when we used shifts, rotations, and quadratic surface alignment parameters. In this case, the alignment corrections were found using hierarchical constraints between sensor and ladder levels. The values of shift and rotation parameters agree with the values from the previous rigid body alignment. However, forward and backward sensors in ladders of the sixth layer have unrealistically large quadratic surface deformations. We attributed this to the lower occupancy of the forward and backward sensors of the outermost layer due to missing tracks in the vertex detector: the cosmic tracks passing through this area are more likely to not be correctly reconstructed. Installation of the vertex detector in its proper position in the Belle II detector cavity would correct the problem.
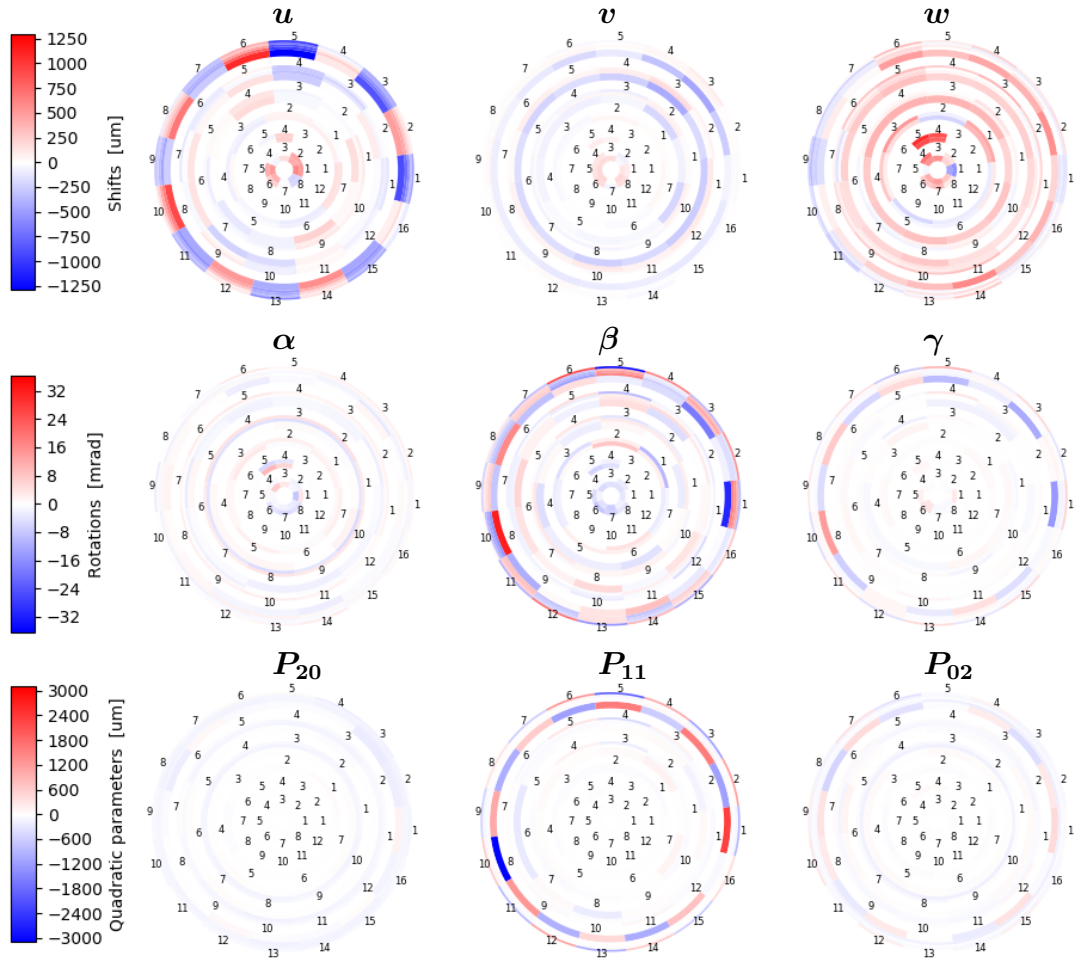
Figure D.3: Alignment results for PXD-SVD combined commissioning

E. Monitoring of weak modes

In Chapter 7 we described the monitoring procedures for the χ^2 invariant modes of the Belle II vertex detector. Monte Carlo studies were performed for cosmic, $\Upsilon(4S)$ and $e^+e^- \to \mu^+\mu^-$ samples. Monte Carlo monitoring results for cosmic samples are reported in Figures 7.4 and 7.5. Monte Carlo monitoring results using other samples are shown in this chapter: for $\Upsilon(4S)$, in Figures E.1 and E.2, and for $e^+e^- \to \mu^+\mu^-$ in Figures E.3 and E.4.

To improve cosmic results, we have to use collision tracks, since bundles of collision tracks have different topology than bundles of collision tracks. The $\Upsilon(4S)$ result improves the results in our monitoring tool. The first is the suppression of χ^2 invariant modes. These modes depend not only on the nominal geometry, but also on the topology of the track bundle used for calculation of alignment. The telescope case shows the monitoring result closest to the nominal geometry. Yet the asymmetric pattern in the distribution of hits in sensor overlaps for the telescope mode indicates the weak mode is still present to some degree.

The best sensitivity is shown using $e^+e^- \to \mu^+\mu^-$, where all χ^2 invariant modes are clearly recognized from nominal geometry - with the exception of the telescope mode. Again this weak mode can be recognized using the asymmetry in the distribution of hits in sensor overlaps. We note here that the telescope weak mode is mostly eliminated using enough cosmic tracks in alignment: it is one of the major reasons for using cosmic tracks in alignment.

Nominal

Radial expansion

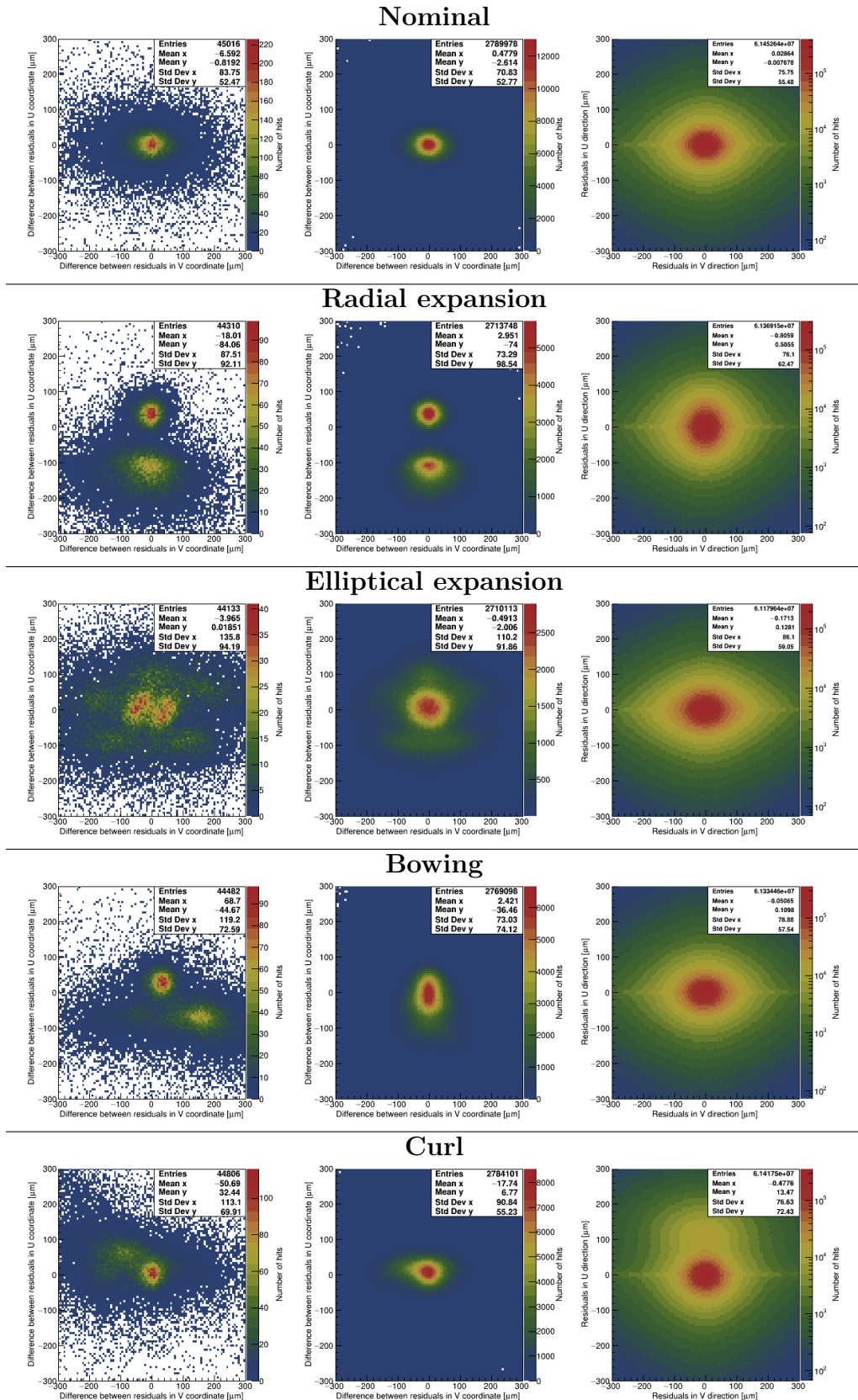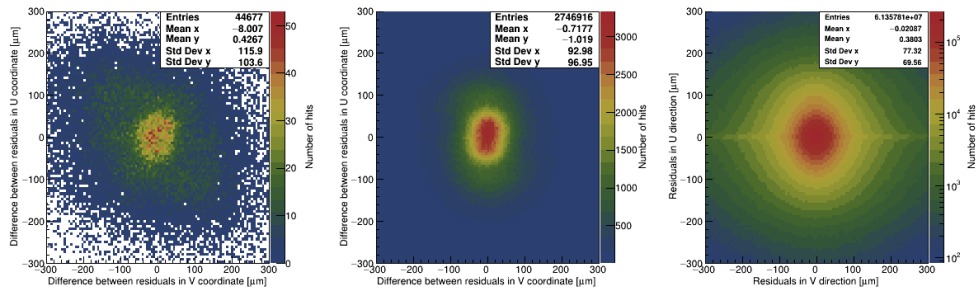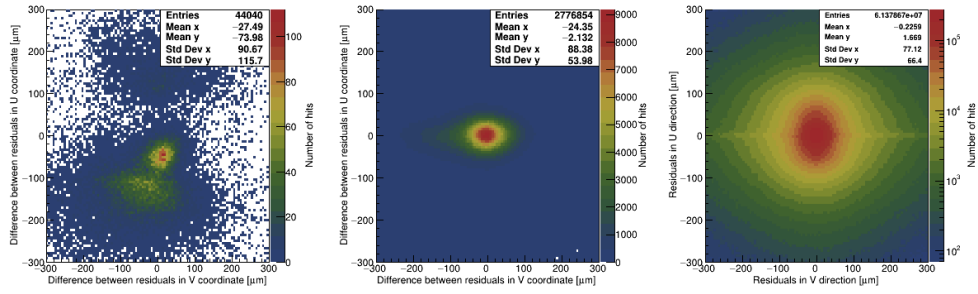# Elliptical expansion

Bowing

Curl

Figure E.1: Validation plots for nominal geometry and weak modes by simulated $\Upsilon(4S)$: difference distribution for hits in overlapping sensors with different (left) and the same (center) position in a ladder, residual distribution for other hits (right)
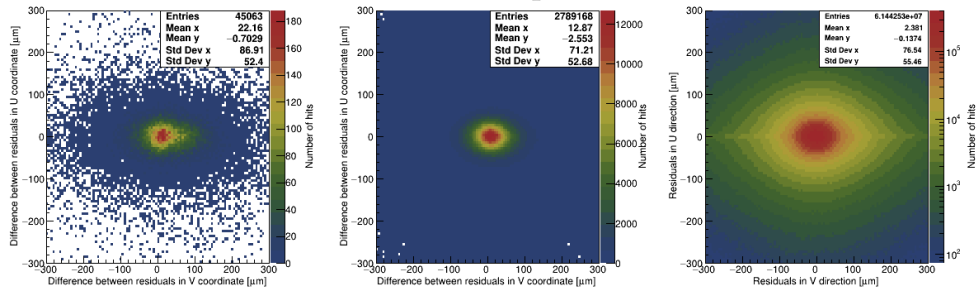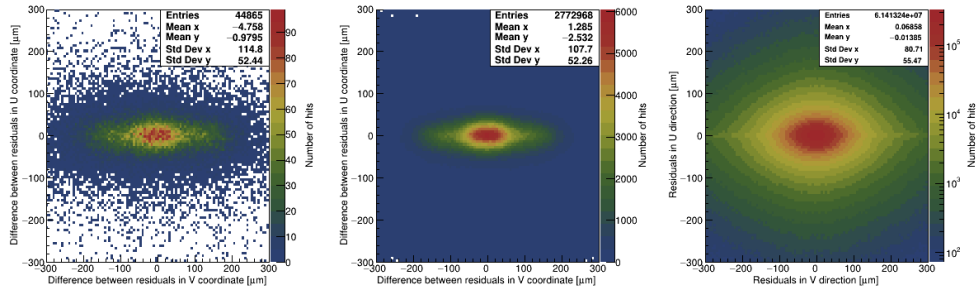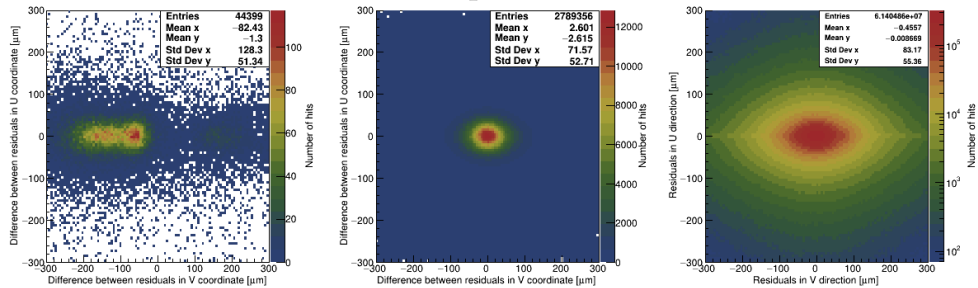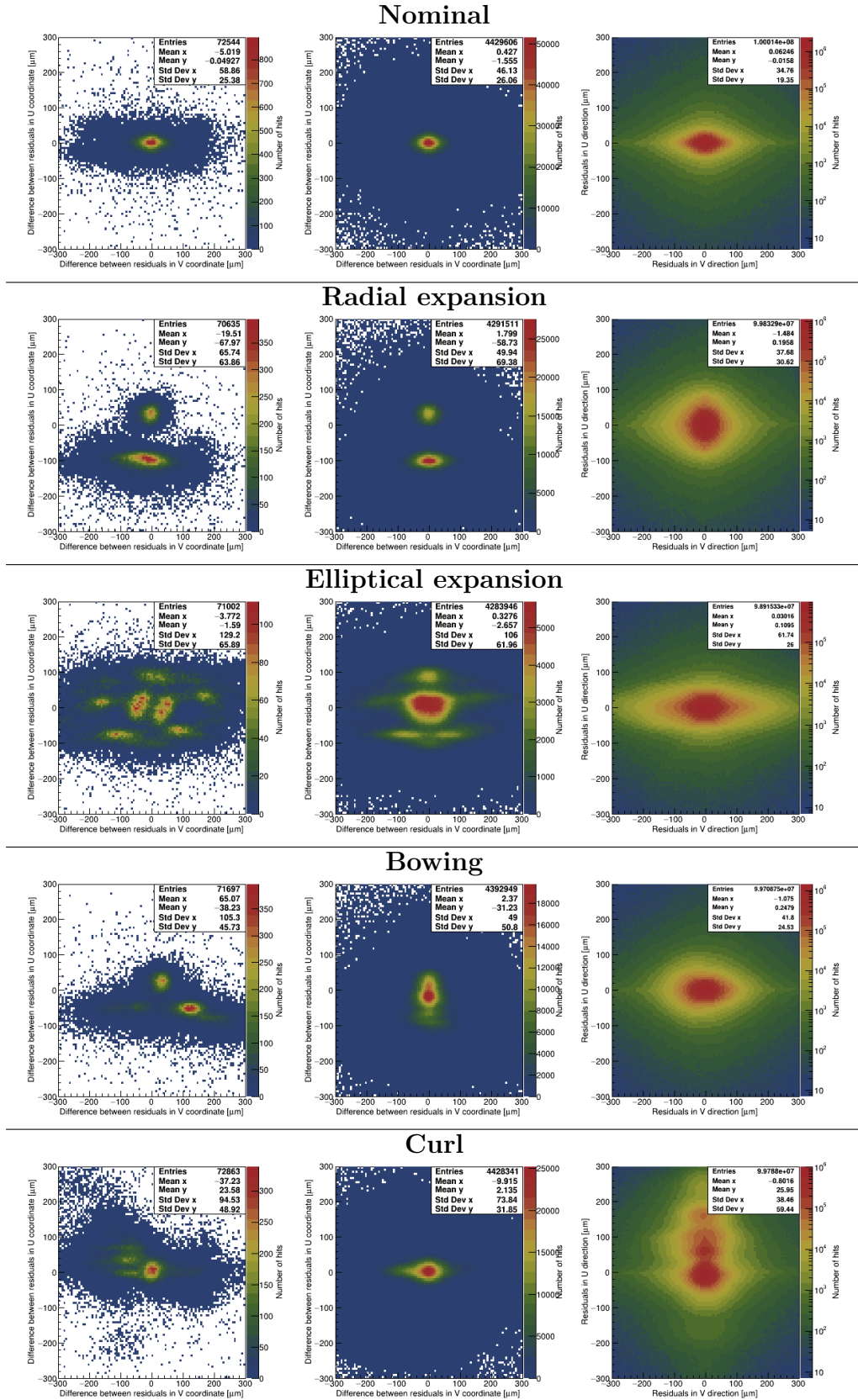
Clamshell

Twist

Telescope

Skew

Z expansion

Figure E.2: Validation plots for nominal geometry and weak modes by simulated $\Upsilon(4S)$: difference distribution for hits in overlapping sensors with different (left) and the same (center) position in a ladder, residual distribution for other hits (right)
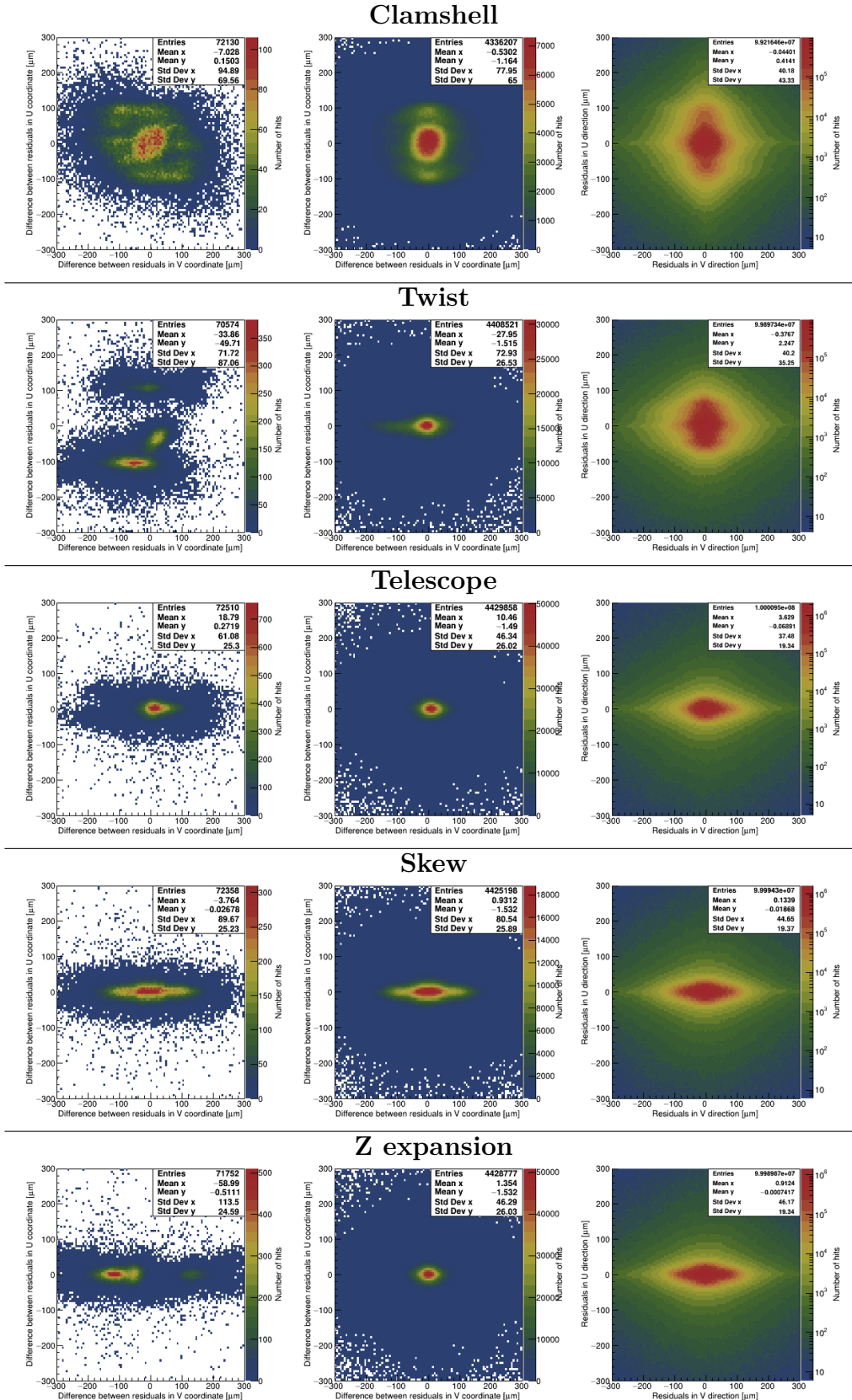
Nominal

Radial expansion

Elliptical expansion

Bowing

Curl

Figure E.3: Validation plots for nominal geometry and weak modes by simulated $e^+e^- \rightarrow \mu^+\mu^-$: difference distribution for hits in overlapping sensors with different (left) and the same (center) position in a ladder, residual distribution for other hits (right)

Figure E.4: Validation plots for nominal geometry and weak modes by simulated $e^+e^- \to \mu^+\mu^-$: difference distribution for hits in overlapping sensors with different (left) and the same (center) position in a ladder, residual distribution for other hits (right)

F. Monitoring results for collisions

Results for the cosmic sample collected in experiment 7 are discussed in Chapter 7. After cosmic data taking, Belle II started to collect collision data, and the alignment monitoring results for this campaign are discussed here. The presentation starts with sensor surface deformation results and the χ^2 invariant modes' plots follow.

F.1   Monitoring sensor surface deformations

For collision data, quadratic and cubic surface deformations were calculated and eliminated. A small quartic deformation was indentified in some sensors (e.g. 4.10.2). The surface monitoring plot can be found in Figure F.1 and extracted alignment parameters are in Table F.1. The value of the P_{04} parameter corresponds with the value observed with the cosmic sample. According to observations using cosmic and collision samples, quartic surface deformations in the large rectangular silicon sensors are proved. The error of the monitoring tool is 20.35 μm. The error value is two times higher than the observed value using cosmic sample. The number of collected hits in this sensor is similar to the sensor used in the cosmic sample. The precision is probably related to the number of hits on a track. We use two times more hits in the vertex detector and the central drift chamber in the cosmic sample. In summary, quartic deformations do not affect the precision because the values of deformation are compatible with the error of deformation measurement.
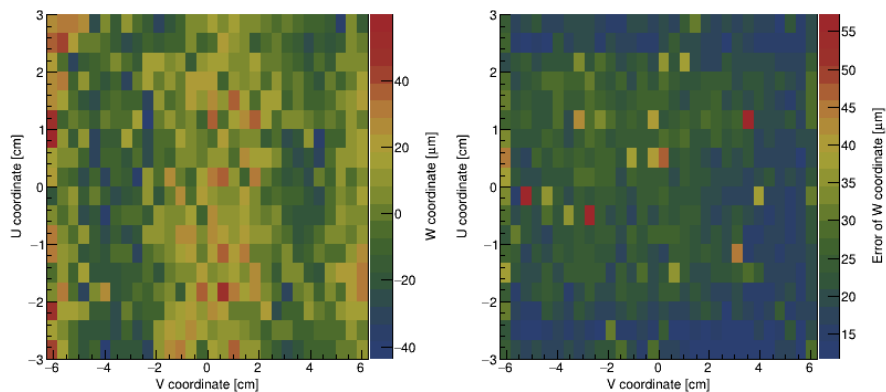

Figure F.1: Quartic deformation of sensors in early Phase 3: w residual distribution as a function of u and v coordinates for strip sensor 4.10.2 after applying rigid body, quadratic, and cubic parameters (left); projected error of w residual on sensor surface (right).

P_u	-0.78 ± 0.25 μm	P_α	0.17 ± 0.18 μm			
P_v	-0.53 ± 0.30 μm	P_β	0.64 ± 0.19 μm	P_{04}	10.89 ± 0.32 μm
P_w	-0.04 ± 0.10 μm			P_{13}	-1.80 ± 0.45 μm
		P_{03}	-5.51 ± 0.29 μm	P_{22}	-0.53 ± 0.52 μm
P_{02}	0.63 ± 0.22 μm	P_{12}	3.08 ± 0.44 μm	P_{31}	-2.63 ± 0.49 μm
P_{11}	-1.60 ± 0.32 μm	P_{21}	-4.01 ± 0.43 μm	P_{40}	-1.49 ± 0.32 μm
P_{20}	-0.23 ± 0.25 μm	P_{30}	0.84 ± 0.29 μm			

Table F.1: Monitoring of 4.10.2 sensor shift (left top), rotation (center top), quadratic (left bottom), cubic (center bottom) and quartic (right) parameters in Phase 3 early

F.2 Validation plots for χ^2 invariant modes

The procedure to find χ^2 invariant modes was described earlier and its result can be found in Figure F.2. From monitoring plots, no weak mode is identified. Though the spread of the results is higher compared to nominal geometry, we can conclude there are no weak modes with amplitude significantly higher than detector and tracking resolution.
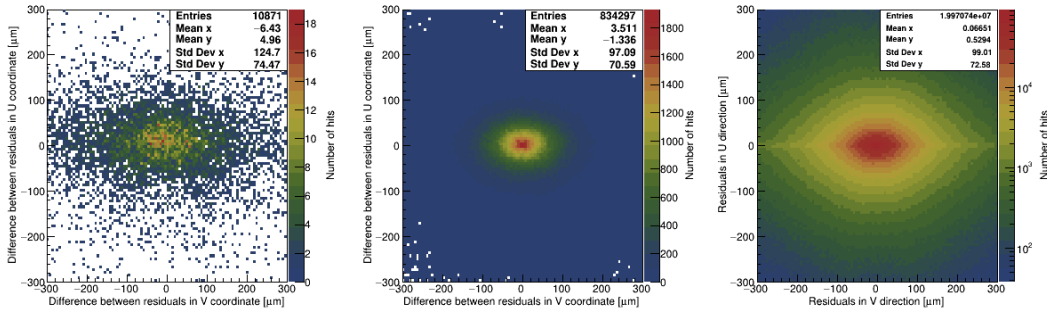

Figure F.2: Validation result for cosmic data in experiment 7: difference distribution for hits in overlapping sensors with different (left) and the same (center) position in a ladder, residual distribution for other hits (right)

G. m_{bc} fitting function shapes

In Chapter 8 we introduce probability distributions (pdfs) used for fitting m_{bc} distributions in individual channels. The fitted values of pdf shapes are shown in figures of this section. The fits were done using a simulated signal or background samples.

G.1 Fits for $B^0 \rightarrow D^-\pi^+$ events

The signal pdf is described as a Crystal Ball distribution in Eq. (8.15) with fitted parameters in Table 8.9 and is shown in Figure G.1.
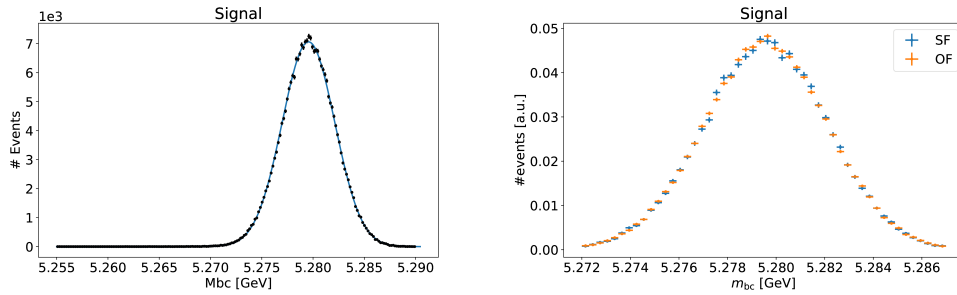
Figure G.1: Fit of a Crystall Ball shape for signal $B^0 \rightarrow D^-\pi^+$ simulated events (left) and comparison between SF (orange) and OF (blue) events (left).

The continuum background pdf is described as an Argus distribution in Eq. (8.16) with extracted parameters in Table 8.9 and is shown in Figure G.2.
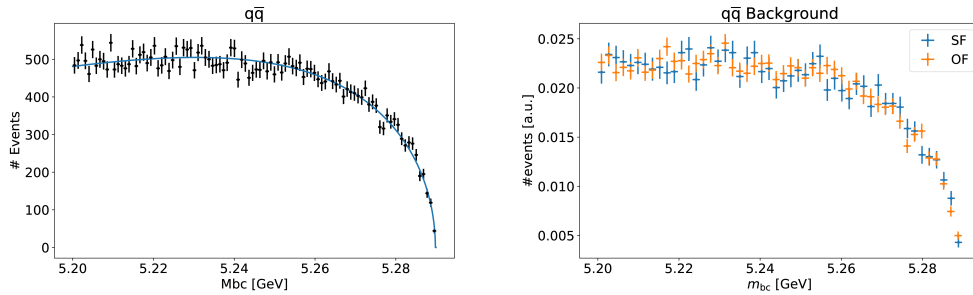

Figure G.2: Fit of an Argus shape for continuum background $B^0 \rightarrow D^-\pi^+$ simulated events (left) and comparison between SF (orange) and OF (blue) events (left).

The $b\bar{b}$ pdf is described as sum of Argus and Crystal Ball shapes in Eq. (8.17) with fitted parameters in Table 8.9 and is shown in Figure G.3.

G.2 Fits for $B^0 \rightarrow J/\psi(\rightarrow \mu^+\mu^-)K_S^0$ events

The signal pdf was described as a Crystal Ball distribution in Eq. (8.15) with fitted parameters in Table 8.10 and is shown in Figure G.4. The background pdf
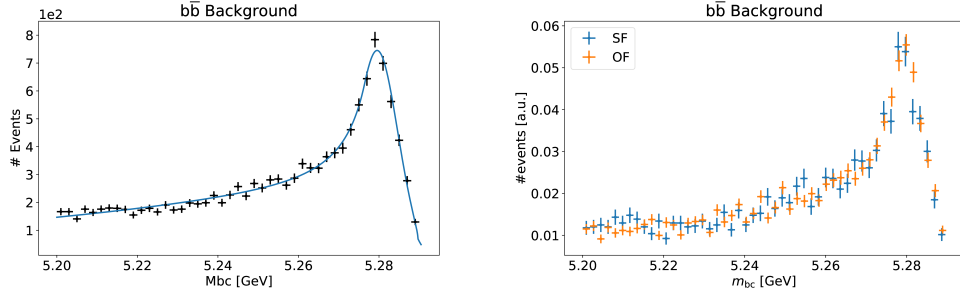
Figure G.3: Fit of summed shapes for $b\bar{b}$ background $B^0 \rightarrow D^-\pi^+$ simulated events (left) and comparison between SF (orange) and OF (blue) events (left).

was described as a sum of Argus and Gaussian distributions in Eq. (8.19) with fitted parameters in Table 8.10 and is shown in Figure G.4.
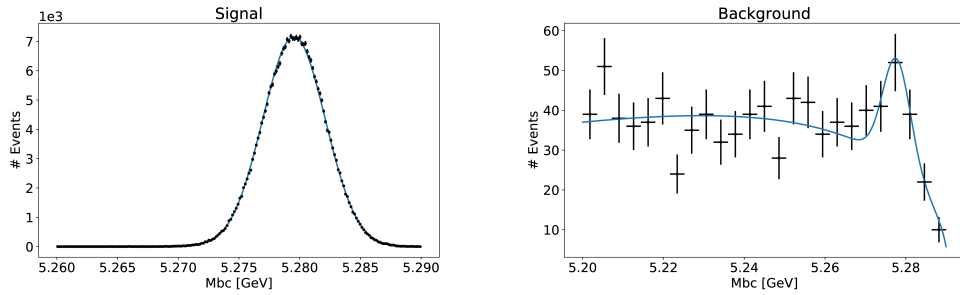

Figure G.4: Fits of shapes for signal (left) and background (right) $B^0 \rightarrow J/\psi(\mu^-\mu^+)K_S^0$ events

G.3 Fits for $B^0 \rightarrow J/\psi(\rightarrow e^+e^-)K_S^0$ events

The signal pdf was described as a Crystal Ball shape in Eq. (8.15) with fitted parameters (in Table 8.11 and) is presented in Figure G.5. The background pdf was described as a sum of Argus and Gaussian distributions in Eq. (8.19) with fitted parameters in Table 8.11 and is shown in Figure G.5.
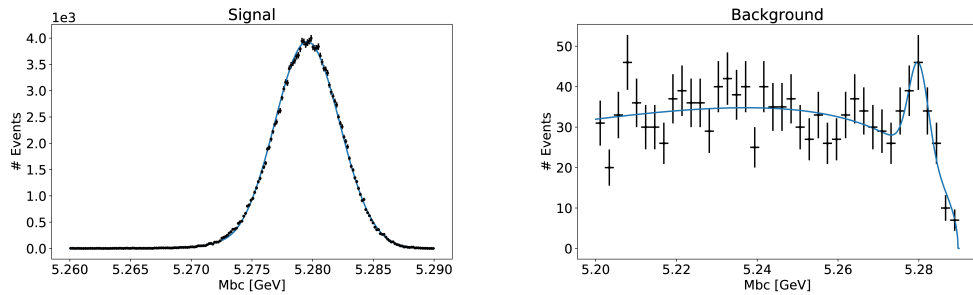

Figure G.5: Fits of shapes for signal (left) and background (right) $B^0 \rightarrow J/\psi(e^-e^+)K_S^0$ events

H. Asymmetry measurement

Using the prompt analysis results, the asymmetry between the number of events with B^0 tag and $\overline{B}^0$ tag for $J/\psi K^0_S$ channel can be measured. The asymmetry can be defined as:

$$\mathcal{A}_{\mathrm{CP}}(\Delta t) \equiv \frac{g^+(\Delta t) - g^-(\Delta t)}{g^+(\Delta t) + g^-(\Delta t)} = S_{\mathrm{f}} \sin(\Delta m_{\mathrm{d}} \Delta t) - C_{\mathrm{f}} \cos(\Delta m_{\mathrm{d}} \Delta t), \qquad \text{(H.1)}$$

where all parameters $f^{\pm}(\Delta t)$ can be found in Eq. (1) and the required expansion of the equation due to tag flavour algorithm results into:

$$\mathcal{A}_{\mathrm{CP}}(\Delta t) = -\Delta w + (1 - 2w)(S_f \sin(\Delta m_{\mathrm{d}} \Delta t) - C_f \cos(\Delta m_{\mathrm{d}} \Delta t)). \qquad \text{(H.2)}$$

Equivalently, for mixing, the asymmetry between the number of events with opposite flavour and same flavour for $B^0 \to \pi^+ D^-$ channel can be defined as:

$$\mathcal{A}_{\mathrm{mix}}(\Delta t) \equiv \frac{g^{\mathrm{OF}}(\Delta t) - g^{\mathrm{SF}}(\Delta t)}{g^{\mathrm{OF}}(\Delta t) + g^{\mathrm{SF}}(\Delta t)} = -\Delta w + (1 - 2w) \cos(\Delta m_{\mathrm{d}} \Delta t). \qquad \text{(H.3)}$$

In both Eq. (H.2) and (H.3) the variable Δw is neglected.

In Figure H.1 m_{bc} distributions with fit for non-divided $B^0 \to D^- \pi^+$ sample is shown. In Figure H.2 the Δt distribution for $B^0 \to \pi^+ D^-$ candidates is shown, where the background expectation is subtracted to show only the signal distributions.

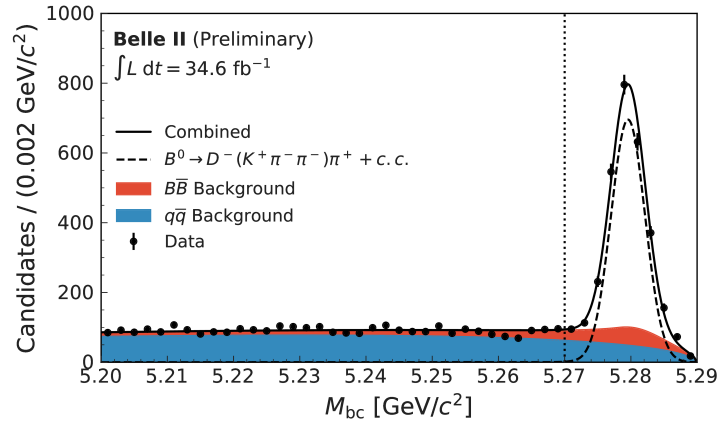Figure H.1: Combined result of m_{bc} for $B^0 \to D^- \pi^+$ channel [71]

In Figure H.3 m_{bc} distributions with fit for merged samples of $B^0 \to J/\psi(e^+e^-)K^0_S$ and $B^0 \to J/\psi(\mu^+\mu^-)K^0_S$ is shown. In Figure H.4 the Δt distribution for $B^0 \to J/\psi K^0_S$ candidates is shown, where the background expectation is subtracted to show only signal distributions.

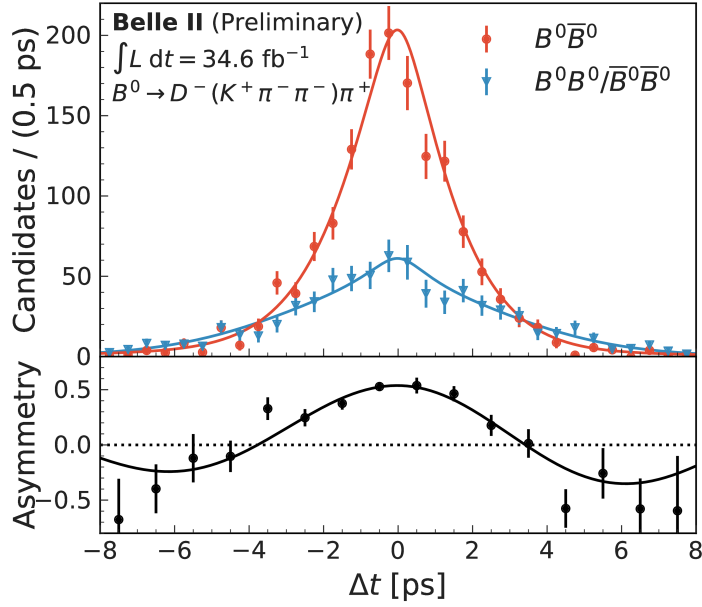Figure H.2: Combined results for Δt_{rec} for $B^0 \to D^-\pi^+$ candidates: the signal Δt distributions (top) obtained from the fit is shown for the events with the opposite flavour (red) and same flavour (blue); the asymmetry between the number of events with the opposite flavour and the same flavour (bottom) [71]
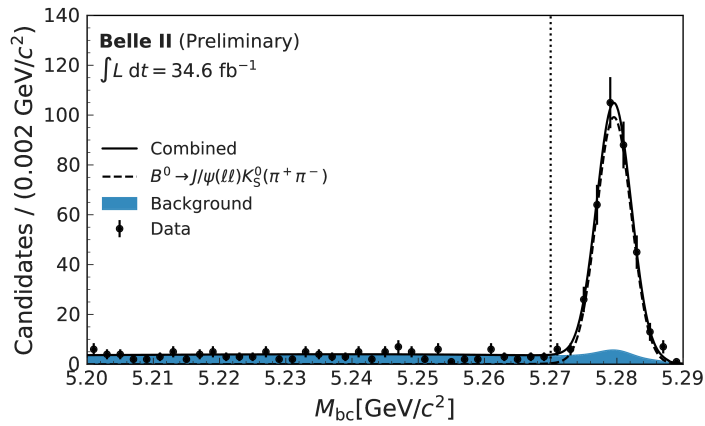

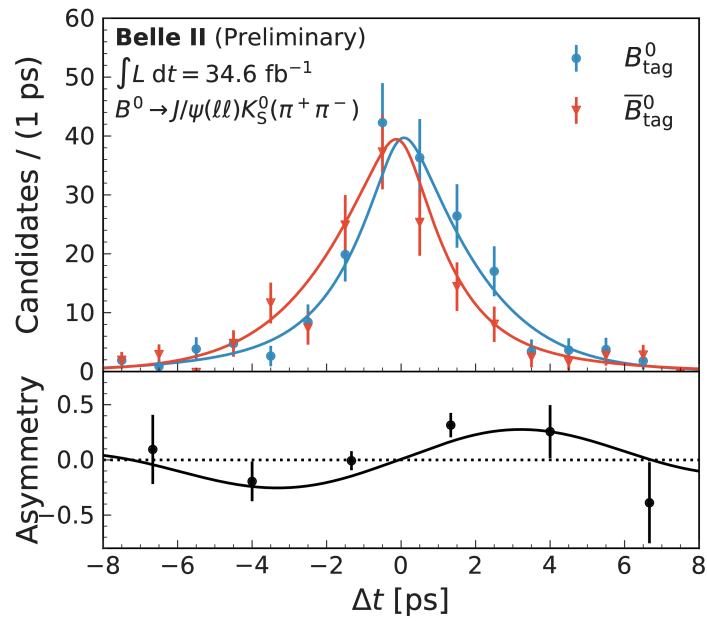Figure H.3: Combined result of m_{bc} for $B^0 \to J/\psi K_S^0$ (bottom) channels [71]

Figure H.4: Combined result of Δt_{rec} for $B^0 \rightarrow J/\psi K_S^0$ candidates: the signal Δt distributions (top) obtained from the fit is shown for the events win whichere the signal candidate is accompanied by B^0 (blue) or $\overline{B}^0$ (red); the asymmetry between number of events with the B^0 tag or $\overline{B}^0$ tag [71]